

โครงสร้าง สมบัติทางแสงและทางแม่เหล็กของโครงสร้างนาโนเจือแม่เหล็ก
กลุ่มซิงค์ออกไซด์ เตรียมโดยวิธีการสลายตัวทางความร้อนโดยตรง



นายเกียรติศักดิ์ น้อยพา

วิทยานิพนธ์นี้เป็นส่วนหนึ่งของการศึกษาตามหลักสูตรปริญญาวิทยาศาสตรดุษฎีบัณฑิต
สาขาวิชาฟิสิกส์
มหาวิทยาลัยเทคโนโลยีสุรนารี
ปีการศึกษา 2558

**STRUCTURE, OPTICAL AND MAGNETIC
PROPERTIES OF DILUTE MAGNETIC OXIDE
ZnO-BASED NANOSTRUCTURES PREPARED BY
A DIRECT THERMAL DECOMPOSITION METHOD**



**A Thesis Submitted in Partial Fulfillment of the Requirements for the
Degree of Doctor of Philosophy in Physics
Suranaree University of Technology
Academic Year 2015**

**STRUCTURE, OPTICAL AND MAGNETIC PROPERTIES OF
DILUTE MAGNETIC OXIDE ZnO-BASED NANOSTRUCTURES
PREPARED BY A DIRECT THERMAL
DECOMPOSITION METHOD**

Suranaree University of Technology has approved this thesis submitted in partial fulfillment of the requirements for the Degree of Doctor of Philosophy.

Thesis Examining Committee

(Assoc. Prof. Dr. Prayoon Songsiriritthigul)

Chairperson

(Prof. Dr. Santi Maensiri)

Member (Thesis Advisor)

(Assoc. Prof. Dr. Rattikorn Yimnirun)

Member

(Dr. Saroj Rujirawat)

Member

(Asst. Prof. Dr. Supree Pinitsoontorn)

Member

(Prof. Dr. Sukit Limpijumnong)

Vice Rector for Academic Affairs
and Innovation

(Prof. Dr. Santi Maensiri)

Dean of Institute of Science

เกียรติศักดิ์ น้อยพา : โครงสร้าง สมบัติทางแสงและทางแม่เหล็กของโครงสร้างนาโน
เจือแม่เหล็กกลุ่มซิงค์ออกไซด์ เตรียมโดยวิธีการสลายตัวทางความร้อน โดยตรง
(STRUCTURE, OPTICAL AND MAGNETIC PROPERTIES OF DILUTE MAGNETIC
OXIDE ZnO-BASED NANOSTRUCTURES PREPARED BY A DIRECT THERMAL
DECOMPOSITION METHOD) อาจารย์ที่ปรึกษา : ศาสตราจารย์ ดร.สันติ แม่นศิริ,
203 หน้า.

ในงานวิจัยนี้ การเจือแม่เหล็กกลุ่มซิงค์ออกไซด์ด้วยโลหะทรานซิชัน (TM = Co, Mn, Ni and Cu) และแรเอิร์ท (RE = Tb and Er) ถูกสังเคราะห์ขึ้นโดยวิธีการสลายตัวทางความร้อนโดยตรง โครงสร้างและรูปร่างลักษณะของตัวอย่างที่เตรียมได้ถูกวิเคราะห์ด้วยเทคนิค XRD TEM HRTEM และ SAED จากผลการศึกษาพบว่า การเจือสารแม่เหล็กกลุ่มโลหะทรานซิชันและแรเอิร์ทสามารถลดอุณหภูมิในการเตรียมวัสดุนาโนซิงค์ออกไซด์ที่มีความเป็นผลึกสูงและมีโครงสร้างแบบเวอร์ทไอซ์ ขนาดของผลึกและแลตทิซพารามิเตอร์ค่อยๆ เปลี่ยนไปเมื่อทำการเจือแม่เหล็กกลุ่มซิงค์ออกไซด์ด้วยโลหะทรานซิชันและแรเอิร์ท จากการวิเคราะห์ห้วงค์ประกอบทางเคมีด้วยเทคนิค XPS พบว่า การเจือด้วยโลหะทั้งสองกลุ่มทำให้ปริมาณอะตอมของซิงค์และออกซิเจนลดลง จากผลดังกล่าวอาจเป็นเพราะอะตอมของซิงค์ถูกแทนที่ด้วยไอออน TM^{2+} และ RE^{3+} จากปรากฏการณ์ดังกล่าว ทำให้เกิดการขาดหายไปของออกซิเจน (oxygen vacancy) จากเทคนิค XANES แสดงให้เห็นว่า เลขออกซิเดชันของโลหะที่เจือกลุ่ม Co Mn และ Ni คือ +2 +3 และ +2 ตามลำดับ ในทางตรงกันข้าม โลหะกลุ่ม Cu ที่ถูกเจือลงไปในตัวอย่างมีเลขออกซิเดชันเป็น 0 +1 (Cu^0/Cu^{1+}) และ +2 (Cu^{2+}) นอกจากนี้แล้ว ด้วยเทคนิคเดียวกันแสดงให้เห็นว่าตัวอย่างที่เจือด้วยกลุ่มโลหะ Tb และ Er มีเลขออกซิเดชันเป็น +3 จากการศึกษาสมบัติการดูดกลืนของแสงด้วยเทคนิค UV-Vis และการเปล่งแสงด้วยเทคนิค PL พบว่า ช่องว่างของแถบพลังงานของตัวอย่างมีการเปลี่ยนแปลงด้วยการเจือสารกลุ่มโลหะทรานซิชันและกลุ่มแรเอิร์ท จากการศึกษาสมบัติทางแม่เหล็ก พบว่า ตัวอย่างที่ยังไม่ได้เจือแสดงพฤติกรรมทางแม่เหล็กแบบไดอา ในขณะที่สารตัวอย่างที่ถูกเจือด้วยโลหะทรานซิชันแสดงสมบัติทางแม่เหล็กแบบพาราและเฟอร์โร ที่อุณหภูมิห้องและต่ำกว่าอุณหภูมิห้อง ค่าแมกเนไตเซชันอิ่มตัวสูงสุดของตัวอย่าง $Zn_{0.925}Co_{0.075}O$ $Zn_{0.925}Mn_{0.075}O$ $Zn_{0.975}Ni_{0.025}O$ และ $Zn_{0.950}Cu_{0.050}O$ ที่วัดได้มีค่า 0.072 emu/g 0.055 emu/g 0.388 emu/g และ 0.0109 emu/g ตามลำดับ จากการศึกษาด้วย modified Curie-Weiss law (θ) พบว่าค่าอุณหภูมิ Curie-Weiss ของตัวอย่าง $Zn_{0.925}Co_{0.075}O$ และ $Zn_{0.925}Mn_{0.075}O$ มีค่าติดลบ แสดงให้เห็นว่าเกิดอันตรกิริยาแม่เหล็กแบบพาราอันเนื่องมาจากไอออนเดี่ยวๆ หรืออันตรกิริยาแม่เหล็กแบบเอนติเฟอร์โรอันเนื่องมาจากการจับคู่

ของไอออน ซึ่งอธิบายด้วยอันตรกิริยาแบบ superexchange สำหรับอันตรกิริยาแบบเฟอร์โรในสารตัวอย่างนี้อธิบายด้วยอันตรกิริยาแบบ F -center exchange สำหรับในกลุ่มตัวอย่างที่เจือด้วยโลหะ Tb และ Er จะแสดงสมบัติแม่เหล็กแบบพาราและจะมากขึ้นเมื่อเพิ่มความเข้มข้นของการเจือ มีเพียงตัวอย่างที่เจือด้วยความเข้มข้นที่ 2.5% เท่านั้นที่แสดงสมบัติทางแม่เหล็กแบบเฟอร์โร จากการศึกษาด้วย modified Curie-Weiss law พบว่าค่าอุณหภูมิ Curie-Weiss (θ) มีค่าติดลบ แสดงให้เห็นว่าเกิดอันตรกิริยาแม่เหล็กแบบพาราหรือแอนติเฟอร์โร สำหรับความเป็นแม่เหล็กแบบเฟอร์โรของระบบซิงค์ออกไซด์ที่เจือด้วยโลหะกลุ่มแรเอิร์ทสามารถอธิบายด้วยอันตรกิริยาการแลกเปลี่ยนแบบ RKKY



สาขาวิชาฟิสิกส์

ปีการศึกษา 2558

ลายมือชื่อนักศึกษา _____

ลายมือชื่ออาจารย์ที่ปรึกษา _____

ลายมือชื่ออาจารย์ที่ปรึกษาร่วม _____

ลายมือชื่ออาจารย์ที่ปรึกษาร่วม _____

KIATTISAK NOIPA : STRUCTURE, OPTICAL AND MAGNETIC
PROPERTIES OF DILUTE MAGNETIC OXIDE ZnO-BASED
NANOSTRUCTURES PREPARED BY A DIRECT THERMAL
DECOMPOSITION METHOD. THESIS ADVISOR : PROF. SANTI
MAENSIRI, Ph.D. 203 pp.

MAGNETIC PROPERTIES/DILUTE MAGNETIC OXIDE/ ZnO-BASED
NANOSTRUCTURES/ DIRECT THERMAL DECOMPOSITION

In this dissertation, TM-doped ZnO (TM = Co, Mn, Ni and Cu) and RE-doped ZnO (RE = Tb and Er) were successfully synthesized by a direct thermal decomposition method. The structures and the morphology of the prepared samples were investigated by XRD, TEM, HRTEM and SAED. The doping of TM and RE ions lead to the decreasing of prepared temperature for a formation of highly crystalline ZnO wurtzite structure. An average crystallites sized and lattice parameter of a and c were slightly changed by doping of TM and RE atoms. XPS analysis found that the samples were slightly decreased zinc and oxygen atoms by doping, expected that Zn atoms were substituted by TM^{2+} and RE^{3+} ions. These phenomena induced oxygen vacancy form on surface of the samples. XANES spectra of Co, Mn, and Ni K -edges reveal that the Co, Mn, and Ni oxidation states are mainly +2, +3 and +2, respectively. In contrast, Cu valence states in the samples are mixed state of $\text{Cu}^0/\text{Cu}^{1+}$ and Cu^{2+} . Moreover, XANES spectra of Tb and Er L_3 -edges show that the valence state of Tb and Er ions in the samples is +3. The UV-visible optical absorption spectra and PL presented a band gaps of all the samples were changed by doping of TM and

RE ions. The nanocrystalline of undoped ZnO sample exhibits diamagnetic behavior at room temperature, whereas the TM- and RE-doped ZnO samples exhibit paramagnetism and ferromagnetism at room and below room temperature. The highest saturation magnetizations (M_s) for $Zn_{0.925}Co_{0.075}O$, $Zn_{0.925}Mn_{0.075}O$, $Zn_{0.975}Ni_{0.025}O$ and $Zn_{0.950}Cu_{0.050}O$ samples are 0.072 emu/g, 0.055 emu/g, 0.388 emu/g and 0.0109 emu/g, respectively. The fitting of modified Curie-Weiss law for Co- and Mn-doped ZnO nanorods ($x = 0.075$) show the negative Curie-Weiss temperature (θ). This analysis suggests that only ion show paramagnetic behavior and the paired ions become antiferromagnetic coupled, probably through superexchange mechanism. The ferromagnetism in this system can be explained by F -center exchange. In the case of RE-doped ZnO, revealing the paramagnetism increase with increasing Tb and Er concentrations, whereas the Tb-doped ZnO nanorods of $x = 0.025$, the ferromagnetic interaction are dominant. The fitting of modified Curie-Weiss law shows the negative θ values, indicating para/antiferromagnetic interactions among magnetic ions. The RKKY exchange interaction couple is an indirect exchange interaction by the s conduction electrons, have been considerable attention for explanation of ferromagnetism in RE-doped ZnO system.

School of Physics

Academic Year 2015

Student's Signature_____

Advisor's Signature_____

Co-advisor's Signature_____

Co-advisor's Signature_____

ACKNOWLEDGMENTS

I would like to express my deepest and sincere gratitude to my supervisor Prof. Dr. Santi Maensiri for their effective scientific supervision, instructive guidance, generous personal encouragement and supporting. I would like to thank Assoc. Prof. Dr. Rattikorn Yimmirun and Dr. Saroj Rujirawat my co-advisor for the inspiration they provided to ensure the completion of this dissertation. I would like to especially thank Assoc. Prof. Dr. Prayoon Songsiriritthigul and Asst. Prof. Dr. Supree Pinitsoontorn for serving on my PhD committee. I wish to thank Advance Materials Physics (AMPL), the Center for Scientific and Technological Equipment, Suranaree University of technology for research facilities supporting. I would like to give special thanks to SUT-PhD scholarship (Grant No.SUT-PhD/04/2554) for my PhD study and financial support for research presentation in both inside and outside the country. I would like to thank School of Physics, Institute of science, Suranaree University of Technology for providing many research facilities, NANOTEC-SUT Center of Excellence on Advanced Functional Nanomaterial from Suranaree University of Technology for the financial support. I would like to thank AMP group members for their friendship and guidance during work.

Finally, I would like to thank my parents for their never-ended supporting and sacrifices they made, to bring me up and give me the good life.

Kiattisak Noipa

CONTENS

	Page
ABSTRACT IN THAI.....	I
ABSTRACT IN ENGLISH.....	III
ACKNOWLEDGEMENTS.....	V
CONTENTS.....	VI
LIST OF TABLES.....	XI
LIST OF FIGURES.....	XII
LIST OF ABBREVIATIONS.....	XXVI
CHAPTER	
I INTRODUCTION.....	1
1.1 Background and significance of study.....	1
1.2 Objectives of the dissertation.....	5
1.3 Limitations of study.....	6
1.4 Location of the research.....	6
1.5 Anticipated outcomes.....	6
1.6 Dissertation structure.....	7
II LITERATURE REVIEWS.....	8
2.1 Dilute magnetic semiconductors.....	8
2.2 Dilute magnetic oxides.....	10

CONTENS (Continued)

	Page
2.3 Theoretical models for explaining ferromagnetism in DMSs and DMOs	
2.3.1 Zener Model.....	14
2.3.2 The RKKY model.....	15
2.3.3 The double-exchange model.....	16
2.3.4 The bound magnetic polaron model.....	18
2.3.5 Transition metal clustering model.....	21
2.3.6 Other Mechanisms.....	22
2.4 Properties of ZnO.....	23
2.5 ZnO-based dilute magnetic semiconductors.....	25
2.6 Potential spintronic devices based on DMS materials.....	31
III EXPERIMENTAL PROCEDERURE.....	33
3.1 Sample preparation.....	33
3.2 Thermogravimetric and differential thermal analysis.....	39
3.3 Phase identification, structure, characterization and morphology.....	40
3.3.1 X-ray diffraction (XRD).....	40
3.3.2 Transmission electron microscopy (TEM), HRTEM and SAED.....	42
3.4 X-ray photoelectron spectroscopy (XPS).....	42
3.5 Optical properties and valence state determination.....	44
3.5.1 UV-visible spectroscopy (UV-Vis).....	44

CONTENS (Continued)

	Page
3.5.2 X-ray absorption near-edge structure (XANES).....	45
3.5.3 Photoluminescence (PL).....	47
3.6 Magnetic measurement.....	48
IV RESULTES AND DISCUSSION.....	50
4.1 Phase formation and composition.....	50
4.2 TM-doped ZnO nanorods.....	52
4.2.1 Structural characterization, morphology and chemical compositions of TM-doped ZnO (i.e. TM = Co, Mn, Ni and Cu).....	52
4.2.2 The absorpion and photoluminescence of TM-doped ZnO Nanorods (i.e. TM = Co, Mn, Ni and Cu).....	92
4.2.3 The magnetic properties of magnetic ions in Co-, Mn- and Ni-doped ZnO nanorods.....	112
4.2.4 The magnetic properties of nonmagnetic ions in Cu-doped ZnO.....	126
4.3 RE-doped ZnOnanorods.....	130
4.3.1 Structural characterization, morphology and chemical compositions of RE-doped ZnO (i.e. RE = Tb and Er).....	130
4.3.2 The absorption and photoluminescence of RE-doped ZnO nanorods (i.e. RE = Tb and Er).....	148

CONTENS (Continued)

	Page
4.3.3 The magnetic properties of magnetic ions in Tb-and Er-doped ZnO Nanorods.....	158
V CONCLUSION AND SUGGESTION.....	166
5.1 Structure characterization, morphology and chemical composition of undoped ZnO and ZnO doped with 3 <i>d</i> - and 4 <i>f</i> -cations.....	166
5.2 Optical properties of undoped ZnO and ZnO doped with 3 <i>d</i> -and 4 <i>f</i> -cations.....	168
5.3 Magnetic properties of undoped ZnO and ZnO doped with 3 <i>d</i> -and 4 <i>f</i> -cations.....	169
5.4 Suggestion for future work on ZnO doped with 3 <i>d</i> -and 4 <i>f</i> -cations.....	171
REFERENTES.....	173
APPENDICES.....	186
APPENDICE A RESULTS AND DISSCUSSION ON NiO AND Fe-DOPED NiO SYSTEM.....	187
APPENDICE B PUBLICTION AND PRESENTATION.....	201
CURRICULUM VITAE.....	203

LIST OF TABLES

Table	Page
2.1 Lists of some dilute magnetic oxides.....	13
2.2 A comparison of magnetic interaction.....	18
2.3 Some nanostructures of ZnO-based dilute magnetic oxides reported in literature.....	30
3.1 List of the materials used for ZnO nanorods preparation, quoting their source and purity 38	
4.1 Summary of crystallite size of undoped ZnO and TM-doped ZnO nanorods thermally decomposed at 300 °C at for 6 h.....	59
4.2 Summary of lattice constant (<i>a</i> and <i>c</i>) of undoped ZnO and TM-doped ZnO nanorods thermally decomposed at 300 °C at for 6 h.....	60
4.3 Actual atomic concentrations of Zn, Co, Mn, Ni, Cu and O in undoped ZnO with nominally TM-doped ZnO nanorods calculated by XPS analysis.....	70
4.4 Results of Co 2p _{3/2} , O ₁ and O ₂ XPS spectra for Co-doped ZnO nanorods with x = 0.025, 0.050, 0.075 and 0.100.....	71
4.5 Fitting results of Mn 2p _{3/2} , O ₁ , O ₂ and O ₃ XPS spectra for Mn-doped ZnO nanorods with x = 0.025, 0.050, 0.075 and 0.100.....	71

LIST OF TABLES (Continued)

Table	Page
4.6 The binding energy and atomic percentages of $Cu2p_{3/2}$, energy shift and atomic percentages of O_1 and O_2 calculated by XPS spectra of undoped ZnO and Cu-doped ZnO nanorods.....	83
4.7 Summary of band gap energy (E_g) of undoped ZnO and TM-doped ZnO nanorods prepared at 300 °C for 6 h.....	97
4.8 Summary of magnetization of Co-, Mn- and Ni-doped ZnO at room- temperature.....	114
4.9 Summary of crystallite size and lattice constant (a and c) of undoped ZnO and RE-doped ZnO nanorods thermally decomposed at 300 °C for 6 h.....	131
4.10 Actual atomic concentrations of Zn, Tb, Er and O in undoped ZnO and nominally RE-doped ZnO nanorods calculated by XPS analysis.....	138
4.11 The binding energy and atomic percentages of $Tb4d$, O_1 and O_2 calculated by XPS spectra of undoped ZnO and Tb-doped ZnO nanorods.....	145
4.12 The binding energy and atomic percentages of $Er4d$, O_1 and O_2 calculated by XPS spectra of undoped ZnO and Er-doped ZnO nanorods.....	145
4.13 Summary of band gap energy (E_g) of undoped ZnO and RE-doped ZnO nanorods prepared at 300 °C for 6 h.....	154

LIST OF FIGURES

Figure	Page
2.1 Two types of semiconductors: (a) a nonmagnetic semiconductor (b) a dilute magnetic semiconductor: a nonmagnetic semiconductor to which a dilute concentration of ions carrying an unpaired spin has been added.....	10
2.2 Computed values of the Curie temperature T_C for various p -type semiconductors containing 5% of Mn and 3.5×10^{20} holes per cm^3	10
2.3 Direct super-exchange interaction: Anti-ferromagnetic coupling of adjacent TM cations through a shared anion.....	14
2.4 Indirect super-exchange interaction: Ferromagnetic coupling of localized spins through the conduction electrons.....	15
2.5 Double-exchange mechanisms in mixed-valence manganites.....	17
2.6 Representation of magnetic polarons model.....	20
2.7 A schematic energy level diagram for a ferromagnetic coupling between two Co ions via a donor electron trapped in the oxygen vacancy.....	21
2.8 Stick and ball representation of ZnO-hexagonal wurtzite.....	23
2.9 Illustration of various structures used for magnetic random access memory (MRAM) and hard disk drive (HDD) storage applications.....	32

LIST OF FIGURES (Continued)

Figure	Page
3.1 A schematic view of the preparation samples by direct thermal decomposition method.....	36
3.2 A schematic view of the characterization and data analysis.....	37
3.3 Diagram of thermogravimetric and differential thermal analysis.....	39
3.4 (a) The Bragg reflection from a particular set of the lattice planes separated by a distance d and (b) θ is a half of the total angle by which the incident beams is detected.....	41
3.5 Schematic diagram of the XPS.....	44
3.6 XANES and EXAFS regions of X-ray absorption spectrum.....	46
3.7 (a) Schematic diagram of the XAS (b) Schematic measured of the XANES.....	46
3.8 Typical experimental set up for PL measurements.....	48
3.9 Schematic diagram of the VSM.....	49
4.1 (a) TG-DTA of undoped ZnO sample and (b) DTA data for TM- And RE-doped ZnO sample with $x = 0.025$	51
4.2 XRD patterns of thermally decomposed undoped ZnO sample in air at 400 °C for 6 h and undoped ZnO prepared in air at 300 °C for 6 h.....	54
4.3 XRD patterns of thermally decomposed undoped ZnO in air at 400 °C for 6 h (a) and (b) Co-doped ZnO prepared in air at 300 °C for 6 h.....	54

LIST OF FIGURES (Continued)

Figure	Page
4.4 (a) XRD patterns of undoped ZnO sample thermally decomposed in air at 400 °C for 6 h and undoped ZnO sample prepared in air at 300 °C for 6 h and (b) the XRD patterns of Mn-doped ZnO samples prepared in air at 300 °C for 6 h with $x = 0.025, 0.050, 0.075$ and 0.100 , respectively.....	55
4.5 (a) XRD patterns of undoped ZnO sample thermally decomposed ZnO in air at 400 °C for 6 h and undoped ZnO sample prepared in air at 300 °C for 6 h and (b) the XRD patterns of Ni-doped ZnO samples prepared in air at 300 °C for 6 h with $x = 0.025, 0.050, 0.075$ and 0.100 , respectively.....	56
4.6 XRD patterns of undoped ZnO (calcined at 400 °C) (a) and Cu-doped ZnO in air at 300 °C for 6 h for $x = 0.025$ (b), $x = 0.050$ (c) , $x = 0.075$ (d) and $x = 0.100$ (e), respectively. The inset shows XRD patterns precursor calcined in air at 300 °C for 6 h.....	57
4.7 An average crystallite size of undoped ZnO sample prepared at 400 °C for 6 h, (a) Co-,Mn- and Ni-doped ZnO nanorods and (b) Cu-doped ZnO nanorods prepared at 300 °C for 6 h.....	61
4.8 Lattice constant of undoped ZnO sample prepared at 400 °C for 6 h, (a) a parameter and (b) c parameter of Co-, Mn- and Ni-doped ZnO nanorods prepared at 300 °C for 6 h, respectively.....	62

LIST OF FIGURES (Continued)

Figure	Page
4.9 Lattice constant of undoped ZnO sample prepared at 400 °C for 6 h, (a) <i>a</i> parameter and (b) <i>c</i> parameter of Cu-doped ZnO nanorods prepared at 300 °C for 6 h.....	63
4.10 TEM bright field, and high-resolution TEM (HRTEM) images with corresponding SEAD patterns of undoped ZnO sample prepared in air at 400 °C for 6 h.....	64
4.11 TEM bright field, and high-resolution TEM (HRTEM) images with corresponding SEAD patterns of undoped ZnO sample prepared in air at 400 °C for 6 h (a) and Co-doped ZnO samples prepared in air at 300 °C for 6 h with $x = 0.025$ (b), $x = 0.050$ (c), $x = 0.075$ (d), and $x = 0.100$ (e).....	65
4.12 TEM bright field, and high-resolution TEM (HRTEM) images with corresponding SEAD patterns of undoped ZnO sample prepared in air at 400 °C for 6 h (a) and Mn-doped ZnO samples prepared in air at 300 °C for 6 h with $x = 0.025$ (b), $x = 0.050$ (c), $x = 0.075$ (d), and $x = 0.100$ (e).....	66

LIST OF FIGURES (Continued)

Figure	Page
4.13 TEM bright field, and high-resolution TEM (HRTEM) images with corresponding SEAD patterns of undoped ZnO sample prepared in air at 400 °C for 6 h (a) and (b) Ni-doped ZnO samples prepared in air at 300 °C for 6 h with $x = 0.025$	67
4.14 TEM bright field, and high-resolution TEM (HRTEM) images with corresponding SEAD patterns of undoped ZnO sample prepared in air at 400 °C for 6 h (a) and Cu-doped ZnO samples prepared in air at 300 °C for 6 h with $x = 0.025$ (b), $x = 0.050$ (c), $x = 0.075$ (d), and $x = 0.100$ (e).....	68
4.15 XPS spectra of TM-doped ZnO nanorods with the survey scan.....	69
4.16 Zn _{2p} X-ray photoelectron spectra (XPS) of Co-doped ZnO samples prepared in air at 300 °C for 6 h with $x = 0.025$, 0.050, 0.075 and 0.100 compared with undoped ZnO.....	73
4.17 Zn _{2p} X-ray photoelectron spectra (XPS) of Mn-doped ZnO samples prepared in air at 300 °C for 6 h with $x = 0.025$, 0.050, 0.075 and 0.100 compared with undoped ZnO.....	74
4.18 Zn _{2p} X-ray photoelectron spectra (XPS) of Ni-doped ZnO samples prepared in air at 300 °C for 6 h with $x = 0.025$ compared with undoped ZnO.....	75

LIST OF FIGURES (Continued)

Figure	Page
4.19 High-resolution scan of O1s for Co-doped ZnO with $x = 0.025$ (a), 0.050(b), $x = 0.075$ (c) and $x = 0.100$ (d) compared with undoped ZnO (e).....	76
4.20 High-resolution scan of O1s for Mn-doped ZnO with $x = 0.025$ (a), 0.050(b), $x = 0.075$ (c) and $x = 0.100$ (d) compared with undoped ZnO (e).....	77
4.21 High-resolution scan of O1s for undoped ZnO (a) and Ni-doped ZnO for $x = 0.025$ (b).....	78
4.22 High-resolution scans of Co2p for Co-doped ZnO samples prepared in air at 300 °C for 6 h with $x = 0.025, 0.050, 0.075$ and 0.100.....	80
4.23 High-resolution scans of Mn2p for Mn-doped ZnO samples prepared in air at 300 °C for 6 h with $x = 0.025, 0.050, 0.075$ and 0.100.....	81
4.24 High-resolution scans of Ni2p for Ni-doped ZnO samples prepared in air at 300 °C for 6 h with $x = 0.025$	82
4.25 Zn2p X-ray photoelectron spectra (XPS) of Cu-doped ZnO samples prepared in air at 300 °C for 6 h with $x = 0.025, 0.050, 0.075$ and 0.100 compared with undoped ZnO.....	84
4.26 High-resolution scans of O1s for Cu-doped ZnO with $x = 0.025$ (a), 0.050(b), $x = 0.075$ (c) and $x = 0.100$ (d) compared with undoped ZnO.....	85

LIST OF FIGURES (Continued)

Figure	Page
4.27 High-resolution scans of $Cu2p$ for Cu-doped ZnO samples prepared in air at 300 °C for 6 h with $x = 0.025, 0.050, 0.075$ and 0.100, respectively.....	87
4.28 Room-temperature optical absorbance spectra of undoped ZnO nanorods calcined at 400 °C for 6 h and TM-doped ZnO nanorods prepared in air at 300 °C for 6 h, (a) Co-doped ZnO, (b) Mn-doped ZnO and (c) Ni-doped ZnO nanorods, respectively.....	94
4.29 Room-temperature optical absorbance spectra of undoped ZnO nanorods calcined at 400 °C for 6 h and Cu-doped ZnO nanorods prepared in air at 300 °C for 6 h.....	94
4.30 Plot of $(ah\nu)^2$ as a function of photon energy $(h\nu)$ for undoped ZnO nanorods prepared in air at 400 °C for 6 h and TM-doped ZnO nanorods prepared in air at 300 °C for 6 h. (a) Co-doped ZnO, (b) Mn-doped ZnO and (c) Ni-doped ZnO nanorods, respectively.....	98
4.31 Plot of $(ah\nu)^2$ as a function of photon energy $(h\nu)$ for undoped ZnO nanorods prepared in air at 400 °C for 6 h and Cu-doped ZnO nanorods prepared in air at 300 °C for 6 h.....	99

LIST OF FIGURES (Continued)

Figure	Page
4.32 Band gap versus doping concentration of undoped ZnO nanorods calcined at 400 °C for 6 h and TM-doped ZnO nanorods prepared in air at 300 °C for 6 h, respectively.....	100
4.33 Band gap versus doping concentration of undoped ZnO nanorods calcined at 400 °C for 6 h and Cu-doped ZnO nanorods prepared in air at 300 °C for 6 h, respectively.....	100
4.34 (a) Co-K-edge X-ray absorption near-edge structure (XANES) for Co-doped ZnO ($x = 0.025, 0.015, 0.075$ and 0.100) samples, CoO and Co ₃ O ₄ are reference materials for Co ²⁺ and Co ³⁺ , compared with the Zn K-edge XANES spectrum in ZnO (b).....	104
4.35 (a) Mn-K-edge X-ray absorption near-edge structure (XANES) for Mn-doped ZnO ($x = 0.025, 0.015, 0.075$ and 0.100) samples, MnO, Mn ₂ O ₃ and MnO ₂ are reference materials for Mn ²⁺ , Mn ³⁺ and Mn ⁴⁺ , compared with the Zn K-edge XANES spectrum in ZnO (b).....	105
4.36 (a) Ni-K-edge X-ray absorption near-edge structure (XANES) for Ni-doped ZnO ($x = 0.025$) samples, NiO is reference materials for Ni ²⁺ , compared with the Zn K-edge XANES spectrum in ZnO (b).....	106

LIST OF FIGURES (Continued)

Figure	Page
4.37 Cu-K-edge X-ray absorption near-edge structure (XANES) for Cu-doped ZnO ($x = 0.025$) samples, Cu ₂ O and CuO are reference materials for Cu ¹⁺ and Cu ²⁺ , respectively.....	107
4.38 Room temperature photoluminescence spectra of undoped ZnO and TM-doped ZnO nanorods, (a) Co-doped ZnO (b) Mn-doped ZnO and (c) Ni-doped ZnO samples, under 325 nm light excitation.....	108
4.39 Room temperature photoluminescence spectra of undoped ZnO and Cu-doped ZnO nanorods, under 325 nm light excitation.....	111
4.40 The magnetization magnetic measurement (M) versus applied magnetic field (H) were performed on undoped ZnO, (a) Co-doped and (b) Mn-doped ZnO Nanorods with different the transition metal content obtained at 293 K from VSM measurement.....	113
4.41 The magnetization magnetic measurement (M) versus applied magnetic field (H) was performed on Zn _{0.975} Ni _{0.025} O at 293 K from VSM measurement.....	114
4.42 Schematic diagrams showing the F-center exchange mechanism in TM-doped ZnO nanorods.....	118
4.43 Schematic diagram of oxygen-vacancy-induced ferromagnetism through overlapping of polarons.....	119

LIST OF FIGURES (Continued)

Figure	Page
4.44 Schematic diagrams of the interstitial site and the substitution site Mn in a ZnO lattice after doping.....	119
4.45 $M \times H$ curves for $Zn_{0.925}Co_{0.075}O$ (a), $Zn_{0.925}Mn_{0.075}O$ (b) and $Zn_{0.975}Ni_{0.025}O$ (c) samples taken at $T=50K$ and $293K$, showing the existence of ferromagnetism.....	122
4.46 (a) and (b) display the temperature-dependent magnetization ($M-T$) curves of Co- and Mn- doped ZnO samples, respectively. Inset (a) and (b): the modified curie-weiss fitting to the data between 150 K and 300 K under 1 kOe as a function of temperature and fitting result using the modified Curie-weiss law.....	125
4.47 The temperature dependent magnetization ($M-T$) curve of $Zn_{0.975}Ni_{0.025}O$ sample was recorded using VSM magnetometer in temperature range of 50 to 293 K with a magnetic field at 1000 Oe.....	126
4.48 (a) the magnetization magnetic measurement (M) versus applied magnetic field (H) were performed on undoped ZnO and Cu-doped with different Cu ions content obtained at 293 K from VSM measurement and (b) $M \times H$ curves for Cu-doped ZnO ($x=0.025$) sample taken at $T= 50K$ and $293K$	129

LIST OF FIGURES (Continued)

Figure	Page
4.49 XRD patterns of undoped ZnO sample thermally decomposed in air at 400 °C for 6 h and undoped ZnO prepared in air at 300 °C for 6 h (a) and (a) the XRD patterns of Tb-doped ZnO samples prepared in air at 300 °C for 6 h with $x = 0.025, 0.050, 0.075$ and 0.100, respectively.....	132
4.50 XRD patterns of undoped ZnO sample thermally decomposed in air at 400 °C for 6 h and undoped ZnO prepared in air at 300 °C for 6 h (a) and (b) the XRD patterns of Er-doped ZnO samples prepared in air at 300 °C for 6 h with $x = 0.025, 0.050, 0.075$ and 0.100, respectively.....	133
4.51 An average crystallite size of undoped ZnO prepared at 400 °C for 6 h, Tb- and Er-doped ZnO nanorods prepared at 300 °C for 6 h.....	134
4.52 Lattice constant of undoped ZnO prepared at 400 °C for 6 h, (a) a parameter and (b) c parameter of Tb- and Er-doped ZnO nanorods prepared at 300 °C for 6 h, respectively.....	135
4.53 TEM bright field, High-resolution TEM (HRTEM) images with corresponding SEAD patterns of undoped ZnO sample prepared in air at 400 °C for 6 h (a) and Tb-doped ZnO samples prepared in air at 300 °C for 6 h with $x = 0.025$ (b), $x = 0.050$ (c), $x = 0.075$ (d), and $x = 0.100$ (e)....	136

LIST OF FIGURES (Continued)

Figure	Page
4.54 TEM bright field, High-resolution TEM (HRTEM) images with corresponding SEAD patterns of undoped ZnO sample prepared in air at 400 °C for 6 h (a) and Er-doped ZnO samples prepared in air at 300 °C for 6 h with $x = 0.025$ (b), $x = 0.050$ (c), $x = 0.075$ (d), and $x = 0.100$ (e).....	137
4.55 (a) XPS spectra of undoped ZnO, (b) Tb-doped ZnO nanorods and (c) Er-doped ZnO nanorods with the survey scan mode.....	139
4.56 Zn2p X-ray photoelectron spectra (XPS) of Tb-doped ZnO samples prepared in air at 300 °C for 6 h with $x = 0.025$, 0.050, 0.075 and 0.100 compared with undoped ZnO.....	141
4.57 Zn2p X-ray photoelectron spectra (XPS) of Er-doped ZnO samples prepared in air at 300 °C for 6 h with $x = 0.025$, 0.050, 0.075 and 0.100 compared with undoped ZnO.....	142
4.58 High-resolution scan of O1s for Tb-doped ZnO with $x = 0.025$ (a), 0.050(b), $x = 0.075$ (c) and $x = 0.100$ (d).....	143
4.59 High-resolution scan of O1s for Er-doped ZnO with $x = 0.025$ (a), 0.050(b), $x = 0.075$ (c) and $x = 0.100$ (d).....	144

LIST OF FIGURES (Continued)

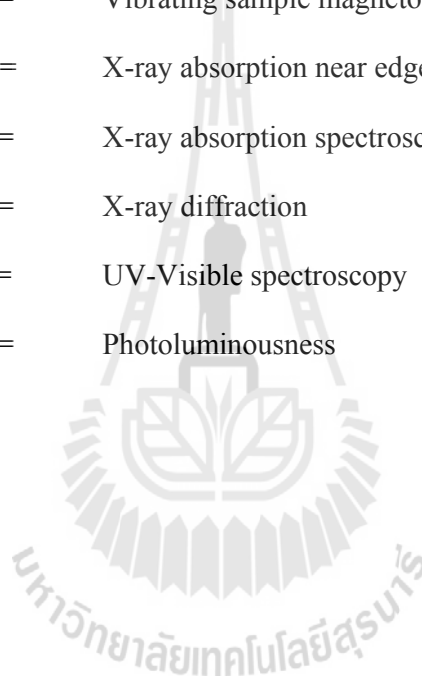
Figure	Page
4.60 (a) Tb L_3 -edge XANES spectra of the Tb-doped ZnO and (b) Er L_3 -edge XANES spectra of Er-doped ZnO as well as of those Standard Tb and Er acetates, respectively.....	149
4.61 Room-temperature optical absorbance spectra of undoped ZnO nanorods calcined at 400 °C for 6 h and RE-doped ZnO nanorods prepared in air at 300 °C for 6 h, (a) Tb-doped ZnO and (b) Er-doped ZnO nanorods, respectively.....	152
4.62 Plot of $(ah\nu)^2$ as a function of photon energy ($h\nu$) for undoped ZnO and RE-ZnO nanorods, (a) Tb-doped ZnO nanorods and (b) Er-doped ZnO nanorods prepared in air at 300 °C for 6 h, respectively.....	153
4.63 Band gap versus doping concentration of undoped ZnO calcined at 400 °C for 6 h, Tb-doped ZnO and Er-doped ZnO nanorods prepared in air at 300 °C for 6 h, respectively.....	154
4.64 Room temperature photoluminescence spectra of undoped ZnO and RE-doped ZnO nanorods, (a) Tb-doped ZnO nanorods (Inset shows schematically emission process) and (b) Er-doped ZnO nanorods under 325 nm light excitation.....	157

LIST OF FIGURES (Continued)

Figure	Page
4.65 The magnetization magnetic measurements (M) versus applied magnetic field (H) were performed on undoped ZnO, (a) Tb-doped and (b) Er-doped ZnO nanorods with different the rare-earth metal content obtained at 293 K from VSM measurement.....	159
4.66 $M \times H$ curves for $Zn_{0.975}Tb_{0.025}O$ and $Zn_{0.900}Er_{0.100}O$ samples taken at $T = 50$ K and 293 K, showing the existence of ferromagnetism and paramagnetism respectively.....	160
4.67 display the temperature-dependent magnetization ($M-T$) curves of Tb-doped ZnO nanorods with $x = 0.025$ was studied in field of 1 kOe. Inset: The modified curie - weiss fitting to the data between 150 K and 293 K under 1 kOe as a function of temperature and fitting result using the modified Curie-weiss law.....	164

LIST OF ABBREVIATIONS

TEM	=	Transmission electron microscopy
TGA	=	Thermo gravimetric analysis
VSM	=	Vibrating sample magnetometer
XANES	=	X-ray absorption near edge structure
XAS	=	X-ray absorption spectroscopy
XRD	=	X-ray diffraction
UV-Vis	=	UV-Visible spectroscopy
PL	=	Photoluminescence



CHAPTER I

INTRODUCTION

1.1 Background and significance of the study

Diluted magnetic semiconductors (DMSs), or sometimes referred to as semimagnetic semiconductors, are semiconducting materials in which a fraction of the host cations can be substitutionally replaced by magnetic ions or appropriate rare earths. Much of the attention on DMS materials is due to its potential application in what are now called “spintronics” devices which exploit spin in magnetic materials along with charge of electrons in semiconductors. Transition metals that have partially filled d states (Sc, Ti, V, Cr, Mn, Fe, Co, Ni, and Cu) and rare earth elements that have partially filled f states (e.g. Eu, Tb, Er) have been used as magnetic atoms in DMS. The partially filled d states or f states contain unpaired electrons, in terms of their spin, which are responsible for their exhibiting magnetic behavior. For developing applicable spintronic devices, the ferromagnetic Curie temperature (T_c) of DMSs should be above room temperature. Dietl et al. (2000) predicted that 5% Mn-doped ZnO should exhibit room-temperature ferromagnetism (RT-FM) mediated by additional holes. This theoretical work stimulated a large number of experimental investigations searching for RT-FM in oxide-based diluted magnetic semiconductors (O-DMSs). Many oxide semiconductors, including In_2O_3 , TiO_2 , ZnO , SnO_2 and CeO_2 doped with various transition metal ions have been shown to exhibit RT-FM (Coey, 2006). Among them, ZnO-based DMSs have been extensively studied as they hold

great potential for the applications in magneto electronics, photo-electronics, spin-electronics and microwave devices due to their wide band gap (~ 3.37 eV) and high exciton binding energy (60 meV) (Partha et al., 2013). For the practical applications in magneto electronic devices, spin electronic devices and so on, a DMS should be ferromagnetic above room temperature. Theoretical work predicted that transition metal (TM) doped ZnO would show ferromagnetic behavior above 300 K. The ferromagnetism measured at various temperatures was reported in Co, Ni, Mn, and Fe-doped ZnO (Pivin et al., 2008). However, there are still controversies on the results of ZnO-based DMSs studies. According to the Zener model, ferromagnetism is mediated by holes in the valence band, and the concentration of such holes should be above 10^{20} per cm^3 in order to get a T_c higher than RT. Coey et al. (2005) proposed an impurity band exchange model to explain RT-FM in O-DMSs. In this model magnetic interaction is mediated by impurity band donors and the ferromagnetic transition occurs when the number of bound magnetic polarons reaches the percolation threshold. For enhancing T_c , effective hybridization at the Fermi level between the donor states and the $3d$ states of the magnetic dopant is required. Recently, the mechanism of carrier-mediated FM has also been proposed to explain the FM in Co-doped TiO_2 (Akdogan et al., 2007), Co-doped ZnO (Xu et al., 2011) and Fe-doped SnO_2 (Coey, 2004). In addition, rare earth atoms have partially filled f -orbitals, which carry magnetic moments and may take part in magnetic coupling as in the case of TMs with partially filled d -orbitals. Actually, recent experiments showed that rare earth metals such as Gd and Eu doped GaN exhibited ferromagnetic coupling (Zhou et al., 2008). On the other hand, rare earth ions are good luminescence centers due to their narrow and intense emission lines originated from $4f$ intrashell

transitions, and many investigations on the pure optical properties of Eu-doped ZnO (Tan et al., 2011), Tb-doped ZnO (Sharma et al., 2011) and Er-doped ZnO (Chen et al., 2011) have been carried out. Compared with TM doped ZnO, little attention has been paid to the ferromagnetic properties of rare earth metal doped ZnO. Therefore, it is of great importance to explore the magnetic properties of rare earth metal-doped ZnO and promote its applications such as in magneto electronic optical electronic and spin electronic devices.

Recently, many studies on TM-doped ZnO and RE-doped ZnO have been reported. For example, Zhang et al. (2008) reported RT-FM in Mn-doped ZnO hollow spheres using colloidal carbon spheres as template. These results revealed that hysteresis curve was clearly observed when the calcination temperature was lower than 900 °C. The values of saturation magnetization (M_s) of 0.030, 0.022 and 0.013 emu/g, and the coercive field (H_c) of 105, 95 and 88 Oe were obtained for samples calcined at 550, 650 and 900 °C samples, respectively. M_s and H_c decrease slightly with increasing calcination temperature. However, the ferromagnetic behavior disappeared when the temperature was increased to 1200 °C. The value of M_s in Mn-doped ZnO varied widely. In experimental findings, no secondary phases like $ZnMn_2O_4$ or Mn_3O_4 were observed, which indicated that the carrier-induced and double-exchange mechanisms could explain the origin of the ferromagnetism. Xu et al. (2009) also reported RT-FM in single-phase $Zn_{1-x}Co_xO$ ($x = 0.02, 0.04$) powders synthesized by a co-precipitation process. These results showed the coercive fields (H_c) and saturation magnetization (M_s) were 79 Oe and 0.017 emu/g for $x = 0.02$, respectively. These values increased to 131 Oe and 0.048 emu/g for $x = 0.04$. The expansion of M_s was possibly caused by increasing in electrons which induced

more effective ferromagnetic couplings during doped Co^{2+} ions (the carrier-induced ferromagnetism). Zhao et al. (2010) also reported the RT-FM in Ni-doped ZnO ($\text{Zn}_{1-x}\text{Ni}_x\text{O}$; $x = 0.001$ to $x = 0.01$) powders that were prepared by the sol-gel route. The photoluminescence (PL) spectra of products are constituted of a near-band-edge emission peak in ultraviolet region at 390 nm and defect-related deep-level emission peak in the visible region at 476 nm and exhibited a ferromagnetic behavior with small coercive field and small remanence. The maximum saturation magnetization was $0.076 \mu_{\text{B}}/\text{Ni}$ at $x = 1.0\%$. Collectively, these results strongly indicated that ferromagnetism was induced by doping with Ni ions and was an intrinsic property of powder. Qi et al. (2010) also reported RT-FM in transparent $\text{Zn}_{1-x}\text{Er}_x\text{O}$ ($x = 0.04, 0.05$ and 0.17) films which were grown on glass substrates by radio-frequency (RF) reactive magnetron sputtering. The magnetic moment per erbium ion decreased from $0.60 \mu_{\text{B}}/\text{Er}$ ($x = 0.04$) to $0.20 \mu_{\text{B}}/\text{Er}$ ($x = 0.17$) with increasing Er concentration. The consistent drop in moment per Er ion at higher Er concentration could be due to an increasing occurring of antiferromagnetic coupling between Er pairs occurring at shorter separation distance, which was similar to the system of Cu-doped ZnO. Wu et al. (2012) also found RT-FM in nanocrystalline Tb-doped ZnO films with a thickness of 67 nm prepared by ion beam sputtering with a base pressure of 1.9×10^{-6} Torr on Al_2O_3 (1120) at room temperature by using multilayer δ -doping technique. They found that the sample showed the saturation magnetization of the films ($0.38 \mu_{\text{B}}/\text{Tb}$) is much lower than that of free Tb^{3+} ion ($9 \mu_{\text{B}}/\text{Tb}$). It is commonly believed that the natural defects in ZnO films are donors.

At present, most studies reported on TM-doped ZnO and RE-doped ZnO have been synthesized by several methods. Especially, RE-doped ZnO has been made

on films by sputtering technique, which is much more complex and is much higher cost. Little research has focused on the synthesis and magnetic properties of nanocrystalline ZnO-based DMOs prepared by a simple and cost effective method. Therefore, this research investigates the synthesis, structure, and magnetic properties of ZnO-based nanostructures, which are synthesized by a simple direct thermal decomposition method. The present synthesis method has several advantages such as being cost effective, requiring less synthesis time, requiring low temperature for processing and the amount of final product one compared with other methods. The prepared samples are characterized by thermo gravimetric analysis (TGA), X-ray diffraction (XRD), transmission electron microscopy (TEM), UV-Vis spectroscopy (UV-vis), photoluminescence (PL) and vibrating sample magnetometry (VSM). The oxidation states of various transition metal and rare earth metal ions are also investigated by X-ray photoelectron spectroscopy (XPS) and X-ray absorption near edge structures (XANES).

1.2 Objectives of the dissertation

The objectives of this research are as follows:

1.2.1 To study the synthesis of dilute magnetic oxide ZnO-based nanostructures by a simple direct thermal decomposition method.

1.2.2 To characterize the synthesized dilute magnetic oxide ZnO-based nanostructures by TG-DTA, XRD, TEM, UV-Vis, PL, VSM, XPS and XANES.

1.2.3 To study the origin of ferromagnetism in dilute magnetic oxide ZnO-based nanostructures for further study on spintronic devices.

1.3 Limitations of study

1.3.1 This study focuses on the synthesis of dilute magnetic oxide ZnO-based nanostructures in the form of nanoparticles and nanorods by a simple direct thermal decomposition method.

1.3.2 Synthesis of $Zn_{1-x}M_xO_2$ nanostructures with M are TM (Co, Mn, Ni and Cu) and RE (Tb and Er) metal ions for $x = 0.025, 0.05, 0.075,$ and 0.10 is conducted.

1.3.3 The synthesis is carried out only at $300\text{ }^\circ\text{C}$ for 6 h in air, and the concentration of dopant is varied from $x = 0.025$ to 0.10 .

1.3.4 Study of the effect of transition metal concentration on magnetic properties of dilute magnetic oxide ZnO-based systems is included.

1.3.5 The morphology, structure, and magnetic properties of the $Zn_{1-x}M_xO$ nanostructures are compared with those of the pure ZnO.

1.4 Location of research

Advanced Materials Physics (Amp.) Laboratory, School of Physics, Institute of Science, Suranaree University of Technology, Nakhon Ratchasima, Thailand.

1.5 Anticipated outcome

1.5.1 Skill and expertise on synthesis and characterization techniques of the dilute magnetic oxide ZnO-based nanostructures.

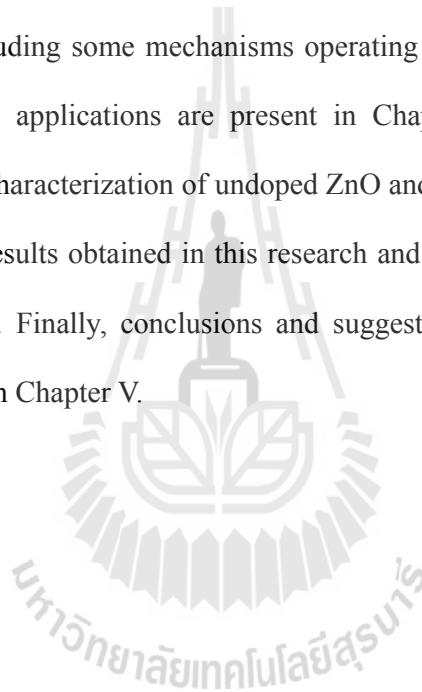
1.5.2 Understanding of the physical properties of dilute magnetic oxide materials both TM-doped ZnO and RE-doped ZnO systems.

1.5.3 Opening the door to dilute magnetic oxide materials at the nano-scale which can be developed for future technology.

1.5.4 Publication of research articles in ISI journals.

1.6 Dissertation structure

The thesis is divided into five chapters. Review of literature which is relevant to this research, including some mechanisms operating in DMS and DMO materials and potential device applications are present in Chapter II. Chapter III presents the preparation and characterization of undoped ZnO and M (TM and RE)-doped ZnO samples. Then, the results obtained in this research and discussions of the results are given in Chapter IV. Finally, conclusions and suggestion are described and future works are proposed in Chapter V.



CHAPTER II

LITERATURE REVIEWS

This chapter presents a review of the background of dilute magnetic semiconductors (DMSs) and diluted magnetic oxides (DMOs) in the varieties form including nanoparticles, thin films and so on. The potential of magnetic impurity phase in dilute magnetic semiconductors and dilute magnetic oxide were included in this chapter. Furthermore, this chapter reviews the mechanisms operative and potential applications in DMS and DMO materials.

2.1 Dilute magnetic semiconductors

With respect to magnetic properties, semiconductors can be classified in terms of the amount and distribution of magnetic dopants as magnetic semiconductors, dilute magnetic semiconductors, and non-magnetic semiconductors. Magnetic semiconductors such as magnetite, europium and chromium chalcogenides have a periodic array of magnetically ordered spins in their crystal structure. These materials received intensive attention in the late 1960s since the exchange interaction between the electrons in the semiconductor bands and the localized *d* electrons at the magnetic sites give rise to a number of intriguing phenomena, but were abandoned later since they are difficult to grow and have a low Curie temperature, well below 100 K (Ohno, 1998).

Diluted magnetic semiconductors (DMSs) are doped with a small amount of magnetic ions, i.e. ions carrying unpaired spins, making nonmagnetic and semiconductors magnetic. They are one of the most promising candidates for spintronic applications, which take advantage of the charge and spin of electrons in a single material system. A DMS is a nonmagnetic semiconductor (or alloy of nonmagnetic semiconductors) (see Figure 2.1(a)) that is doped with a magnetic element which is usually 3d transition metal (TM) ions such as V, Mn, Fe, Co or Ni, which induce ferromagnetism in the semiconductor host (see Figure 2.1(b)). Therefore, a number of different semiconductor hosts have been investigated to test their magnetic properties. In the past most attention has been paid to Mn-doped GaAs (Nagai et al., 2001) and Mn-doped InAs systems (Munekata et al., 1989). However, due to their reported low Curie temperatures (T_C) which are around 170 K for Mn-doped GaAs (Ohno, 1998) and 35 K for Mn-doped InAs (Ohno et al., 2002), they are not suitable for practical applications as their T_C are quite low. Therefore, there is a large incentive for developing new DMS materials which are ferromagnetic above room temperature. Some theoretical works predicted room temperature ferromagnetism in TM doped oxide semiconductors.

Furthermore, the calculations of Dietl, Matsukura, and Ohno (2000) showed that Mn-doped ZnO would exhibit ferromagnetism above room temperature and predicted the values of T_C for 5% of Mn-doped ZnO as shown in Figure 2.2. The data (Figure 2.2) demonstrate that the T_C for II-VI compound semiconductors other than ZnO is below room temperature, whereas for semiconductor spintronics it is necessary to design and grow ferromagnetic semiconductor materials with high T_C

above room temperature and high thermal equilibrium stability during the device fabrication process (Pearson et al., 2005).

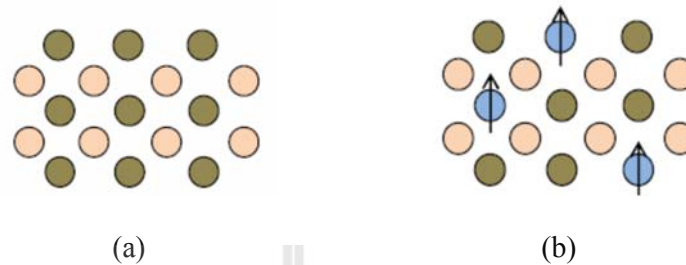


Figure 2.1 Two types of semiconductors: (a) a nonmagnetic semiconductor (b) a dilute magnetic semiconductor: a nonmagnetic semiconductor to which a dilute concentration of ions carrying an unpaired spin has been added. (Ohno, 1998).

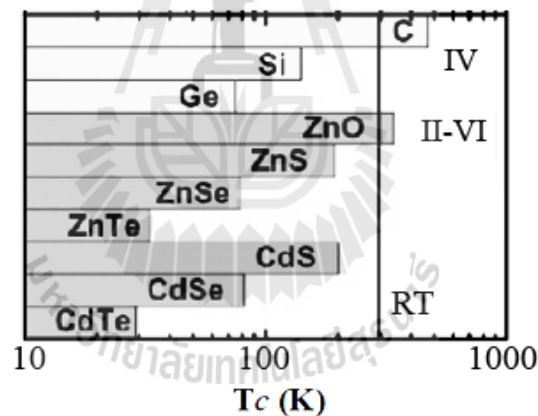


Figure 2.2 Computed values of the Curie temperature T_c for various p -type semiconductors containing 5% of Mn and 3.5×10^{20} holes per cm^3 (Dietl, Matsukura, and Ohno, 2000).

2.2 Dilute magnetic oxides

Dilute magnetic oxides (DMOs) are transparent, wide-bandgap materials that behave ferromagnetically when doped with a few percent of a magnetic $3d$

cation. The magnetism, which appears well below the cation percolation threshold, cannot be understood in terms of the conventional theory of magnetism in insulators; nor can a carrier-mediated ferromagnetic exchange mechanism account for the magnitude of the Curie temperatures, which are well in excess of 400 K. The phenomenon is observed in thin films and nanocrystals, but not in well-crystallized bulk material. In particular, the calculations of Dietl et al. (2000) showed that Mn-doped ZnO would exhibit ferromagnetism above room temperature. Sato et al. (2000) have also investigated ferromagnetism of ZnO-based DMS by *ab initio* electronic structure calculations based on the local spin density approximation and they reported ferromagnetic ordering of *3d* transition metal ions in ZnO. These theoretical predictions initiated a number of experimental studies of TM-doped ZnO (Dai, Meng, and Li, 2013). In addition, the discovery of room temperature ferromagnetism in Co-doped anatase TiO₂ thin films has also generated much interest in the Co-doped TiO₂ system as a potential oxide-based DMS (Matsumoto et al., 2001).

While some of these works reported the observation of ferromagnetism above room temperature, the origin of ferromagnetism in these systems is not well understood yet. The early studies on a variety of oxides, with data on T_C and moment per dopant cation are summarized in Table 2.1. Thus, several models of FM have been proposed for these DMOs, including a new exchange mechanism involving donor electrons in an impurity (Coey, Venkateshan, and Fitzgerald, 2005), the carrier (electron) mediated exchange mechanism (Ueda, Tabata, and Kawai, 2001), superexchange or double exchange interaction and a defect mediated mechanism like Bound Magnetic Polaron model (BMP) (Coey et al., 2005). In addition to

the magnetic doping effect, oxygen vacancies have been proposed to play an important role in the magnetic origin for DMOs, leading to be the exchange interactions between localized electron spin moments. Nevertheless, the main unresolved question is whether the observed ferromagnetism originates from uniformly distributed TM ions in the host matrix or whether it is due to the precipitation of secondary phases such as metallic clusters. If a DMS contains TM ions below their equilibrium solubility limit no secondary phases are expected. In this case, since the strength of magnetism is proportional to the number of TM ions substituted on the cation sites in a DMS, the realization of high T_c ferromagnetism is difficult. On the other hand, at higher TM dopant concentrations doped transition metals start to form unwanted metallic clusters. For this reason, to achieve a high T_c ferromagnetism in a single phase DMS, non-equilibrium sample preparation techniques such as low temperature thermal cleaning method for Si molecular beam epitaxy (MBE) and ion implantation are required. Ion implantation is widely used in silicon technology for integrated circuits due to its reliability, precision and reproducibility. It has also proven to be a reliable method for injecting transition metals into a host semiconductor material beyond their solubility limits (Zhou et al., 2008).

Table 2.1 Lists of some dilute magnetic oxides.

Material	Band gap, E _g (eV)	Doping	Moment (μ_B)	T _C (K)	Reference
TiO ₂	3.2	V – 5%	4.2	>400	Hong et al., 2004
		Co – 1-2%	0.3	>300	Matsumoto et al., 2001
		Co – 7%	1.4	>650	Shinde et al., 2003
		Fe – 2%	2.4	300	Wang et al., 2003
SnO ₂	3.5	Fe – 5%	1.8	610	Coey et al., 2004
		Co – 5%	7.5	650	Ogale et al., 2003
ZnO	3.3	V – 15%	0.5	>350	Saeki et al., 2001
		Mn – 2.2%	0.16	>300	Sharma et al., 2003
		Fe – 5%	0.75	550	Han et al., 2002
		Co – 10%	2.0	280-300	Ueda et al., 2001
		Ni – 0.9%	0.06	>300	Radovanovic and Gamelin, 2003
Cu ₂ O	2.0	Co – 5%	0.2	>300	Kale et al., 2003
		Mn – 0.3%	0.6	>300	Yu, Y. L. et al., 2005
In ₂ O ₃	3.7	Fe – 5%	1.4	>600	He et al., 2005
		Cr – 2%	1.5	900	Ohno, 1998
(In _{1-x} Sn _x) ₂ O ₃	3.5	Mn – 5%	0.8	>400	Philip et al., 2004
CeO ₂	3.4	Co – 3%	6.0	~800	Tiwari et al., 2006
(La,Sr)TiO ₃	-	Co – 2%	3.0	>400	Herranz et al., 2006
		Fe – 1.5%	-	-	Maensiri et al., 2007
		Co – 1.5%	0.10 – 0.25	-	Wongsaprom et al., 2007

2.3 Theoretical models for explaining ferromagnetism in DMSs and DMOs

In a nutshell, the mechanisms pertinent to magnetism are direct super-exchange (anti-ferromagnetic), indirect super-exchange (could be ferromagnetic), carrier-mediated exchange (ferromagnetic) including the much celebrated double exchange mechanism, and magnetic polarons, to cite a few.

2.3.1 Zener model

In the Zener model, the direct interaction between d shells of the adjacent TM atoms (super-exchange) lead to an anti-ferromagnetic configuration of the d shell spins because the Mn- d shell is half-filled. The zener model as shown in Figure 2.3, the direct super-exchange interaction (Anderson et al., 1950) between half filled d -shell electrons of TM cations and completely filled p -orbitals of anion is anti-ferromagnetic. Since the d -shell electrons from both adjacent TM atoms occupy the same p -level, their spins must be opposite according to Pauli Exclusion Principle. This leads to an anti-ferromagnetic coupling of nearest-neighbor TM cations through a shared anion.

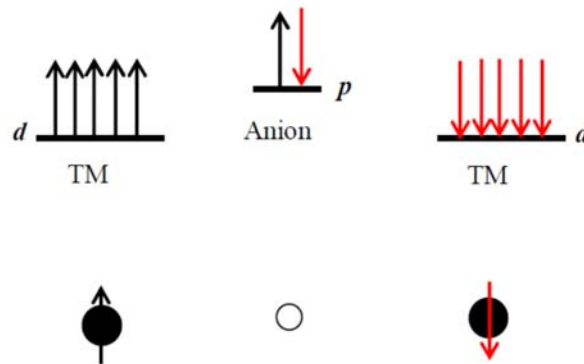


Figure 2.3 Direct super-exchange interaction: Anti-ferromagnetic coupling of adjacent TM cations through a shared anion (Zener et al., 1951).

On the other hand, the indirect coupling (see Figure 2.4) of spins through the conduction electrons tends to align the spins of the incomplete d shells in a ferromagnetic manner. It is only when this dominates over the direct super-exchange coupling between adjacent d -shells that ferromagnetism is possible.

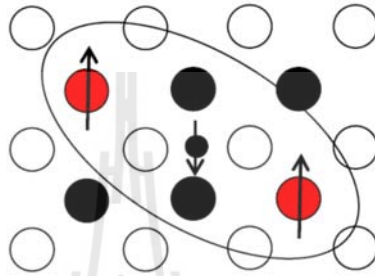


Figure 2.4 Indirect super-exchange interaction: Ferromagnetic coupling of localized spins through the conduction electrons (Zener et al., 1951).

2.3.2 The RKKY model

Early attempts to understand the magnetic behavior of DMS systems are based on models in which the local magnetic moments are assumed to interact with each other via Ruderman-Kittel-Kasuya-Yoshida type (RKKY) interactions. The basic idea behind the RKKY interaction is based on the exchange coupling between the magnetic ion and the conduction band electrons. It should be mentioned that s and d wave functions are orthogonal and would not lead to any interaction in perfect one electron system. The conduction electron is magnetized in the vicinity of the magnetic ion, with the polarization decaying with distance from the magnetic ion in an oscillatory fashion. This oscillation causes an indirect super-exchange interaction (RKKY) between two magnetic ions on the nearest or next nearest magnetic

neighbors. This coupling may result in a parallel (ferromagnetic) or an anti-parallel (anti-ferromagnetic) setting of the moments dependent on the separation of the interacting atoms. The RKKY interaction between Mn spins via delocalized carriers has been used to explain the ferromagnetism observed in PbSnMnTe (Story et al., 1986). However, if the carriers come from Mn-*d* states and are localized, which are far from being free electron like the RKKY interaction may not be realistic.

2.3.3 The double-exchange model

In some oxide compound, ferromagnetic exchange interaction is due to mixed valence number of magnetic ions. The basis has been proposed by Zener (1951) for ferromagnetic compounds of manganese with perovskite structure such as $\text{La}_{1-x}\text{Ca}_x\text{MnO}_3$ (Roy et al., 1998) and $\text{La}_{1-x}\text{Sr}_x\text{MnO}_3$ (Anane et al., 1995). The oxidation of La is +3 but that of dopant ions, Ca and Sr are +2 which imply mixed valence number of Mn^{3+} (d^4) and Mn^{4+} (d^3) at fraction of $1-x$ and x respectively. Both Sr^{2+} and Ca^{2+} doping introduce holes in part of Mn 3*d* state. The *d* electron is hopping from Mn^{3+} to the adjacent Mn^{4+} via central O^{2-} is considered as Mn^{3+} electron transferring to central O^{2-} simultaneously with O^{2-} electron transferring to Mn^{4+} . The mechanism is called “double exchange” as shown in Figure 2.5. Combined with the onsite Hund’s coupling, the double exchange interaction leads to a ferromagnetic alignment of the local magnetic moments (Gennes de, 1960). Parallel spin alignment is favored because it increases the hopping probability and therefore decreases the kinetic energy of spin-polarized electrons. The double exchange interaction gains energy through a *d*-electron hopping and occurs when E_F crosses *d* band. It is likely that double exchange interaction is short ranged because carriers have *d*-band character.

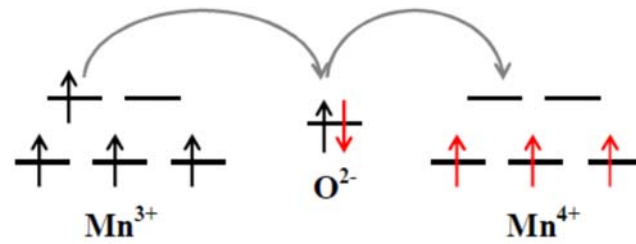


Figure 2.5 Double-exchange mechanisms in mixed-valence manganites (Bettina, 2010).

In contrast, with super-exchange, (1) the electrons do move between two cations ion via the intermediate ligand (e.g. oxygen) in double exchange but they do not in super-exchange (2). In super-exchange, the ferromagnetic or anti-ferromagnetic alignment occur between two cations with same valence state while double-exchange interaction occurs only when valence state of cation atom is different to that of another mixed valence compound. The magnetic interaction as shown in Table 2.2.

Table 2.2 A comparison of magnetic interaction.

Interaction	Definition
RKKY	Indirect exchange coupling of magnetic moments over relatively large distance via band electrons due to the Coulomb exchange. It becomes efficient when a high concentration of free carriers is present such as in metals for which it was developed.
Direct super-exchange	Direct coupling of magnetic ions through overlap of magnetic orbitals.
Indirect super-exchange	Spins of two magnetic ions are correlated due to the exchange interaction between each of the two ions and the valence p -band.
Double-exchange	Couples magnetic ions in different charge state by virtual hopping of the “extra” electron from one ion to the other through interaction with p -orbitals.

2.3.4 The bound magnetic polaron model

In addition to the models mentioned above, an alternative model considers whether ferromagnetic ordering of the Mn moments could originate from carriers (holes) that are present in the material, but localized at the transition-metal impurity (Berciu and Bhatt, 2001). Furthermore, ferromagnetism in DMS has been accounted for by the formation of bound magnetic polaron (Dietl, Matsukura, and Ohno, 2002). The bound magnetic polarons are formed by the alignment of the spins of many transition-metal ions with that of much lower number of weakly bound carriers such

as excitons within a polaron radius. The basic idea is schematically illustrated in Figure 2.6. The localized holes of the polarons act on the transition-metal impurities surrounding them, thus producing an effective magnetic field and aligning all spins. As temperature decreases the interaction distance (boundary) grows. Neighboring magnetic polarons overlap and interact via magnetic impurities forming correlated clusters of polarons. One observes a ferromagnetic transition when the size of such clusters is equal to the size of the sample. This model is inherently attractive for low carrier density systems such as many of the electronic oxides. The polaron model is applicable to both *p*-type and *n*-type host materials (Sarma, Hwang, and Kaminski, 2003). Even though the direct exchange interaction of the localized holes is anti-ferromagnetic, the interaction between bound magnetic polarons may be ferromagnetic for sufficiently large concentrations of magnetic impurities. This enables ferromagnetic ordering of the Mn ions in an otherwise insulating or semi-insulating material. Recently, Coey et al. (2005) applied this model to diluted magnetic oxides. They proposed that the ferromagnetic exchange coupling of TM ions in *n*-type diluted magnetic oxides is mediated by the shallow donor electrons trapped by the oxygen vacancy that tend to form bound magnetic polarons within their hydrogenic orbits (see Figure 2.6). This direct ferromagnetic coupling is called *F*-center exchange (FCE), where the *F*-center resembles Kasuya's bound magnetic polaron (Kasuya, 1970).

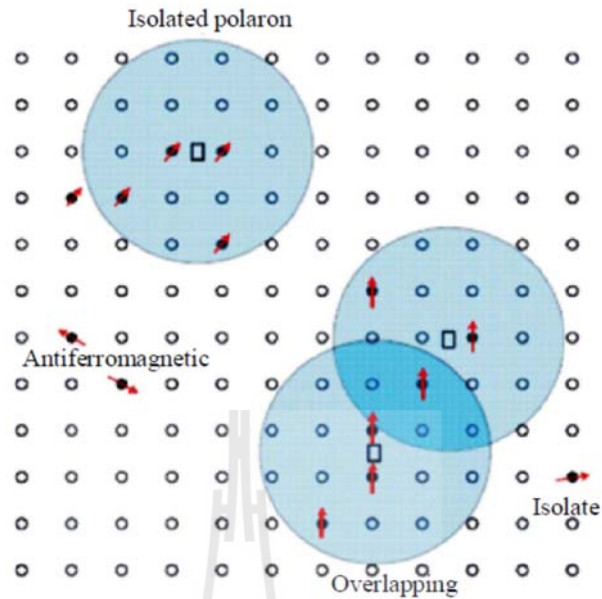


Figure 2.6 Representation of magnetic polarons. A donor electron couples its spin antiparallel to impurities with a half-full or more than half-full $3d$ shell. The figure is drawn for magnetic cation concentration $x = 0.1$ and when the orbital radius of the magnetic cation is sufficiently large. Cation sites are represented by small circles. Oxygen is not shown; the unoccupied oxygen sites are represented by squares (Coe et al., 2005).

After all this discussion of the BMP model, the knowledge on defects in diluted magnetic oxides become very important. The oxygen defects in BMP model are responsible for the shallow donors and strongly stabilize the ferromagnetic ground state. The oxygen vacancies at the percent level are documented for TiO_2 (Yahia, 1963) and ZnO (Kohan, Ceder, Morgan, and Walle, 2000). For ZnO , Zn interstitials (Zn_i) are also reported as a shallow donor (Lee, Jeong, Cho, and Park, 2002). Recently, the electronic structure calculations of Patterson (2005) reported that the

oxygen vacancy with a spin half strongly promote ferromagnetic coupling of Co ions in Co doped ZnO, as schematically presented in Figure 2.7.

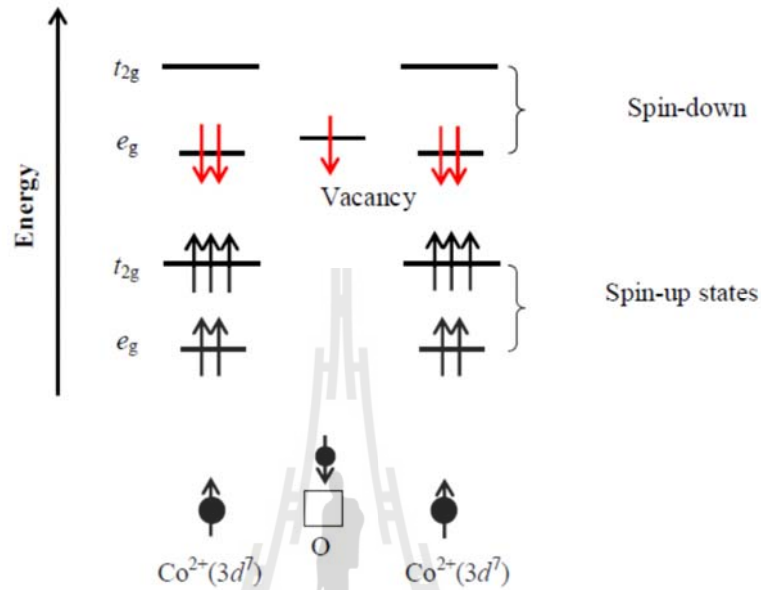


Figure 2.7 A schematic energy level diagram for a ferromagnetic coupling between two Co ions via a donor electron trapped in the oxygen vacancy (Patterson, 2005).

2.3.5 Transition metal clustering model

Another theoretical model to explain the origin of observed ferromagnetism in a DMS is proposed by Schilfgaarde and Mryasov (2001) using local density functional calculations. They reported that the TM impurities in a DMS may form very small ferromagnetic clusters (just a few atoms in dimension) which are difficult to detect by most structural characterization techniques. The detection of small magnetic clusters in the oxide matrix is one important experimental challenge.

2.3.6 Other Mechanisms

The magnetic behavior which is normally expected from dilute magnetic oxides was proposed by Coey and Rode (2007), If the magnetic dopants were distributed at random on the cation sites in the oxide materials, isolated ions, pairs and small clusters will form at dopant concentration x below the percolation threshold. The coupling among cations which share an oxygen ligand is superexchange, which is usually antiferromagnetic. Curie weiss susceptibility is defined by:

$$\chi = \frac{M}{H} = \frac{N_A g^2 \mu_B^2 s(s+1)}{3k_B(T-\theta)} = \frac{C}{T-\theta} \quad (2.1)$$

where $c = N_A g^2 \mu_B^2 s(s+1)/3k_B$. In addition, effective moment (μ_{eff}) in materials was calculated by using expression of Equation 2.2.

$$\mu_{eff} = g\sqrt{s(s+1)}\mu_B = \sqrt{\frac{3k_B C M_w}{N_A}} \quad (2.2)$$

where k_B , C , M_w and N_A are Boltzmann constant (1.38×10^{-16} erg/k), Curie constant, molecular weight of $Zn_{1-x}M_xO$ (M = dopants) and Avogadro number (6.02×10^{23}). Moreover, the susceptibility is included by a temperature-dependent term x_o (sum Pauli, Landau and core susceptibilities) in Equation 2.1 for fitting to calculate of those values at high temperature which is closed to room temperature and is called “modified Curie-weiss law” (Peleckis et al. (2006); Duan et al. (2011)).

Isolated ions and small clusters give curie-like contribution to susceptibility as:

$$\chi = \frac{M}{H} = \frac{N_A g^2 \mu_B^2 s(s+1)}{3k_B T} = \frac{C}{T} \quad (2.3)$$

There is no long-range magnetic order. The anticipated paramagnetic behavior is what actually observed in well-crystallized diluted magnetic oxide.

2.4 Properties of ZnO

Like most of the group II-VI binary compound semiconductor, ZnO crystallize in either cubic zinc-blende or hexagonal wurtzite structure (see Figure 2.8) where each ion is surround by four counter-ions at the corner of a tetrahedron (Özgür et al., 2005). At ambient conditions the thermodynamically stable phase is wurtzite while zinc-blende structure can be stable only when growth on cubic substrate. However, ZnO also can exist in rocksalt (NaCl) structure under high pressure.

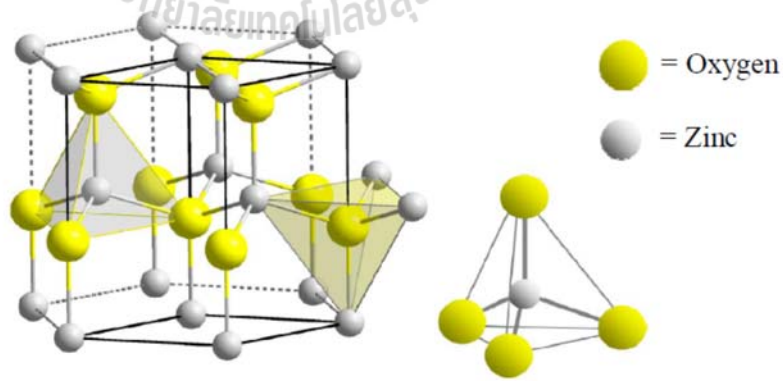


Figure 2.8 Stick and ball representation of ZnO-hexagonal wurtzite structures (Fierro, 2006).

The wurzite structure has a hexagonal unit cell belonging to space group C_{6v}^4 with ideal arrangement of $c/a = (8/3)^{1/2}$ and $u = 3/8$. For stable ZnO wurzite structure, the lattice parameter deviates from ideal arrangement. The lattice constants mostly range from 3.2475 to 3.2501 Å for a , from 5.2042 to 5.2075 Å for c , and from 0.3817 to 0.3856 Å for u . Most important, Zn- and O- plane stack alternatively along c -axis which gives the crystal a defined polarity, i.e. the basal planes are polar; whereas the side panels of the hexagonal unit cell contains both Zn and O atoms hence they are electrically neutral. Electrically, ZnO occurs naturally as an n-type semiconductor due to the presence of defects (Shen et al., 2008). It is a direct band gap material ($E_g = 3.5$ eV) and can be increased to ~ 4.0 eV by substituting Zn sites with Mg. It also has a very large exciton binding energy of ~ 60 MeV (compared with GaN, which is an indirect band gap material with lower exciton binding energy of ~ 25 MeV). This makes ZnO ideal for small wavelength optical electronic applications; especially where it is readily available in bulk single crystal form; and improved epitaxial growth techniques can grow thin transparent film of ZnO. Hence ZnO has attracted vast amount of interests for its applications to UV light emitter, varistor, transparent high power electronics, surface acoustic devices, piezoelectric transducers and gas sensors apart from its potential applications in DMS.

ZnO-based materials have attracted intense attention in the searching for high T_C ferromagnetic DMS materials since Dietl et al. (2002) predicted that ZnO-based DMSs could exhibit ferromagnetism above room temperature upon doping with transition elements such as Mn (on the order of 5% or more) in p -type (on the order of 10^{20} per cm^3) materials. This in simple terms is in part due to the strong p - d hybridization, which involves the valence band in the host, owing to small nearest

neighbor distance and small spin rephrasing *spin-orbit* interaction. Even though the common wisdom indicates hole exchange to be dominant, Sato, and Katayama-Yoshida (2000) predicted that the ferromagnetic state $\text{Co}^{2+}(d7)$ in Co-doped ZnO could be stabilized by *sd* hybridization, pointing to the possibility that high Curie-temperature ferromagnetic materials could be realized in *n*-type ZnO as well. These types of predictions, in addition to that by Dietl et al. (2000), set off a flurry of intensive experimental activity for transition metal doped ZnO as potential DMS materials with applications in spintronics. Various types of nanoparticles can be synthesized by many methods such as gas evaporation, laser vaporization, ionized beam deposition, sol-gel processing, freeze drying, etc. So far, various types of ZnO nanoparticles can be synthesized by many methods. The general formula for the diluted magnetic oxides is (Coey, Venkateshan, and Fitzgerald, 2005)



where A is a nonmagnetic cation, M is a magnetic TM cation. O is the oxygen, δ represents a donor defect and $n = 1$ or 2. An electron associated with a donor defect will be confined in a hydrogenic orbital (Coey et al., 2004).

2.5 ZnO-based dilute magnetic semiconductors

Zinc oxide diluted with transition metals has attracted much attention recently, especially since the emergence of spintronics, the field of semiconductor spin electronics that seeks to exploit the spin degree of freedom of charge carriers in semiconductors (Peng et al., 2005). It is widely expected that new and novel functionalities for electronics and photonics can be derived from the injection, transfer

and detection of carrier spin at room temperature. DMSs are considered as ideal systems for spintronics. DMSs based on ZnO doped with TM and/or RE metals like Co, Cu, Mn, Ni, Tb and Er for example, has been predicted theoretically to be very good candidates for room temperature ferromagnetism (Dietl et al., 2000). Many methods exist for the synthesis of ZnO nanostructures which are summarized as follows.

Yen et al. (2007) reported the preparation of Co-doped ZnO nanoparticles by thermal hydrolysis method synthesized by mixing of zinc acetate ($\text{CH}_3(\text{COO})_2\text{Zn}\cdot 2\text{H}_2\text{O}$) and 1% weight of cobalt acetate ($\text{CH}_3(\text{COO})_2\text{Co}\cdot 4\text{H}_2\text{O}$) dissolved in diethylene glycol solution and heat at 230 °C. The ferromagnetism of the sample was observed at room temperature. The measured magnetization corresponds to net ferromagnetic moment of $0.023 \mu_{\text{B}}/\text{Co}^{2+}$. The result may be attributed mainly to the cobalt atoms to replace the interstitial sites of the ZnO matrix surrounding the oxygen vacancies, in which the Co^{2+} ion coordinated with the oxygen site tetrahedrally in the ZnO matrix.

Zhang et al. (2008) summarized the Mn-doped ZnO hollow nanospheres prepared by hydrothermal method using 5.5 g $\text{Zn}(\text{CH}_3\text{COO})_2\cdot 2\text{H}_2\text{O}$ that was first dissolved in 50 ml deionized water to form a solution of concentration 0.5 M. Then 0.61 g Mn ($\text{CH}_3\text{COO})_2\cdot 4\text{H}_2\text{O}$ was dissolved in the above solution, the molar ratio of $\text{Mn}^{2+}:\text{Zn}^{2+}$ cation was 1:0. The solution was sealed in Teflon lined autoclave and hydrothermally treated at 170 °C for 8 h. The products were centrifuged, washed, dried at 90 °C for 10 h, and calcined at different temperature (550, 650, 900 and 1200 °C) for 30 min in air. The samples exhibit different magnetic behaviors. The M_s values are 0.030, 0.022 and 0.013 emu/g, and the H_c are 105, 95 and 88 Oe for 550,

650 and 900 °C samples, respectively. M_s and H_c decrease slightly with increasing calcination temperature. Coey et al. (2006) proposed the isolated Mn ions, antiferromagnetic pairs and ferromagnetic polarons coexisted in the Mn-doped ZnO system. The isolated Mn ions and antiferromagnetic pairs do not contribute to the measured M_s . Only partial Mn ions were induced to ferromagnetic coupling. This was the reason why a small value of M_s was usually obtained. In addition, Tb implanted ZnO single crystals by hydrothermal method grown on ZnO(0001) (Zhou et al., 2008). For an atomic concentration of 1.5%, annealing at 823 K leads to an increase of the saturation magnetization per implanted Tb ion up to 1.8 μ_B at room temperature. However, the ferromagnetic properties disappear completely upon annealing at 1023 K. This behavior is related to the formation of oxide complexes or nanoparticles.

Qi et al. (2009) reported the fabrication of the Er-doped ZnO ($x = 0, 0.04, 0.05$ and 0.17) thin films were grown by radiofrequency (RF) reactive magnetron sputtering using Zn (99.99%, purity) and Er (99.996%, purity) together as targets on glass substrates. The sputtering chamber was evacuated by a molecular pump to a base pressure below 2×10^5 Pa. During sputtering, the substrate temperature was kept at RT. Oxygen was introduced into the chamber as the reactive gas and the flow rate was controlled at 20 sccm. All the films were ferromagnetic at RT except for $x = 0$ (pure ZnO). As the Er concentration increased, the magnetic moment per erbium ion, which was obtained from the saturation magnetization divided by the total number of Er, decreased from 0.60 μ_B/Er ($x = 0.04$) to 0.20 μ_B/Er ($x = 0.17$). The consistent drop in estimated moment per Er ion at higher Er concentration could be due to an

increasing occurrence of antiferromagnetic coupling between Er pairs occurring at shorter separation distances, which was similar to the system of Cu-doped ZnO.

The synthesis of Ni-doped ZnO powder ($Zn_{1-x}Ni_xO$; e.g. $x = 0.043, 0.074$ and 0.224) by thermal co-decomposition of a mixture of bis (acetyl acetonato) zinc(II)hydrate and bis (dimethyl glyoximato) nickel(II)complexes was studied by Hilo, Dakhel, and Mohamed (2009). The sample preparation technique is easy; appropriate amounts of fine powders of the two complexes were totally mixed together in methanol until total dissolving. The methanol was then evaporated and the mixture was placed in a closed aluminum crucible for sintering at $400\text{ }^\circ\text{C}$ for 4 h in its dissolving vapor atmosphere in order to provide partial oxygen deficit. After that, the yield was well mixed by an agate mortar and pestle, cold pressed (at about 750 MPa) into a tablet and annealed in the same crucible for crystallization at $600\text{ }^\circ\text{C}$ for 8 h. The measured magnetization curves have been corrected for the paramagnetic component and the saturation magnetization of the ferromagnetic component is obtained. The saturation magnetization for samples with Ni% less than 8% are almost the same $M_s = 0.005\text{ emu/g}$. They believe that the FM in the Ni-doped ZnO could be due to the exchange coupling between localized d -spins on the Ni ions mediated by free delocalized carriers.

Daniel et al. (2012) reported the synthesis of $Zn_{1-x}M_xO$ powders (where $x = 0$ o $x = 0.01$, and $M = Mn, Fe$ or Co) by the sol-gel process. It is observed of the $M(H)$ measured at 2 K that the Co- and Mn-doped ZnO displayed saturation magnetizations (M_s) of approximately 2 and 3.2 emu/g, respectively. No remanence (M_r) was observed, indicating that a superparamagnetic behavior in these samples. However, the Fe-doped sample showed a ferromagnetic behavior with

$M_s \sim 0.34$ emu/g, $M_r \sim 0.05$ emu/g and coercivity (H_c) ~ 1090 Oe. Already at room temperature, the $M(H)$ measurements reveal a purely paramagnetic behavior for Mn- and Fe-doped ZnO, indicating that the Curie temperature (T_C) is below 300 K. However, a weak superparamagnetic behavior was observed in the Co-doped sample, indicating that $T_C > 300$ K. A detailed magnetic analysis suggests the presence of small spurious anti-ferromagnetic phase in the $Zn_{0.99}Fe_{0.01}O$ sample, which was not observed via XRD.

ZnO nanowires prepared by heating the Zn powders in a vertical tubular furnace (thermal evaporation method) were also studied by Yang et al. (2012). In this work the Zn powders and Au-coated Si substrates were placed on the lower and upper holders in the center of the quartz tube, respectively. The gas flow rate of nitrogen (N_2) was 1.5 standard liters per min (slm), with the substrate temperature being maintained at 900 °C for 1 h. The core ZnO nanowires in the present study exhibited a weak ferromagnetism at 300 K (coercivity = 136 Oe; retentivity = 2.52×10^{-6} emu), as well as at 10 K (coercivity = 348 Oe; retentivity = 4.12×10^{-6} emu). Although the existence of ferromagnetism in transition-metal-doped thin films remains controversial, they reveal that the diamagnetic behavior and saturation magnetization are enhanced and reduced, respectively, not only by the Cu-sputtering but also by the subsequent thermal annealing, which is attributed to the increased number of adjacent Cu atoms.

Other techniques of synthesis and reported observed magnetizations of ZnO-based DMSs reported in the literature are also summarized in Table 2.3.

Table 2.3 Some nanostructures of ZnO-based dilute magnetic oxides reported in literature.

Doping	Synthesis methods	Morphologies	Magnetization	References
Co-3%	hydrothermal	flakes	0.0118 emu/g	(Xu et al., 2010)
Co- 3%	hydrothermal	nanorods	0.012 emu/g	(Wang et al., 2009)
Co- 3%	chemical co-precipitation	nanorods	0.00036 emu/g	(Hao, H. et al., 2012)
Co-5%	precipitation	nanorods	0.0048 emu/g	(Xu et al., 2011)
Co-4%	co-precipitation	nanopowders	0.048 emu/g	(Xu et al., 2009)
Co-5%	solid state	nanoparticles	0.66 emu/g	(Pal et al. 2010)
Cu-2%	sputtering	films	~0.15 μ_B /Cu	(Ran et al., 2009)
Cu-2%	chemical	nanopowders	0.66 μ_B /Cu	(Liu et al., 2009)
Mn-1%	chemical	nanospheres	0.030 emu/g	(Zhang et al., 2008)
Mn-2%	CVD	nanoparticles	0.295 emu/g	(Sharma et al., 2012)
Mn-2.2%	Solid state	nanoparticles	0.008 emu/g	(Jayakumar et al., 2006)
Ni-5%	hydrothermal	nanorods	0.40 emu/g	(Cheng et al., 2008)
Ni-5%	direct thermal-decomposition	nanorods	~0.35 emu/g	(Saravanan et al., 2012)
Ni-7.4%	co-precipitation	nanopowders	0.005emu/g	(El-Hilo et al., 2009)
Tb	sputtering	films	0.38 μ_B /Tb	(Wua et al., 2012)
Tb-1.5%	hydrothermal	Single crystals	1.8 μ_B /Tb	(Zhou et al., 2008)
Er-4%	sputtering	films	~0.6 μ_B /Er	(Qi et al., 2009)
Er-1.7%	sputtering	films	0.20 μ_B /Er	(Qi et al., 2010)

2.6 Potential spintronic devices based on DMS materials

There are two different approaches for realizing spintronic devices. One is metal-based spintronics which uses ferromagnetic metals and the second one is semiconductor-based spintronics consisting of ferromagnetic semiconductors. Conventional electronics has developed with the exploitation of the electronic charge properties of carriers in semiconductor materials, as can be seen in present electronic and optoelectronic semiconductor devices. For example, various types of memory chips, information processors, and light emitting devices utilize the charge properties of carriers through materials by electrical control. However, the electron has another degree of freedom that can be used, namely spin, which is an intrinsic angular momentum of the electron. The spin state of an electron is represented by the spin quantum number, which can assume the values $+1/2$ (spin-up) and $-1/2$ (spin-down) with respect to a reference magnetic field. Spintronics or spin electronics refers to an emerging research area that focuses on employing spin in charge based electronics (Zutic et al., 2004). Spin dependent effects controlled by electrical and optical tools can render new functionalities into existing electronic devices or create new devices. Spintronics has already shown its success by using ferromagnetic metals in the computer industry, in the form of hard disk drive (HDD) read heads which use the giant magneto-resistance (GMR) effect. GMR is the effect that the resistance depends on the relative magnetic orientation (parallel or anti-parallel) of neighboring magnetic layers in multilayer structures in which two (or more) ferromagnetic layers are separated by a nonmagnetic metal spacer (Binasch et al., 1989). GMR-based technology formed the main contribution to the enormous increase of the storage density in hard disks during the last decade. Nowadays, the tunneling magneto-

resistance (TMR) effect is employed in HDD read heads and magnetic random access memory (MRAM), which are the most successful examples of spintronics in terms of applications (see Figure 2.9).

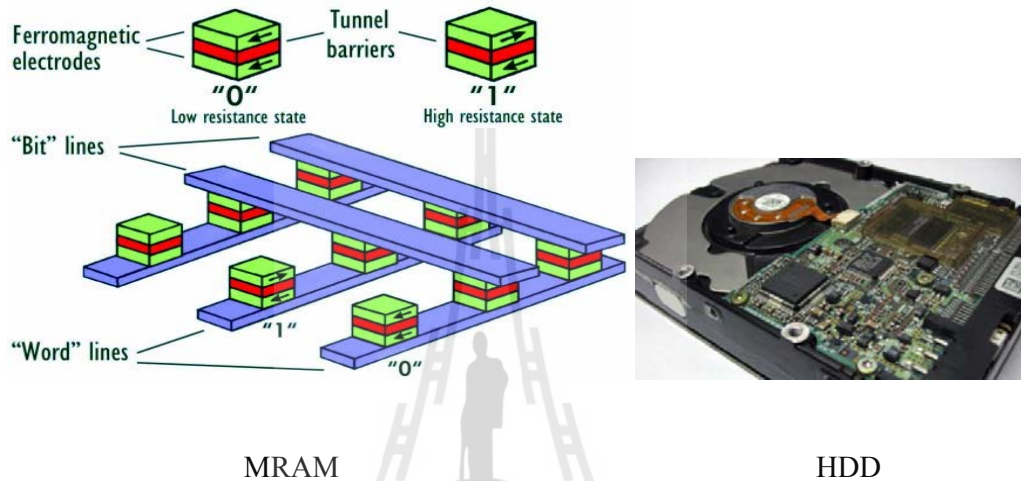
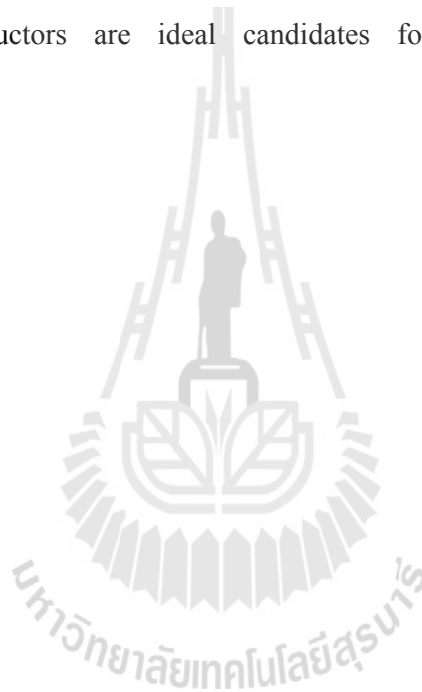


Figure 2.9 Illustration of various structures used for magnetic random access memory (MRAM) and hard disk drive (HDD) storage applications (Stöhr and Siegmann, 2006).

Considering that the spin dependent effects in HDD and MRAM are present in metal only or metal-oxide structures, however, semiconductor spintronics has much more progress than metal/oxide spintronics, since most electronic devices used in information processing are based on semiconductors. Among the most promising prospects of semiconductor spintronics are combined memory and logic at the single device level, enabling reprogrammable logic circuits, and the development of building blocks for solid state quantum computation. For successful spintronic applications comprising non-magnetic semiconductors (Awschalom et al., 2007), spin injection,

spin manipulation, and spin detection should be demonstrated. Alternatively, intrinsic spin-ordering can be realized, since semiconductors can be made magnetic by doping magnetic elements (Ohno, 1998).

In dilute magnetic semiconductors, ferromagnetism is mediated by carriers that in turn can be controlled by doping, light, and electric fields, as has been well established in conventional charge-based semiconductor technology. Therefore dilute magnetic semiconductors are ideal candidates for semiconductor spintronic applications.



CHAPTER III

EXPERIMENTAL PROCEDURE

This chapter describes the preparation of the undoped ZnO and ZnO doped with *3d*- and *4f*-cations by a simple direct thermal decomposition method. The prepared samples were characterized by TGA, XRD, TEM, XPS, UV-visible, XANES, PL and VSM. In this research, NiO and Fe-doped NiO system were also studied. Note that, the results and discussion on NiO system are not included in this chapter because it is not the main theme of the work. Therefore, it is only presented in the appendix I as addition information.

3.1 Sample preparation

At present, most studies reported on TM-doped ZnO and RE-doped ZnO have been synthesized by several methods. Especially, RE-doped ZnO has been made on films by sputtering technique, which are much more complex and are much higher cost. Little research has focused on the synthesis and magnetic properties of nanocrystalline ZnO-based DMOs by a simple and cost effective method. Therefore, this research investigates the synthesis, structure, and magnetic properties of ZnO-based nanostructures, which are synthesized by a simple direct thermal decomposition method. The present synthesis method has several advantages such as being cost effective, requiring less synthesis time, requiring low temperature for processing and the amount of final product one compared with other methods.

In the work of 3*d*-cation (Co, Mn, Ni and Cu)-doped ZnO and 4*f*-cation (Tb and Er)-doped ZnO samples were prepared using the direct decomposition route (Saravanan et al., 2012; Noipa et al., 2014). High purity Zn(CH₃CO₂)₂ (99.99% Purity, Aldich), (CH₃COO)₂Co.4H₂O (99.999%, Purity, Aldich), C₄H₆MnO₄.4H₂O (99.99%, Purity, Aldrich), C₄H₆NiO₄.4H₂O (99.99+%, Purity, Aldrich), Cu(CO₂CH₃)₂.H₂O (99.99+ % Purity, Aldich), (C₂H₃O₂)₃Tb. xH₂O (99.9%, Purity, Aldrich) and (C₂H₃O₂)₃Er. xH₂O (99.9%, Purity, Aldrich) were selected as starting materials. They were mixed using a mortar and pestle for several minutes until homogeneous mixture powder was obtained. For each sample, the mole ratio of M:Zn (where M is TM and RE) was kept corresponding to the nominal composition of Zn_{1-x}M_xO (i.e. M = 0, 0.025, 0.050, 0.075 and 0.100) and then the mixed powder was placed in an alumina crucible that was covered by alumina lid before loading it into the furnace, and was thermally decomposed in air at 300 °C for 6 h. It is worth noting that the thermal decomposition in air at 300 °C for 6 h could not provide a phase formation of a pure phase with the ZnO wurtzite structure for undoped ZnO sample. Thus, the thermal decomposition in air at 400 °C for 6 h was also carried for undoped ZnO sample. The sample preparation using direct thermal decomposition method and characterization are schematically shown in Figure 3.1 and Figure 3.2, respectively.

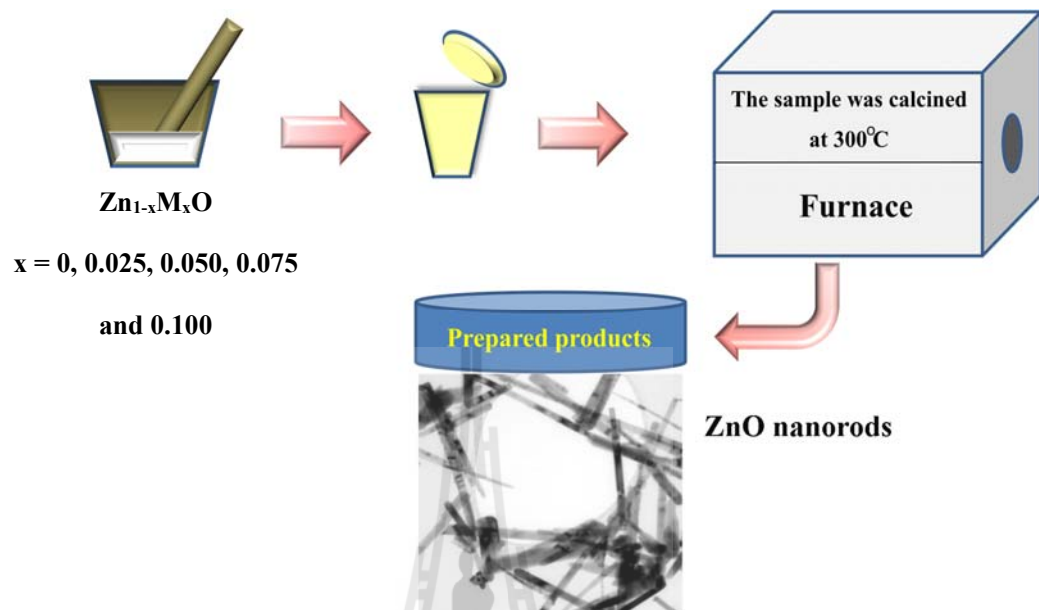


Figure 3.1 A schematic view of the preparation of $Zn_{1-x}M_xO$ samples by direct thermal decomposition method.



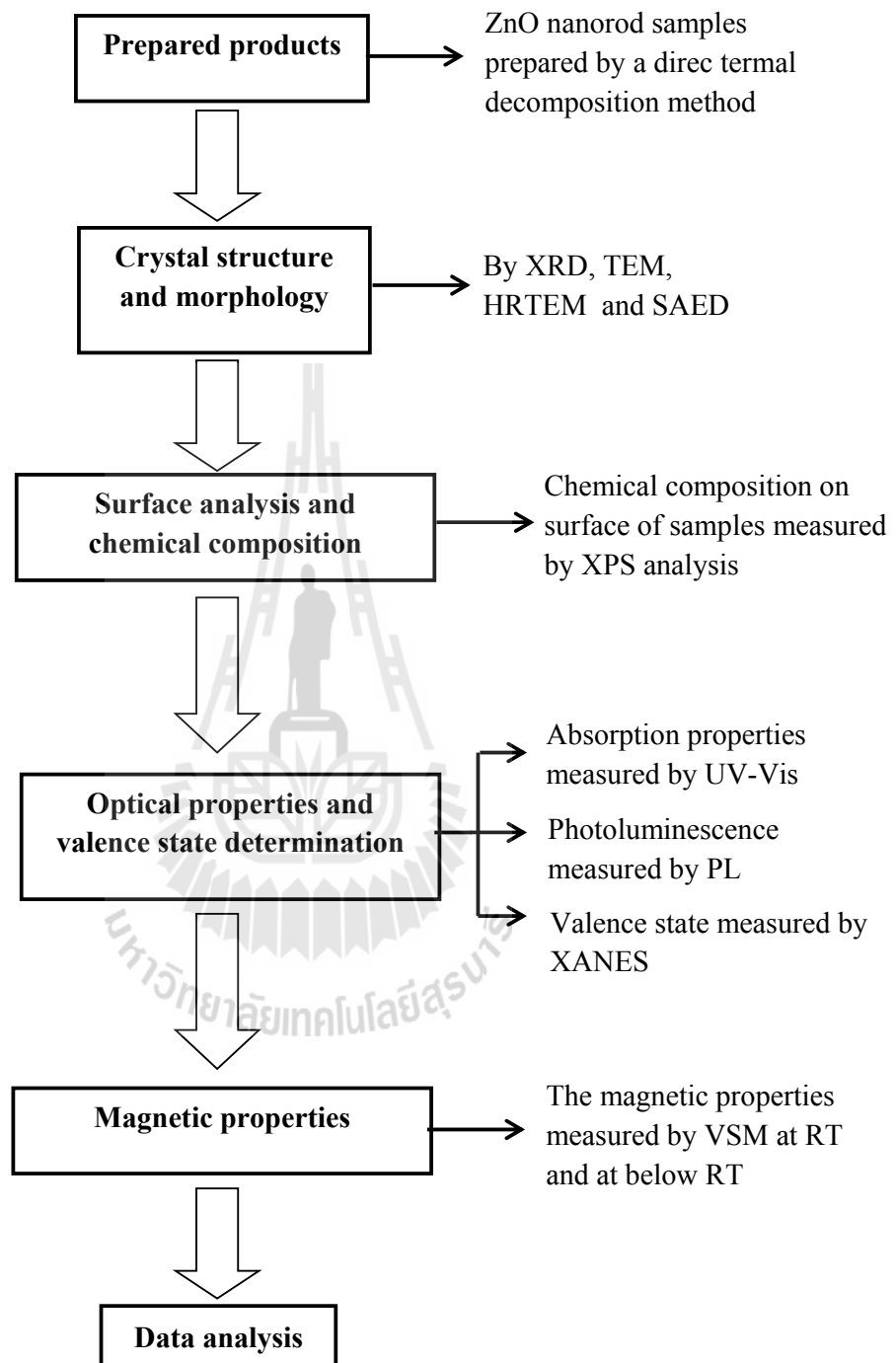


Figure 3.2 A schematic view of the characterization and data analysis.

Table 3.1 List of the materials used for ZnO nanorods preparation, quoting their source and purity.

Materials	source	purity
Zinc acetate ($C_4H_6O_4Zn$), $M_w= 183.48$	Sigma-Aldrich	99.99%
Cobalt (II) acetate tetrahydrate ($(CH_3COO)_2Co \cdot 4H_2O$), $M_w=249.08$	Sigma-Aldrich	99.999%
Manganese (II) acetate tetrahydrate ($C_4H_6MnO_4 \cdot 4H_2O$), $M_w= 245.09$	Sigma-Aldrich	99.99%
Nickel (II) acetate tetrahydrate ($C_4H_6NiO_4 \cdot 4H_2O$), $M_w= 248.84$	Sigma-Aldrich	99.99+%
Copper (II) acetate monohydrate ($(C_2H_3O_2)_2Cu \cdot H_2O$) $M_w=199.65$	Sigma-Aldrich	99.99+%
Terbium (III) acetate hydrate ($(C_2H_3O_2)_3Tb \cdot xH_2O$), $M_w= 336.06$	Sigma-Aldrich	99.9%
Erbium (III) acetate hydrate ($(C_2H_3O_2)_3Er \cdot xH_2O$), $M_w= 329.40$	Sigma-Aldrich	99.9%

3.2 Thermogravimetric and differential thermal analysis

Considering that the thermal analysis (TGA) were conducted to understand the thermal behavior of the samples. To determine the temperature of possible decomposition and crystallization of the powder, the precursors were subjected to thermogravimetric and differential thermal analysis. The schematic of TGA equipment is shown in Figure 3.3. The TG and DTA are the techniques used to measure the change in mass of the sample when it is subjected to a heating rate ($5\text{ }^{\circ}\text{C}/\text{min}$) and under flowing gas (e.g., dried air, Ar or N_2) in controlled atmosphere. The measurement of changes in the mass of the sample as a function of temperature shows in purity, crystallization, and decomposition behavior. The temperature difference between the sample and the reference (e.g. Al_2O_3 or SiC) was recorded using thermocouple, as both are subjected to the same temperature program. During a temperature program, the temperature of the samples will differ from that of the reference due to the difference in heat capacity between the sample and reference.

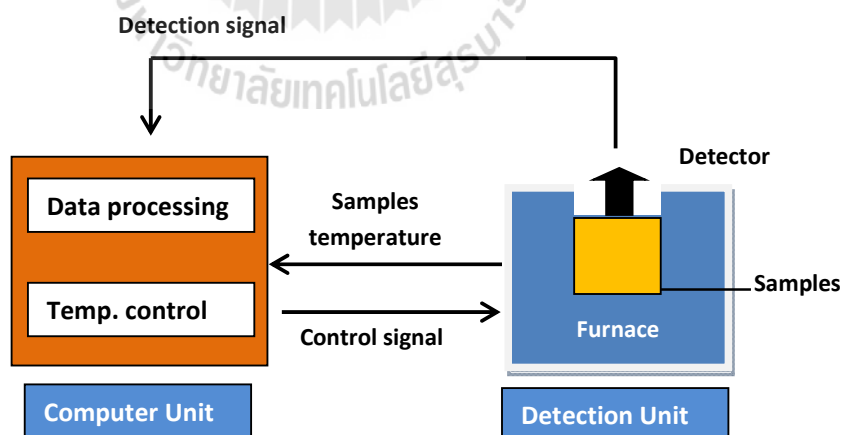


Figure 3.3 Diagram of thermogravimetric and differential thermal analysis (Adapted from Baik et al., 2005)

3.3 Phase Identification, structure, characterization and morphology

3.3.1 X-Ray diffraction (XRD)

The structure of prepared products was characterized by X-ray diffraction (XRD) using $\text{CuK}\alpha$ radiation with $\lambda = 0.15418$ nm (Phillips X'Pert MPD) and optimum scan rate for 2θ was 20-80 degree. The Bragg's Law condition is satisfied by different d -spacings in polycrystalline materials. Plotting the angular position and intensities of the resultant diffraction peaks of the radiation produces a pattern, which is characteristic of the sample. Where a mixture of different phases is present, the resultant diffractogram is formed by addition of the individual patterns. Bragg's Law, the condition for constructive interference, is given in Equation 3.1

$$n\lambda = 2d\sin\theta \quad (3.1)$$

where n is an integer, λ is the wavelength ($\lambda = 0.15418$ nm) of the X-ray radiation and θ is angle of incident, and d is the distance between lattice planes. X-ray diffraction pattern can be analyzed to reveal a sample's crystal structure and orientation, as well as d , the distance between lattice planes and lattice parameters a , b and c (see Figure 3.4).

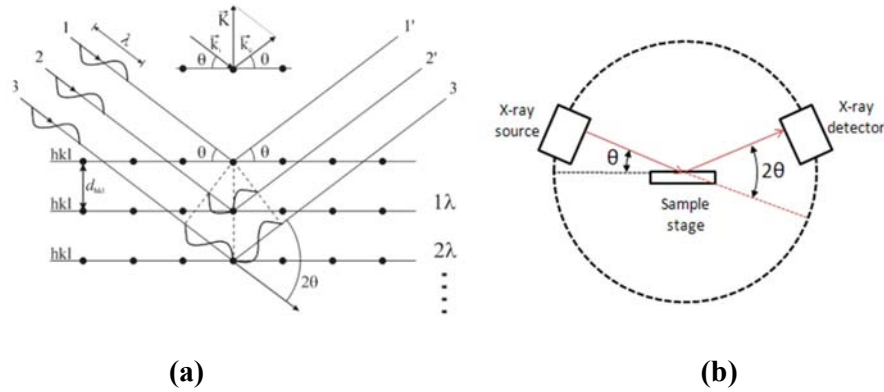


Figure 3.4 (a) The Bragg reflection from a particular set of the lattice planes separated by a distance d and (b) θ is a half of the total angle by which the incident beams is detected (Bouloudenine et al., 2005).

The average crystallite size of materials was calculated by Scherrer's equation (Köseoglu, 2013) (Equation 3.2) from the reflection of the plane.

$$D = 0.9\lambda/\beta\cos\theta \quad (3.2)$$

where λ is the incident wavelength of CuK_{α} radiation, θ is the diffraction angle, and β is the FWHM in radians. In the case of ZnO, the lattice parameter of hexagonal crystal should be calculated using the following formula (Nam et al., 2013):

$$\sin^2\theta = \frac{\lambda^2}{4} \left[\frac{4}{3} \left(\frac{h^2+hk+k^2}{a^2} \right) + \frac{l^2}{c^2} \right] \quad (3.3)$$

where θ is the diffraction angle, λ is the incident wavelength of CuK_{α} radiation ($\lambda = 0.15418$ nm) and h, k and l are all Miller's indices.

3.3.2 Transmission electron microscopy (TEM), High-resolution transmission electron microscopy (HRTEM) and Selected area electron diffraction (SAED)

The morphologies of dilute magnetic oxide ZnO-based samples are examined by transmission electron microscopy (TEM; FEI, TECNAI G2 20). TEM is a microscopy technique whereby a beam of electrons is transmitted through and ultra thin specimen, interacting with the specimen as it passes through it. An image is formed from the electron transmitted through the specimen, magnified and focused by an objective lens and appearing on an imaging screen. High-resolution transmission electron microscopy (HRTEM) is also used to determine the *d*- spacing of lattice fringe in the samples at an atomic scale. In addition, selected area electron diffraction (SAED) used to determine the spotty ring patterns of electron diffraction which can be identified the types of material structures.

3.4 X-ray photoelectron spectroscopy (XPS)

X-ray Photoelectron Spectroscopy (XPS) also known as electron spectroscopy for Chemical Analysis (ESCA) is the most widely used surface analysis technique because it can be applied to a broad range of materials and provides valuable quantitative and chemical state information from the surface of the material being studied (Chen et al., 2005). The average depth of analysis for an XPS measurement is approximately 5 nm. PHI XPS instruments provide the ability to obtain spectra with a lateral spatial resolution as small as 7.5 μm . Spatial distribution information can be obtained by scanning the micro focused x-ray beam across the sample surface. Depth distribution information can be obtained by combining XPS measurements with ion

milling (sputtering) to characterize thin film structures. The information XPS provides about surface layers or thin film structures is important for many industrial and research applications where surface or thin film composition plays a critical role in performance including: nanomaterials, photovoltaics, catalysis, corrosion, adhesion, electronic devices and packaging, magnetic media, display technology, surface treatments, and thin film coatings used for numerous applications. XPS is typically accomplished by exciting a samples surface with mono-energetic Al K_{α} X-rays causing photoelectrons to be emitted from the sample surface. An electron energy analyzer is used to measure the energy of the emitted photoelectrons. From the binding energy and intensity of a photoelectron peak, the elemental identity, chemical state, and quantity of a detected element can be determined. Physical Electronics XPS instruments function in a manner analogous to SEM/EDS instruments that use a finely focused electron beam to create SEM images for sample viewing and point spectra or images for compositional analysis. With the PHI XPS instruments, a finely focused x-ray beam is scanned to create secondary electron images for sample viewing and point spectra or images for compositional analysis. The size of the x-ray beam can be increased to support the efficient analysis of larger samples with homogeneous composition. In contrast to SEM/EDS which has a typical analysis depth of 1-3 μm , XPS is a surface analysis technique with a typical analysis depth of less than 5 nm and is therefore better suited for the compositional analysis of ultra-thin layers. Hence, our samples were made on flat bulk for measurement, with X-ray photo electronic spectroscopy (XPS: AXIS ULTRA^{DLD}, Kratos analytical, Manchester UK.).

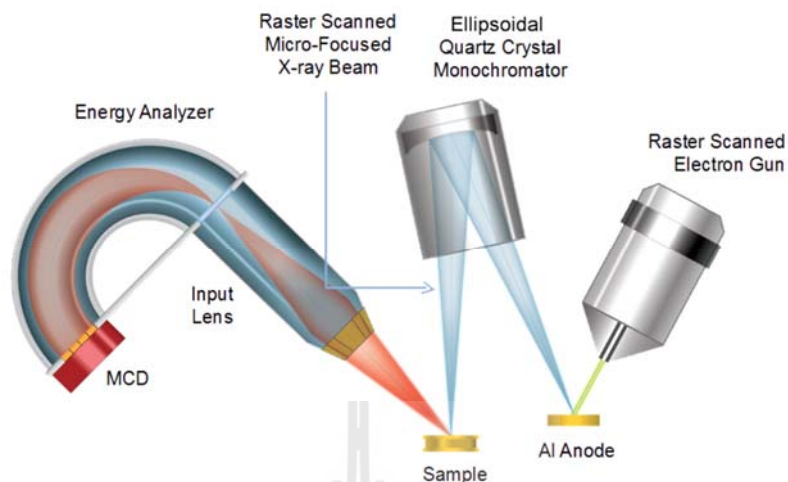


Figure 3.5 Schematic diagram of the XPS (Siegbahn and Edvarson, 1956).

3.5 Optical properties and valence state determination

3.5.1 UV-visible spectroscopy (UV-Vis)

Room temperature absorption spectra of dilute magnetic oxide ZnO-based samples were recorded using an UV-VIS-NIR scanning spectroscopy (UV-3101PC; Shimadzu, Japan) with the range of 200-800 nm. Ultraviolet-visible spectroscopy or ultraviolet-visible spectrophotometry (UV-Vis or UV/Vis) refers to absorption spectroscopy or reflectance spectroscopy in the ultraviolet-visible spectral region (Caglar et al., 2012). This means it uses light in the visible and adjacent (near-UV and near-infrared (NIR)) ranges. The absorption or reflectance in the visible range directly affects the perceived color of the chemicals involved. In this region of the electromagnetic spectrum, molecules undergo electronic transitions. This technique is complementary to fluorescence spectroscopy, in that fluorescence deals with transitions from the excited state to the ground state, while absorption measures transitions from the ground state to the excited state. UV-Vis spectroscopy is

routinely used in analytical chemistry for the quantitative determination of different analysis, such as transition metal ions, highly conjugated organic compounds, and biological macromolecules. Spectroscopic analysis is commonly carried out in solutions but solids and gases may also be studied.

3.5.2 X-ray absorption near-edge structure (XANES)

The Tb and Er L_3 edge and Zn, Co, Mn, Ni and Cu K edge were studied using XANES in fluorescence mode at the BL5.2 Station at Siam Photon Laboratory (Synchrotron Light Research Institute (Public Organization), SLRI) in Nakhon Ratchasima, Thailand. X-ray absorption spectroscopy (XAS) is an element specific technique and is broken into 2 regimes consisting of x-ray absorption near-edge structure (XANES) and extended x-ray absorption fine-structure (EXAFS)(as shown in Figure 3.6), which contain related but slightly different information about an element's local coordination and chemical state. An x-ray is absorbed by an atom when the energy of the x-ray is transferred to a core-level electron (K, L, or M shell) which is ejected from the atom. The atom is left in an excited state with an empty electronic level (a core hole). Any excess energy from the x-ray is given to the ejected photo-electron (see Figure 3.7(a)). XAS measures the energy dependence of the x-ray absorption coefficient $\mu(E)$ at and above the absorption edge of a selected element. $\mu(E)$ can be measured two ways. First way is Transmission mode as shown in Equation 3.4. The absorption is measured directly by measuring what is transmitted through the sample. Second way is fluorescence mode (see Equation 3.5). The re-filling of the deep core hole is detected. Typically the fluorescent x-ray is measured (see Figure 3.7(b)).

$$\mu(E)t = -\ln(I/I_0) \quad (3.4)$$

$$\mu(E) \propto I_f / I_0 \quad (3.5)$$

where I_0 is the x-ray intensity hitting, I is the intensity transmitted, $\mu(E)$ is absorption coefficient, t is a material of thickness, and I_f is the fluorescence intensity.

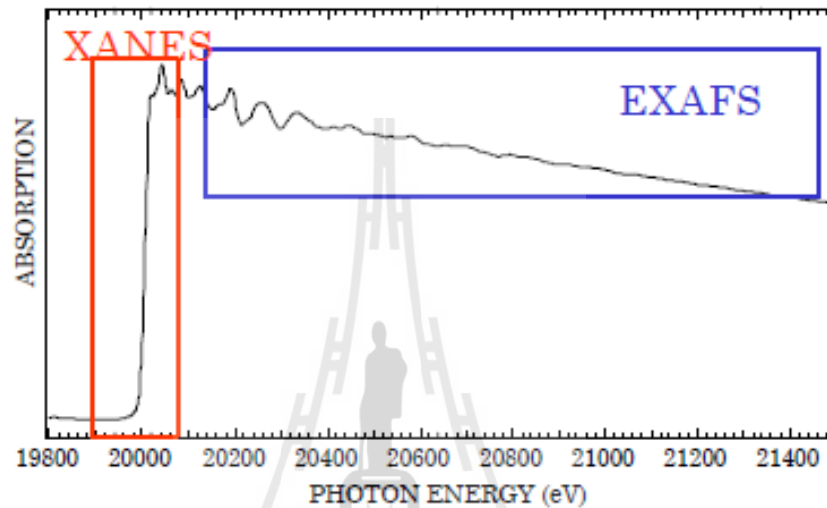


Figure 3.6 XANES and EXAFS regions of X-ray absorption spectrum (Adapted from xafs.org, 2008).

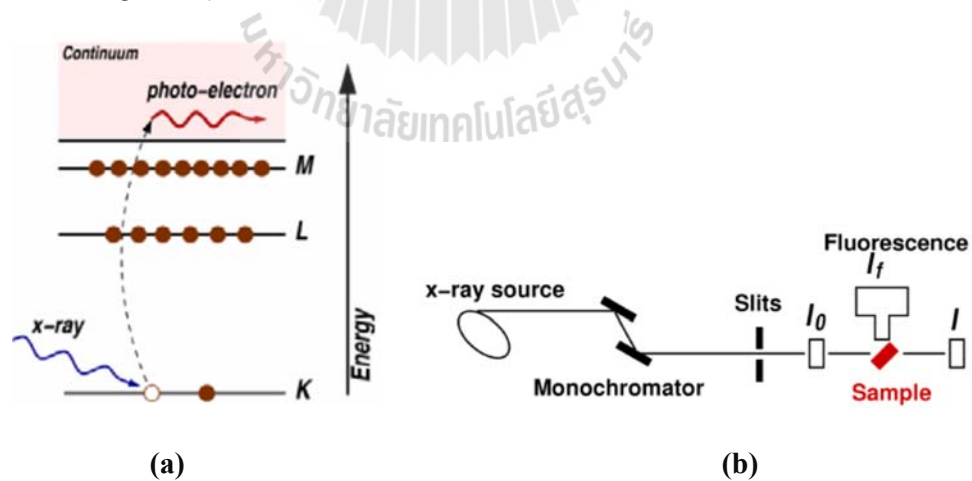


Figure 3.7 (a) Schematic diagram of the XAS (b) Schematic measured of the XANES (from xafs.org, 2008).

3.5.3 Photoluminescence (PL)

Photoluminescence (abbreviated as PL) is light emission from any form of matter after the absorption of photons (electromagnetic radiation). It is one of many forms of luminescence (light emission) and is initiated by photoexcitation (excitation by photons), hence the prefix photo. Following excitation various relaxation processes typically occur in which other photons are re-radiated. Time periods between absorption and emission may vary: ranging from short femtosecond-regime for emission involving free-carrier plasma in inorganic semiconductors (Hayes and Deveaud, 2002) up to milliseconds for phosphorescent processes in molecular systems; and under special circumstances delay of emission may even span to minutes or hours. Observation of photoluminescence at a certain energy can be viewed as indication that excitation populated an excited state associated with this transition energy. While this is generally true in atoms and similar systems, correlations and other more complex phenomena also act as sources for photoluminescence in many-body systems such as semiconductors. PL depend on the nature of the optical excitation. The excitation energy selects the initial photoexcited state and govern the penetration depth of the incident light. The PL signal often depends on the density of photoexcited electrons and the intensity of the incident beam can be adjusted to control this parameter. When the type or quality of material under investigation varies spatially, the PL signal will change with excitation position. In addition, pulses optical excitation provides a powerful means for studying transient phenomena. Short laser pulses produce virtually instantaneous excited populations, after which the PL signal can be monitored to determine recombination rates. In this work, photoluminescence spectra (PL: PerkinElmer LS-55B, PerkinElmer Instrument, Waltham, MA, USA)

were obtained at room temperature using a Xenon lamp as an excitation wavelength of 325 nm. A typical PL set-up is shown in Figure 3.8. Generally, the densities of defects and oxygen vacancies affect significantly the optical properties.

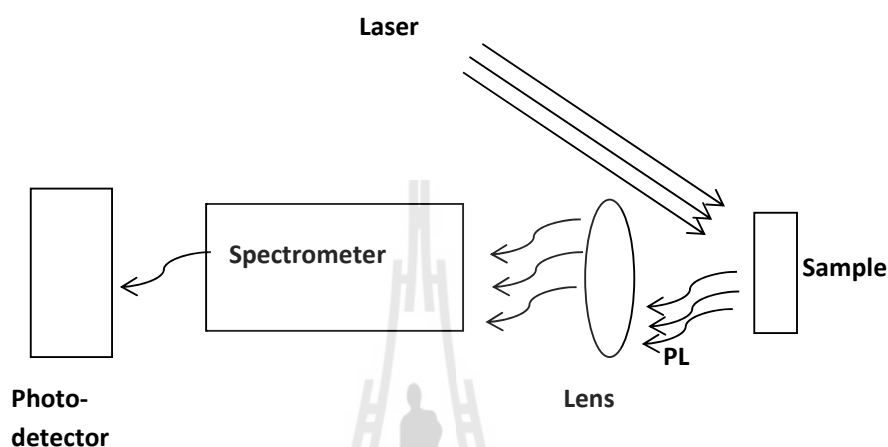


Figure 3.8 Typical experimental set up for PL measurements (Adapted from Timothy, 2000).

3.6 Magnetic measurement

The magnetic properties of the samples are investigated at RT and below RT by using a vibrating sample magnetometer (VSM; VersaLabTM, PPMS[®]). A Vibrating sample magnetometer (VSM) measures the magnetic properties of a large variety of materials such as diamagnetic, paramagnetic, ferromagnetic and antiferromagnetic. For the measurement, powder were weighed, then place in a small sample holder located at the end of a sample rod mounted in an electromechanical transducer for measurement. The sample is vibrated parallel to the field direction; an electro magnet provides the magnetizing field, a vibrator mechanism to vibrate the sample in the magnetic field, and detection coils which generate signal voltage due to the changing

flux emanating from the vibrating sample. The output measurement displays the magnetic moment as function of a magnetic field or the temperature dependent of magnetization. The measurement can be made at RT and below RT (293 K to 50K) in field rang of 10000 Oe to 30000 Oe. The VSM is shown schematically in Figure 3.9.

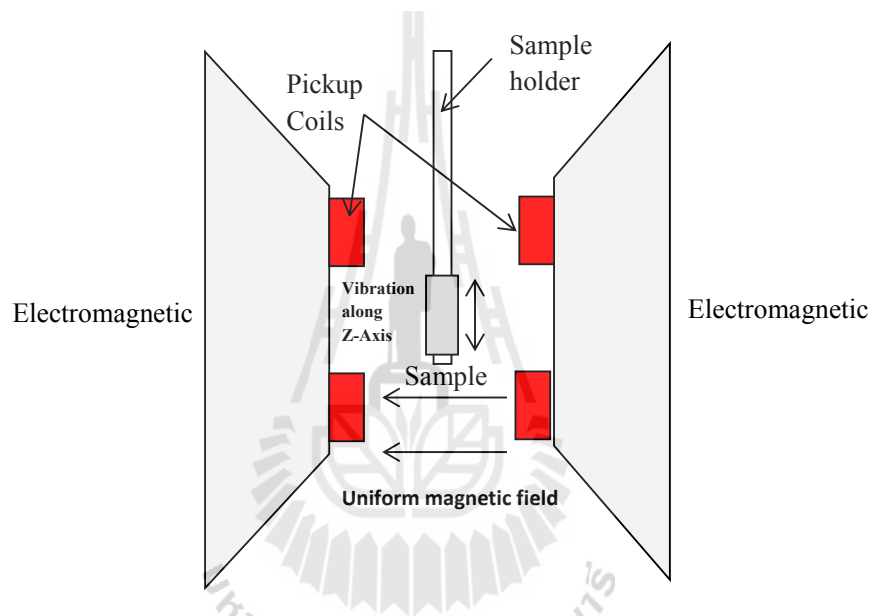


Figure 3.9 Schematic diagram of the VSM (Adapted from Smith, 1956).

CHAPTER IV

RESULTES AND DISCUSSION

In this chapter, the experimental results and discussion for undoped and M-doped-ZnO samples are discussed. It is divided into three parts. The first part is TGA analysis for a phase formation and composition of the TM- and RE-doped ZnO samples, The second part is the characterization of direct thermal decomposed TM-doped ZnO samples (where TM = Co, Mn and Ni, respectively.) using XRD, TEM, HRTEM, XPS, XANES, UV-Vis, PL and VSM. In addition, the magnetic properties of nonmagnetic ion in Cu-doped ZnO nanorods are included in this part. The third part is the characterization of RE-doped ZnO samples (where RE = Tb and Er) using XRD, TEM, HRTEM, XPS, XANES, UV-Vis, PL and VSM. Detail of these results and discussion are presented. The origin of ferromagnetism in the prepared samples is also discussed.

4.1 Phase formation and composition

Typical TG and DTA curves of the powder precursor calcination for undoped, Co-, Mn-, Ni-, Cu-, Tb- and Er-doped ZnO samples from 25 °C up to 1000 °C with heating rate of 5 °C/min are shown in Figure 4.1(a) and Figure 4.1(b). The thermogravimetric (TG) curves show a major weight loss at ~100 °C and from ~150 °C up to ~334 °C for the undoped ZnO samples (as shown in Figure 4.1(a)). The clear plateau formed between 334 °C to 1000 °C on TG curve revealing the formation of

ZnO as a decomposition product. The DTA curve shows both physical conditions happened as endothermic reaction since the maxima of the temperature are $\sim 100^\circ\text{C}$ and $\sim 250^\circ\text{C}$, respectively.

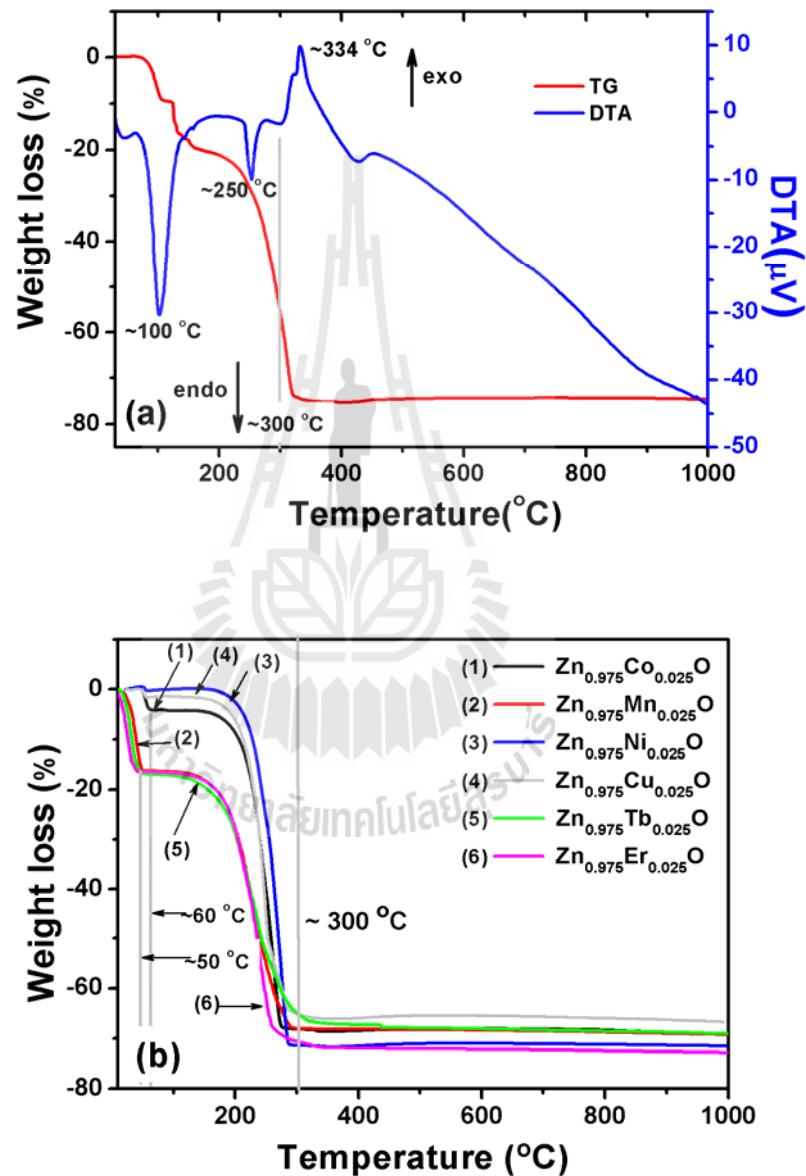


Figure 4.1 (a) TG-DTA of undoped ZnO sample and (b) DTA data for TM- and RE-doped ZnO samples with $x = 0.025$.

Moreover, on the DTA a curve not only shows the endothermic reaction but also shows the exothermic effect. The peaks observed at ~ 334 °C indicates that the thermal events can be associated with the burnout of organic species involved in the precursor powder (e.g. organic mass remained from acetate materials), of the residual carbon or due to direct crystallization of ZnO from the amorphous component. No change in the mass or any thermal activity was observed over 400 °C. Attractively, the TG curves in Figure 4.1(b) show the maximum weight loss close to 71.4% with step from ~ 47 °C up to ~ 300 °C for Mn-, Tb- and Er-doped ZnO samples and ~ 63 °C up to ~ 300 °C for Co-, Ni- and Cu-doped ZnO sample, respectively. No further weight loss and no thermal effect were observed around ~ 300 °C, indicating that no decomposition occurred around this temperature. This phenomenon suggests that TM- and RE-doping can be reduced preparation temperature for a formation of hexagonal ZnO, in comparison with undoped ZnO. Hence, the doped samples were thermally decomposed in air at 300 °C and were kept at this temperature for 6 h.

4.2 TM-doped ZnO nanorods

This part we will discuss on structural characterization, morphology, chemical composition, absorption, photoluminescence and magnetic properties of Co-, Mn-, Ni- and Cu-doped ZnO nanorods.

4.2.1 Structural characterization, morphology and chemical compositions of TM-doped ZnO (i.e. TM = Co, Mn, Ni and Cu)

The XRD patterns of the thermally decomposed undoped ZnO at 300 °C, a relative weak peak of ZnO and some other peaks of zinc acetate materials were

observed while the thermal decomposition increased above 400 °C, all of the diffraction peaks show the ZnO wurtzite structure which is corresponding to the standard data (JCPDS, 36-1451) for undoped ZnO sample as shown in Figure 4.2. XRD patterns of Co- and Mn-doped ZnO nanorods in Figure 4.3 and Figure 4.4 exactly show the same peak patterns which can be indexed as the ZnO wurtzite structure in the standard data (JCPDS, 36-1451). This indicates that the wurtzite structure is not affected by Co and Mn substitution. Moreover, the XRD patterns of Ni-doped ZnO nanorods in Figure 4.5 present a peak pattern, which is confirmed a formation of the ZnO wurtzite structure for $Zn_{0.975}Ni_{0.025}O$ sample while the nanocrystalline Ni-doped ZnO samples with concentration of $x > 0.025$ presented impurity phases of Ni metal and NiO. Figure 4.6 illustrates the XRD patterns of the nanocrystalline Cu-doped ZnO with different doping concentrations. For comparison, the XRD pattern for undoped ZnO (calcined at 400 °C) is also shown in Figure 4.6(a). The diffraction peaks correspond to (100), (002), (101), (102), (110), (103), (200), (112) and (201) planes of the standard data (JCPDS, 36-1451), whereas the precursor calcined at 300 °C presents impurity phase in XRD patterns (as shown inset). Figures 4.6(b) - 4.6(e) are XRD patterns of Cu-doped ZnO (i.e., $Zn_{1-x}Cu_xO$) nanocrystals with $x = 0.025, 0.050, 0.075$ and 0.100 , respectively. Impurity phases of CuO, Cu₂O, and Cu are also detected showing the peaks at 38.95, 42.29 and 43.29 of the 2θ which were consistent with those of the CuO (200) (JCPDS, 45-0937), Cu₂O (200) (JCPDS, 05-0667) and Cu (111) (JCPDS, 04-0836) metal diffractions, respectively. All the samples have impurity phases except the $Zn_{0.975}Cu_{0.025}O$ sample showing only pure phase of ZnO. Therefore, the secondary phases of those peaks can be attributed to the low Ni and Cu solubility in ZnO structure. In addition, the doping

of TM ions (i.e. TM= Co, Mn, Ni and Cu) leads to the decrease of prepared temperature for a formation of wurtzite ZnO structure. This mechanism under our study is not well understood and future study is needed.

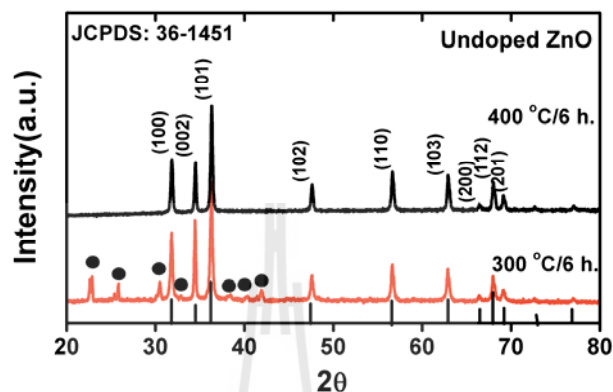


Figure 4.2 XRD patterns of thermally decomposed undoped ZnO sample in air at 400 °C for 6 h and undoped ZnO prepared in air at 300 for 6 h.

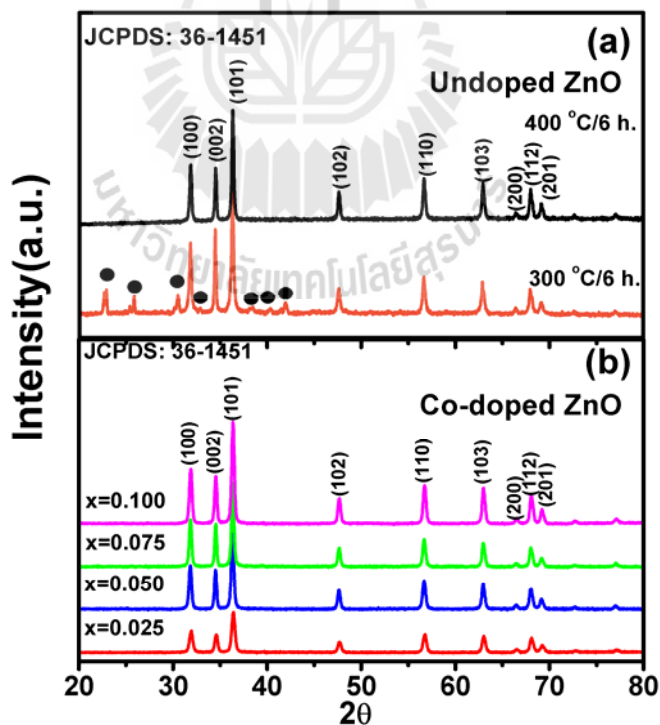


Figure 4.3 XRD patterns of thermally decomposed undoped ZnO sample in air at 400 °C for 6 h (a) and (b) Co-doped ZnO samples prepared in air at 300 °C for 6 h.

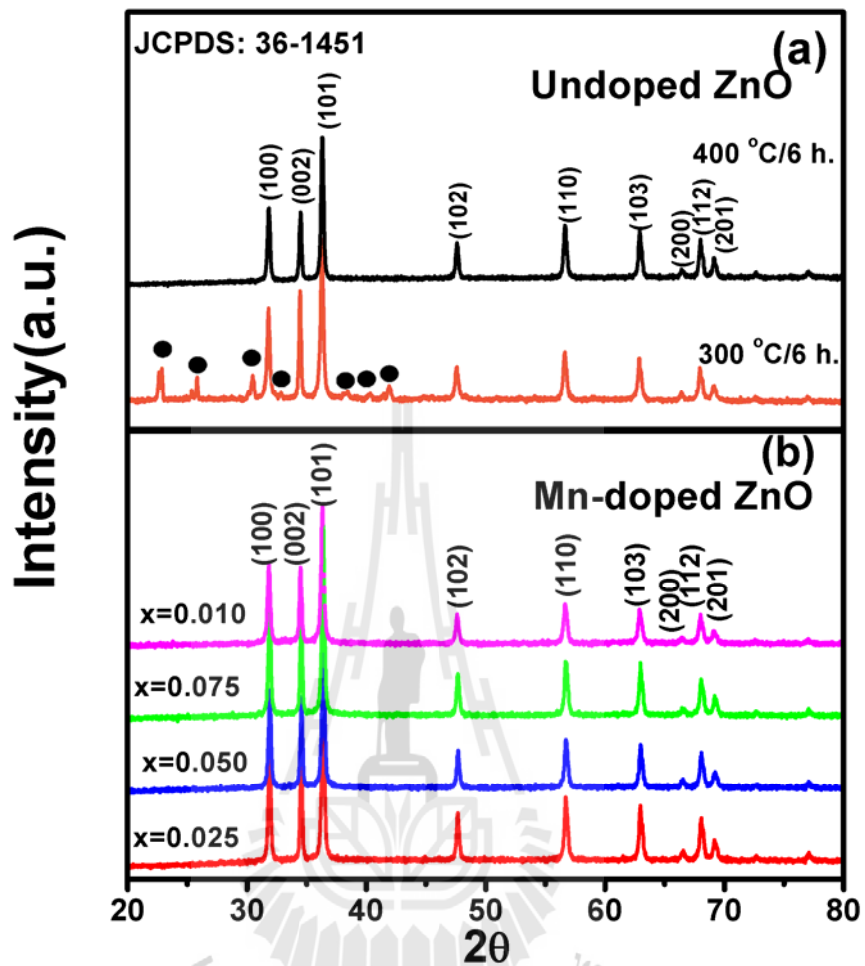


Figure 4.4 (a) XRD patterns of undoped ZnO sample thermally decomposed in air at 400 °C for 6 h and undoped ZnO sample prepared in air at 300 °C for 6 h and (b) the XRD patterns of Mn-doped ZnO samples prepared in air at 300 °C for 6 h with $x = 0.025, 0.050, 0.075$ and 0.100 , respectively.

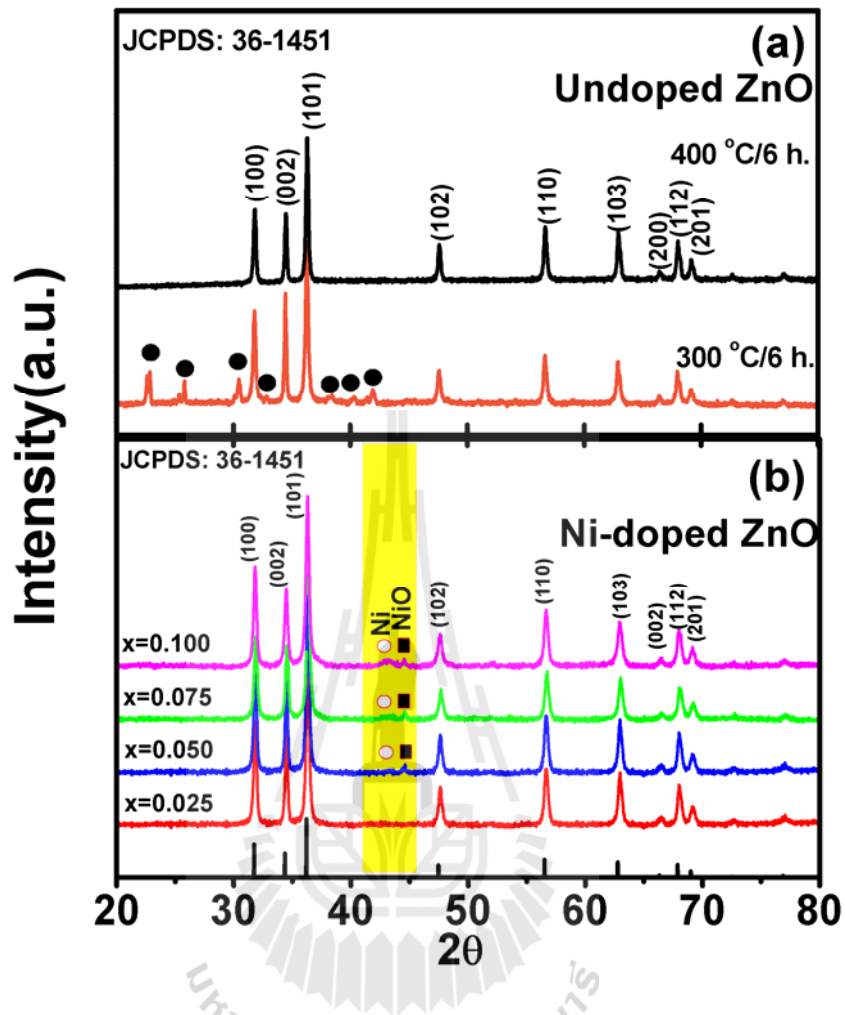


Figure 4.5 (a) XRD patterns of undoped ZnO sample thermally decomposed ZnO in air at 400 °C for 6 h and undoped ZnO sample prepared in air at 300 °C for 6 h and (b) the XRD patterns of Ni-doped ZnO samples prepared in air at 300 °C for 6 h with $x = 0.025, 0.050, 0.075$ and 0.100 , respectively.

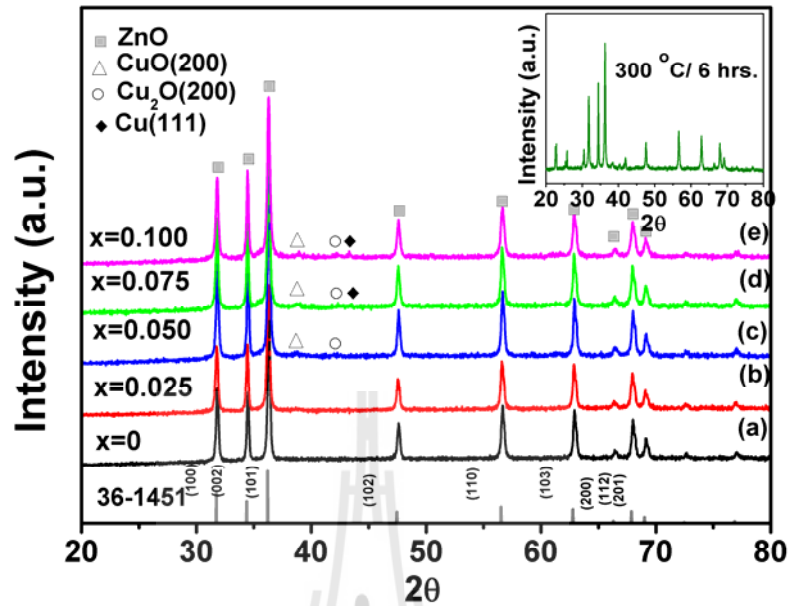


Figure 4.6 XRD patterns of undoped ZnO (calcined at 400 °C) (a) and Cu-doped ZnO in air at 300 °C for 6 h for $x = 0.025$ (b), $x = 0.050$ (c), $x = 0.075$ (d) and $x = 0.100$ (e), respectively. The inset shows XRD patterns precursor calcined in air at 300 °C for 6 h.

The average crystallite sizes (D) of ZnO nanorods are calculated by the Debye-Scherrer formula as follows:

$$D = 0.9\lambda/\beta\cos\theta \quad (4.1)$$

where λ is the wavelength of X-ray (0.154 nm), θ is the Bragg angle of X-ray diffractions, β is the FWHM (full width at half maximum) for the corresponding peak. The average crystallite sizes and the lattice parameters (a and c) were calculated from (100), (002), (101), (102), (110) and (103) peaks and the results are summarized

in Table 4.1 and Table 4.2. For comparison, average crystallite sizes and lattice parameters of Co-, Mn- and Ni-doped ZnO are also shown in Figure 4.7(a), Figure 4.8(a) and 4.8(b). As a result, average crystallite sizes and lattice parameters a and c of the Co-doped ZnO samples with x varying from 0.025 to 0.075 decrease with increasing the Co concentration. These values are smaller than those of lattice $a = 0.32488$ nm and $c = 0.52066$ nm in the standard data (JCPDS, 36-1451). This phenomenon is a proof of the incorporation of Co ions inside the ZnO crystal lattice due to the smaller ionic radius of Co^{2+} (0.65\AA) replaced larger ionic radius of Zn^{2+} (0.74\AA) (Bouloudenine et al., 2005). Hence, Co incorporation will lead to shrink of the ZnO lattice and decreases crystallite size. Furthermore, an average crystallites size of the Mn-doped ZnO does not changed, then the values of a and c increase with the value of x increasing. This variation indicates that the lattice of ZnO begins expanding with increasing the Mn content. There was an effect of doping on the values of lattice parameters but on crystallite size. It means that the dopants inhibit the growth of nanocrystals, indicating the dopants may distribute in the surface of ZnO nanorods. These results are consistent with previous report and are not in a good agreement with earlier reports for Mn-doped ZnO nanowires by Baik et al. (2005) and Mn-doped ZnO thin films by Xu et al. (2006). The wurtzite lattice parameters and average crystallite sizes decrease with doping the Ni atoms where $x = 0.025$; this phenomenon is a proof of the incorporation of Ni ions inside the ZnO crystal lattice due to the smaller ionic radius of Ni^{2+} (0.69\AA) replaced larger ionic radius of Zn^{2+} (0.74\AA). Hence, Ni incorporation will lead to the decrease in crystallite size. And then the values increase with increasing the value of x and these values are almost unchanged when $x > 0.025$, indicating that the high dopants may distribute in

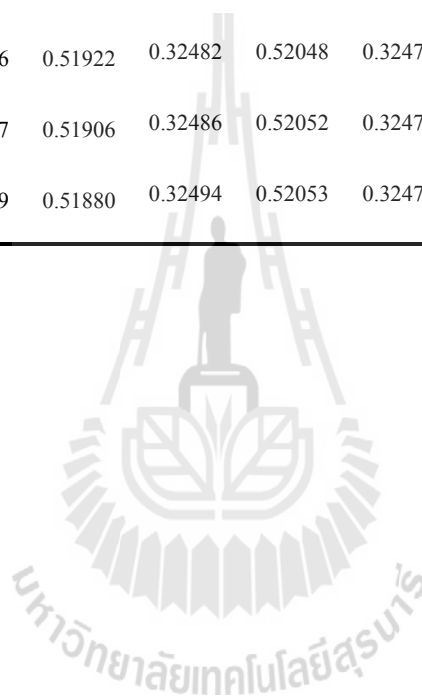
the surface of ZnO nanorods and the second phases were formed. Ordinarily, the valence state of Cu could be assumed to be +1 or/and + 2 in the Cu-doped ZnO. The radius of Cu^{1+} and Cu^{2+} ions are 0.96 Å and 0.72 Å, respectively. From our results, the crystallites size (Figure 4.7(b)) and lattice parameter of c in Cu-doped ZnO samples (see Figure 4.9(a)) are smaller than those of the undoped sample, with increase of Cu contents of $x = 0.025$ to 0.050, whereas parameter of a increases (see Figure 4.9(b)) with increasing the Cu content. This is possibly due to the substitution of Cu^{2+} ion into the Zn site. A similar observation was also reported for in ZnO:Cu films (Yang et al., 2012). However, Ligang et al. (2006) reported that when Cu^{1+} ions substituted Zn^{2+} ions, the lattice constant increased. The Cu^{1+} , Cu^{2+} substituted and the Cu^{2+} interstitial might be the main impurities in Cu-doped ZnO samples. Both Cu^{1+} substitute and Cu^{2+} interstitial would affect the concentration of the interstitial ZnO, oxygen vacancies, and Zn vacancies.

Table 4.1 Summary of crystallite size of undoped ZnO and TM-doped ZnO nanorods thermally decomposed at 300 °C at for 6 h.

Doping level	Crystallite size (nm)			
	Co	Mn	Ni	Cu
$x = 0.000$	36.90 ± 0.8500	36.90 ± 0.8500	36.90 ± 0.8500	36.90 ± 0.8500
$x = 0.025$	33.20 ± 0.9600	37.80 ± 0.9700	33.20 ± 0.8700	32.80 ± 0.9500
$x = 0.050$	29.90 ± 0.8700	38.10 ± 0.9500	36.80 ± 0.8600	36.50 ± 0.8800
$x = 0.075$	28.30 ± 0.9800	37.92 ± 0.8600	37.30 ± 0.9800	35.70 ± 0.9700
$x = 0.100$	32.80 ± 0.8500	38.05 ± 0.7800	37.80 ± 0.9500	35.80 ± 0.8600

Table 4.2 Summary of lattice constant (a and c) of undoped ZnO and TM-doped ZnO nanorods thermally decomposed at 300 °C at for 6 h.

Doping level	lattice constant, $a = b$ and c (nm)							
	Co		Mn		Ni		Cu	
	a	c	a	c	a	c	a	c
$x = 0.000$	0.32477	0.52041	0.32477	0.52041	0.32477	0.52041	0.32477	0.52041
$x = 0.025$	0.32448	0.51970	0.32478	0.52044	0.32454	0.51980	0.32487	0.52038
$x = 0.050$	0.32436	0.51922	0.32482	0.52048	0.32472	0.52038	0.32488	0.52034
$x = 0.075$	0.32427	0.51906	0.32486	0.52052	0.32474	0.52040	0.32486	0.52035
$x = 0.100$	0.32419	0.51880	0.32494	0.52053	0.32471	0.52043	0.32487	0.52034



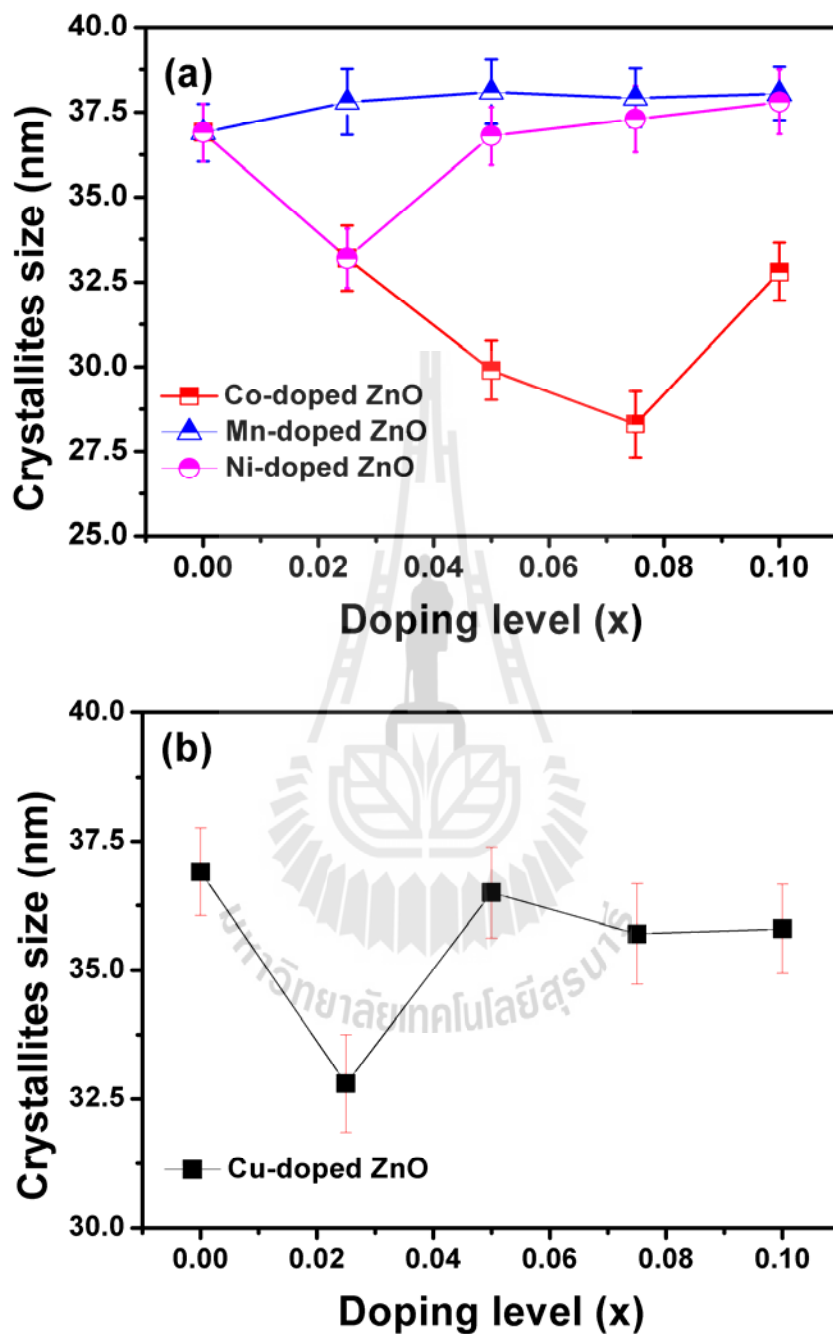


Figure 4.7 An average crystallite size of undoped ZnO sample prepared at 400 °C for 6 h, (a) Co-, Mn- and Ni-doped ZnO nanorods and (b) Cu-doped ZnO nanorods prepared at 300 °C for 6 h.

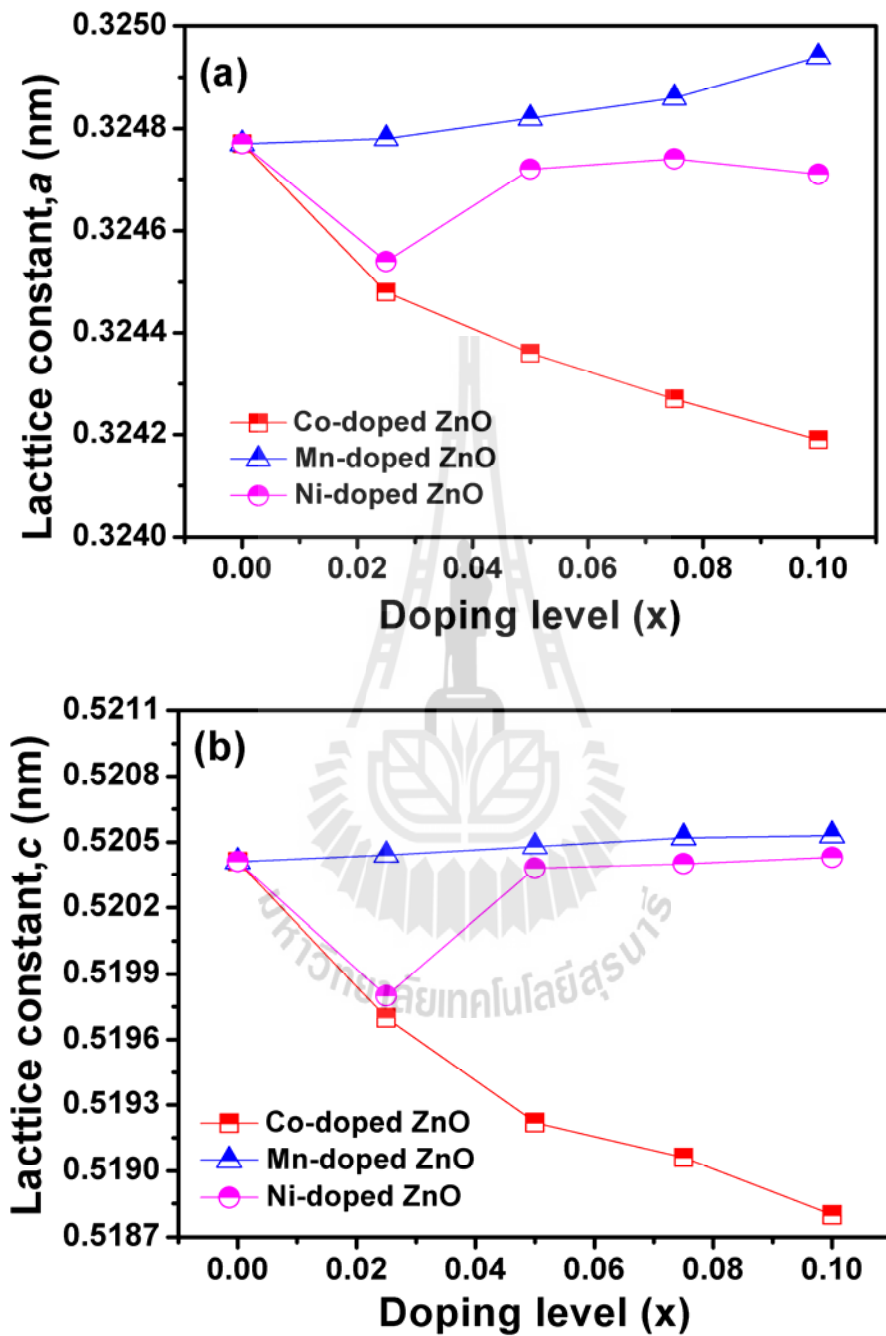


Figure 4.8 Lattice constant of undoped ZnO sample prepared at 400 °C for 6 h, (a) *a* parameter and (b) *c* parameter of Co-, Mn- and Ni-doped ZnO nanorods prepared at 300 °C for 6 h, respectively.

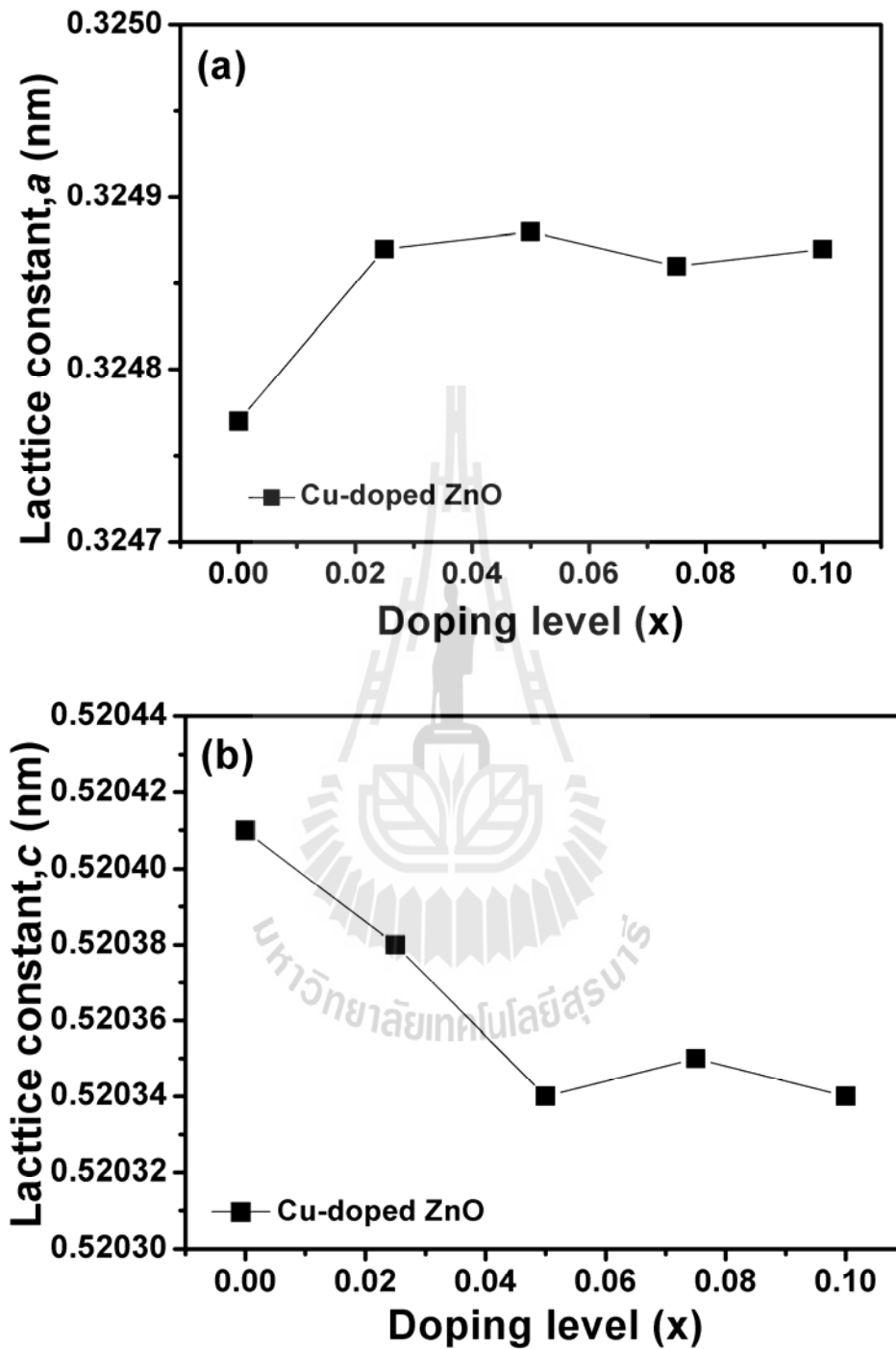


Figure 4.9 Lattice constant of undoped ZnO sample prepared at 400 °C for 6 h, (a) *a* parameter and (b) *c* parameter of Cu-doped ZnO nanorods prepared at 300 °C for 6 h.

The morphology and structure of the ZnO and Co-, Mn-, Ni-, Cu-doped ZnO nanorods were investigated by TEM. Figure 4.10 shows the TEM bright field images of undoped ZnO sample consisting of both nanoparticles with particle size of about 21 nm and nanorods of 46 nm in diameter with 105 to 275 nm in length. Figures 4.11 - 4.14 show TEM images of Co, Mn-, Cu- (with x varies from 0,025 to 0.100) and Ni-doped ZnO nanorods samples (with $x = 0.025$), revealing a mixture of nanorods with various in diameters and in length; most of nanorods are straight in morphology and smooth in surface as shown in the inset of Figure 4.14. And also high resolution TEM (HRTEM) micrographs show the interplanar distance of fringes of ~ 0.26 nm corresponding to the (002) plane of wurtzite ZnO. The selected-area electron diffractions (SAED) show spotty ring patterns, revealing their highly crystalline ZnO wurtzite structure (JCPDS, 36-1451). These are consistent with those of (100), (101), (102) and (110) planes of the XRD results.

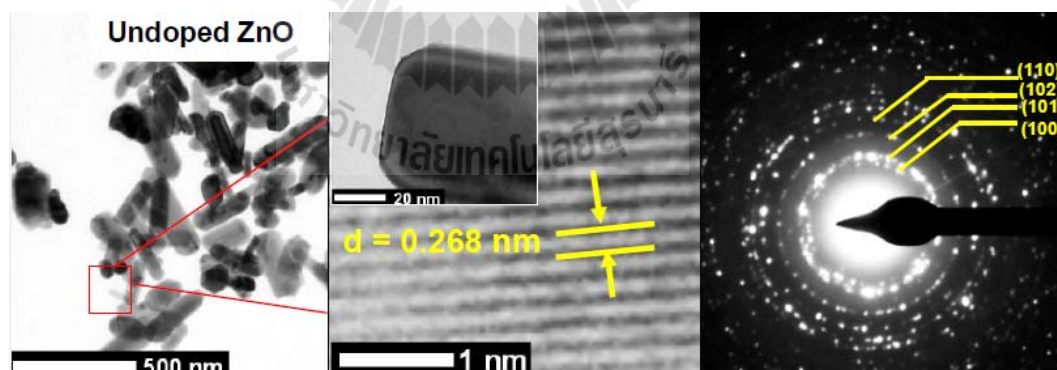


Figure 4.10 TEM bright field and high-resolution TEM (HRTEM) images with corresponding SEAD patterns of undoped ZnO sample prepared in air at 400 °C for 6 h.

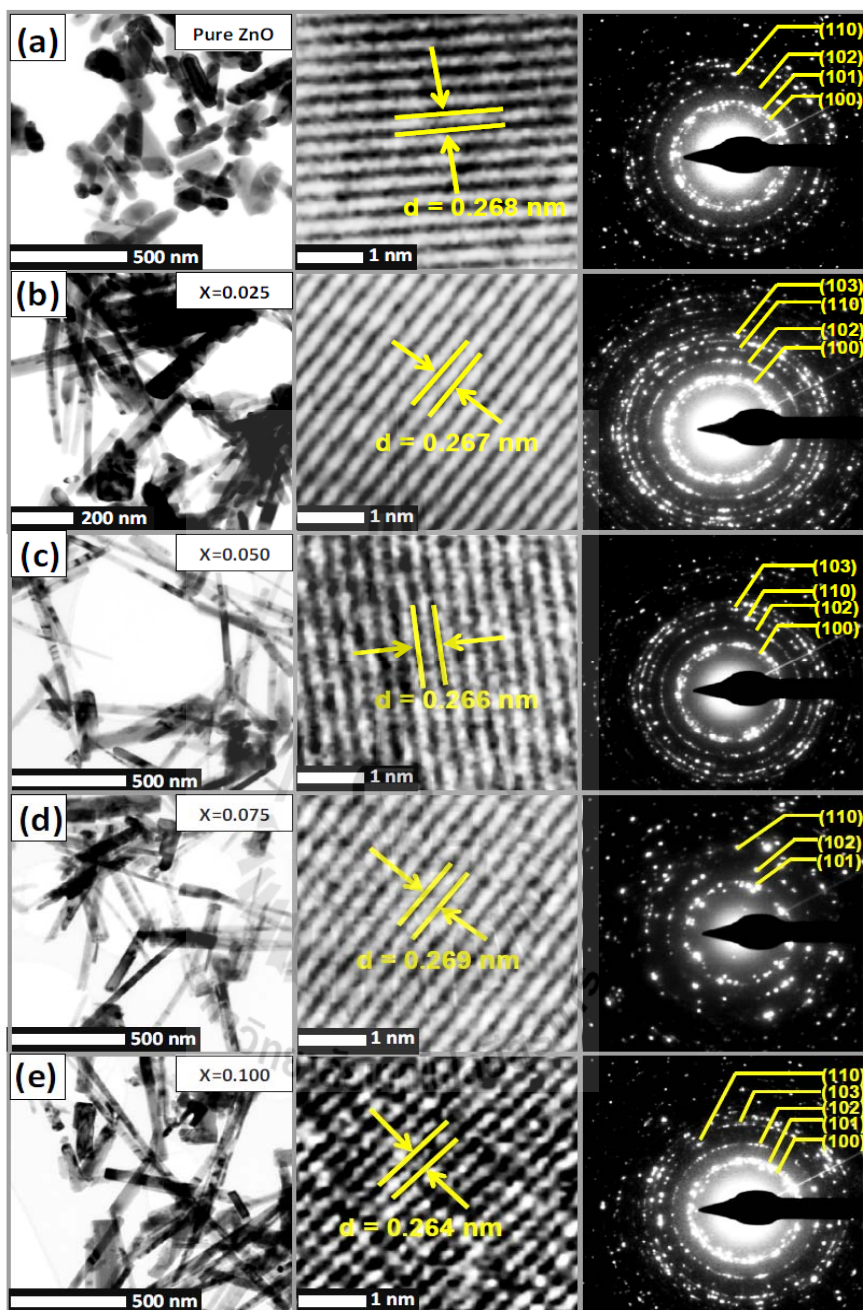


Figure 4.11 TEM bright field and high-resolution TEM (HRTEM) images with corresponding SEAD patterns of undoped ZnO sample prepared in air at 400 °C for 6 h (a) and Co-doped ZnO samples prepared in air at 300 °C for 6 h with $x = 0.025$ (b), $x = 0.050$ (c), $x = 0.075$ (d), and $x = 0.100$ (e).

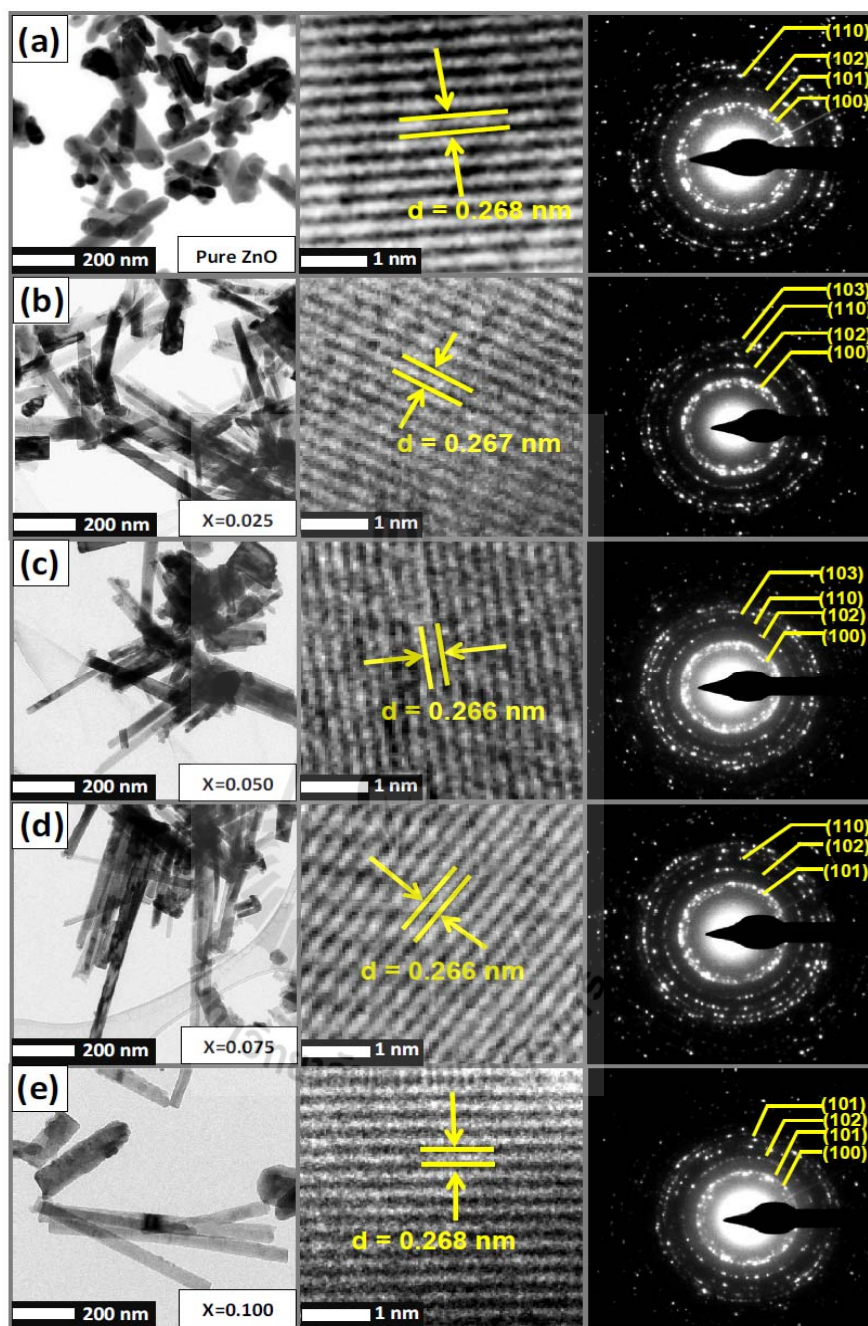


Figure 4.12 TEM bright field and high-resolution TEM (HRTEM) images with corresponding SEAD patterns of undoped ZnO sample prepared in air at 400 °C for 6 h (a) and Mn-doped ZnO samples prepared in air at 300 °C for 6 h with $x = 0.025$ (b), $x = 0.050$ (c), $x = 0.075$ (d), and $x = 0.100$ (e).

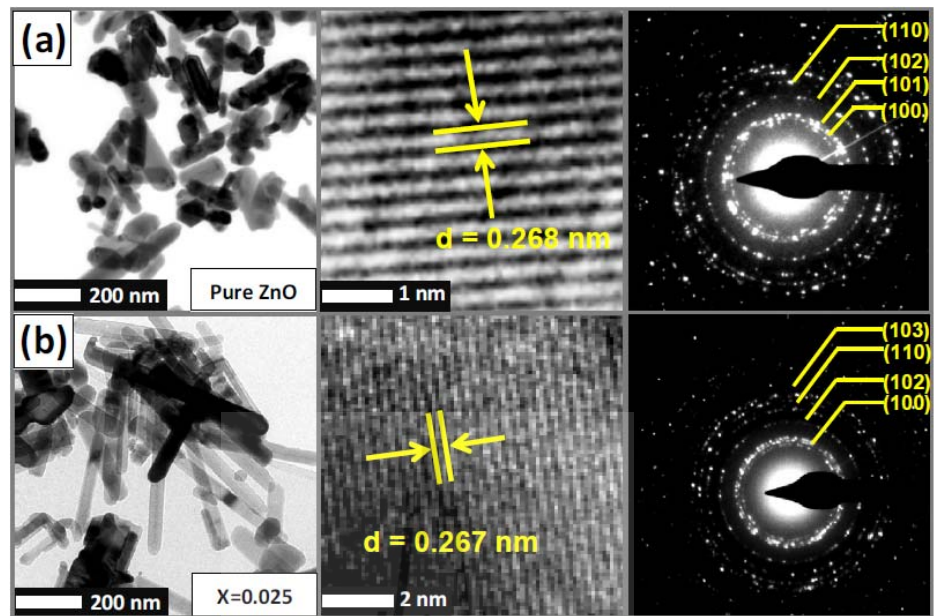
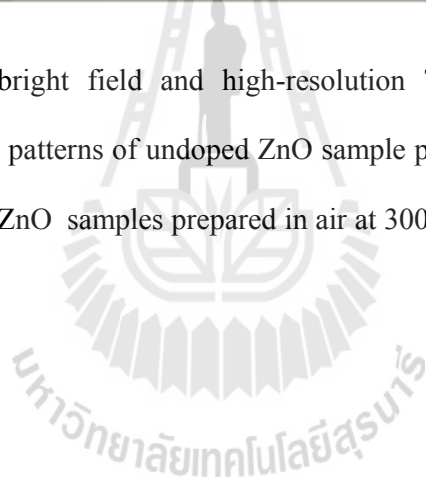


Figure 4.13 TEM bright field and high-resolution TEM (HRTEM) images with corresponding SEAD patterns of undoped ZnO sample prepared in air at 400 °C for 6 h (a) and (b) Ni-doped ZnO samples prepared in air at 300 °C for 6 h with $x = 0.025$.



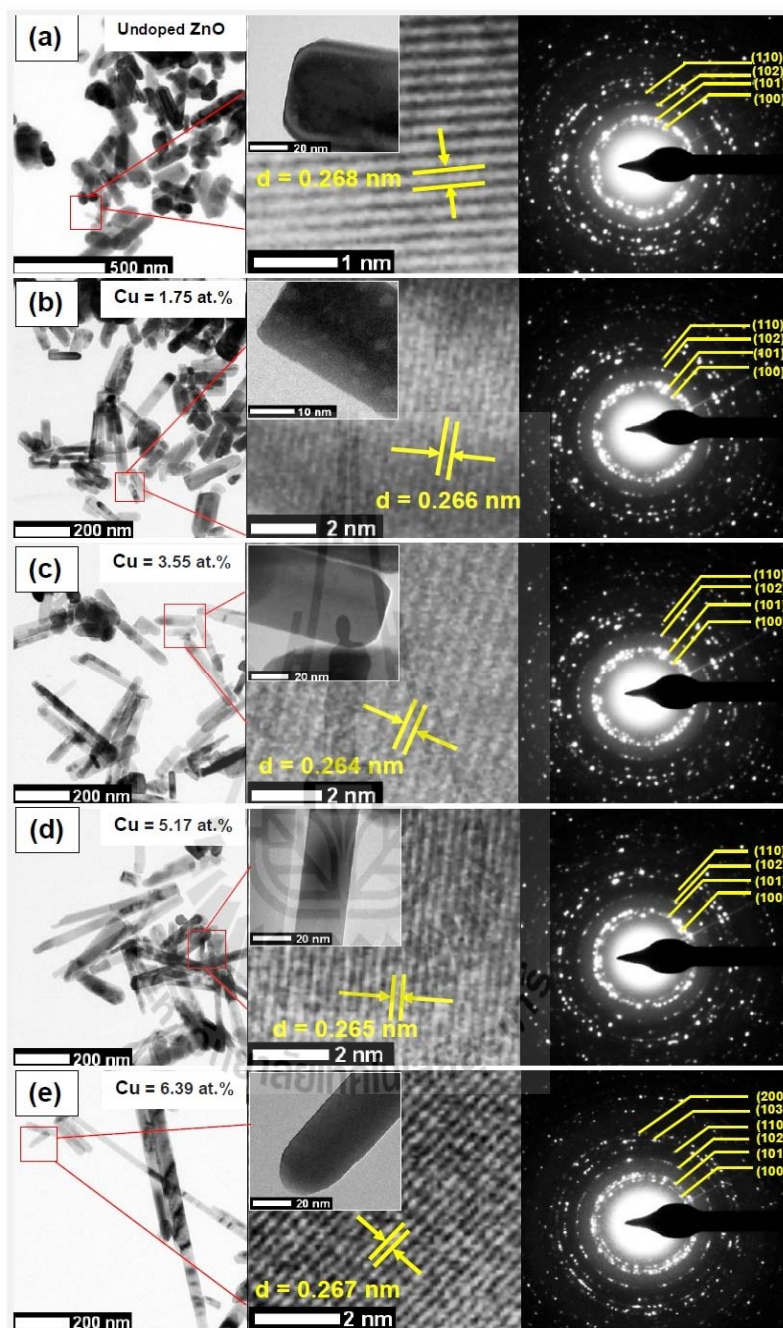


Figure 4.14 TEM bright field and high-resolution TEM (HRTEM) images with corresponding SEAD patterns of undoped ZnO sample prepared in air at 400 °C for 6 h (a) and Cu-doped ZnO samples prepared in air at 300 °C for 6 h with $x = 0.025$ (b), $x = 0.050$ (c), $x = 0.075$ (d), and $x = 0.100$ (e).

The chemical compositions of undoped and TM-doped ZnO nanorods were investigated by XPS analysis. All binding energies have been corrected for the charging effect with reference to the C 1s line at 284.6 eV. The survey scans (as shown in Figure 4.14) show peaks corresponding to Zn, Co, Mn, Ni, Cu and O. This indicates that there are no other magnetic impurities for each prepared sample.

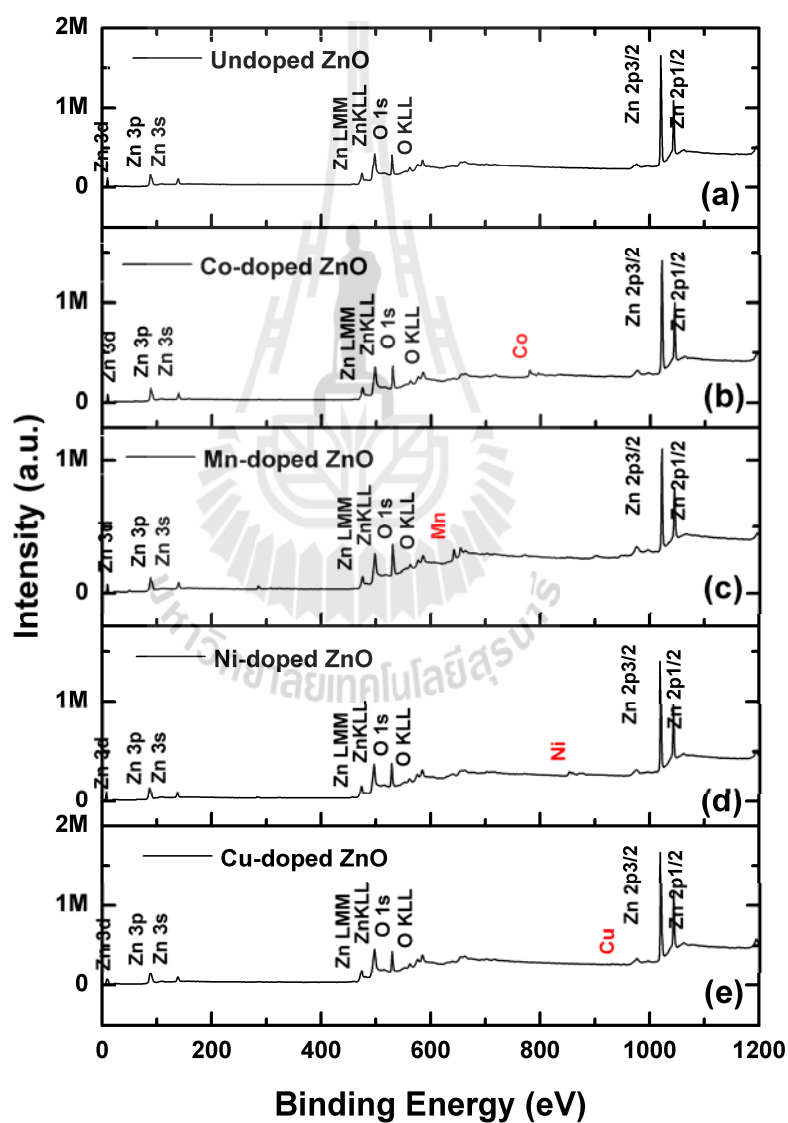


Figure 4.15 XPS spectra of TM-doped ZnO nanorods with the survey scan mode.

Table 4.3, indicates that all the samples are composed of Zn, Co, Mn, Ni, Cu and O, demonstrating an increase in actual atomic concentrations with the increase of nominal TM-doping in ZnO nanorods (doping level). And also shows that atomic percentage ratio of TM is less than the nominal composition in the precursor. The difference between the actual and the nominal TM concentration is probably due to the dilution of TM ions in the ZnO systems. In addition, compared to undoped ZnO, it was found that the TM-doped ZnO nanorods were slightly decrease zinc and oxygen atoms, beyond that expected for Zn replacement by TM ions. These phenomena induced oxygen vacancy in the ZnO host matrix. Moreover, the X-ray photoelectron spectroscopy (XPS) was also performed to determine the percentage of oxygen-deficient regions and valence state of TM in the ZnO matrix.

Table 4.3 Actual atomic concentrations of Zn, Co, Mn, Ni, Cu and O in undoped ZnO with nominally TM-doped ZnO nanorods calculated by XPS analysis.

Doping level	Atomic percentages (at%) of dopants in TM-doped ZnO samples											
	Co			Mn			Ni			Cu		
	Zn 2p	Co 2p	O 1s	Zn 2p	Mn 2p	O 1s	Zn 2p	Ni 2p	O 1s	Zn 2p	Cu 2p	O 1s
x = 0	49.93	-	50.07	49.93	-	50.07	49.93	-	50.07	49.93	-	50.07
x = 0.025	49.91	2.02	48.07	49.57	1.41	49.02	49.32	1.60	49.08	49.62	1.75	48.63
x = 0.050	49.73	4.83	45.44	48.11	3.40	48.49	-	-	-	49.30	3.55	47.15
x = 0.075	46.19	5.47	48.34	47.16	6.18	46.66	-	-	-	48.56	5.17	46.27
x = 0.100	44.50	9.37	46.13	45.24	8.28	46.48	-	-	-	48.48	6.39	45.13

Table 4.4 Results of Co 2p_{3/2}, O₁ and O₂ XPS spectra for Co-doped ZnO nanorods with x = 0.025, 0.050, 0.075 and 0.100.

Doping level	BE of Co ²⁺ in 2p 3/2 (eV)	Atomic percentages (at.%) of Co ²⁺	BE of O1s (eV)		Atomic percentages (at.%) of O ₁ and O ₂ (eV)	
			O ₁	O ₂	O ₁	O ₂
x = 0	-	-	530.35	531.48	40.83	9.24
x = 0.025	780.91	2.02	529.53	531.06	33.31	14.76
x = 0.050	780.82	4.83	529.86	531.39	32.76	12.68
x = 0.075	780.38	5.47	530.72	531.36	30.60	17.74
x = 0.100	780.22	9.37	530.41	531.48	31.60	14.53

Table 4.5 Fitting results of Mn 2p_{3/2}, O₁, O₂ and O₃ XPS spectra for Mn-doped ZnO nanorods with x = 0.025, 0.050, 0.075 and 0.100.

Doping level	Atomic percentages (at.%) of Mn 2p _{3/2}				Atomic percentages (at.%) of O ₁ , O ₂ and O ₃ (eV)			
	Mn 2p	~641 (eV)	~642 (eV)	~643 (eV)	O1s	~530.3 (eV)	~531.6 (eV)	~532.4 (eV)
		Mn ²⁺	Mn ³⁺	Mn ⁴⁺		O ₁	O ₂	O ₃
x = 0	-	-	-	-	50.07	40.83	9.24	-
x = 0.025	1.41	0.41	0.60	0.40	49.02	36.02	10.15	2.84
x = 0.050	3.40	0.98	1.37	1.05	48.49	22.50	18.04	7.95
x = 0.075	6.18	2.09	2.64	1.45	46.66	20.02	19.32	7.32
x = 0.100	8.28	2.15	3.84	2.29	46.48	25.24	15.80	5.44

Figures 4.16 - 4.18 shows the Zn 2p core level peaks in the XPS spectra of the undoped ZnO and TM-doped ZnO samples. These peaks correspond to the position of Zn 2p in the undoped ZnO and this confirms the existence of Zn²⁺ oxidation state with a binding energy of about 1021.45 eV in all the samples except

the Gaussian resolving is performed on Mn-doped ZnO samples, two peaks centered at 1020.40 eV and 1021.23 eV were obtained as shown in Figure 4.17. The peak center centered at 1021.23 eV corresponds to the binding energy of Zn 2p_{3/2} of undoped ZnO, whereas the peak centered at 1020.40 eV corresponds to for the Zn 2p_{3/2} of Mn-doped ZnO. This shift of binding energy is due to the substitution of part of lattice Zn in ZnO by Mn²⁺ ions and a formation of Zn-Mn bonding structure (Duan et al., 2011). The typical O 1s spectra in Figures 4.19 - 4.21 were consistently fitted by two nearly Gaussian curve centered at ~ 530.3 eV and ~ 531.5 eV with respective notice as O₁, and O₂ respectively for atomic percentages of oxygen in each region on the surface of undoped ZnO and TM-doped ZnO samples (Li et al., 2008; Ghajari et al., 2013). The atomic percentages of O₁, and O₂ can be calculated by using XPS analyses and the results are shown in Table 4.4 and Table 4.5. The low binding energy centered at ~ 530.3 eV(O₁) is corresponded to O²⁻ ions on wurtzite structure of hexagonal ZnO. The high binding energy located at ~ 531.5 eV(O₂) is attributed to O²⁻ ions in the oxygen deficient regions with in a matrix of ZnO. These results suggest that there are some oxygen vacancies in the samples. In additional peak, we observed the binding energy centered at ~ 532.4 eV(O₃) for Mn-dope ZnO samples as shown in Figure 4.20, which is associated to the presence of loosely bound oxygen on the surface such as chemisorbed and dissociated oxygen species or hydroxyl group (Xia et al., 2011).

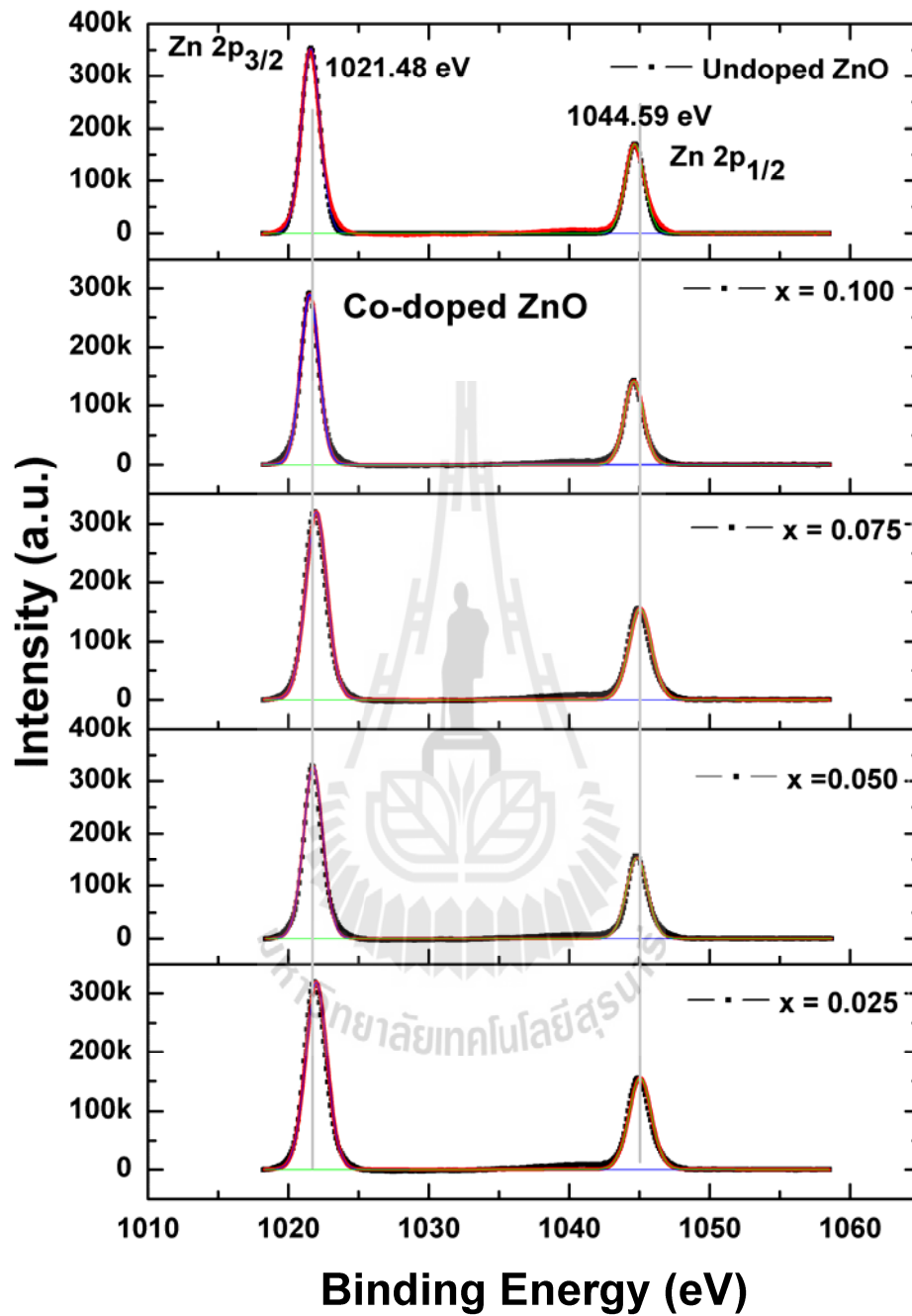


Figure 4.16 Zn2p X-ray photoelectron spectra (XPS) of Co-doped ZnO samples prepared in air at 300 °C for 6 h with $x = 0.025, 0.050, 0.075$ and 0.100 compared with undoped ZnO.

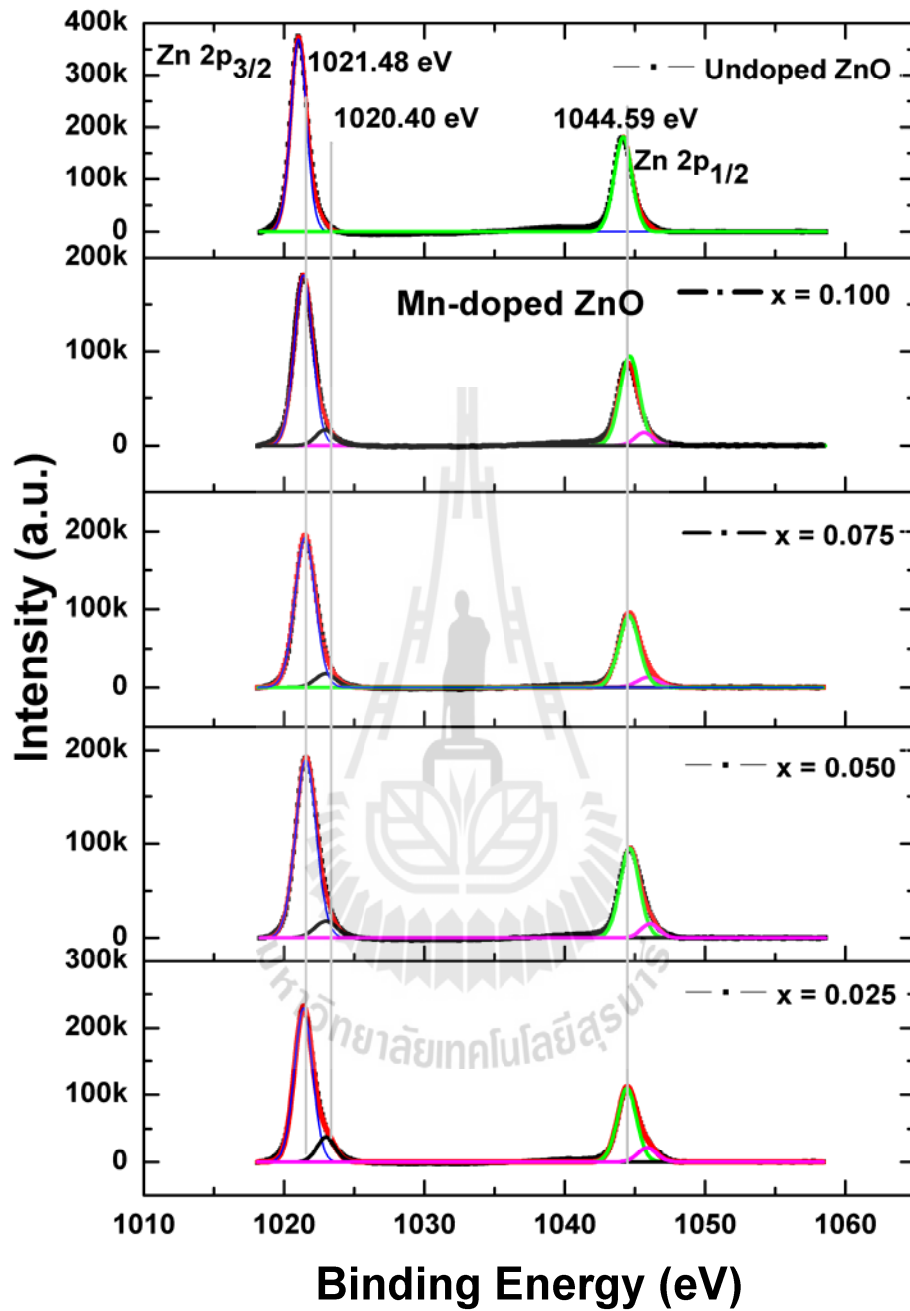


Figure 4.17 Zn2p X-ray photoelectron spectra (XPS) of Mn-doped ZnO samples prepared in air at 300 °C for 6 h with $x = 0.025, 0.050, 0.075$ and 0.100 compared with undoped ZnO.

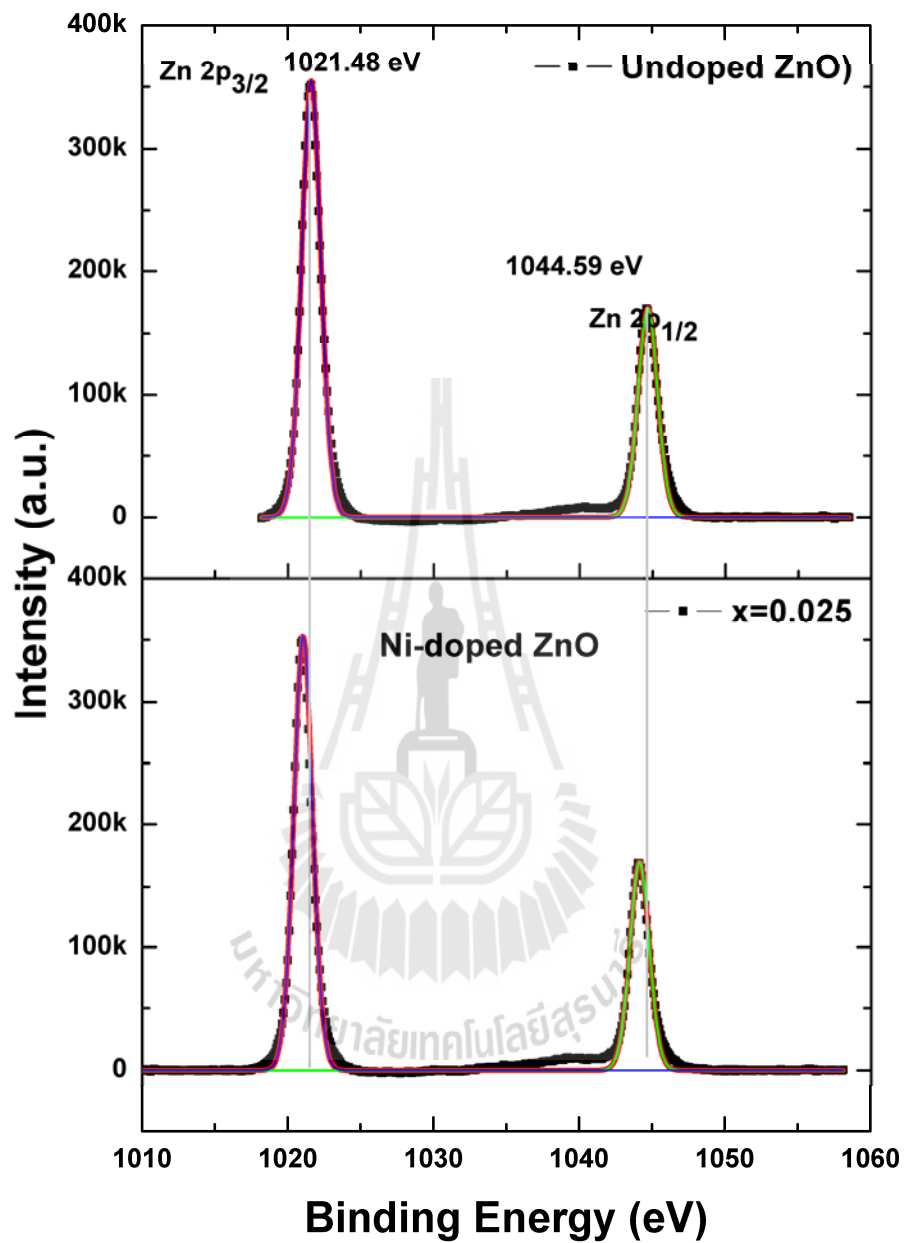


Figure 4.18 Zn2p X-ray photoelectron spectra (XPS) of Ni-doped ZnO samples prepared in air at 300 °C for 6 h with $x = 0.025$ compared with undoped ZnO.

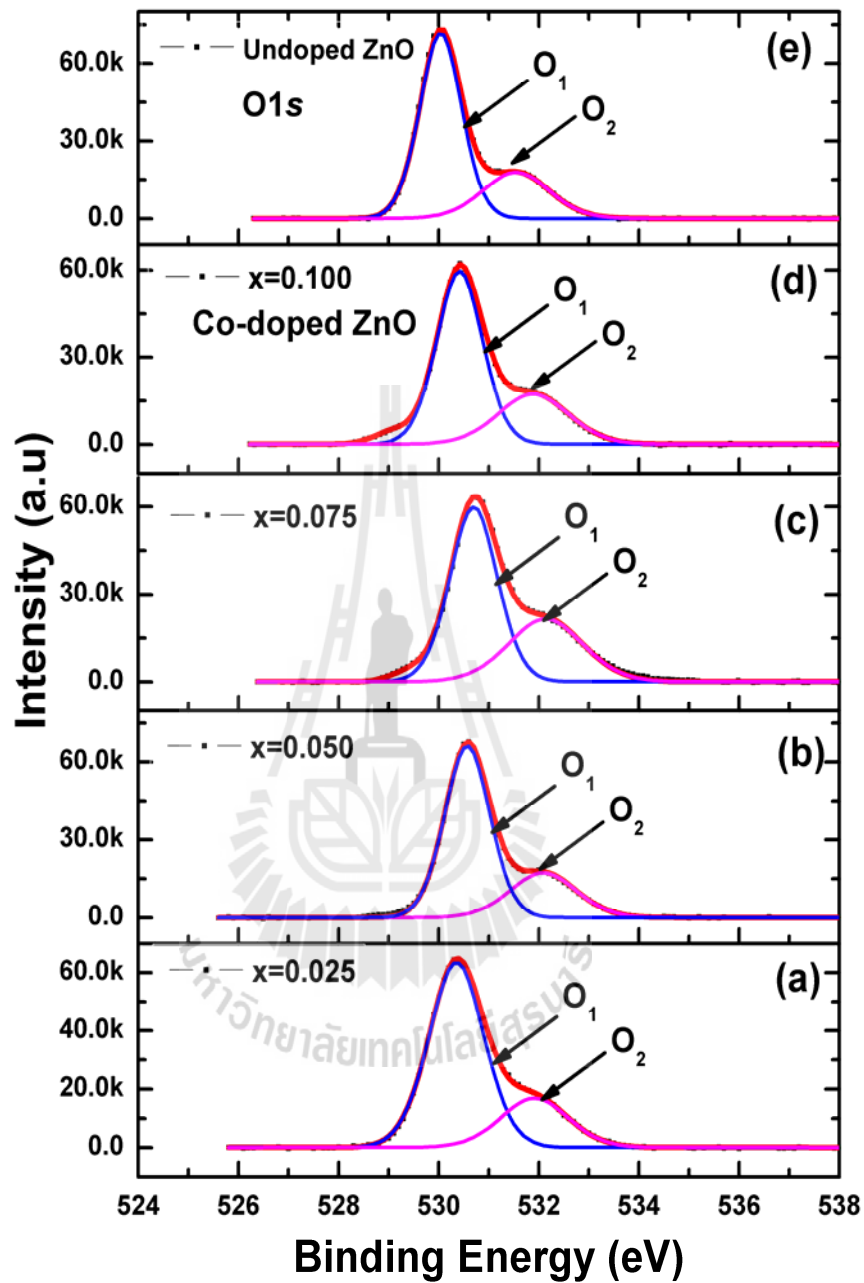


Figure 4.19 High-resolution scan of O1s for Co-doped ZnO with $x = 0.025$ (a), 0.050 (b), $x = 0.075$ (c) and $x = 0.100$ (d) compared with undoped ZnO(e).

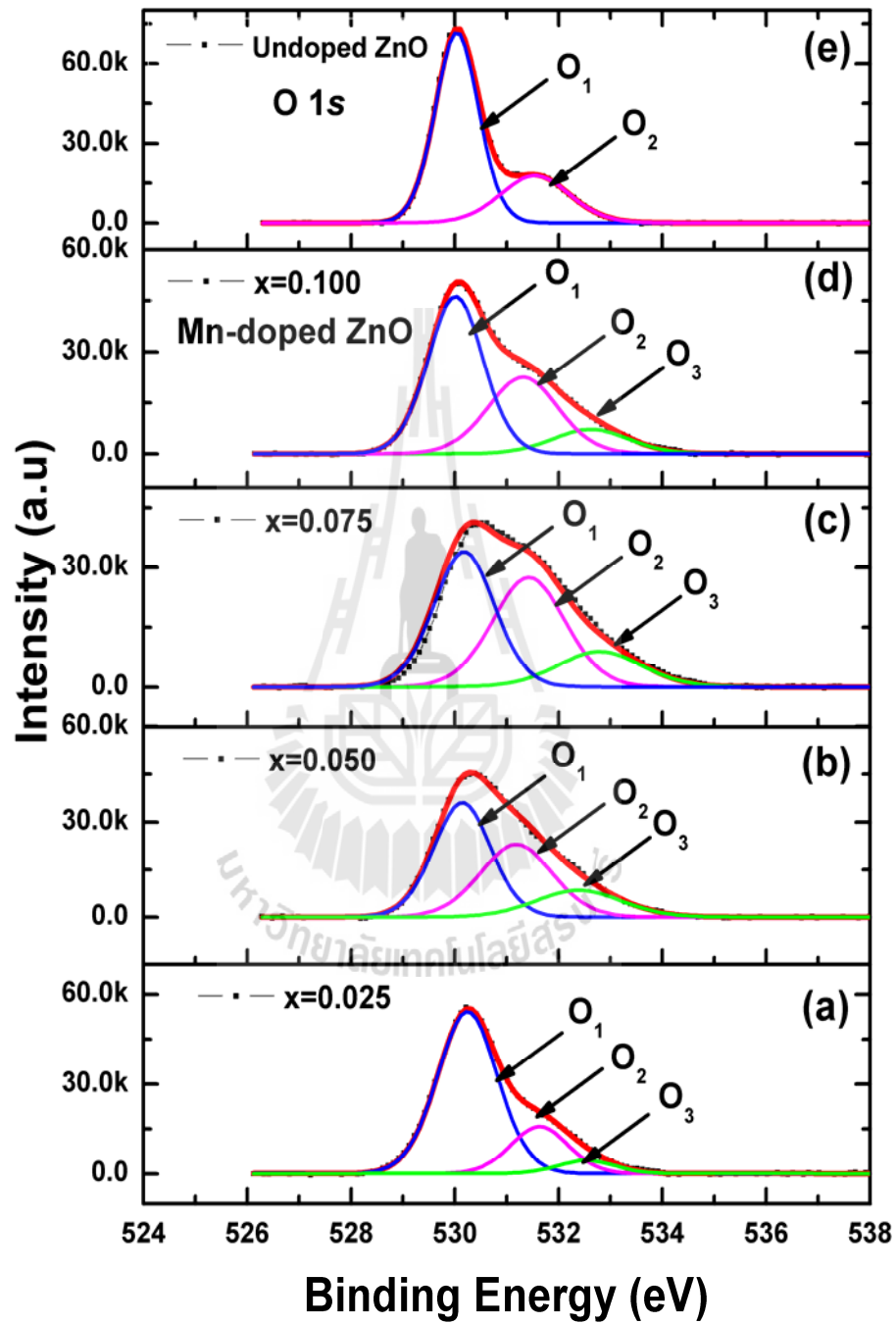


Figure 4.20 High-resolution scan of O1s for Mn-doped ZnO with $x = 0.025$ (a), 0.050 (b), $x = 0.075$ (c) and $x = 0.100$ (d) compared with undoped ZnO(e).

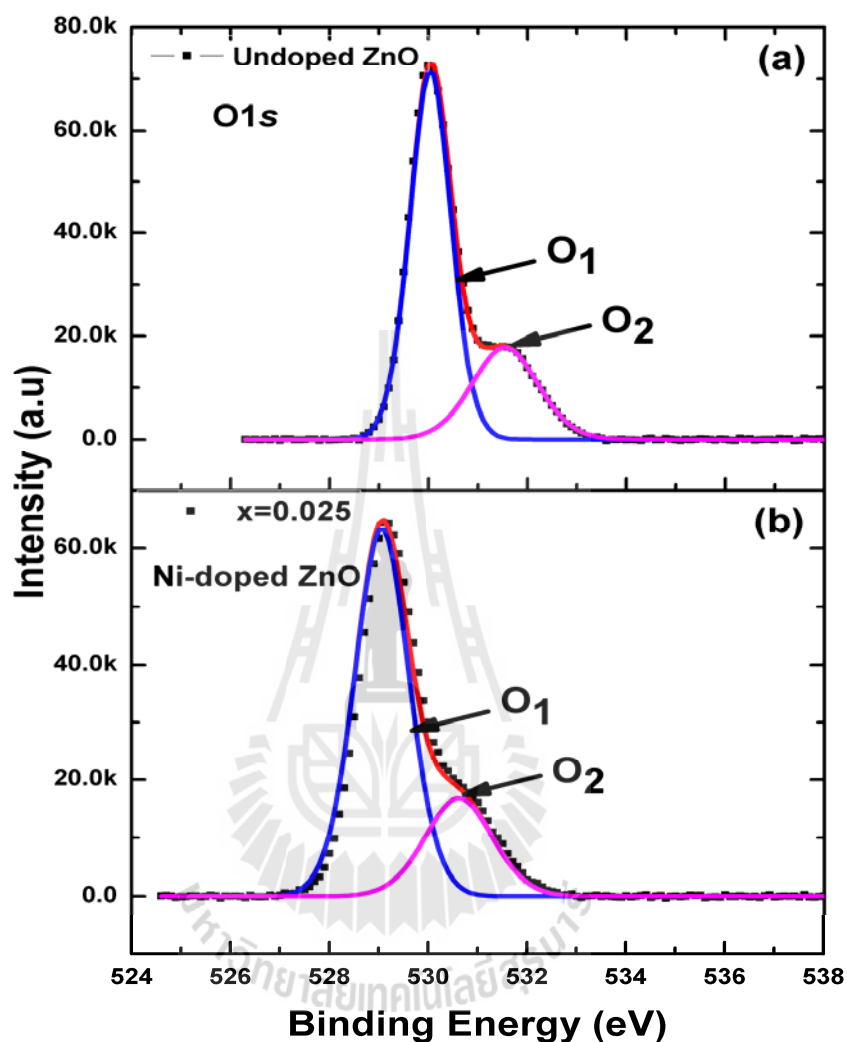


Figure 4.21 High-resolution scan of O1s for undoped ZnO (a) and Ni-doped ZnO for $x = 0.025$ (b).

The oxidation states of TM ions were investigated by measuring the Co 2p_{3/2}, Mn 2p_{3/2}, Ni 2p_{3/2} and Cu 2p_{3/2} XPS spectra, as shown in Figures 4.22 - 4.24. Figure 4.22 shows the high-resolution scan of Co 2p_{3/2}, identifying the exact peak location of Co 2p_{3/2} at 780 eV and of Co2p_{1/2} at 795.6 eV (as listed in Table 4.4) with relative two

shake-up satellites of the main peaks presenting at slightly higher energies. The satellite at about 786 eV is considered a feature of Co^{2+} ions, which confirms the 2+ oxidation state of the incorporated dopant. Therefore, we conclude that the dopant atoms are well-incorporated in the host lattice as Co^{2+} on Zn-lattice site. Figure 4.23 shows the high-resolution scan of Mn $2p_{3/2}$, three Gaussian curves located at ~ 641 , ~ 642 and ~ 643 eV could be attributed to Mn^{2+} , Mn^{3+} and Mn^{4+} valence states, respectively. The presence of Mn^{2+} is expected in Mn-doped ZnO samples due to the replacement of Zn^{2+} at the lattice site while Mn^{3+} and Mn^{4+} might be assigned to the plausible $\text{ZnMn}_2\text{O}_4/\text{Mn}_2\text{O}_3$ and $\text{ZnMnO}_3/\text{MnO}_2$ impurity phases, which often appeared in other Mn-doped ZnO (Chen et al., 2005; Duan et al., 2011), although they were not detected by our XRD and HRTEM studies. To make a quantitative atomic percentage of O_1 , O_2 , O_3 and the three valence states of Mn are summarized in Table 4.5. It was found that the Mn^{2+} , Mn^{3+} and Mn^{4+} increases with increasing Mn content and also we observed the oxygen deficient regions (O_2) increasing that reveal that a formation of oxygen vacancy and are confirmed by Mn-doping. Figure 4.24 represents the binding energy of Ni; the result reveals 855.5 eV for $2p_{3/2}$ state and 873.5 eV for $2p_{1/2}$ state. Their satellite peaks were observed at 861.2 eV and 880.1 eV. This confirms the presence of Ni in form of Ni^{2+} and it is neither bonded with oxygen in the form of Ni_2O_4 nor presented in the metallic form.

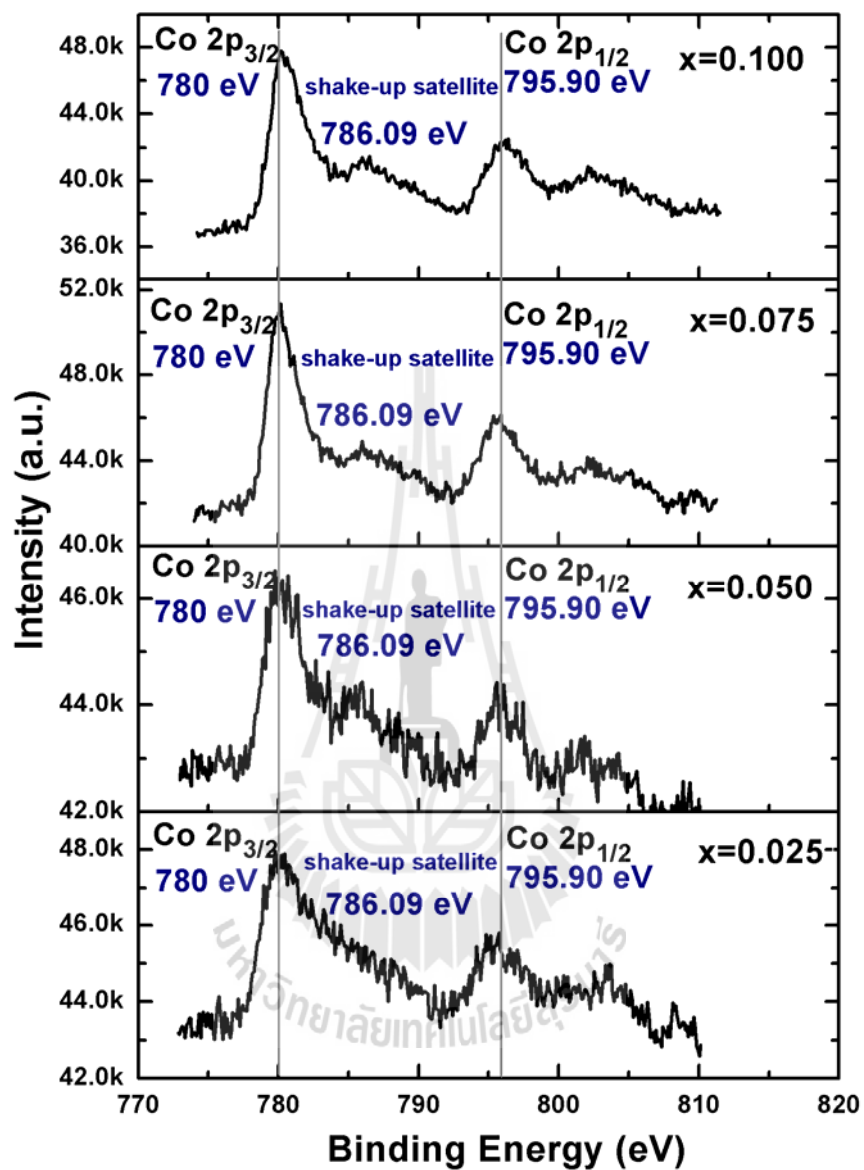


Figure 4.22 High-resolution scans of Co2p for Co-doped ZnO samples prepared in air at 300 °C for 6 h with x = 0.025, 0.050, 0.075 and 0.100.

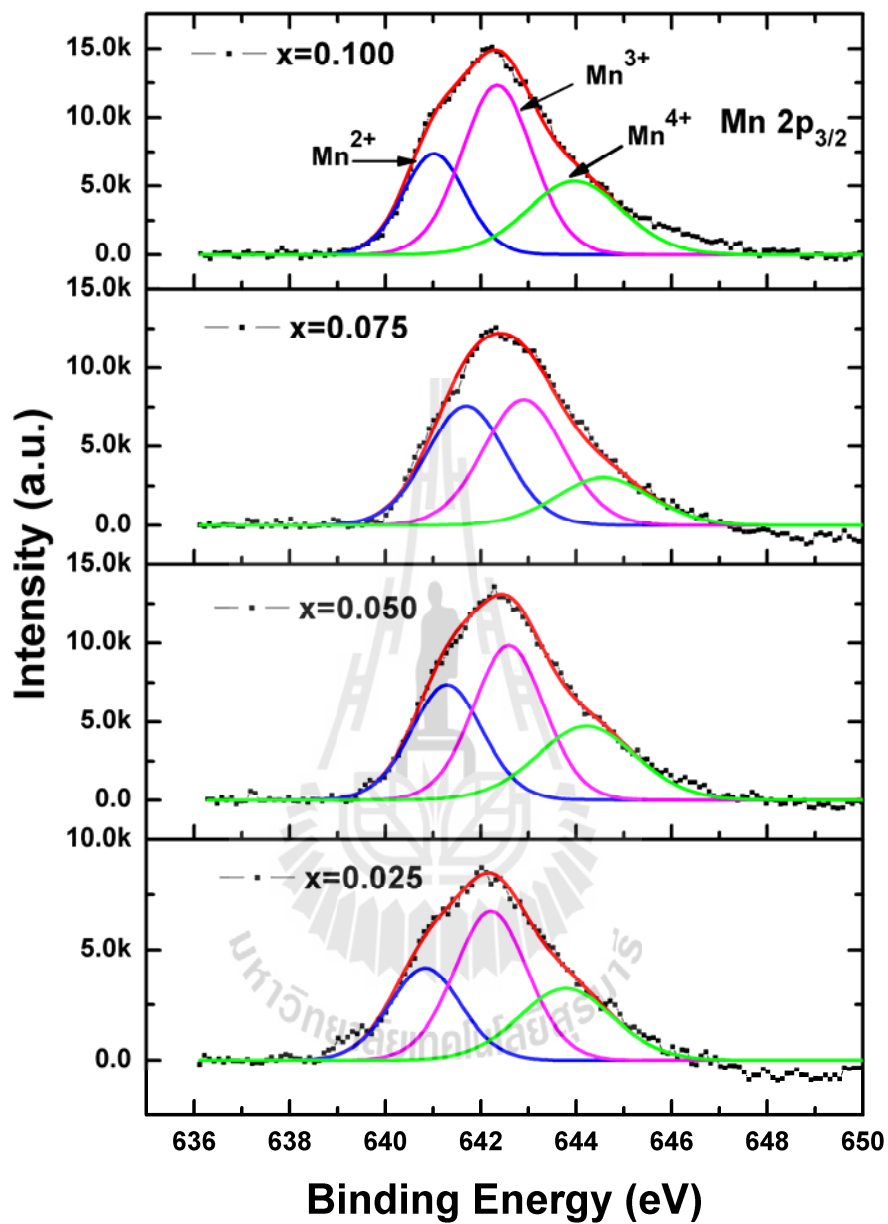


Figure 4.23 High-resolution scans of Mn2p for Mn-doped ZnO samples prepared in air at 300 °C for 6 h with $x = 0.025, 0.050, 0.075$ and 0.100 .

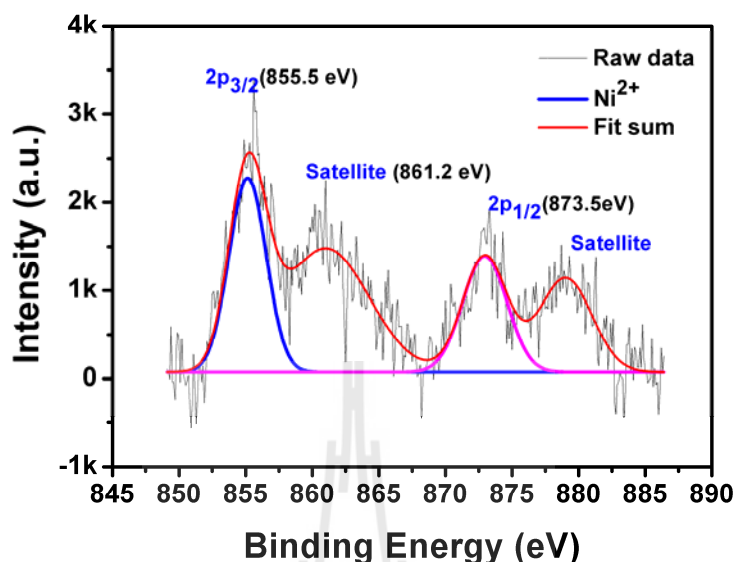


Figure 4.24 High-resolution scans of Ni $2p$ for Ni-doped ZnO samples prepared in air at 300 °C for 6 h with $x = 0.025$.

In the case of nonmagnetic materials, the surface profile of Cu-doped ZnO nanorods was also examined by using XPS analysis. The high resolution spectra shown in Figure 4.25 specifies the binding energy 1021.3 eV and 1044.4 eV for $2p_{3/2}$ and $2p_{1/2}$ of Zn^{2+} state in ZnO (Cagla et al., 2012; Ghajari et al., 2013). Figure 4.26 represents the binding energy of O1s, where the two peaks indicate two different kinds of O elements in the sample. The low binding energy peak at ~ 530.3 eV is corresponded to O^{2-} ions on wurtzite structure of hexagonal ZnO. The high binding energy peak at ~ 531.5 eV is attributed to O^{2-} ions in the oxygen deficient regions with in a matrix of ZnO (Wang et al., 2012; Yang et al., 2013). Furthermore, the percentages of O₁, O₂ and Cu in Cu-doped ZnO samples are summarized in Table 4.6. It can be seen that the percentages of O₂ for Cu-doped ZnO nanorods are higher

than that of the undoped ZnO sample. Especially, a nominal Cu-doped ZnO sample ($x = 0.050$) has the highest percentages of O₂. This is probably related to the substitution of ZnO lattice with Cu ions or / and the reduction of oxygen from ZnO lattice with the impurity phases. Moreover, the XPS results can clearly distinguish Cu²⁺ from metallic copper (Cu⁰) and Cu¹⁺. In general, Cu2p_{3/2} peaks of Cu⁰ and Cu¹⁺ in Cu₂O appear at approximately 932.5 eV and that Cu²⁺ in CuO at around 933.6 eV - 934 eV (Xia et al., 2011; Xu et al., 2012). Actually, the Cu²⁺ has higher binding energy and weak satellite at around 941-946 eV appeared in the Cu2p spectrum, while Cu¹⁺ has not. Since the copper electronic configuration of Cu²⁺ (d^9) is unsaturated, p - d hybridization and then the degeneration can be occurred. When copper reaches the electronic configuration d^{10} (Cu¹⁺), the satellite band disappears and only two peaks are visible in the copper spectrum and also the peak position of Cu¹⁺/ Cu⁰ was shifted by approximately 1.1 eV to higher binding energy (Xu et al., 2012).

Table 4.6 The binding energy and atomic percentages of Cu2p_{3/2}, energy shift and atomic percentages of O₁ and O₂ calculated by XPS spectra of undoped ZnO and Cu-doped ZnO nanorods.

Doping level	Binding energy of Cu 2P _{3/2} (eV)		Atomic percentages of Cu ⁰ , Cu ¹⁺ and Cu ²⁺		Energy shift ΔE (eV)	Binding energy of O1s (eV)		Atomic percentages of O ₁ and O ₂	
	Cu ²⁺	Cu ¹⁺ , Cu ⁰	(Cu ⁰ +Cu ¹⁺)/Cu2p	Cu ²⁺ /Cu2p		O ₁	O ₂	O ₁ /O1s	O ₂ /O1s
x = 0	-	-	-	-	-	530.35	531.48	40.83	9.24
x = 0.025	933.97	932.84	1.41	0.34	1.13	530.33	531.45	39.76	8.87
x = 0.050	933.86	932.80	2.88	0.67	1.06	530.33	531.45	37.89	9.26
x = 0.075	934.06	932.95	4.02	1.15	1.11	530.31	531.48	37.50	8.77
x = 0.100	933.81	932.71	5.58	0.81	1.10	530.34	531.46	36.69	8.44

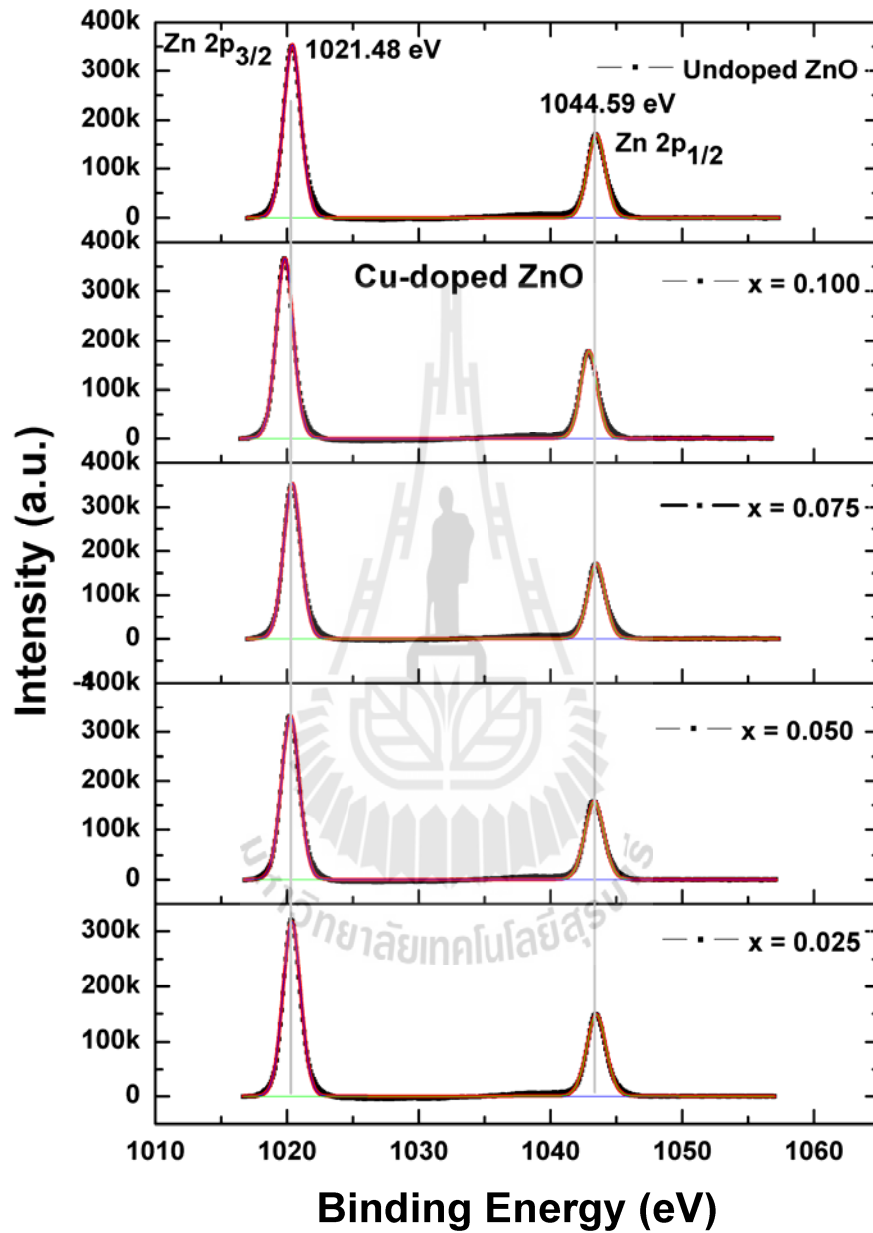


Figure 4.25 Zn2p X-ray photoelectron spectra (XPS) of Cu-doped ZnO samples prepared in air at 300 °C for 6 h with $x = 0.025$, 0.050, 0.075 and 0.100 compared with undoped ZnO.

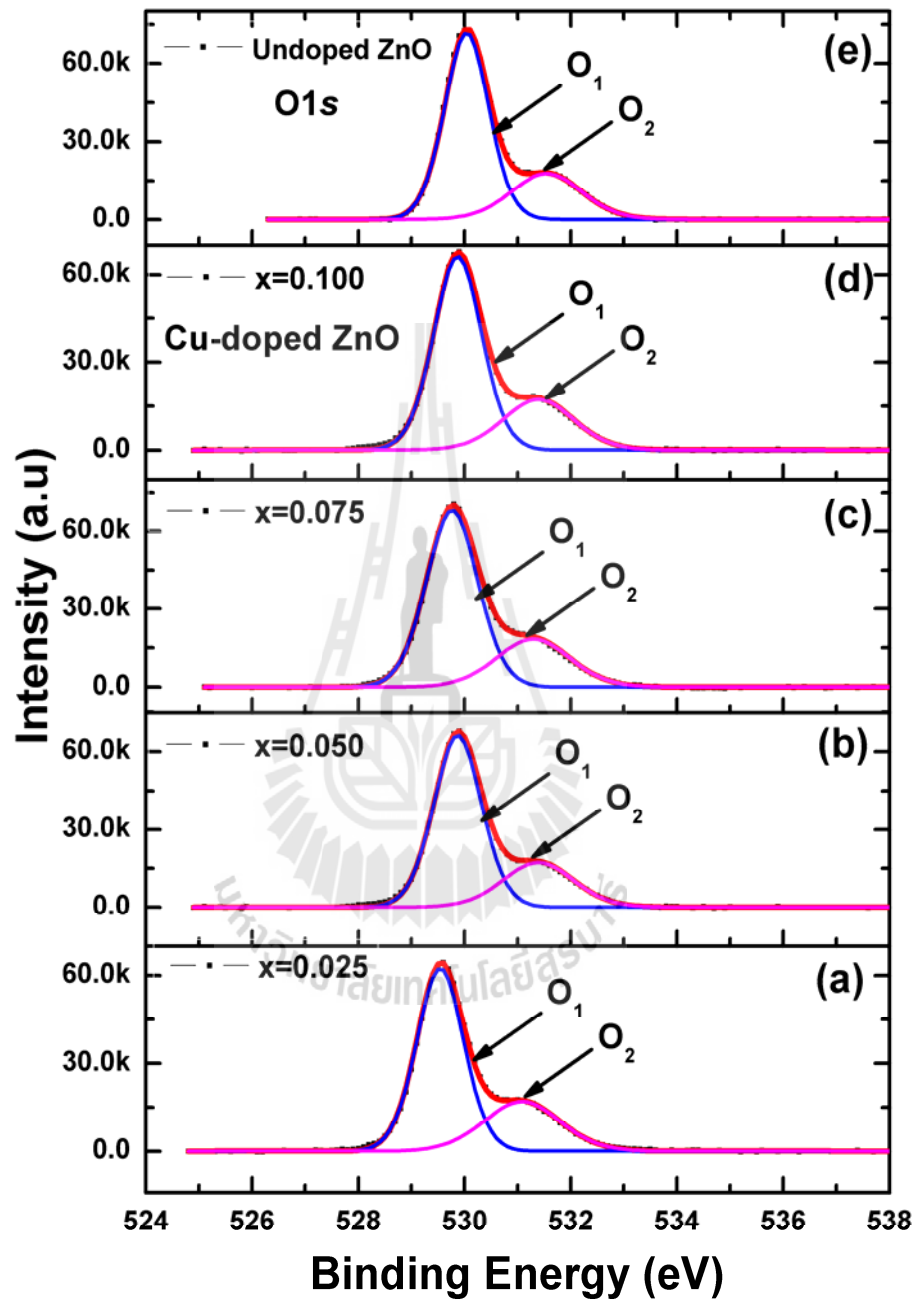


Figure 4.26 High-resolution scans of O1s for Cu-doped ZnO with $x = 0.025$ (a), 0.050 (b), $x = 0.075$ (c) and $x = 0.100$ (d) compared with undoped ZnO.

Figures 4.27(a) - 4.27(d) show the Cu 2p core-level XPS spectra. The $\text{Cu}2p_{3/2}$ and $\text{Cu}2p_{1/2}$ core-levels of all samples are located at ~ 932.82 and ~ 952.21 eV, respectively. Also, it can be seen that the binding energy of $\text{Cu}2p_{3/2}$ was shifted by ~ 1.1 eV to higher energy (as shown in Table 4.6). These results indicate that all of the samples are associated with these two peaks of the mixture of Cu ions state (Cu^{2+} and Cu^{1+}) which is in good agreement with earlier reports on the Cu-doped ZnO films (Caglar et al., 2012; Ghajari et al., 2013). The $\text{Cu}2p_{3/2}$ peak evidently shows the peak located at ~ 932.82 eV revealing the Cu-related phases of Cu, CuO and Cu_2O . After Gaussian fitting, the results of best peak fit to the experimental data gives $(\text{Cu}^{1+} + \text{Cu}^0)/\text{Cu}2p$ and $\text{Cu}^{2+}/\text{Cu}2p$ showing components of major $\text{Cu}^{1+}/\text{Cu}^0$ and minor Cu^{2+} . Hence, the valence state of Cu in the samples is mainly $\text{Cu}^{1+}/\text{Cu}^0$, which is consistent with the XRD results. However, the Cu^{1+} has fully filled $3d$ orbitals ($3d^{10}4s^0$) and hence it does not make any contribution to ferromagnetism in the Cu-doped ZnO samples (Jin et al., 2001; Xia et al., 2011). In contrast, the valence band configuration of CuO (Cu^{2+}) has a $3d^94s^0$ and may therefore trap electron with the Cu $3d$ hole state so the Cu^{2+} ion substitution and oxygen vacancies are the main cause that leads to the ferromagnetism in the Cu-doped ZnO samples. The magnetic properties of the prepared Cu-doped ZnO samples are present in details in Section 4.2.4.

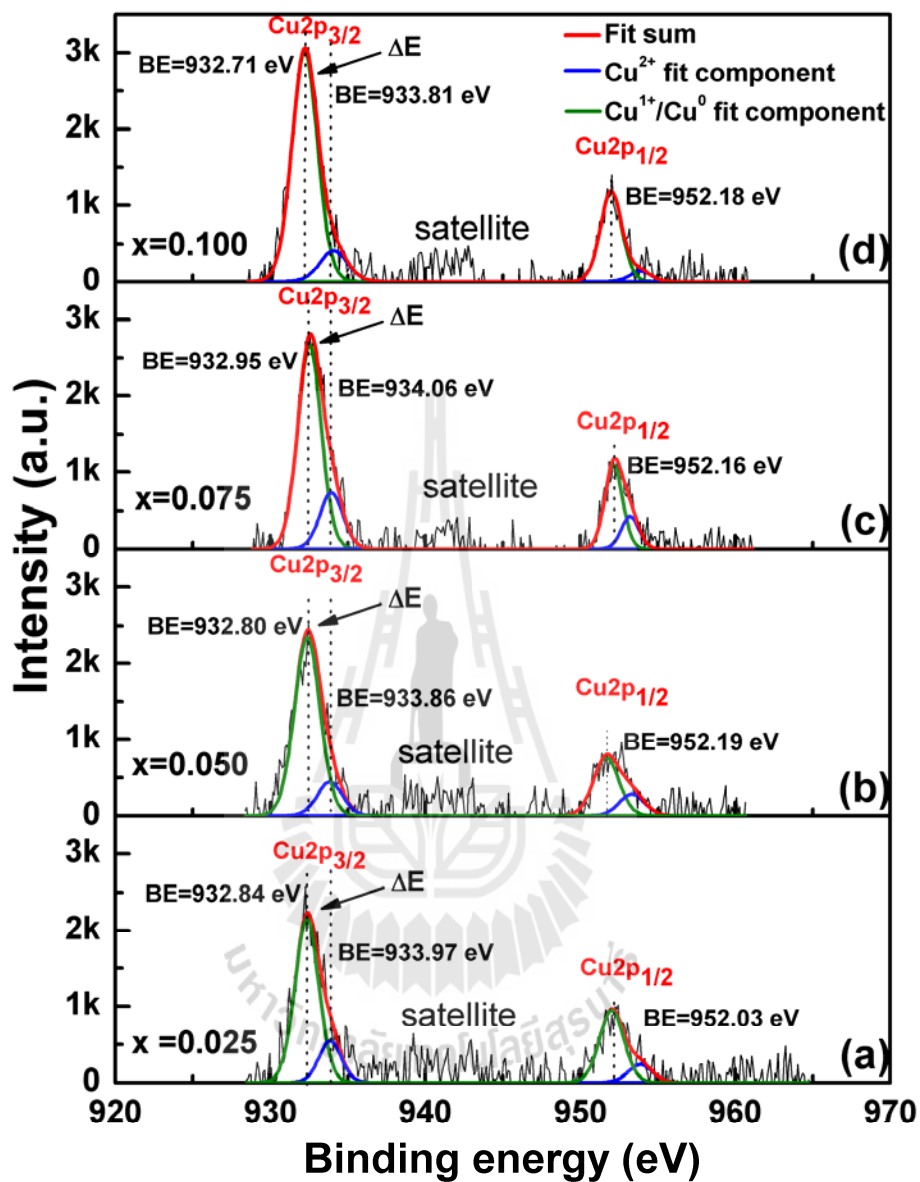
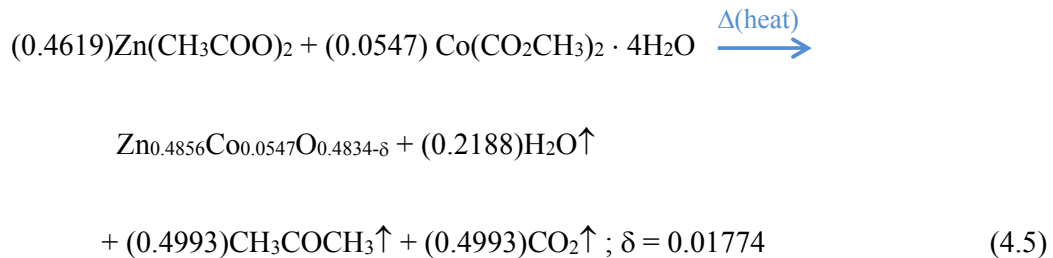
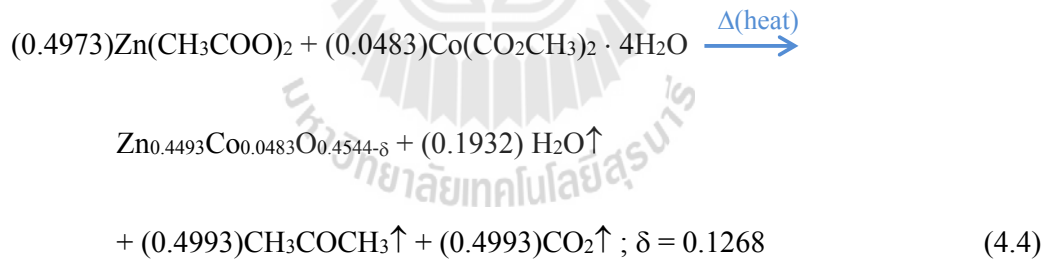
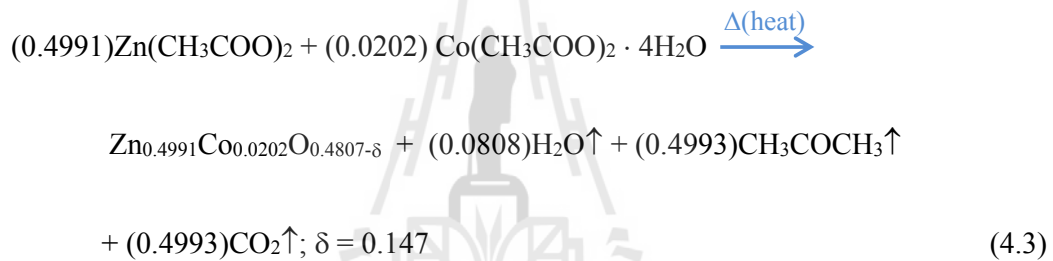
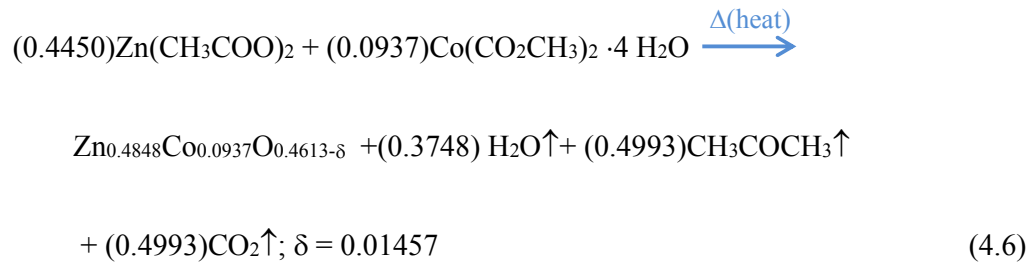


Figure 4.27 High-resolution scans of Cu2p for Cu-doped ZnO samples prepared in air at 300 °C for 6 h with $x = 0.025, 0.050, 0.075$ and 0.100 , respectively.

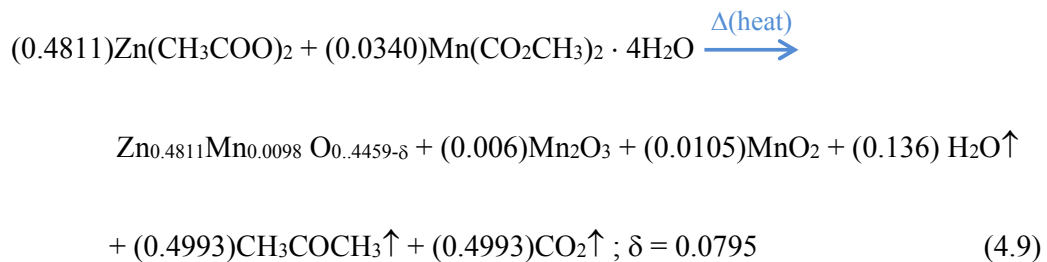
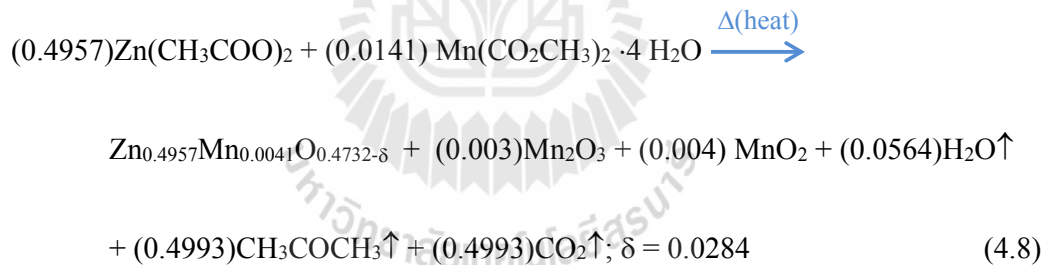
From the data in Tables 4.3, 4.4 and 4.5 calculated by XPS analysis, the formation of TM-doped ZnO nanorods can be explained by the following reactions (Noipa et al., 2014) as given in Equations (4.2) - (4.18), respectively,

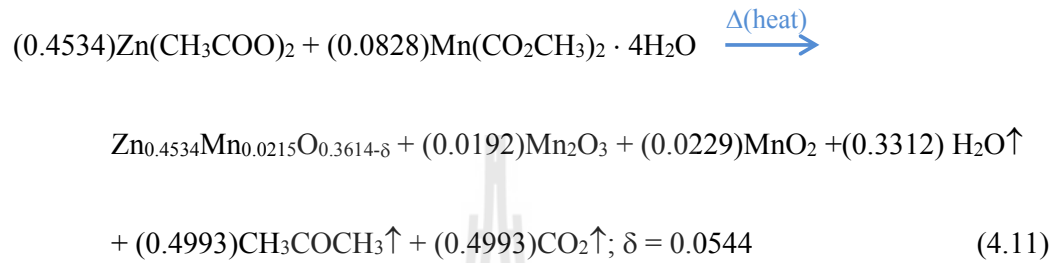
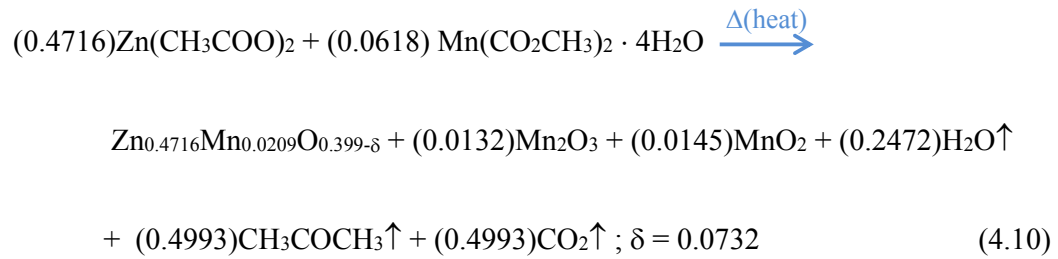
For the samples of Co-doped ZnO with Co = 0, (x = 0), 0.0202 (x = 0.025), 0.0483 (x = 0.05), 0.0547 (x = 0.075) and 0.0937 (x = 0.100):



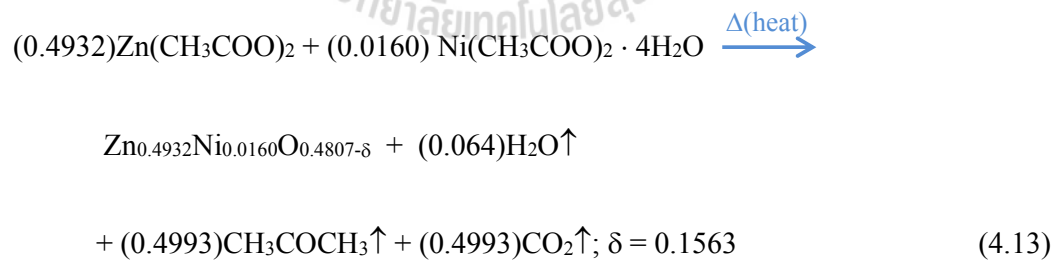


For the samples of Mn-doped ZnO with Mn = 0 (x = 0), 0.0141 (x = 0.025), 0.0340 (x = 0.050), 0.0618 (x = 0.075) and 0.0828 (x = 0.100):

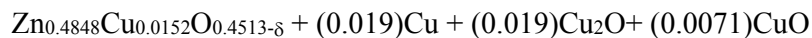
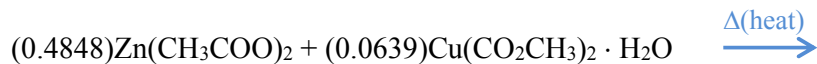
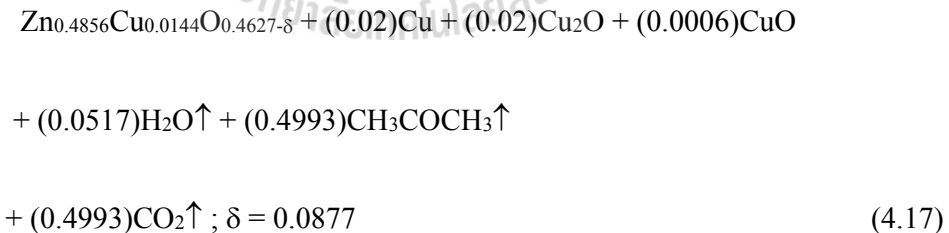
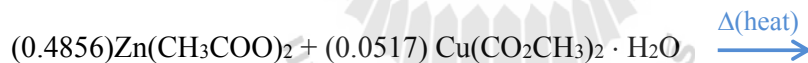
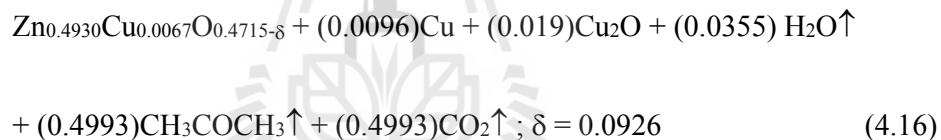
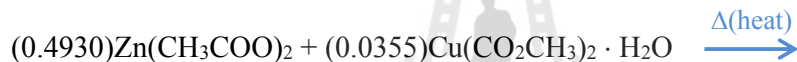
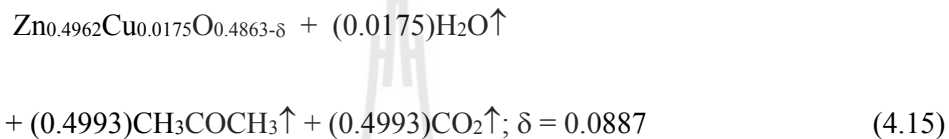
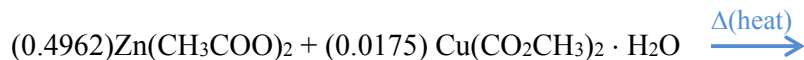
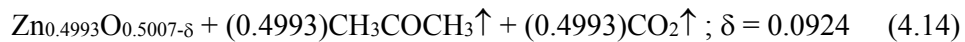


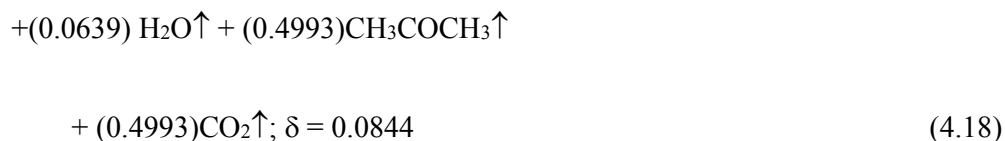


For the samples of Ni-doped ZnO with Ni = 0, (x = 0) and 0.0160 (x = 0.025)



For the samples of Cu-doped ZnO with Cu = 0 (x = 0), 0.0175 (x = 0.025), 0.0355 (x = 0.050), 0.0517 (x = 0.075) and 0.0639 (x = 0.100):





All the process reactions suggest that the thermal events are related to the combustion of acetone (CH_3COCH_3), water (H_2O), carbon dioxide (CO_2) in the precursors and oxygen vacancy concentration (δ) formed on the prepared products.

4.2.2 The absorption and photoluminescence of TM-doped ZnO nanorods (i.e. TM = Co, Mn, Ni and Cu)

The UV-visible optical absorption spectra of the undoped and TM-doped ZnO samples have been carried out at room temperature using UV- visible spectrometer from 200 nm to 800 nm and are shown in Figure 4.28. The absorption edge of undoped ZnO sample is observed around 380 nm and the band edge is found to with increasing TM-content which may be due to the formation of narrow band gap by doping. The optical absorption spectra of the TM-doped ZnO samples show just negative trend of the optical band gap for all TM-doped ZnO samples. Especially, it well known that the sample containing transition metals will have bands from crystal-field transition of ions in tetrahedral coordination. In case of Co-doped ZnO, absorption peak are expected to arise due to electronic transitions from the $^4\text{A}_2$ ground state to the $^4\text{T}_1(\text{P})$ state for the tetrahedral Co(II) (Bylsma et al., 1986; Bouloudenine et al., 2004). In the present Co-dope ZnO nanorods, additional absorption peaks in the visible region are observed. As cobalt concentration increased, the absorbance intensity of the combined peak between 525 nm and 725 nm were strengthened regularly as shown in Figure 4.28(a).

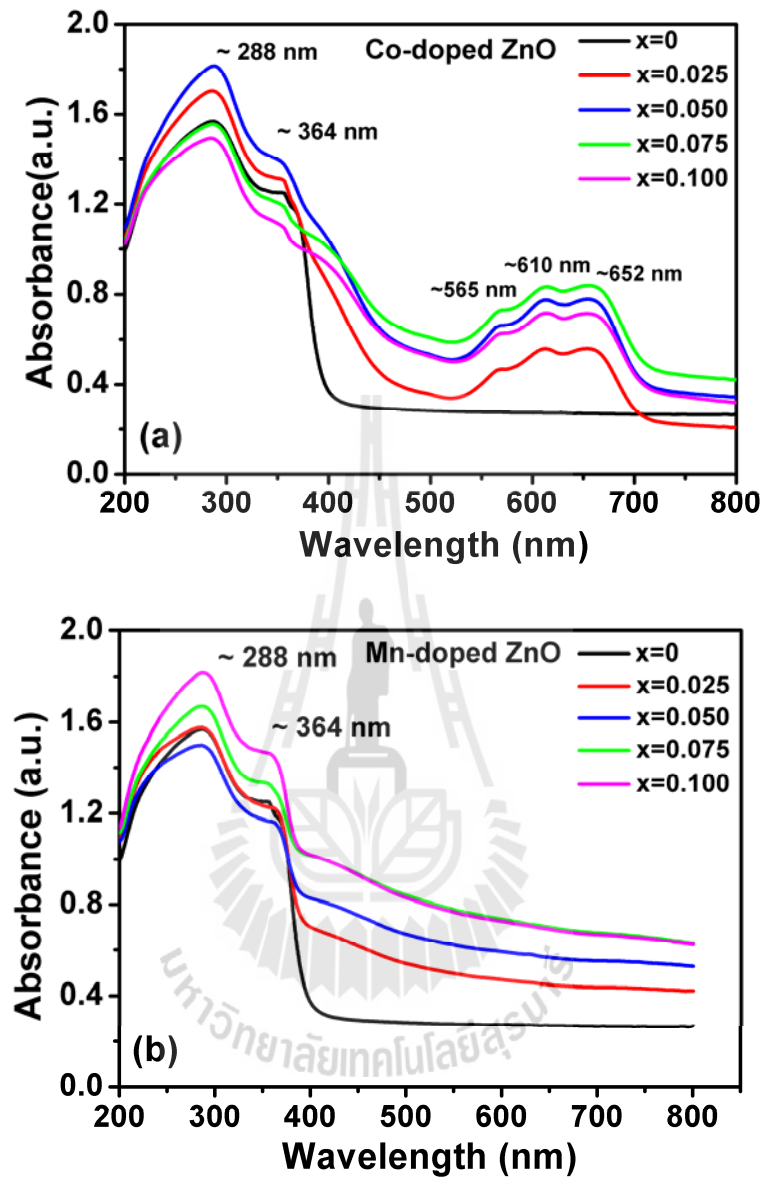


Figure 4.28 Room-temperature optical absorbance spectra of undoped ZnO nanorods calcined at 400 °C for 6 h and TM-doped ZnO nanorods prepared in air at 300 °C for 6 h. (a) Co-doped ZnO, (b) Mn-doped ZnO and (c) Ni-doped ZnO nanorods, respectively.

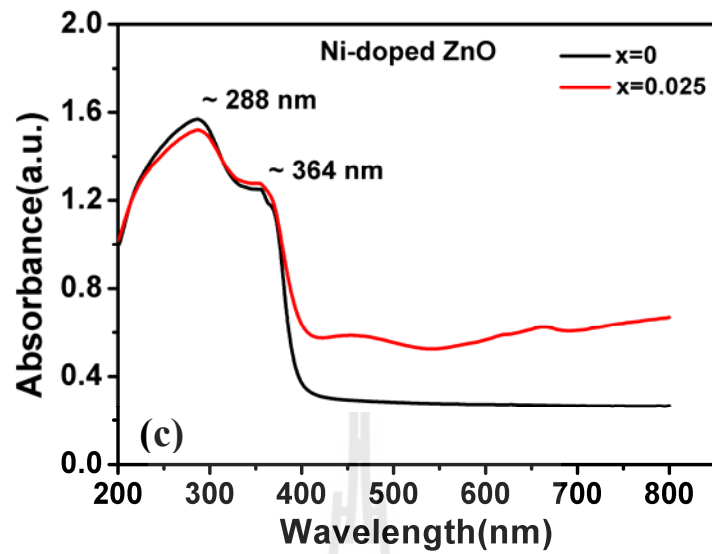


Figure 4.28 Room-temperature optical absorbance spectra of undoped ZnO nanorods calcined at 400 °C for 6 h and TM-doped ZnO nanorods prepared in air at 300 °C for 6 h. (a) Co-doped ZnO, (b) Mn-doped ZnO and (c) Ni-doped ZnO nanorods (Cont.)

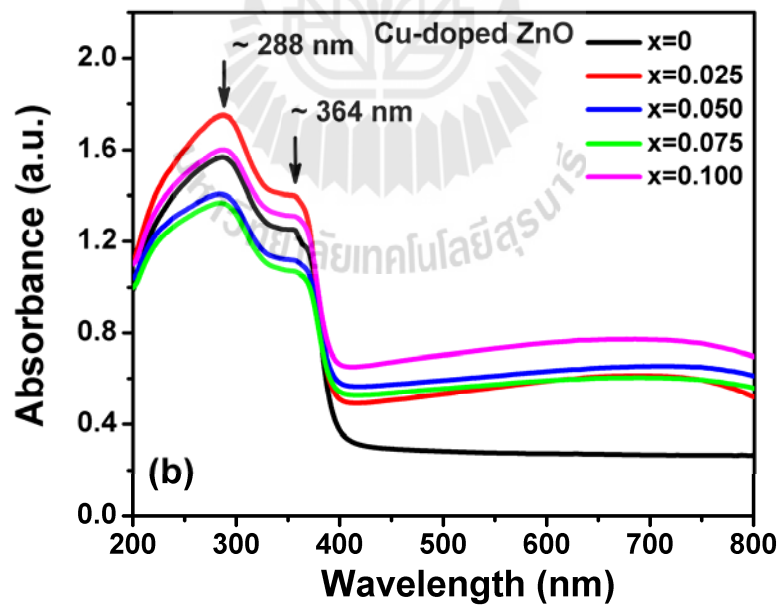


Figure 4.29 Room-temperature optical absorbance spectra of undoped ZnO nanorods calcined at 400 °C for 6 h and Cu-doped ZnO nanorods prepared in air at 300 °C for 6 h.

Compared with the absorption spectra of undoped ZnO sample, it could be easily confirmed that the introduction of Co^{2+} ions into the ZnO leads to the appearance of additional absorption peaks due to the transition involving crystal field levels in the Co^{2+} ions. These transitions were observed in all Co-doped ZnO nanorods as well as defined peaks at 565, 610 and 652 nm indicating that Co^{2+} ions were substituted for Zn^{2+} ions in ZnO. The three absorption peaks at 565 nm (2.19 eV), 610 nm (2.03 eV) and 652 (1.90 nm) are well separated from absorption band edge and are attributed to the presence of Co^{2+} ions in ZnO lattice. The three sharp absorption peaks of Co-doped ZnO samples are due to the $d-d$ crystal field transitions (for the tetrahedral Co^{2+}) ${}^2\text{A}_1(\text{F}) \rightarrow {}^2\text{A}_1(\text{G})$, ${}^4\text{A}_2(\text{F}) \rightarrow {}^4\text{T}_1(\text{P})$ and ${}^2\text{A}_2(\text{F}) \rightarrow {}^2\text{E}_1(\text{G})$, respectively, where A, E and T are generally designations of intermediate energy band (Kwon et al., 2002; Ramachandran et al., 2004). The appearance of these $d-d$ transitions and their growing sharpness with increasing Co content indicate that Co is in the divalent state at the Zn site and supports the inference that the doped Co^{2+} ions are in the high spin ($S=3/2$; $\uparrow\uparrow\uparrow$) state in tetrahedral crystal field symmetry (Elilarased and Chandrasekaram et al., 2013). These electronic transitions suggest that Co^{2+} ions are substituting Zn^{2+} ions in the tetrahedral ZnO. We further observed that with increasing Co content there is trend of increasing absorption in the visible region of the spectrum consistent with higher absorption by the Co ions due to the above mentioned transitions in tetrahedral symmetry. Ordinary, the energy band gaps of TM-doped ZnO nanomaterials were evaluated using the equation relation (Lui et al., 2009; Phokha et al., 2012)

$$\alpha h\nu = A(h\nu - E_g)^m \quad (4.19)$$

where A is a constant, $h\nu$ is revealed that photon energy, α is the optical absorption coefficient near the fundamental absorption edge, E_g is the energy band gap of the material. m is either $1/2$ for a direct or 2 for an indirect dipole-allowed transition. The absorption coefficient was calculated from the optical absorption spectra. The direct energy band gap can be obtained by plotting $(\alpha h\nu)^2$ versus $h\nu$ and extrapolating the linear portion of the absorption edge to find the intercept with energy axis ($y = 0$) as shown in Figure 4.30 and Figure 4.31. The direct energy band gap of the TM-doped ZnO nanorods are also summarized in Table 4.7. Figure 4.30 and Figure 4.31 show the plots of energy gaps versus the doping level (x) of TM-ions in ZnO samples. The band gaps of all the TM-doped ZnO samples slightly decrease with increasing TM atom concentrations except the Cu-doped ZnO sample with $x = 0.100$. These results are very similar to those of TM-doped ZnO nanoparticles reported in literatures (Muthukumaran et al., 2012). Two primary causes may be contributed to variations in energy gap that consist of quantum size effect and electronic structure modifications. Considering the fact that quantum size effect leads to a blue shift of E_g , with decreasing particle size down to less than a few nanometers and hence the decreased band gaps in Figure 4.32 (Co-, Mn-, and Ni-doping) and Figure 4.33 (Cu-doping) are probable not due to this effect because the diameters of the TM-doped ZnO samples are larger than 48 nm and the another one, several author reported that the noticed slight red shift in band gap (E_g) is possibly due to TM doping induced band edge binding (electronic structure modifications). The change in the

energy band gaps of the samples is possible due to the $sp-d$ exchange interactions between the band electrons and the localized d electrons of the TM ions substituting Zn ions. The $s-d$ and $p-d$ exchange interactions give rise to negative correction and positive correction to the conduction-band and the valence-band edges, resulting in a band gap narrowing (Caglar et al., 2012; Muthukumaran et al., 2012). This result confirmed that the ZnO structure was not distorted by the addition of TM, which is in consistent with the XRD results.

Table 4.7 Summary of band gap energy (E_g) of undoped ZnO and TM-doped ZnO nanorods prepared at 300 °C for 6 h.

Doping Level	E_g (eV) of TM-doped ZnO			
	Co	Mn	Ni	Cu
x = 0	3.18	3.18	3.18	3.18
x = 0.025	2.78	3.12	3.11	3.17
x = 0.050	2.68	3.08	-	3.12
x = 0.075	2.55	3.05	-	3.11
x = 0.100	2.57	3.03	-	3.14

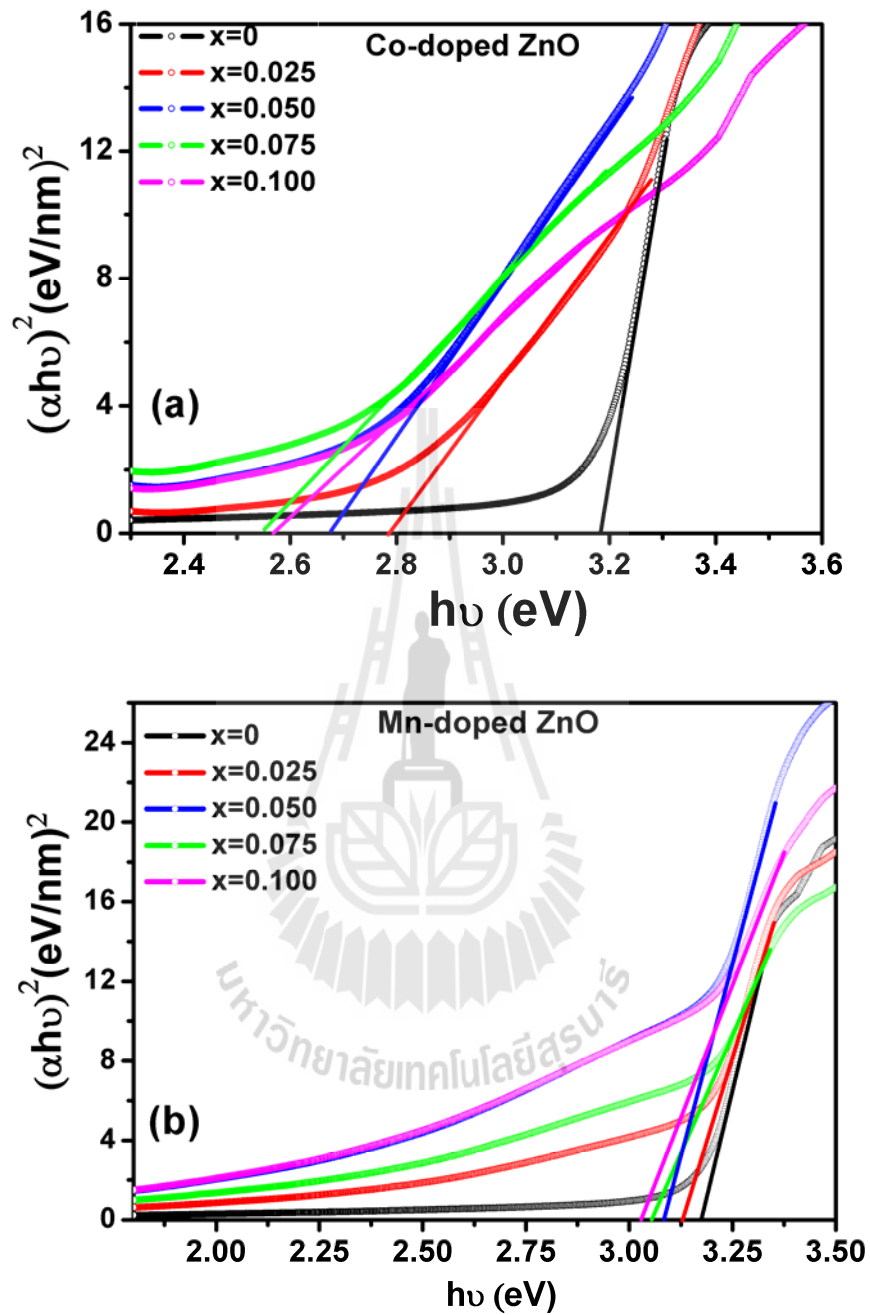


Figure 4.30 Plot of $(\alpha h\nu)^2$ as a function of photon energy ($h\nu$) for undoped ZnO nanorods prepared in air at 400 °C for 6 h and TM-doped ZnO nanorods prepared in air at 300 °C for 6 h. (a) Co-doped ZnO, (b) Mn-doped ZnO and (c) Ni-doped ZnO nanorods, respectively.

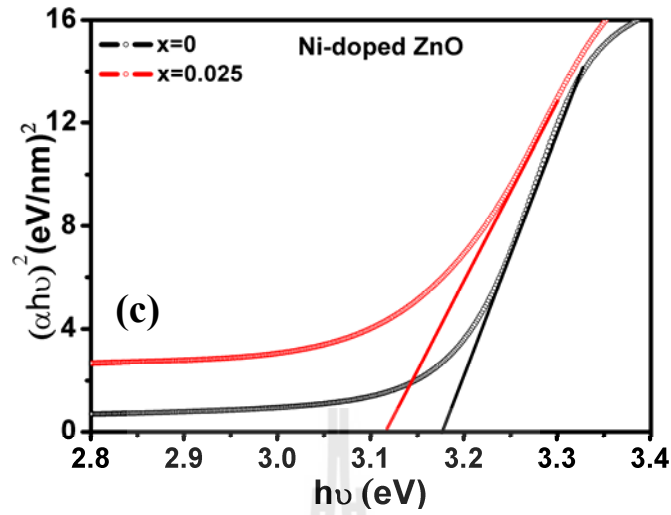


Figure 4.30 Plot of $(\alpha h\nu)^2$ as a function of photon energy ($h\nu$) for undoped ZnO nanorods prepared in air at 400 °C for 6 h and TM-doped ZnO nanorods prepared in air at 300 °C for 6 h. (a) Co-doped ZnO, (b) Mn-doped ZnO and (c) Ni-doped ZnO nanorods (Cont.)

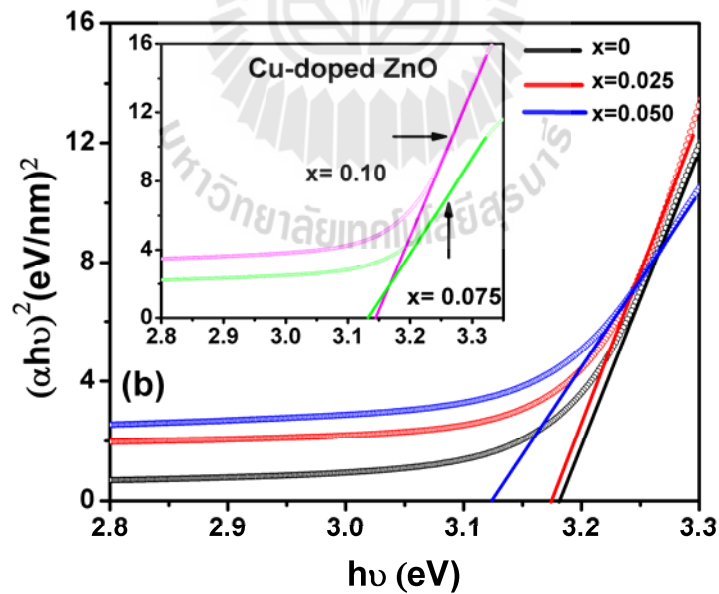


Figure 4.31 Plot of $(\alpha h\nu)^2$ as a function of photon energy ($h\nu$) for undoped ZnO nanorods prepared in air at 400 °C for 6 h and Cu-doped ZnO nanorods prepared in air at 300 °C for 6 h.

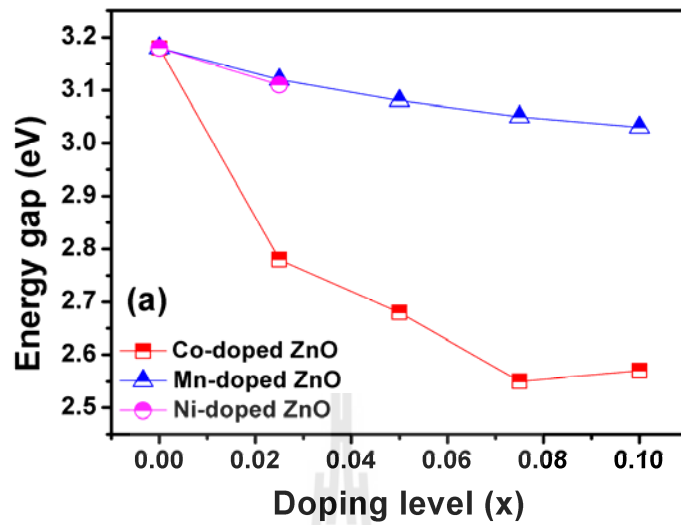


Figure 4.32 band gap versus doping concentration of undoped ZnO nanorods calcined at 400 °C for 6 h and TM-doped ZnO nanorods prepared in air at 300 °C for 6 h, respectively.

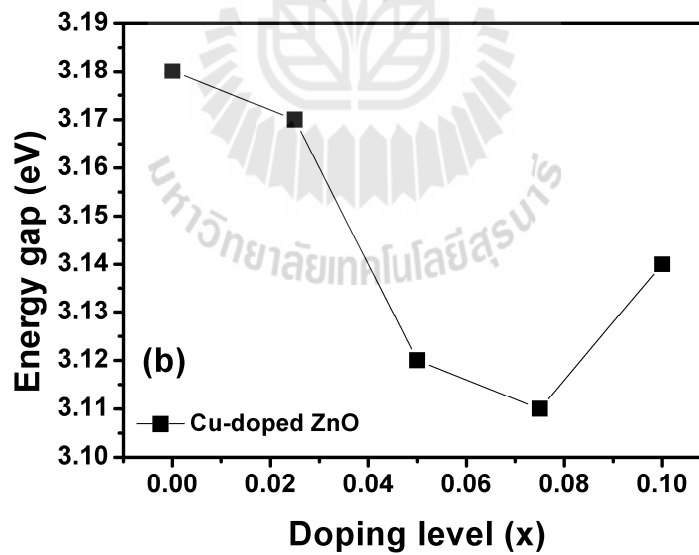
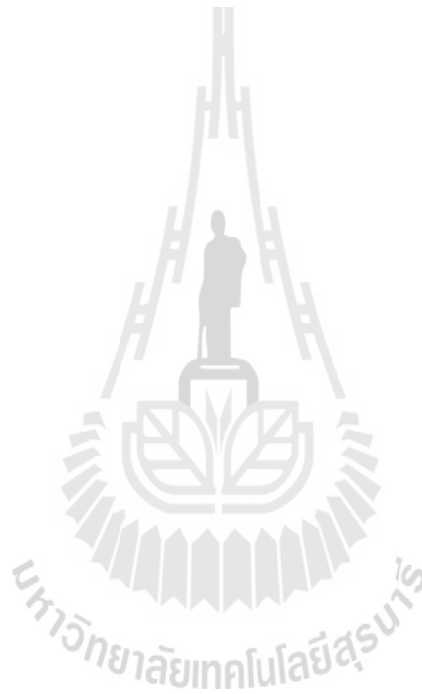


Figure 4.33 band gap versus doping concentration of undoped ZnO nanorods calcined at 400 °C for 6 h and Cu-doped ZnO nanorods prepared in air at 300 °C for 6 h, respectively.

The electronic structures of TM dopants have been characterized by X-ray absorption near-edge structure (XANES) in fluorescence mode. XANES is fingerprint of the empty electronic state for the purpose of probing elements and is extremely sensitive in determining the possible presence of TM clusters in host oxide. Figure 4.34 presents Co *K*-edge XANES spectra obtained for our Co-doped ZnO samples at the room temperature, compared with the standard samples of Co metal, Co(II)O and CO₃O₄ spectra. All spectra have similar features between the XANES of the Co (II) oxide and that of the Co in ZnO. Moreover, the integral amplitude of the pre-edge peak, which is a sign of dipole forbidden transitions (Hsu et al., 2008; de Carvalho et al., 2010) $1s \rightarrow 3d$ is quite similar at future around 7709 eV. Assuming that the integral amplitude of this peak is proportional to the number of $3d$ holes, one could infer the ionization state of Co in the Co-doped ZnO samples. We remark here that the Zn *K*-edge spectrum (Figure 4.34(a)) is not similar to the Co *K*-edge XANES spectra of Co-doped ZnO from Figure 4.34(b). In the XANES spectrum, the pre-edge peak is missing, which is a sign of $4s^0 3d^{10}$ configuration of Zn²⁺. Also, the XANES spectrum is different. In conclusion, it seems that most of Co atoms are placed in environments which are quite similar to that of cobalt (II) oxide and the pre-edge feature is characteristic of substitute Co in the ZnO structure. Hence, the spectra from our samples indicated that Co assumes predominantly the 2+ oxidation state and Co-cluster-free structure, which consistent with the XRD results. Figure 4.35(a) shows the Mn *K*-edge XANES spectra of Mn-doped ZnO samples, with the reference samples of MnO, MnO₂ and Mn₂O₃, respectively. For comparison, the Zn *K*-edge XANES spectrum of ZnO is shifted to the position of Mn-*K*-edge spectrum as shown in Figure 4.35(b). The main peak energy shifts toward high energy and is similar to

Mn₂O₃ reference which reveals that the Mn oxidation state is mainly +3 (Cheng et al., 2013; Han et al., 2012). Furthermore, we observed that an obvious difference between Mn *K*-edge of Mn-doped ZnO and Zn *K*-edge of ZnO in the post-edge region. The difference shows that the chemical environment of Mn in Mn-doped ZnO samples is different from that of Zn in ZnO, which indicates that the Mn³⁺ ions do not substitute for Zn ions in Mn-doped ZnO samples. The normalized XANES spectra for the Ni *K*-edge of Ni in Ni-doped ZnO system are presented in Figure 4.36(a). The data for NiO reference and Ni foil are also shown, being used for energy calibration. From the obtained data, we observed that Ni-doped ZnO samples are close to the NiO curves. In addition, the similarity of feature at the post-edge region between Ni *K*-edge and Zn *K*-edge in ZnO (as shown in Figure 4.36(b)) indicates the chemical environment of Ni is the same as that of Zn in ZnO in the sample with low Ni content ($x = 0.025$), which suggests that a Ni valence state in our sample is 2+ with Ni substitutes at the octahedral sites (Iqbal et al., 2009; Sodatov et al., 2004). Note that we do not observe any variation in the XANES spectra of these edges. The Cu *K*-edge XANES spectra of Cu-doped ZnO and the reference samples are shown in Figure 4.37. The XANES spectrum of Cu foil exhibits the edge absorption at 8979 eV together with a well-resolved doublet in the post edge region. In the case of CuO, where Cu²⁺ exists in octahedral coordination, the edge transition is observed around 8984 eV. These values for Cu foil, Cu₂O and CuO references in the study are in good agreement with those reports in literature. The Cu in Cu-doped ZnO exhibit XANES spectra similar to that of CuO for Cu-doping with $x = 0.025$. However, the slope of the edge absorption around 8984 eV is relatively more and it increases with increasing Cu content which is similar to that of Cu₂O and Cu

reference revealing that a Cu valence state in our samples are mixed state of $\text{Cu}^0/\text{Cu}^{1+}$ and Cu^{2+} ions do not substitute Zn in Cu-doped ZnO samples for high doping level. However, there is a feather in the pre-edge region around 8978 eV, which is observed in some of Cu in Cu-doped ZnO system (Vackar et al., 2013). Moreover, the incorporation of Cu ions in Cu-doped ZnO samples can be confirmed by studying on its optical and magnetic properties.



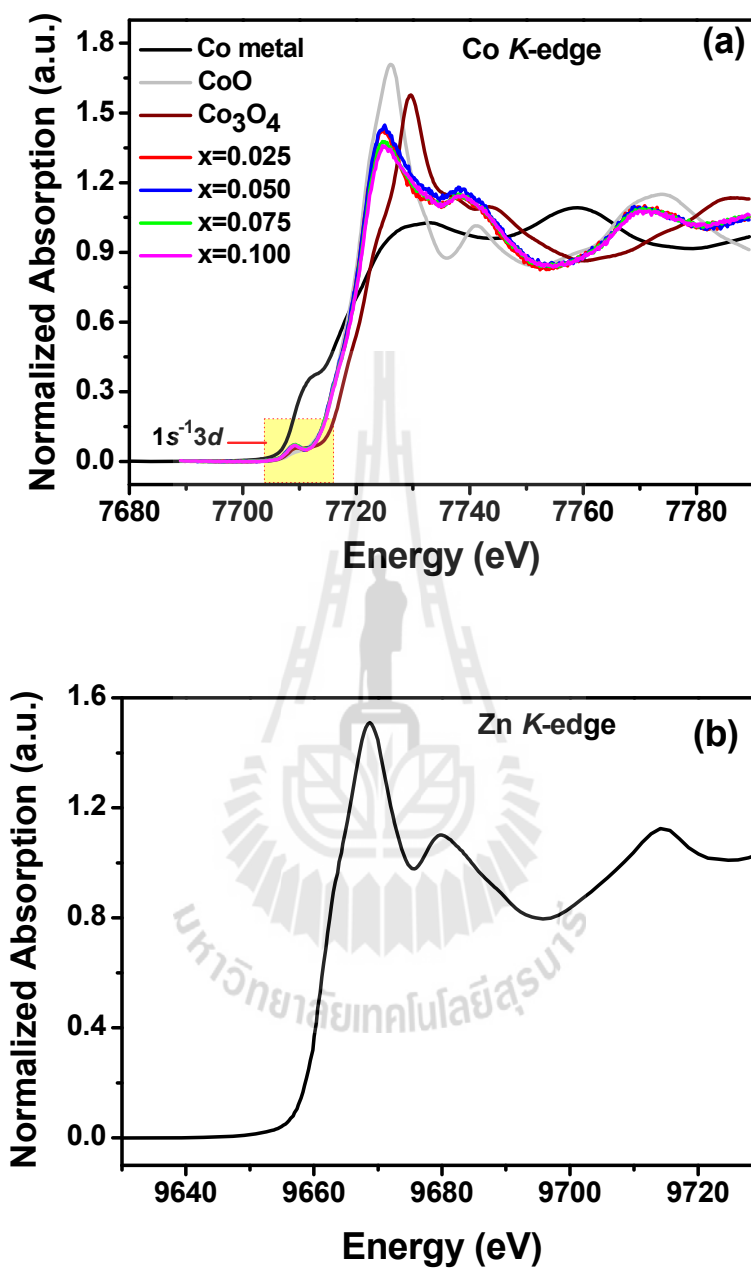


Figure 4.34 (a) Co-K-edge X-ray absorption near-edge structure (XANES) for Co-doped ZnO ($x = 0.025, 0.015, 0.075$ and 0.100) samples, CoO and Co₃O₄ are reference materials for Co²⁺ and Co³⁺, compared with the Zn K-edge XANES spectrum in ZnO (b).

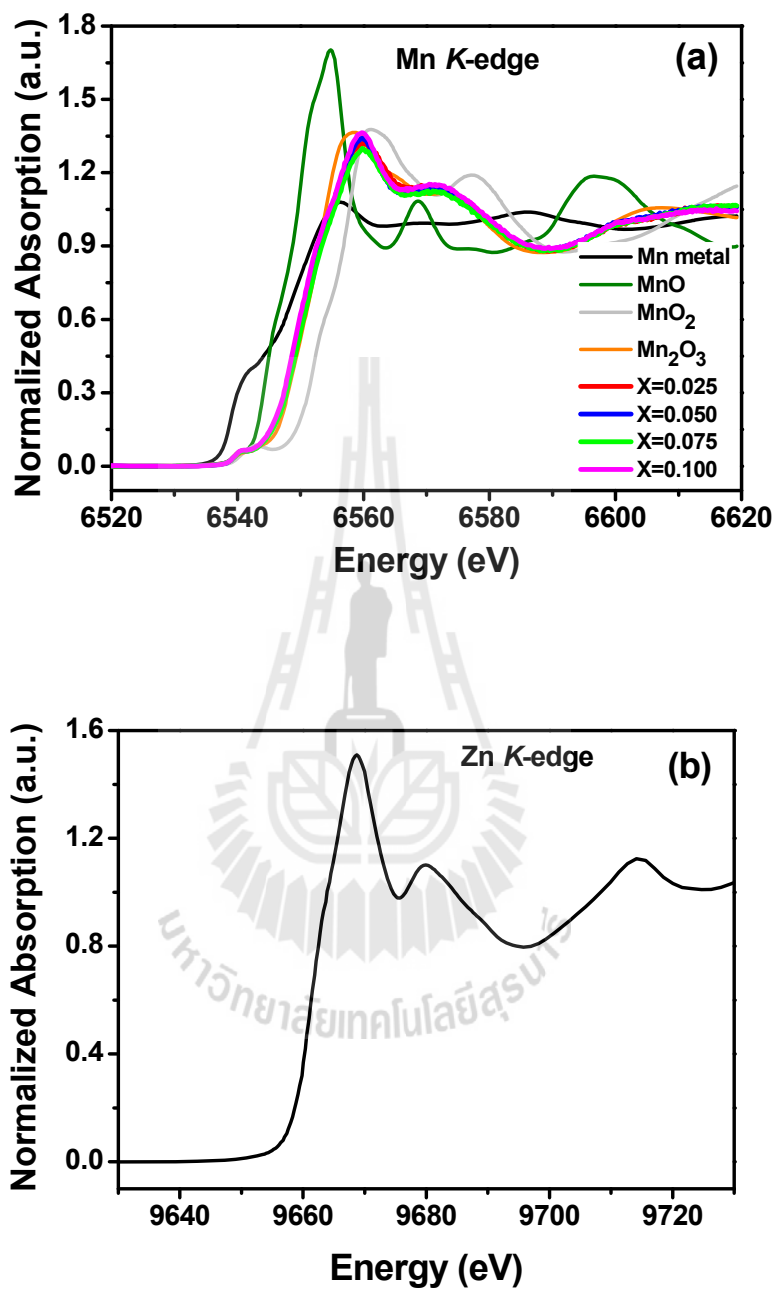


Figure 4.35 (a) Mn-K-edge X-ray absorption near-edge structure (XANES) for Mn-doped ZnO ($x = 0.025, 0.015, 0.075$ and 0.100) samples, MnO, Mn₂O₃ and MnO₂ are reference materials for Mn²⁺, Mn³⁺ and Mn⁴⁺, compared with the Zn K-edge XANES spectrum in ZnO (b).

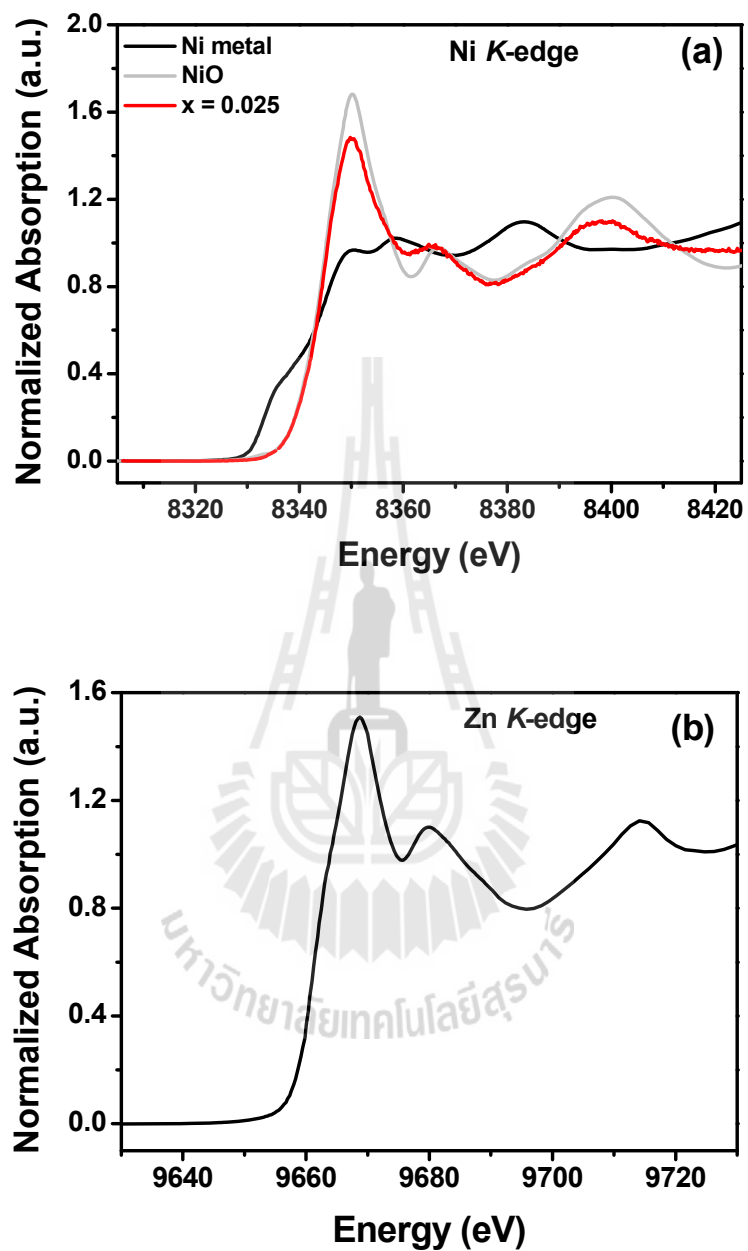


Figure 4.36 (a) Ni-K-edge X-ray absorption near-edge structure (XANES) for Ni-doped ZnO ($x = 0.025$) samples, NiO is reference materials for Ni^{2+} , compared with the Zn K-edge XANES spectrum in ZnO (b).

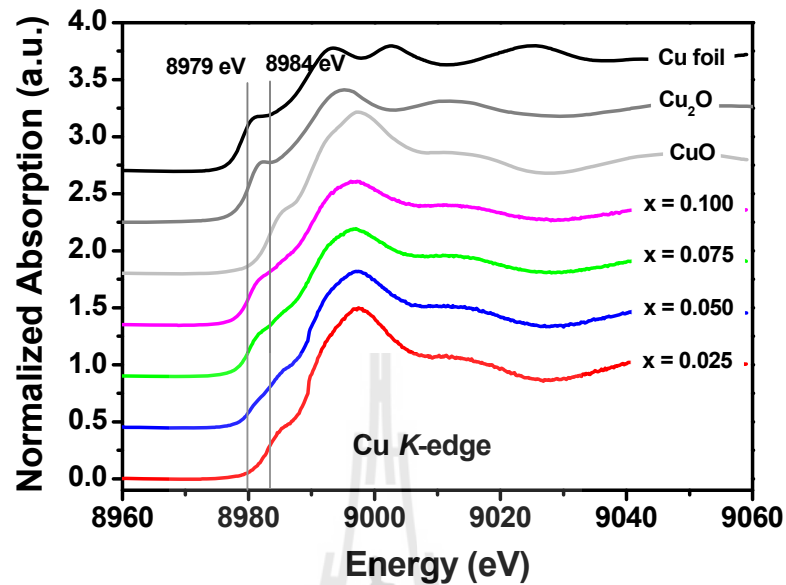
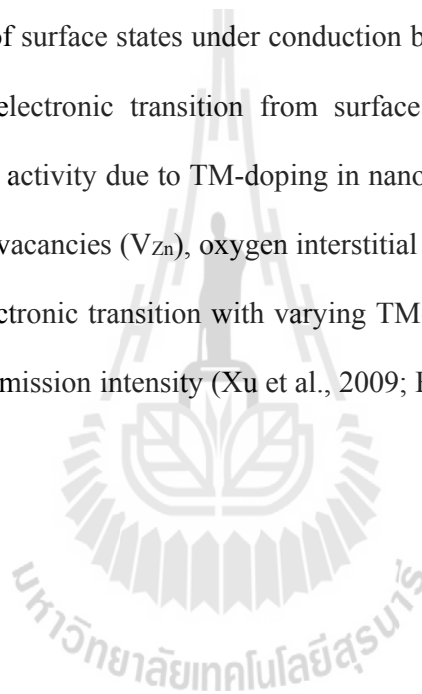


Figure 4.37 Cu-K-edge X-ray absorption near-edge structure (XANES) for Cu-doped ZnO ($x = 0.025$) samples, Cu_2O and CuO are reference materials for Cu^{1+} and Cu^{2+} , respectively.

Photoluminescence spectroscopy is an important tool to study presence of effects and understand the mechanism behind the electronic transitions in materials (Xia et al., 2011; Caglar et al., 2012). The room temperature PL results of the undoped ZnO and TM-doped ZnO samples are shown in Figure 4.38 and Figure 4.39. It is seen that the spectra of all the samples mainly consist of four emission bands including a strong UV emission band at ~ 396 nm (3.11 eV), a weak blue band at ~ 421 nm (2.93 eV), a weak blue-green band at ~ 485 nm (2.54 eV), and a weak green band at ~ 528 nm (2.34 eV) (Ghajari et al., 2013). The UV emission peak shifts a little to lower energy with decreased intensity; the further evidently increase shifts the near band-edge (NBE) to higher wavelength of 421 nm (2.93 eV). This phenomenon is

probably due to the s - p and p - d exchange interaction between the band electrons and the localized ' d ' electron of TM^{2+} ions substituting Zn^{2+} ions. This causes negative and positive correction to the conduction and valence band, and hence leads to band gap narrowing. The additional emission peaks were also observed at around 485 nm (2.54 eV) and 528 nm (2.34 eV). These results are similar to those of V-doped ZnO powders reported by Maensiri et al. (2006). The wavelength centered at 485 nm corresponds to blue emission that might come from the intrinsic defects or extrinsic impurities that from deep levels in the band gap. It may be ascribed to the electron transition from the Zn interstitial level to Zn vacancies level (2.6 eV) according to results in literatures (Zhong et al., 2008). The green-light emissions centered at 528 nm are possibly due to the transition between photo-excited holes and singly ionized oxygen vacancies (Jin-Bock et al., 2001). Moreover, the emission peak intensity decreased by doping TM ions content is probably due to non-radiative recombination processes (Eliarassi and Chandrasekaran, 2013). The weak intensity UV bands at 528 nm observed in the TM-doped ZnO samples are agreed with several reports (Sharma et al., 2009; Yang et al., 2012). This result is due to low density of the oxygen vacancy in these samples. In addition, the broad emission peaks of Co-doped ZnO samples observed in the PL spectra (as show in Figure 4.38(a)) indicate that the wide size distribution of nanoparticles or nanorods. From the variation of UV band gap with the doping concentration of TM-doped ZnO nanorods and photoluminescence results, we conclude that the direct band gap decreases with increasing TM concentration, showing the red-shift of band gap with TM-doping. Such a red shift may be attributed mainly due to the sp - d exchange interaction between the band electrons and the localized d electron of TM ions

substituting ZnO ions in the ZnO lattice. Hence, TM can effectively adjust the band gap of ZnO nanocrystal. Such energy level transition mechanism leads to decrease in intensity of UV emission with TM-doping. A weak blue emission and weak green emission peaks decrease with increasing TM content in ZnO. In general, ZnO has wide band gap between conduction band and valence band. TM-doping in ZnO causes more defect states to occur below the conduction band relax to the defect state results in the energy levels of surface states under conduction band and the gap level in band gap. Therefore the electronic transition from surface state levels, deep levels to conduction band turn activity due to TM-doping in nanocrystal lattice such as oxygen vacancies (V_o), Zinc vacancies (V_{Zn}), oxygen interstitial (Zn_i) and extrinsic impurities. Such variation in electronic transition with varying TM-doping in ZnO may result in the shrinkage in the emission intensity (Xu et al., 2009; Eliarassi et al., 2013).



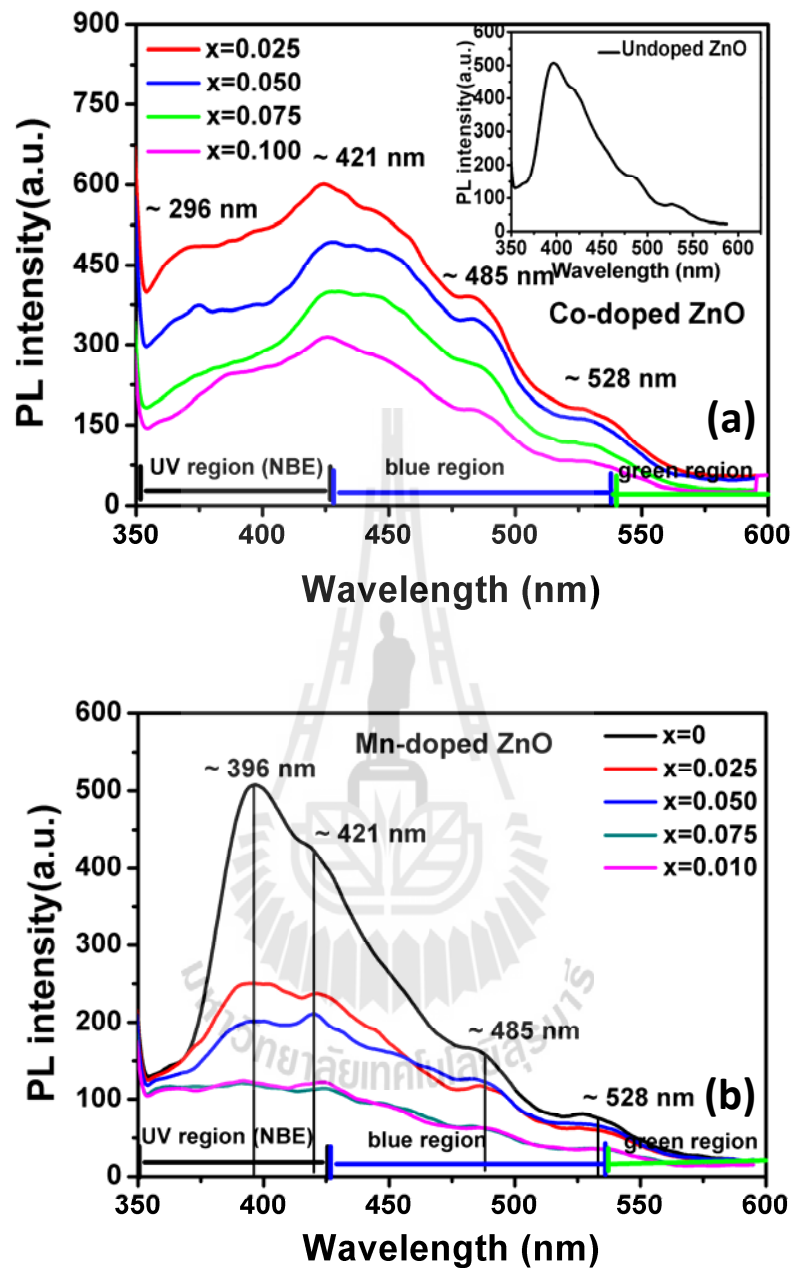


Figure 4.38 Room temperature photoluminescence spectra of undoped ZnO and TM-doped ZnO nanorods, (a) Co-doped ZnO (b) Mn-doped ZnO and (c) Ni-doped ZnO samples, under 325 nm light excitation.

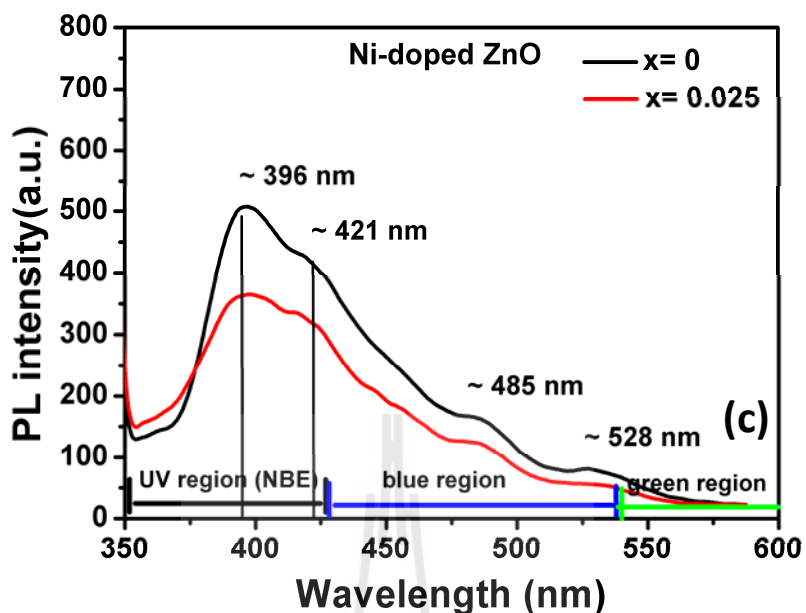


Figure 4.38 Room temperature photoluminescence spectra of undoped ZnO and TM-doped ZnO nanorods, (a) Co-doped ZnO (b) Mn-doped ZnO and (c) Ni-doped ZnO nanorods, under 325 nm light excitation (Cont.)

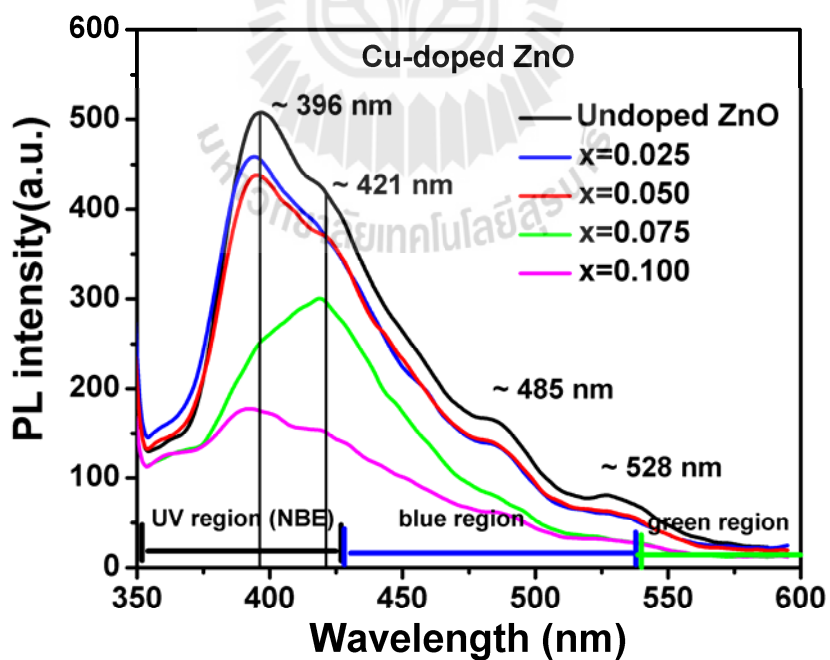


Figure 4.39 Room temperature photoluminescence spectra of undoped ZnO and Cu-doped ZnO nanorods, under 325 nm light excitation.

4.2.3 The magnetic properties of magnetic ions in Co-, Mn- and Ni-doped ZnO nanorods.

The magnetization magnetic measurement (M) versus applied magnetic field (H) were performed on undoped ZnO, Co-doped and Mn-doped nanorods with different the transition metal content obtained at 293 K from VSM measurements are shown in Figure 4.40. The specific magnetization curve presents a diamagnetic behavior for undoped ZnO thermally decomposed in air at 400 °C for 6 h, whereas all samples thermally decomposed in air at 300 °C for 6 h of Co-doped, Mn-doped and Ni-doped ZnO showed a weak ferromagnetic (FM) component in the field range of ± 2000 kOe. Figure 4.40(a), shows the specific saturation magnetization (M_s) value of 0.022 emu/g, 0.034 emu/g and 0.072 emu/g for the $Zn_{1-x}Co_xO$ samples with $x = 0.025, 0.050$ and 0.075 , respectively. Beside, The magnetization of the Co-doped ZnO sample for $x = 0.100$ having with both ferromagnetism (FM) and paramagnetism (PM) increased with increasing magnetic field in the field of ± 10 kOe. The specific saturation magnetization (M_s) value of 0.018 emu/g, 0.032 emu/g and 0.055 emu/g are observed in $Zn_{1-x}Mn_xO$ samples for $x = 0.025, 0.050$ and 0.075 , respectively (Figure 4.40(b)). Furthermore, we found that the magnetization of the $Zn_{1-x}Mn_xO$ sample for $x = 0.100$ showed both FM and PM increased with increasing magnetic field. In the case of Ni-doped ZnO, we focus on the magnetic properties of pure phase for Ni-doped ZnO sample. It can be clearly seen that the $Zn_{1-x}Ni_xO$ nanorod for $x = 0.025$ has a saturation magnetization (M_s) value of 0.388 emu/g and coercivity value (H_c) amounts to about 418 Oe as shown in Figure 4.41, which are higher than $Zn_{0.975}Ni_{0.025}O$ nanorods (M_s : 0.4 emu/g, H_c : 72 Oe) (Zhao et al., 2010)

The magnetization (M) and coercivity (H_c) values of all the samples are summarized in Table 4.8.

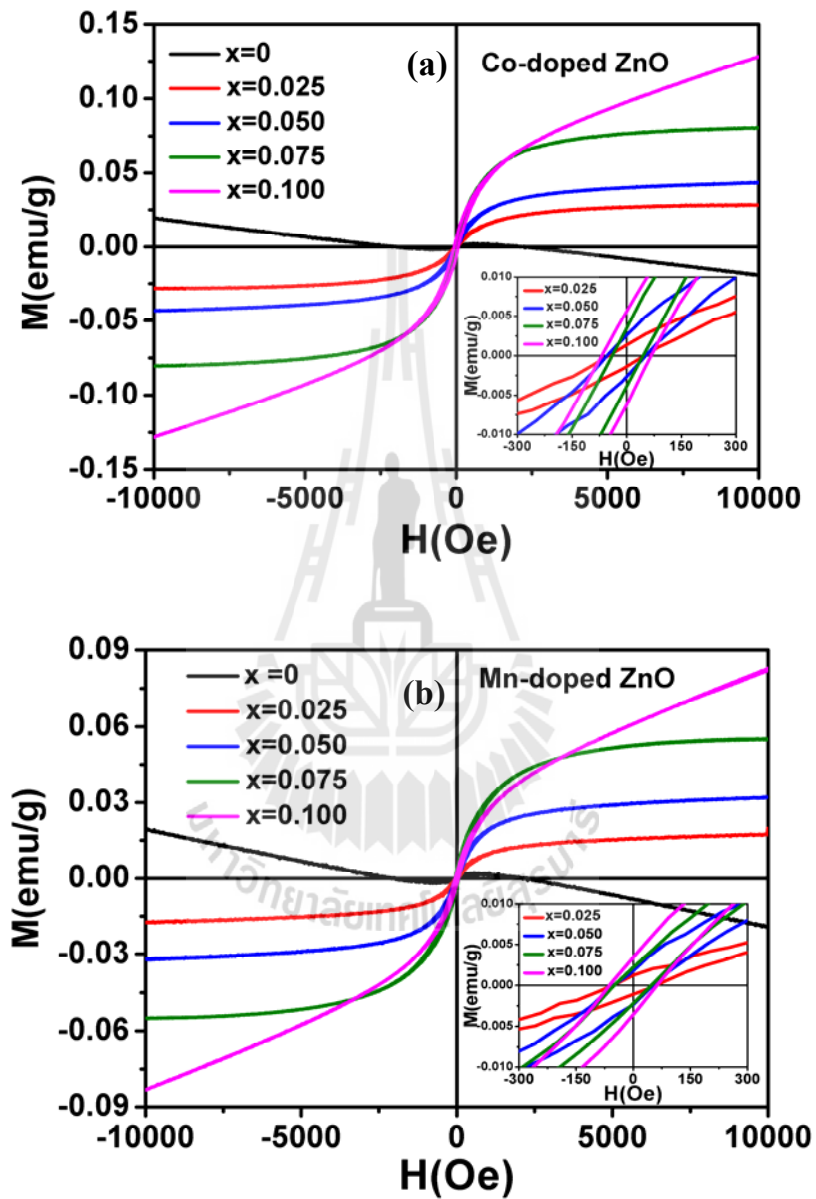


Figure 4.40 The magnetization magnetic measurement (M) versus applied magnetic field (H) were performed on undoped ZnO, (a) Co-doped and (b) Mn-doped ZnO Nanorods with different the transition metal content obtained at 293 K from VSM measurement.

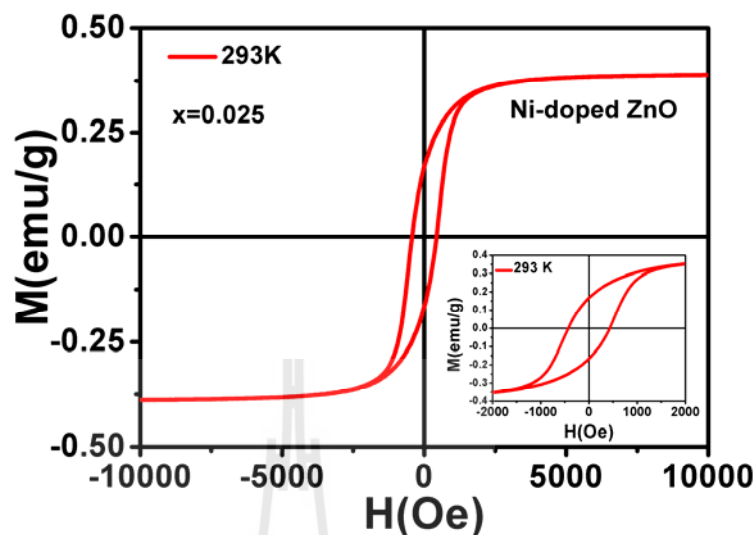


Figure 4.41 The magnetization magnetic measurement (M) versus applied magnetic field (H) was performed on $Zn_{0.975}Ni_{0.025}O$ at 293 K from VSM measurement.

Table 4.8 summary of magnetization of Co-, Mn- and Ni-doped ZnO at room temperature.

Doping level	Co-doped ZnO		Mn-doped ZnO		Ni-doped ZnO	
	M(emu/g)	H_c (Oe)	M(emu/g)	H_c (Oe)	M(emu/g)	H_c (Oe)
x = 0.025	0.022	74.67	0.018	41.72	0.388	418
x = 0.050	0.034	77.26	0.032	43.26	-	-
x = 0.075	0.072	77.74	0.055	46.33	-	-
x = 0.100	0.090	72.84	0.082	55.29	-	-

The magnetization of TM-doped ZnO nanorods are summarized in Table 4.8. The possible origins of the ferromagnetism observed in our sample might be assessed by considering the results from XRD, XPS, XANES and optical measurement. The first possibility is the formation of the secondary phase such as CoO, MnO, MnO₂

and Mn_2O_3 are well known to be antiferromagnetic below their Neel temperature of 293 K, 116 K, 92 K and 76 K, respectively (Yang et al., 2006; Chu et al., 2007). Furthermore, it is also well known that Mn is a paramagnetic material, and cannot contribute to ferromagnetic behavior itself. According to the XRD, XPS, XANES and absorption spectra results clearly showed that there were no Co- and Mn-clusters. Thus, the ferromagnetic behavior of Co- and Mn-doped ZnO nanorods might not be explained in term of the formation of the secondary phases. In addition, the origin of ferromagnetic behavior observed in $\text{Zn}_{0.975}\text{Ni}_{0.025}\text{O}$ nanorods, there are a few of controversial explanations, one of which is the formation of some nanoscale Ni-related secondary phase, such as metallic Ni precipitation and NiO. In fact, NiO phase can be easily ruled out, since bulk NiO is antiferromagnetism with a Neel temperature of 520 K (Schwartz et al., 2012). Secondly, based on our experimental conditions, metallic Ni is also an unlikely source of this ferromagnetism because the synthesis of low Ni diffusion-doped ZnO nanorods is performed in air which can prevent the formation of metallic Ni nanoclusters to some extent. Especially, XRD and HRTEM results clearly show no metallic Ni clusters in the ZnO nanorods. According to the optical and magnetic data, one can see that it is apparent that the ferromagnetic properties of $\text{Zn}_{0.975}\text{Ni}_{0.025}\text{O}$ nanorods have a strong correlation with oxygen vacancies, which is compatible with earlier literatures (Yilmaz et al., 2012). Another probable mechanism, the exact mechanism of intrinsic ferromagnetism in TM-doped oxides is still under debate. A diversity of theories has been proposed, such as super-exchange, double-exchange between the d states of TMs, free-carrier-mediated exchange and sp-d exchange mechanism, etc (Coey et al., 2005). All these proposed theories cannot well agree with the experimental results in DMSs.

In addition to the magnetic doping effect, oxygen vacancy (V_o) defects have been suggested to play an important role in the magnetic origin for oxide DMSs (Coey et al., 2004). The theoretical studies suggest that V_o can cause an obvious change of the band structure of host oxides and makes a significant contribution to the ferromagnetism (Coey et al., 2005). The formation of bound magnetic polarons (BMPs), which include electrons locally trapped by oxygen vacancy, with the trapped electron occupying an orbital overlapping with the d shells of TM neighbors, has also been proposed to explain the origin of ferromagnetism (Liu et al., 2015). Experimentally, oxygen vacancy might easily be generated during various growth processes of the TM-doped ZnO system. On the basis of XPS and experimental results, and the observed green emission centered at 528 nm, the oxygen-vacancy defects lay in the deep levels with localized carriers. Our systematic study shows that oxygen-vacancy defect constituted BMPs are a promising candidate for the origin of room-temperature ferromagnetism in this system. Within the BMP model, the greater density of oxygen vacancy (V_o) yields a greater overall volume occupied by BMPs, thus increasing their probability of overlapping more TM ions into ferromagnetic domains and enhancing ferromagnetism as shown in Figure 4.42. Hence, we expect that $\text{Co}^{2+}-\square-\text{Co}^{2+}$ and $\text{Ni}^{2+}-\square-\text{Ni}^{2+}$ groups will be common in the structure, where \square denotes an oxygen vacancy. An electron trapped in the oxygen vacancy constitutes an F -center (the F -center resembles BMP), where the electron occupies an orbital which overlaps the d shells of both cobalt and nickel neighbors. The radius of the electron orbital is of the order $a_0\varepsilon$, where a_0 is the Bohr radius and ε is the dielectric constant of ZnO. Since $\text{Co}^{2+}(3d^7)$ and $\text{Ni}^{2+}(3d^8)$ only has unoccupied minority spin orbitals, the trapped electron will be \downarrow and the two ions neighbors \uparrow (Figure

4.42). This direct ferromagnetic coupling we call *F*-center exchange (FCE). Further reduction of the average ferromagnetic moment will result from both any antiferromagnetic $\text{Co}^{2+}\text{-O}^{2-}\text{-Co}^{2+}$ superexchange (SE) bonds. According to the superexchange interaction (Lotey et al., 2013), one *p* electron of O would couple with the e_g orbital electron of Co^{2+} . In addition, this electron in the *p* orbital of O must be antiparallel to the e_g orbital electron, which makes the two neighboring Co^{2+} ions antiparallel. Thus, the system exhibits antiferromagnetic behavior. On the other hand, the small observed net magnetism of Co-doped ZnO nanorods can be explained as there are also some isolated Co^{2+} ions outside polarons (as shown in Figure 4.43), which may reduce the net magnetic moment due to their random distribution (Zhao et al., 2010). We expect FCE to be the dominant exchange mechanism in the Co-doped ZnO systems. Our results also give a possible reason why the ferromagnetism and antiferromagnetism can be observed in most Co-doped ZnO DMS nanocrystals. For the Mn-doped ZnO system, the XRD patterns of Mn diffusion-doped ZnO nanorods conserved their hexagonal structure and no other secondary phases related to Mn metal cluster or Mn compounds such as MnO, MnO_2 , Mn_2O_3 , were detected in these samples. In addition, the XPS presence of Mn^{3+} and Mn^{4+} may be assigned to the plausible $\text{ZnMn}_2\text{O}_4/\text{Mn}_2\text{O}_3$ and $\text{ZnMnO}_3/\text{MnO}_2$ impurity phases, which often appeared in other Mn-doped ZnO (Yang et al., 2013), although they were not detected by XRD measurement. However, XPS spectrum of Zn $2p_{3/2}$ of Mn-doped ZnO is also shift of binding energy from 1021.23 eV to 1020.40 eV. This shift of binding energy is due to the formation of the substitution of part of lattice Zn in ZnO by Mn^{2+} ions and the formation of Zn-Mn bonding structure. The main edge energy shifts toward high energy of the Mn *k*-edge XANES spectrum which is similar to

Mn_2O_3 , indicating that the valence of Mn is mainly +3. As a result, Mn ions are first to dissolve into the substitutional sites in ZnO to form Mn^{2+}O_4 tetrahedral coordination and the solubility of substitutional Mn is very low. Then Mn ions enter into the interstitial sites to form Mn^{3+}O_6 octahedral coordination as shown in Figure 4.44. Hence, it is possible that the weak ferromagnetic behavior arises from FCE coupling ($\text{Mn}^{2+}-\square-\text{Mn}^{2+}$). However, we suppose that it is the result of competing effect between the ferromagnetic and antiferromagnetic phase below which indicates that the magnetic interactions between Mn ions are antiferromagnetic. As discussed above, most Mn ions in our nanocrystals enter into the interstitial sites in the ZnO lattice and form Mn^{3+}O_6 groups with octahedral coordination. The neighboring Mn ions in the Mn^{3+}O_6 octahedron would be connected by O^{2-} between them and form of $\text{Mn}^{3+}-\text{O}^{2-}-\text{Mn}^{3+}$ complex with the bond angle of 180° and then the antiferromagnetic coupling was observed. The observed intrinsic ferromagnetism makes these DMSs nanorods potential for future spintronics devices.

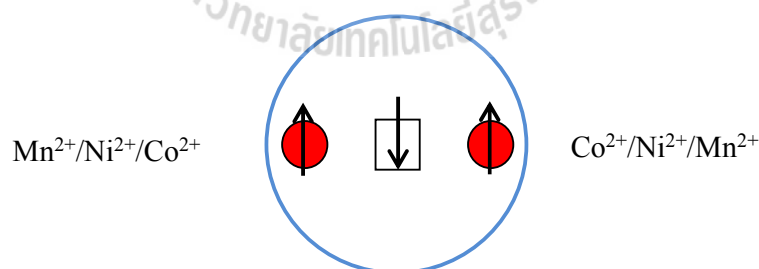


Figure 4.42 Schematic diagrams showing the F-center exchange mechanism in TM-doped ZnO nanorods (adopted from Coey et al., 2004).

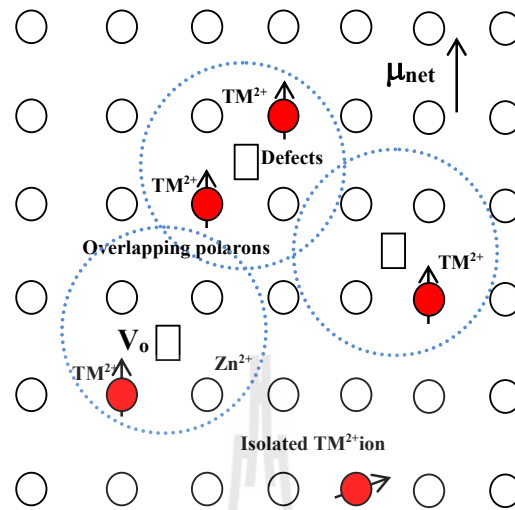


Figure 4.43 Schematic diagram of oxygen-vacancy-induced ferromagnetism through overlapping of polarons (adopted from Coey et al., 2005).

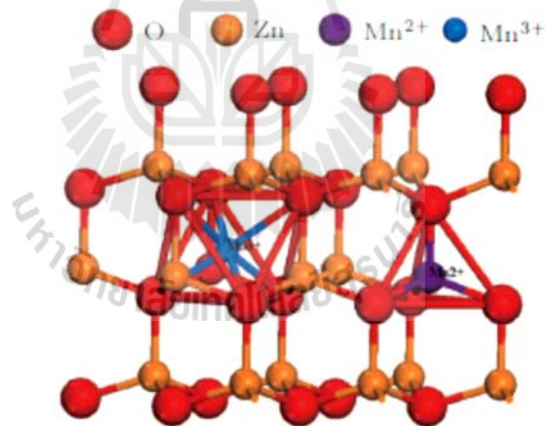


Figure 4.44 Schematic diagrams of the interstitial site and the substitution site Mn in a ZnO lattice after doping. (Yan et al., 2013).

Magnetization magnetic measurements (M) versus applied magnetic field (H) were performed on $\text{Zn}_{0.925}\text{Co}_{0.075}\text{O}$, $\text{Zn}_{0.925}\text{Mn}_{0.075}\text{O}$ and $\text{Zn}_{0.975}\text{Ni}_{0.025}\text{O}$ at 50K and 293K, as shown in Figure 4.45. For $\text{Zn}_{0.925}\text{Co}_{0.075}\text{O}$ and $\text{Zn}_{0.925}\text{Mn}_{0.075}\text{O}$ samples, the magnetization showed a slight increase with decreasing temperature, a coercive field (H_c) of 42.24 Oe was observed for $\text{Zn}_{0.925}\text{Co}_{0.075}\text{O}$, whereas the $\text{Zn}_{0.925}\text{Mn}_{0.075}\text{O}$ sample was obtained a coercive field (H_c) of 46.33 Oe at 293 K. At 50K for the $\text{Zn}_{0.925}\text{Co}_{0.075}\text{O}$ and $\text{Zn}_{0.925}\text{Mn}_{0.075}\text{O}$ samples, a coercive field (H_c) of 52.22 and 73.46, respectively, were obtained as shown in Figure 4.45(a) and Figure 4.45(b). Figure 4.45(c) shows the magnetic properties of $\text{Zn}_{0.975}\text{Ni}_{0.025}\text{O}$ samples, where the maximum applied field at 10 kOe. Figure 6(a) shows the magnetization versus magnetic field (M - H) curves. It can be seen that the $\text{Zn}_{0.975}\text{Ni}_{0.025}\text{O}$ nanorods exhibit a ferromagnetic behavior. The saturation magnetization (M_s) for $\text{Zn}_{0.975}\text{Ni}_{0.025}\text{O}$ sample is 0.415emu/g at 50 K with a coercive field (H_c) of 720 Oe. When the temperature was increased to 293 K, the M - H curve still exhibits hysteresis loop with the M_s is 0.375 emu/g with a coercive field (H_c) of 418 Oe were obtained, respectively. These values are higher than previous report on nanocrystalline $\text{Zn}_{1-x}\text{Ni}_x\text{O}$ (Huang et al., 2007; Zhao et al., 2010) and lower than reported on Ni-doped ZnO nanorods (Cheng et al., 2008).

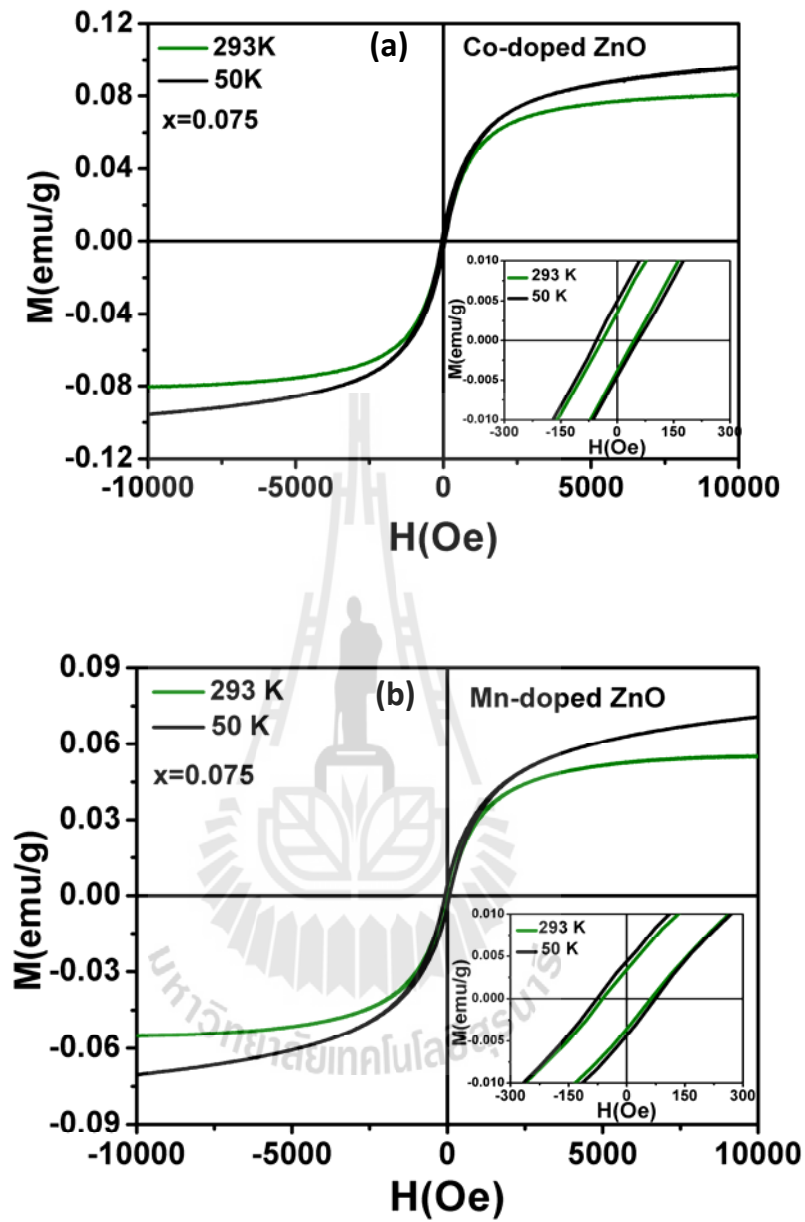


Figure 4.45 $M \times H$ curves for (a) $\text{Zn}_{0.925}\text{Co}_{0.075}\text{O}$, (b) $\text{Zn}_{0.925}\text{Mn}_{0.075}\text{O}$ and (c) $\text{Zn}_{0.975}\text{Ni}_{0.025}\text{O}$ samples taken at $T=50\text{K}$ and 293K , showing the existence of ferromagnetism.

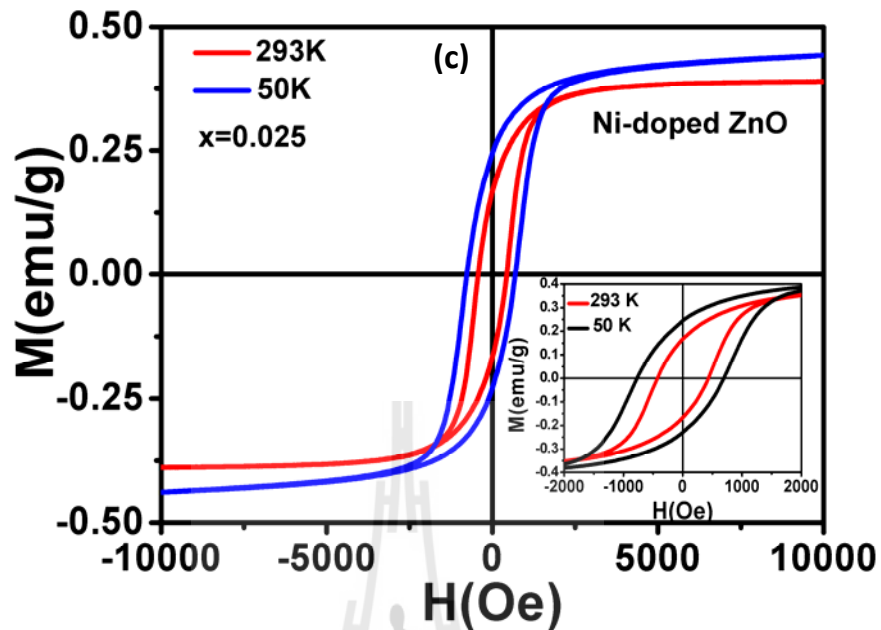


Figure 4.45 $M \times H$ curves for (a) $\text{Zn}_{0.925}\text{Co}_{0.075}\text{O}$, (b) $\text{Zn}_{0.925}\text{Mn}_{0.075}\text{O}$ and (c) $\text{Zn}_{0.975}\text{Ni}_{0.025}\text{O}$ samples taken at $T = 50$ and 293K , showing the existence of ferromagnetism (Cont.)

Figure 4.46(a) and Figure 4.46(b) display the temperature-dependent magnetization (M - T) curves of Co- and Mn-doped ZnO samples, respectively. Data were recorded on warming in an applied field (H) of 1 k Oe, after cooling in a zero field (ZFC). These plots show characteristic behaviors observed in other ZnO-based DMSs, i.e. a magnetization decrease with increasing temperature up to 293 K and Curie temperature are lower than RT, which indicates that no bulk ferromagnetism exists in these samples. Moreover, the field cooling and zero field cooling curves are well in superposition, further supporting the absence of ferromagnetic impurities. The inverse magnetic susceptibility versus temperature ($\chi^{-1}(T)$) curves in temperature range of 50 K - 293 K as illustration in the inset of Figure 4.46.

The para/antiferromagnetic behavior and the magnetic susceptibility can be simply fitted to the modified Curie – Weiss law (Peleckis, Wang and Duo, 2006) quite well in high temperature region (150 K – 293 K).

$$\chi = \frac{C}{T-\theta} + \chi_0 \quad (4.20)$$

Where χ , χ_0 , θ and C are the susceptibility, temperature independent susceptibility (sum of Pauli, Landau and core susceptibilities), the Curie – Weiss temperature and Curie constant, respectively. Using $C = N\mu_{eff}^2/3k_B = Ng^2\mu_B^2s(s+1)/3k_B$, with N = number of magnetic ions/g, k_B = Boltzmann constant, μ_{eff} = effective magnetic moment; $\mu_{eff} = g\mu_B\sqrt{s(s+1)}$. As a result of Co-doped ZnO, χ_0 , θ and C are estimated to be 1.28×10^{-5} emu/g.Oe, -165.46 K, 0.00316 emu.K/g.Oe, respectively. The obtained χ_0 , θ and C values are 1.49×10^{-5} emu/g.Oe, -220.46 K, 0.00912 emu.K/g.Oe for Mn-doped ZnO. From Curie constant we obtain the effective magnetic moment $\mu_{eff} \sim 2.30 \mu_B$, $\sim 2.43 \mu_B$ for Co and Mn ions, respectively. In principle, a $Co^{2+}(d^7)$ ion at a tetrahedral coordination site may assume the high-spin (HS) configuration ($e_g^4t_{2g}^3, \uparrow\downarrow\uparrow\downarrow\uparrow\uparrow$; $s = 3/2$) or Low-spin (LS) (Can et al., 2011) configuration ($t_{2g}^6e_g^1, \uparrow\downarrow\uparrow\downarrow\uparrow\downarrow$; $s = 1/2$). A number of studies suggest that the Co^{2+} ions of Co-doped ZnO adopt the HS configuration. On the other hand, the electron configuration ($e_g^2t_{2g}^2, \uparrow\uparrow\uparrow\uparrow$; $s = 2$) of a HS $Mn^{3+}(d^4)$ is the different as the electron configuration ($t_{2g}^4, \uparrow\downarrow\uparrow\uparrow$; $s = 2/2$) of a LS Mn^{3+} ions in Mn-doped ZnO (Peleckis, Wang and Duo., 2006). Our results are close to the values of HS Co^{2+} ($s = 3/2$, $\mu_{eff} \sim 3.87 \mu_B$) and LS Mn^{3+} ($s = 2/2$, $\mu_{eff} \sim 2.83 \mu_B$). All the samples magnetization

are much smaller than theoretic value suggests that there are competitions of antiferromagnetic and ferromagnetic interaction between Co ions in Co-doped ZnO and Mn ions in Mn-doped ZnO nanorods, respectively. Due to antiferromagnetic competitions, ferromagnetic interactions are suppressed resulting to magnetization of Co and Mn ions are much smaller than theoretic value. Moreover, we obtain θ values for our samples were negative, indicating antiferromagnetic interactions among magnetic ions. Figure 4.47 shows the temperature dependent magnetization ($M-T$) curve of $\text{Zn}_{0.975}\text{Ni}_{0.025}\text{O}$ sample was recorded using VSM magnetometer in temperature range of 50 to 293K with a magnetic field at 1000 Oe, it is clear that the curie temperature (T_c) is well above room-temperature (RT) since the zero-field-cooled (ZFC) and field-cooled (FC) did not converge at RT (Jayakumar et al., 2006). The ZFC and FC curve did not show any blocking nature. Thus, the second phases of NiO can be ruled out as NiO is antiferromagnetic (T_N 520 K). The absence of any other magnetic nano-particle existed in the sample as revealed by XRD, HRTEM and XANES. it is possible that the observed ferromagnetic behavior are possibly due to the intrinsic behavior from some defect structures created because of the particular synthesis conditions.

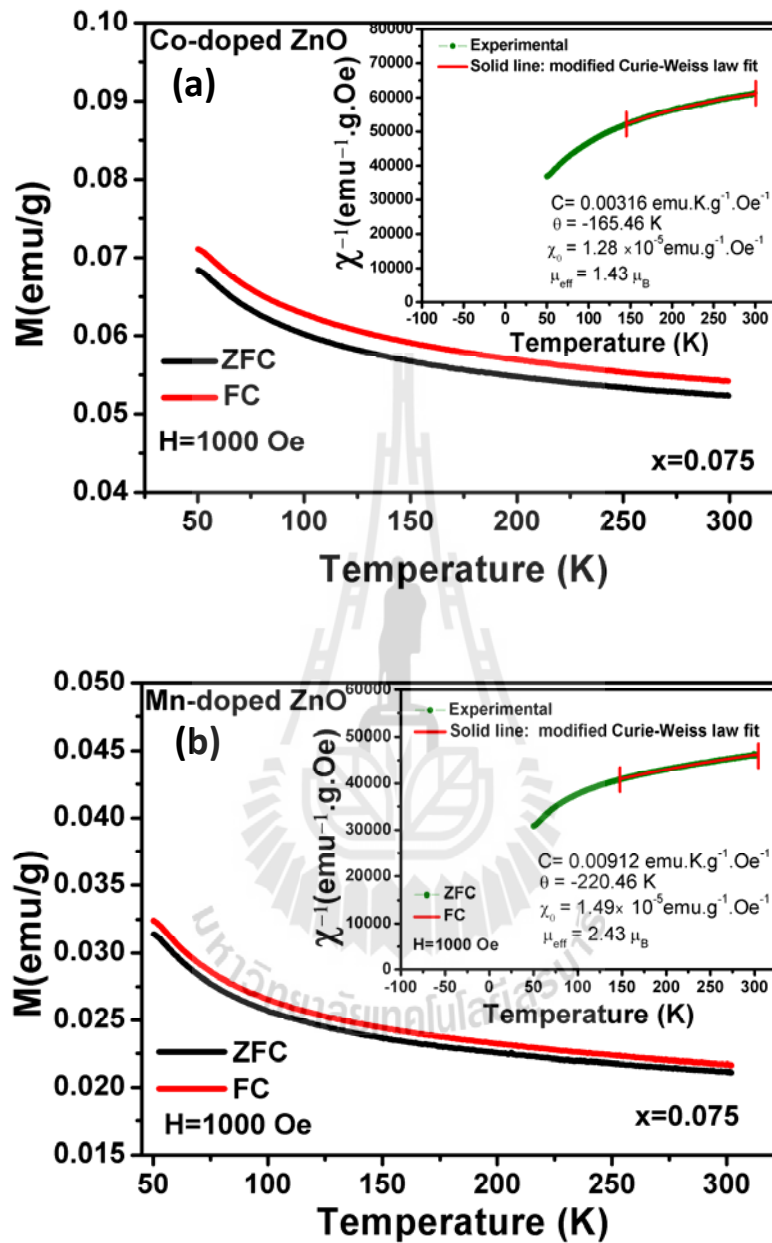


Figure 4.46 (a) and (b) display the temperature-dependent magnetization (M - T) curves of Co- and Mn- doped ZnO samples, respectively. Inset (a) and (b): the modified curie-weiss fitting to the data between 150 K and 300 K under 1 kOe as a function of temperature and fitting result using the modified Curie-weiss law.

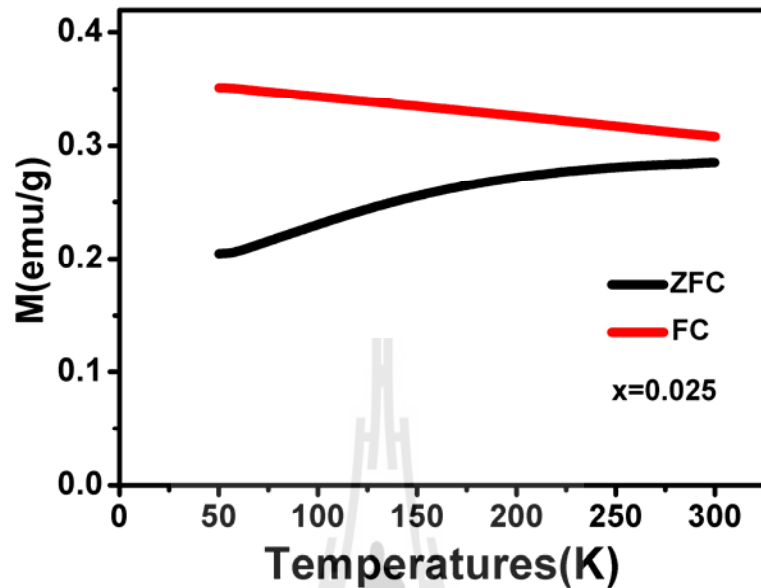


Figure 4.47 shows the temperature dependent magnetization (M - T) curve of $\text{Zn}_{0.975}\text{Ni}_{0.025}\text{O}$ sample was recorded using VSM magnetometer in temperature range of 50 to 293 K with a magnetic field at 1000 Oe.

4.2.4 The magnetic properties of nonmagnetic ions in Cu-doped ZnO

There are many reports suggesting that the ferromagnetic ordering arises from the magnetic ions actually substituting in lattice or from either the clustering or impurities. However, the origin of ferromagnetism in DMOs is not yet well understood. Hence, nonmagnetic element of Cu is a perfect choice to avoid controversies regarding the ferromagnetic ordering for the antiferromagnetic Cu-related secondary phases such as CuO and Cu_2O which may make the interpretation of ferromagnetic in Cu-doped ZnO system easier (Zhong et al., 2008; Lui et al., 2009) Recently, very few studies on the synthesis and magnetic properties of nanocrystalline $\text{Zn}_{1-x}\text{Cu}_x\text{O}$ DMSs have been reported. Sharma et al. (2009)

investigated the room-temperature ferromagnetic properties of dilute magnetic semiconductor ZnO:Cu²⁺ nanorods synthesized by hydrothermal method. They found that these nanorods showed strong ferromagnetic behavior and then the ferromagnetic behavior was suppressed and paramagnetic nature was enhanced at higher doping percentage of Cu atoms. This phenomenon is attributed to the enhanced antiferromagnetic interaction between neighboring Cu-Cu ions suppressed the ferromagnetism. Jin et al. (2011) reported that the enhancement of saturation magnetization and coercivity were simultaneously observed in ZnO:Cu ceramics prepared by high pressure and high temperature (HPHT) method. These results suggested that the magnetic properties of those ceramics can be largely improved by the dense microstructure and various defect states and vibrational modes of lattices are tuned by HPHT. Yang et al. (2012) reported the microstructure and room temperature ferromagnetism of Cu-doped ZnO films synthesized by radio frequency (RF) magnetron sputtering method. They found that oxygen vacancy (V_o) concentration increased with increasing Cu content of x = 5.7 to 18 at.%. The V_o concentration depended on the ratio of Raman spectra peaks ($V_o \sim \frac{\text{Area}_{A1(LO)}}{\text{Area}_{A1(LO)} + \text{Area}_{E2(\text{high})}}$). This result implies that the room temperature ferromagnetism has strong correlation not only with Cu ions but also with V_o. From our results, the PL and UV-Vis spectrum showed that there are some oxygen vacancies forms on the samples which are also confirmed by XPS investigation. Furthermore, the XPS and XANES results demonstrated that of all samples are associated with these of the divalent state (Cu²⁺ and Cu¹⁺) and the Cu-related phase of Cu, CuO and Cu₂O. The doping Cu content of x = 0.025 would possibly increase the density of oxygen vacancies which activate more coupling between Cu ions, leading

to an increase in saturation magnetization. The magnetization curves and their H_c field were obtained by VSM measurements as shown in inset of Figure 4.48. The undoped ZnO sample calcined at 400 °C (as shown in the inset of Figure 4.48(a)) exhibits a diamagnetic behavior. After the diamagnetic background of ZnO and sample holder were subtracted, the hysteresis loops show clear ferromagnetic behavior of those Cu-doped ZnO samples at 293 K (see Figure 4.48(a)). The saturation magnetizations of 0.00876, 0.0109, 0.0100 and 0.00985 emu/g at 10 kOe were observed for the Cu-doped ZnO samples with $x = 0.025$, 0.050, 0.075 and 0.100, respectively. These values are higher than those reported on Cu-doped ZnO nanostructures (Yang et al., 2012). The second phases and metal clusters do not contribute to the ferromagnetism. This is because the $3d$ orbitals in Cu^{1+} ($3d^{10}4s^0$) are fully filled while the existence of impurity phases in the samples results in antiferromagnetism (Xu et al., 2012). Therefore, it is possible that the exchange interactions between the localized d spins on the Cu^{2+} (d^9) ions and oxygen vacancy are the cause of room-temperature ferromagnetism in our Cu-doped samples. The doping Cu contents of $x = 0.025$ and 0.050 would possibly increase the amount of oxygen vacancies which activate more coupling between Cu ions, leading to an increase in saturation magnetization (M_s). According to F -center exchange interaction (Cu^{2+} -□- Cu^{2+}). Although the M_s decreases with increasing Cu ion into the samples with $x = 0.075$ and 0.100, an increased number of Cu atoms occupying adjacent cation positions would result in antiferromagnetic alignment with superexchange interaction (Cu^{2+} - O^{2-} - Cu^{2+}) or arise from impurity phase. Figure 4.48(b) shows the magnetization versus magnetic field (M - H) curve of the Cu-doped ZnO with $x = 0.050$. The M - H curve shows obvious hysteresis loop with the coercive field H_c of 90 Oe at 50K. When

the temperature was increased to 293K, the M - H curve still exhibits hysteresis loop with the H_c of 75 Oe as show in inset of Figure 4.47(b).

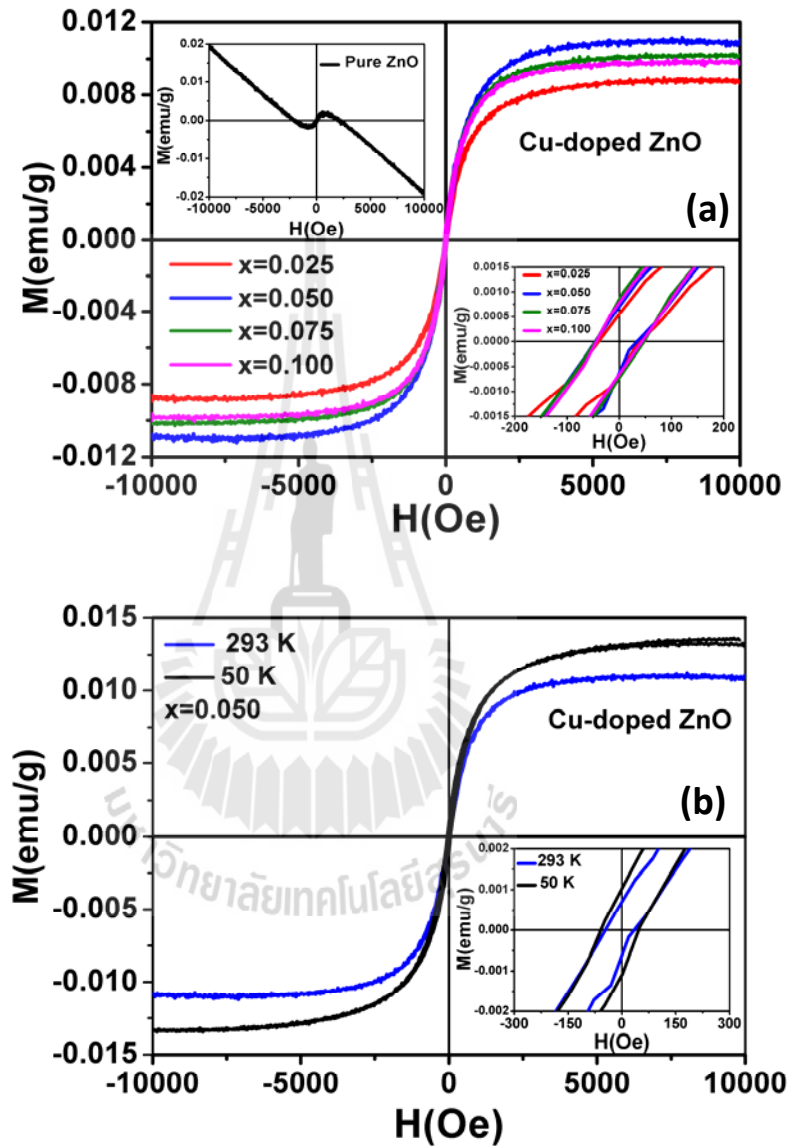


Figure 4.48 (a) the magnetization magnetic measurement (M) versus applied magnetic field (H) were performed on undoped ZnO and Cu-doped with different Cu ions content obtained at 293 K from VSM measurement and (b) $M \times H$ curves for Cu-doped ZnO ($x = 0.025$) sample taken at $T = 50$ K and 293 K.

4.3 RE-doped ZnO nanorods

This part we will discuss on structural characterization, morphology, chemical composition, absorption, photoluminescence and magnetic properties of Tb- and Er-doped ZnO nanorods.

4.3.1 Structural characterization, morphology and chemical compositions of RE-doped ZnO (i.e. RE = Tb and Er)

Figure 4.49 illustrates the XRD patterns of the nanocrystalline Tb- and Er-doped ZnO with different doping concentrations. For comparison, the XRD pattern for undoped ZnO is shown in Figure 4.49(a). The diffraction peaks of undoped ZnO was thermal decomposition in air at 400 °C for 6 h corresponding to (100), (002), (101), (102), (110), (103), (200), (112) and (201) with the standard data (JCPDS, 36-1451). Contradictory, the precursor prepared in air at 300 °C for 6 h shows a relatively weak peak of ZnO and some other peaks of zinc acetate materials. After the thermal decomposition at 300 °C in air, the XRD patterns of all the samples having peaks that correspond to the wurtzite structure of ZnO with the standard data (JCPDS, 36-1451) for Tb- and Er-doped ZnO nanorods with $x = 0.025, 0.050, 0.075$ and 0.100 as shows in Figure 4.49(b) and Figure 4.50(b). And no diffraction peaks of Tb and Er metals and other impurities such as Tb_4O_7 , Tb_7O_{12} , Er_2O_3 phases (Wu et al., 2012). This indicates that the wurtzite structure is not affected by Tb and Er substitutions. It is believed that the absence of Tb_2O_3 and Er_2O_3 related peaks are may be due to the complete substitution of Tb^{3+} and Er^{3+} ions into the Zn^{2+} site or the interstitial site of ZnO revealing not only TM-doped ZnO but also RE-doped ZnO can be reduced the preparation temperature for a formation of wurtzite ZnO structure. The crystallite sizes of all samples were also calculated from x-ray line broadening of

the reflections of (100), (002), (101), (102), (110) and (103) peaks using Scherrer's equation. The lattice parameters of all samples are also calculated from the XRD patterns and the calculated values are summarized in Table 4.9.

Table 4.9 Summary of crystallite size and lattice constant (a and c) of undoped ZnO and RE-doped ZnO nanorods thermally decomposed at 300 °C at for 6 h.

Doping level	crystallite size (nm)		lattice constant, $a = b$ and c (nm)			
	Tb	Er	Tb		Er	
			a	c	a	c
$x = 0.000$	36.90 ± 0.8500	36.90 ± 0.8500	0.32477	0.52041	0.32477	0.52041
$x = 0.025$	58.90 ± 0.9500	54.80 ± 0.9600	0.32489	0.52138	0.32488	0.52126
$x = 0.050$	56.40 ± 0.9200	52.90 ± 0.9500	0.32492	0.52065	0.32491	0.52078
$x = 0.075$	55.50 ± 0.8600	48.70 ± 0.8800	0.32491	0.52057	0.32486	0.52064
$x = 0.100$	55.90 ± 0.8700	46.60 ± 0.8600	0.32489	0.52056	0.32488	0.52056

The crystallite sizes of the samples whose Tb and Er concentration of x varies from 0 to 0.025 have a dramatically increase and then slightly decrease with increasing the Tb and Er concentrations that varies from 0.050 to 0.100 (as shown in Figure 4.51). These results suggest that the effective Tb and Er ions disturb the ZnO crystal structure. Moreover, we observed that the lattice constant " a " and " c " in Tb³⁺ doped ZnO and Er³⁺ doped ZnO nanorod samples are similar trend, the wurtzite structure lattice parameters a and c of the samples increased when $x = 0.025$, then the values decrease with the value of x increasing as show in Figure 4.52. However, these above value are larger than those of lattice $a = 0.32477$ nm and $c = 0.52041$ nm

in the undoped ZnO sample. This phenomenon is a proof of the incorporation of Tb and Er ions inside the ZnO crystal lattice due to the higher radius of Tb^{3+} ($\sim 0.92 \text{ \AA}$) and Er^{3+} ($\sim 0.88 \text{ \AA}$) than the Zn^{2+} ($\sim 0.74 \text{ \AA}$) ions (Singh et al., 2014). Hence, the expansion of lattice will lead to Tb incorporation of the ZnO lattice or interspatial oxygen revealing the increases crystallites size and expand lattice parameters.

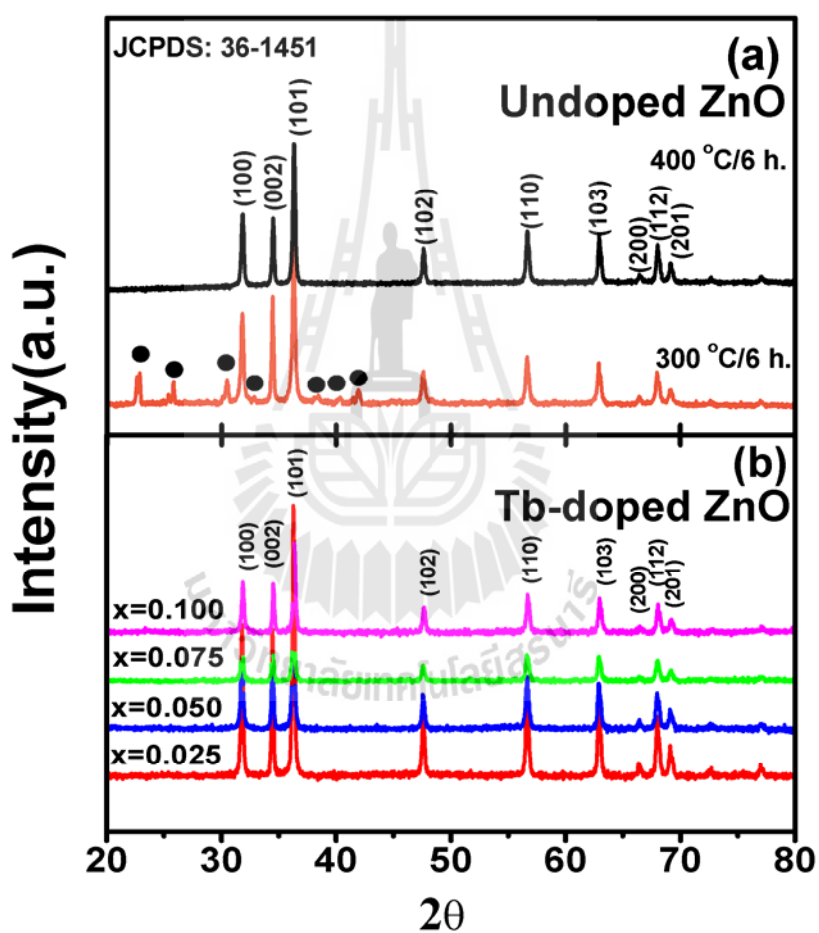


Figure 4.49 XRD patterns of undoped ZnO sample thermally decomposed in air at 400 °C for 6 h and undoped ZnO prepared in air at 300 °C for 6 h (a) and (a) the XRD patterns of Tb-doped ZnO samples prepared in air at 300 °C for 6 h with $x = 0.025$, 0.050, 0.075 and 0.100, respectively.

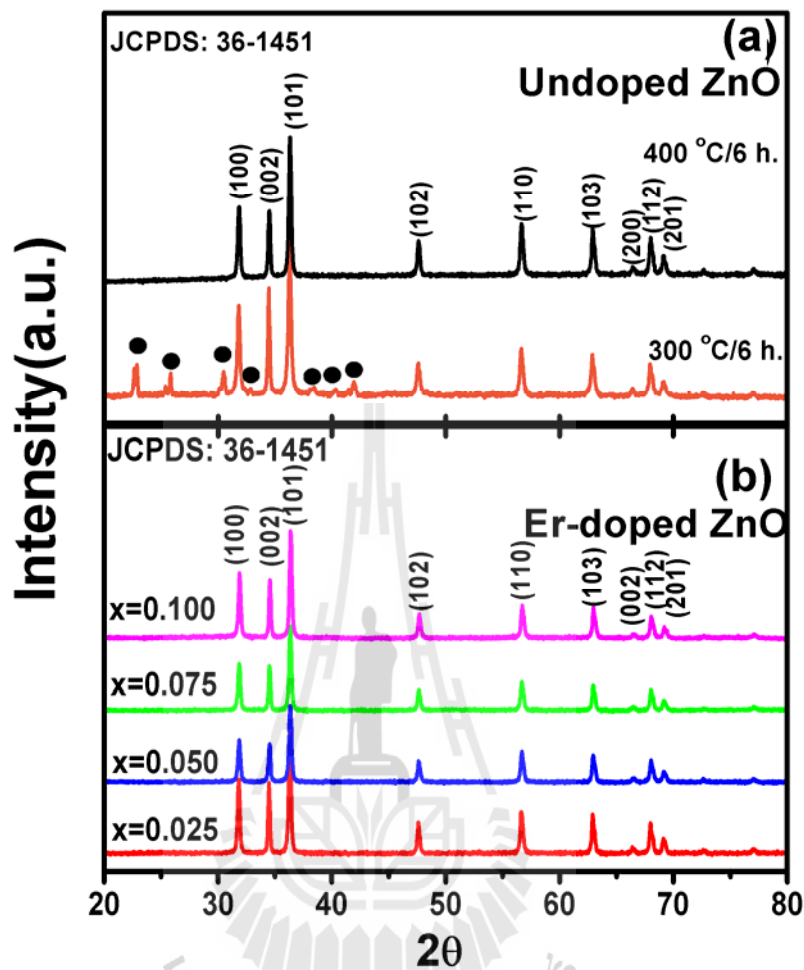


Figure 4.50 XRD patterns of undoped ZnO sample thermally decomposed in air at 400 °C for 6 h and undoped ZnO prepared in air at 300 for 6 h (a) and (b) the XRD patterns of Er-doped ZnO samples prepared in air at 300 °C for 6 h with $x = 0.025$, 0.050, 0.075 and 0.100, respectively.

The morphology and structure of the Tb- and Er-doped ZnO nanorods were investigated by TEM and HRTEM. Figure 4.53 and Figure 4.54 show TEM images of Tb-doped ZnO and Er-doped ZnO nanorods (i.e. $x = 0.025$, 0.050, 0.075 and 0.100). It can be seen that the synthesized material have a mixture of nanorods with different

diameters ranging from 64 nm to 96 nm and length of several μm , and also most of nanorods are straight in morphology and smooth in surface. High-resolution TEM images show that the samples have uniform structure, and no clusters are found on surface layer with lattice spacing of ~ 0.26 nm. The selected-area electron diffractions (SAED) show spotty ring patterns, consistent with those of (100), (101), (102) and (110) planes of the XRD results (JCPDS, 36-1451). These results confirm a formation of ZnO wurtzite structure.

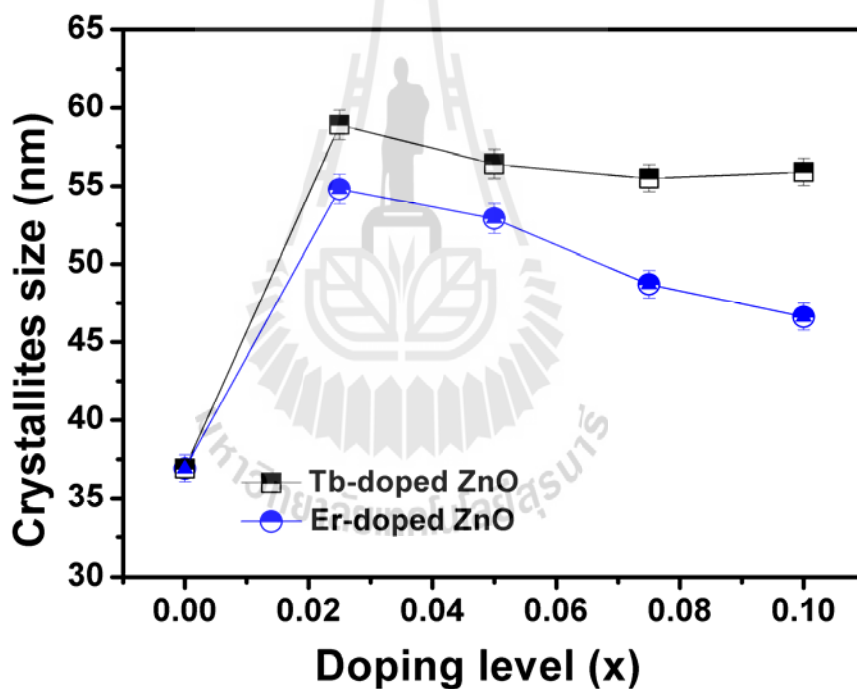


Figure 4.51 An average crystallite size of undoped ZnO prepared at 400 °C for 6 h, Tb- and Er-doped ZnO nanorods prepared at 300 °C for 6 h.

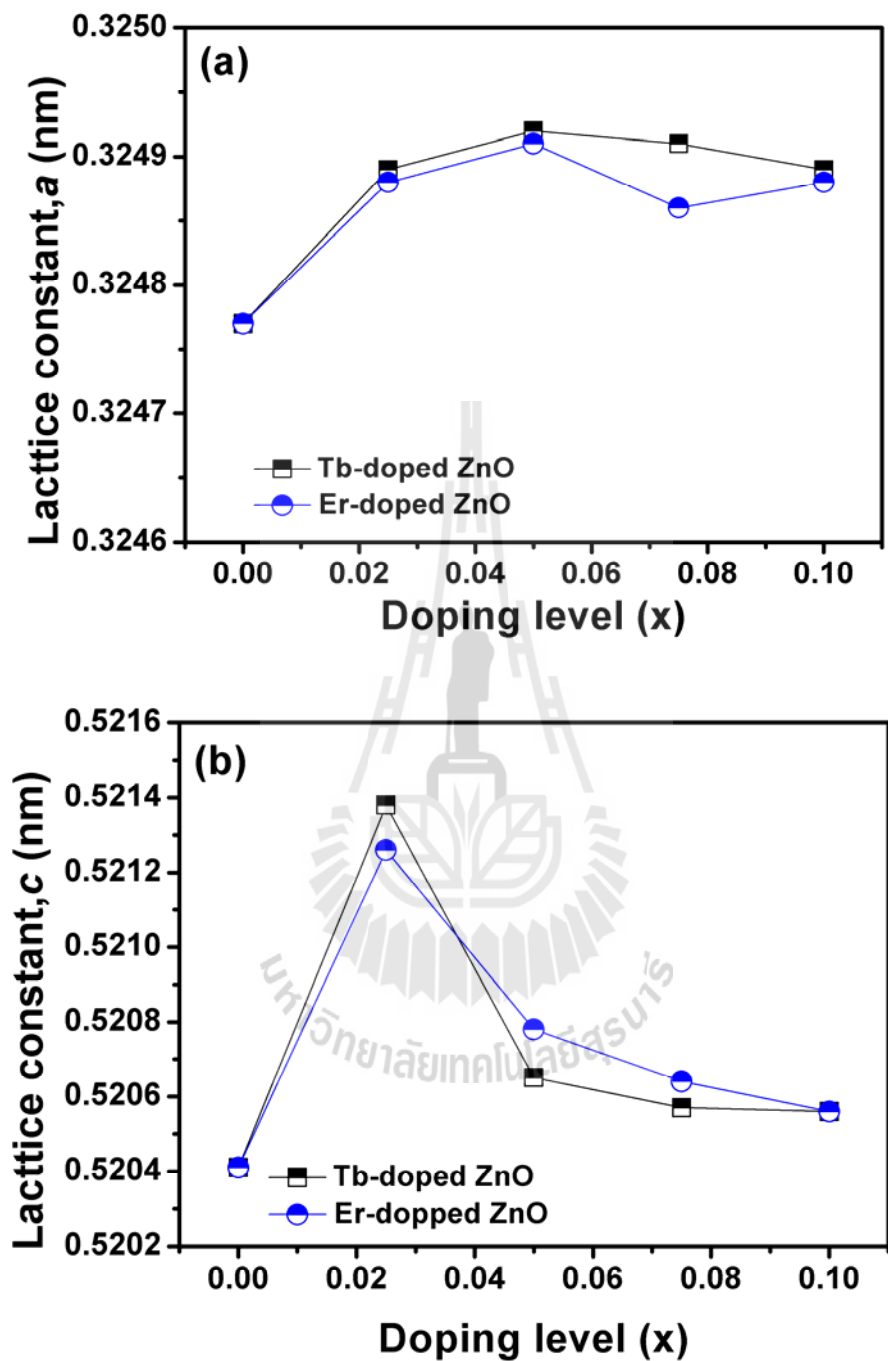


Figure 4.52 Lattice constant of undoped ZnO prepared at 400 °C for 6 h, (a) *a* parameter and (b) *c* parameter of Tb- and Er-doped ZnO nanorods prepared at 300 °C for 6 h, respectively.

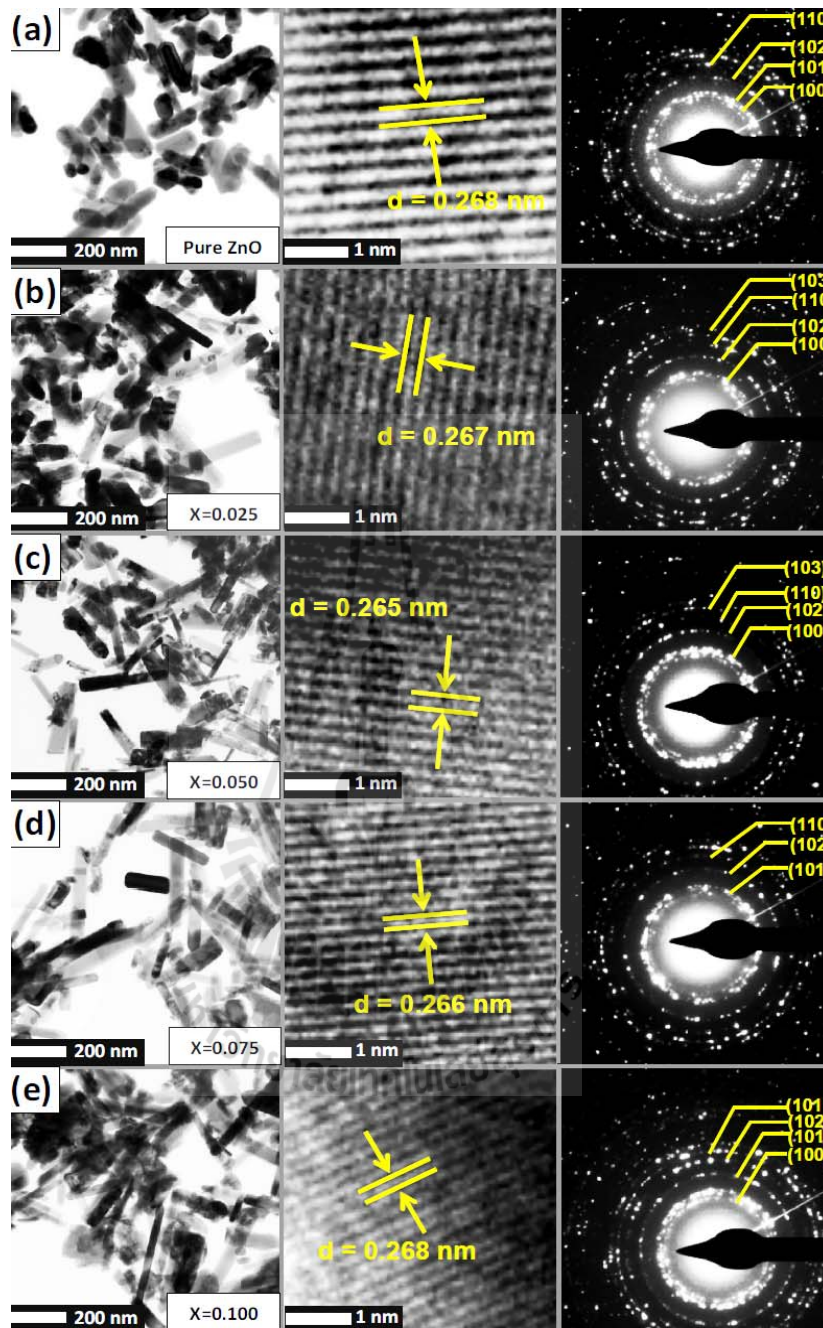


Figure 4.53 TEM bright field, High-resolution TEM (HRTEM) images with corresponding SEAD patterns of undoped ZnO sample prepared in air at 400 °C for 6 h (a) and Tb-doped ZnO samples prepared in air at 300 °C for 6 h with $x = 0.025$ (b), $x = 0.050$ (c), $x = 0.075$ (d), and $x = 0.100$ (e).

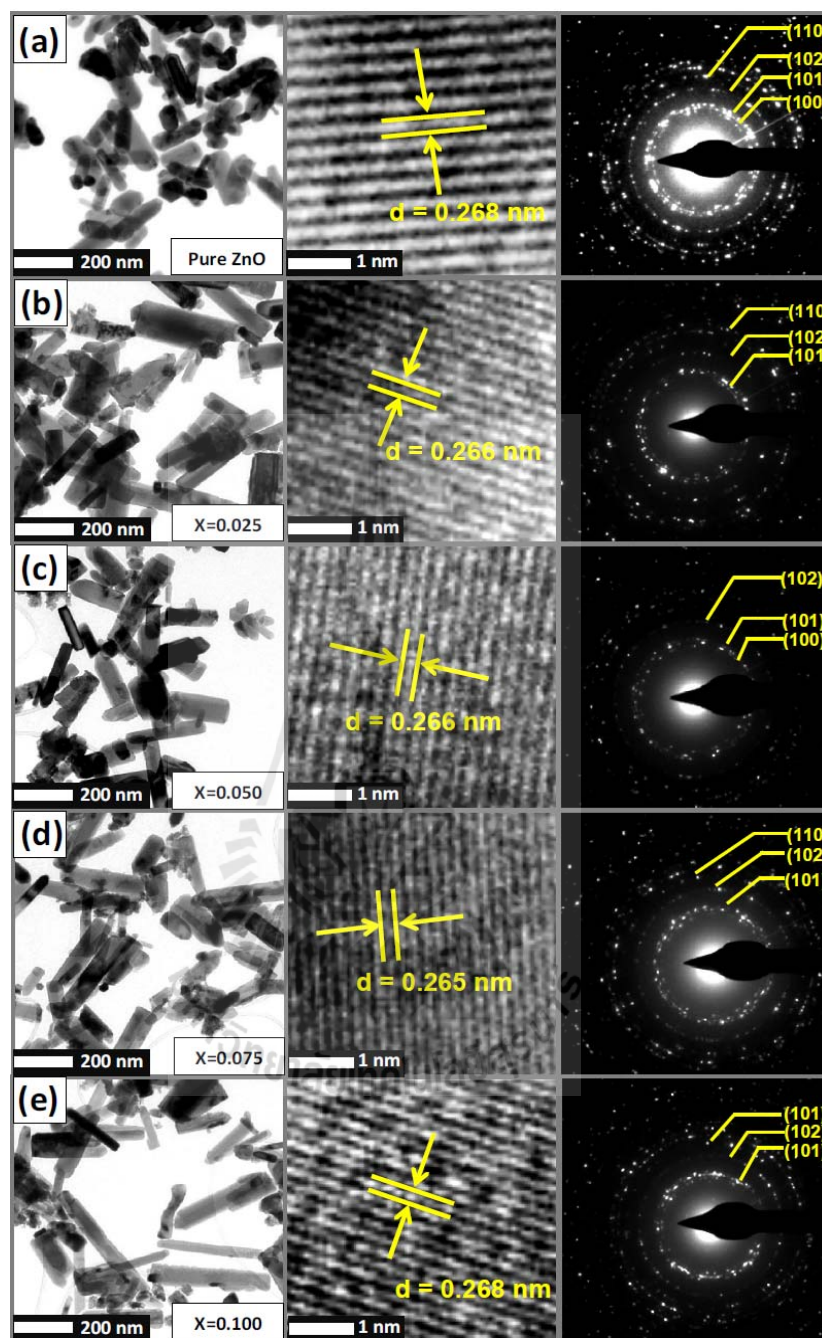


Figure 4.54 TEM bright field, High-resolution TEM (HRTEM) images with corresponding SEAD patterns of undoped ZnO sample prepared in air at 400 °C for 6 h (a) and Er-doped ZnO samples prepared in air at 300 °C for 6 h with $x = 0.025$ (b), $x = 0.050$ (c), $x = 0.075$ (d), and $x = 0.100$ (e).

The chemical compositions of the RE-doped ZnO samples were analyzed by XPS analysis. They are show that all the samples composed with Zn, Tb, Er and O, were confirmed by core-level XPS spectrum as shown in Figure 4.55, demonstrating an increase in actual Tb and Er concentrations with the increase of nominal Tb- and Er-doping in ZnO nanorods that are listed in the Table 4.10.

Table 4.10 Actual atomic concentrations of Zn, Tb, Er and O in undoped ZnO and nominally RE-doped ZnO nanorods calculated by XPS analysis.

Doping level	Atomic percentages (at%) of dopants in RE-doped ZnO samples					
	Tb			Er		
	Zn 2 <i>p</i>	Tb4 <i>d</i>	O 1 <i>s</i>	Zn2 <i>p</i>	Er4 <i>d</i>	O 1 <i>s</i>
x = 0	49.93	-	50.07	49.93	-	50.07
x = 0.025	48.30	1.86	49.84	49.48	1.34	47.18
x = 0.050	49.27	2.45	48.28	48.81	3.80	47.38
x = 0.075	48.24	4.02	47.74	47.21	6.01	46.55
x = 0.100	48.03	6.12	45.85	45.24	8.28	46.48

Furthermore, the atomic percentage ratios of Tb and are also observed. These values are less than the nominal composition in the precursor, evidencing the difference between the actual and the nominal Tb concentration is probably due to the hindering of the dopant incorporation ions in the ZnO systems. Firstly, this may happen because of the difficulties associated with the doping of RE ions into the ZnO host. Firstly, the ionic radii of Tb³⁺ (~ 0.92 Å) and Er³⁺(~ 0.80 Å) are much larger than that of Zn²⁺ion (~ 0.74 Å) and secondly, the substitution creates a charge

imbalance, as Tb^{3+} ions (charge: +3) and Er^{3+} ions (charge: +3) substitute the Zn^{2+} site (charge: +2) in the ZnO host matrix. The charge compensation from the local defect site results in a lattice deformation, which is not desired.

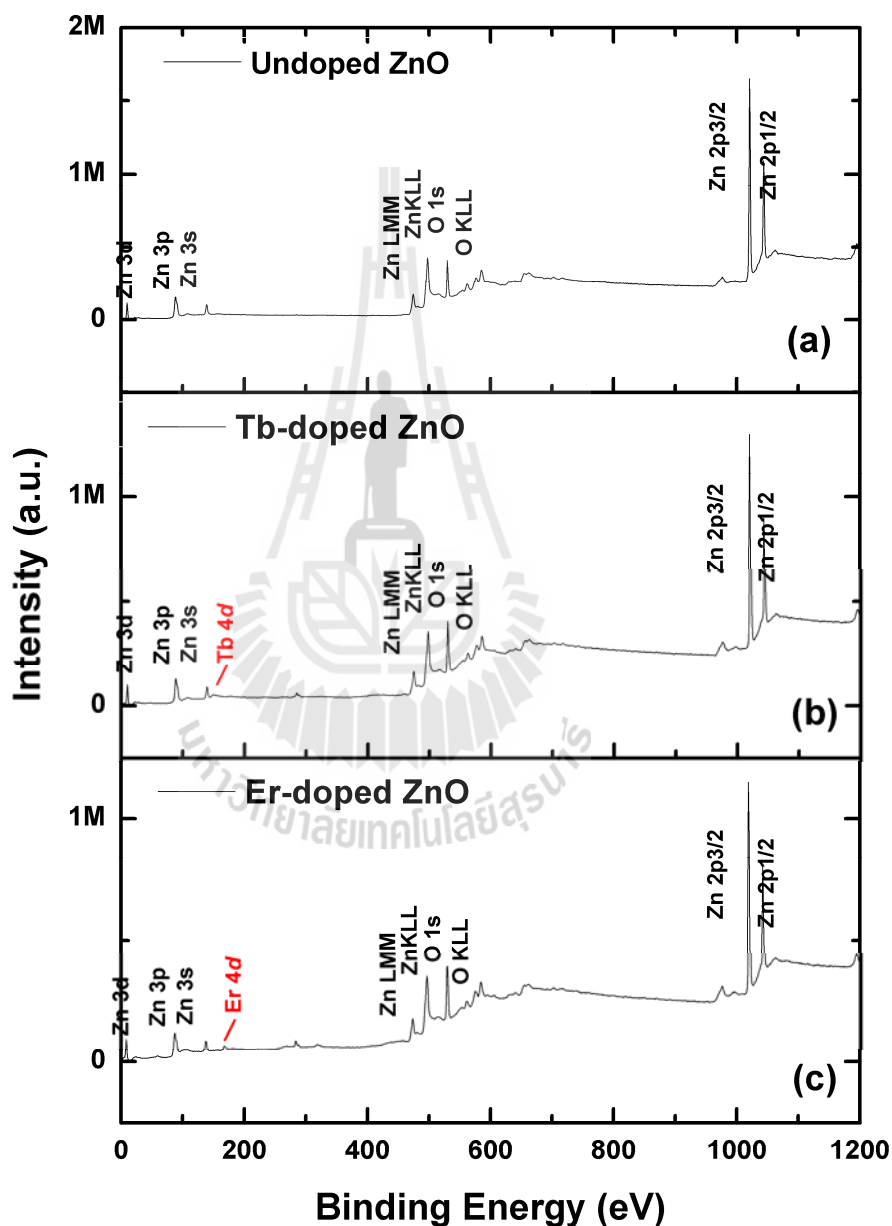


Figure 4.55 (a) XPS spectra of undoped ZnO, (b) Tb-doped ZnO nanorods and (c) Er-doped ZnO nanorods with the survey scan mode.

On the other hand, it was found that the Tb- and Er-doped ZnO nanorods were slightly decrease zinc and oxygen atoms that compared with undoped ZnO, beyond that expected for Zn replacement by Tb and Er. These phenomena induced oxygen vacancy in the ZnO host matrix. The X-ray photoelectron spectroscopy (XPS) was also used to determine the surface composition of Tb-doped ZnO nanorods. All binding energies have been corrected for the charging effect with reference to the C 1s line at 284.6 eV. Figure 4.56 and Figure 4.57 show the Zn 2*p* core level peaks in the XPS spectrum of the undoped ZnO and Tb- and Er-doped ZnO nanorods. These peaks correspond with the position of Zn 2*p* in pure ZnO, and it clearly prove that zinc exists the Zn²⁺ oxidation state with a binding energy of about 1021.45 eV is observed. The typical O 1s in Figure 4.58 and Figure 4.59 can be consistently fitted by two nearly Gaussian curve centers at ~ 530 eV(O₁) and ~ 531.5 eV (O₂). The low binding energy centered at ~ 530.14 eV is corresponding to the coordination of oxygen in Tb-O-Tb and Er-O-Er. The high binding energy located at ~ 531.5 eV is attributed to the coordination of oxygen in Tb-O-Zn and Er-O-Zn (Yang et al., 2005; Jia et al., 2009) which is reduced oxygen vacancy in oxygen deficient region. Moreover, the Core-level XPS result (as shows in Table 4.11 and Table 4.12) can clearly high-resolution spectrum of Tb 4*d* and Er 4*d* peaks evidently shows the peak located at ~ 154eV and ~ 169eV revealing a formation of Tb and Er ions in Tb- and Er-doped ZnO nanorods were incorporated as Tb³⁺ and Er³⁺, respectively. These results are in agreement with the Tb- and Er-doped ZnO nanocrystals reported by previous literature(Fang et al., 2005). The defects of structures affect significantly the magnetic properties by XPS. Further detailed work is required to understand this. Moreover, we found that

the O_2 increases with increasing Tb and Er contents reveals that a number of their oxygen deficient region is very high.

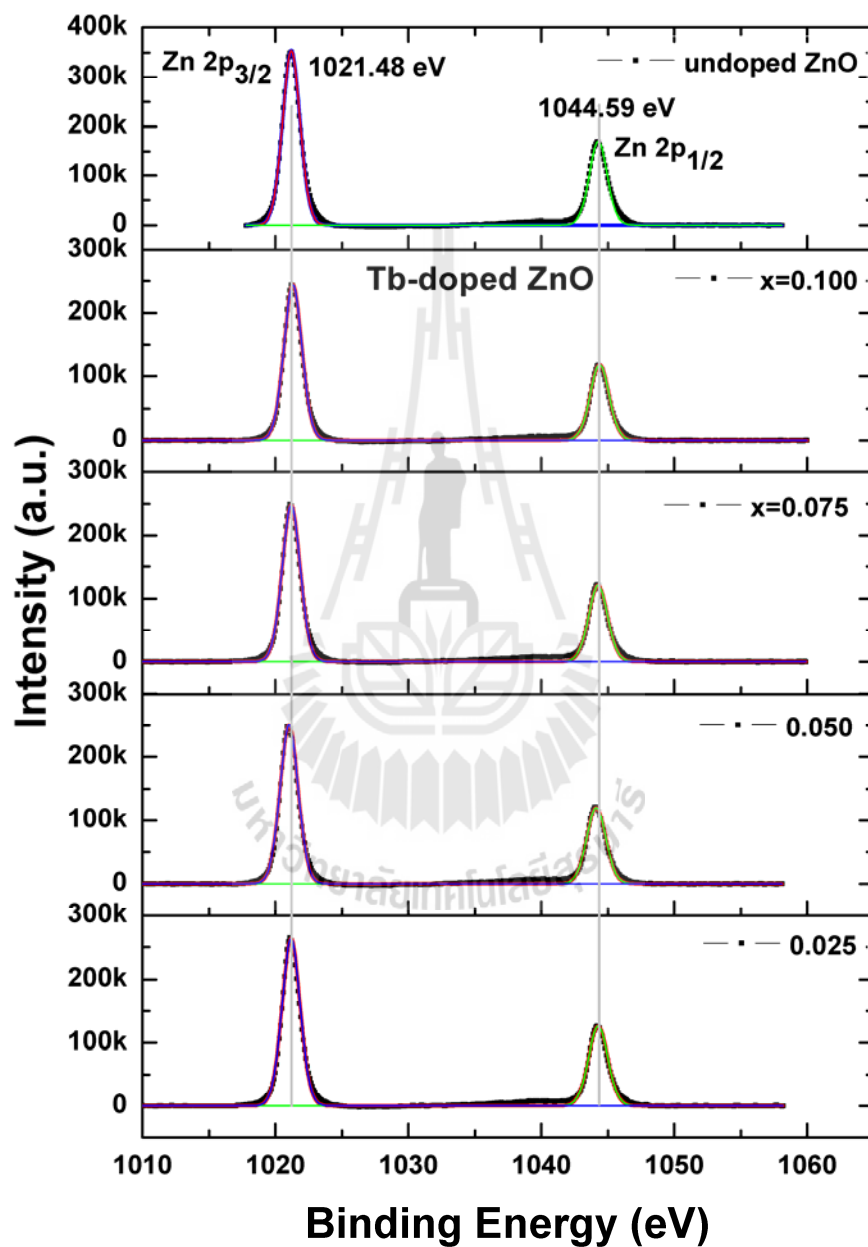


Figure 4.56 Zn2p X-ray photoelectron spectra (XPS) of Tb-doped ZnO samples prepared in air at 300 °C for 6 h with $x = 0.025, 0.050, 0.075$ and 0.100 compared with undoped ZnO.

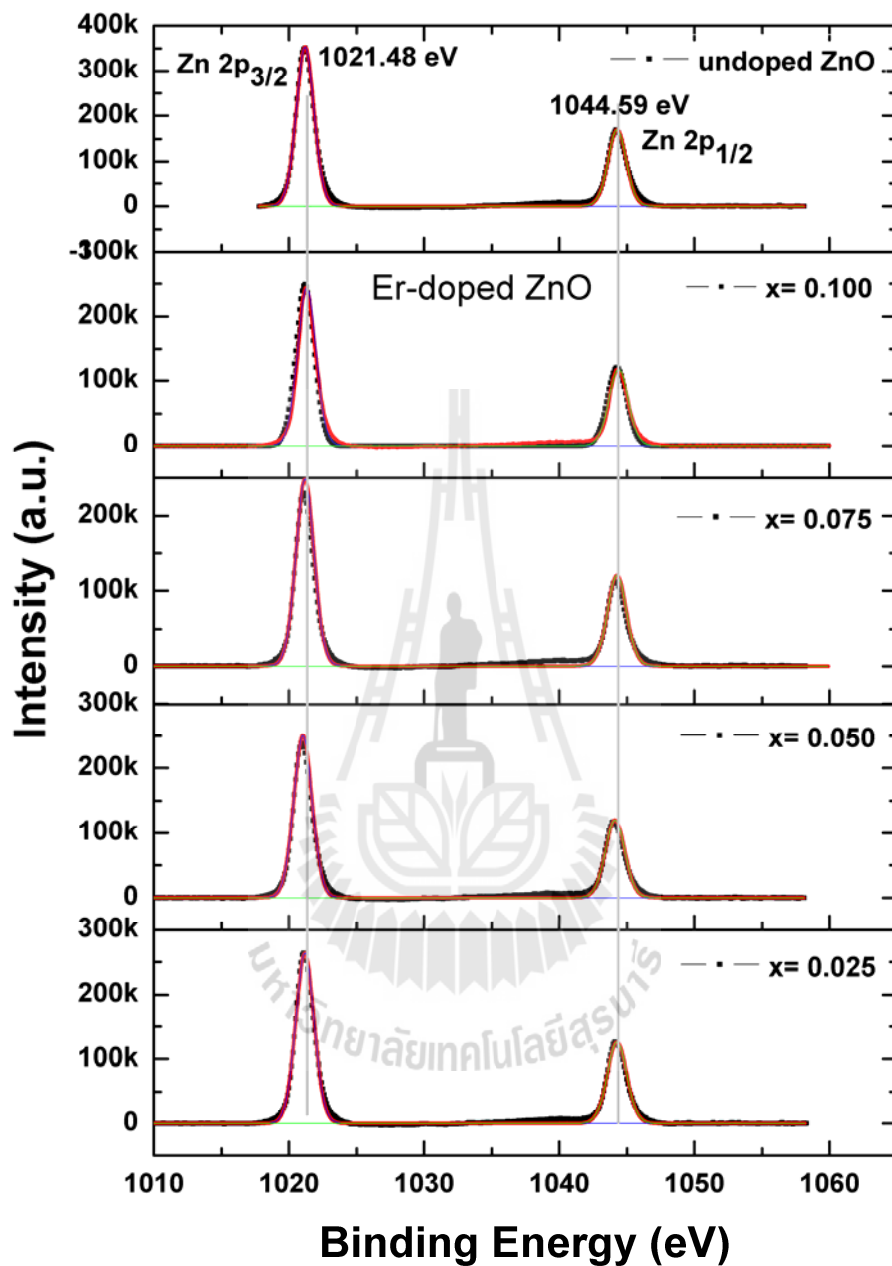


Figure 4.57 Zn2p X-ray photoelectron spectra (XPS) of Er-doped ZnO samples prepared in air at 300 °C for 6 h with $x = 0.025, 0.050, 0.075$ and 0.100 compared with undoped ZnO.

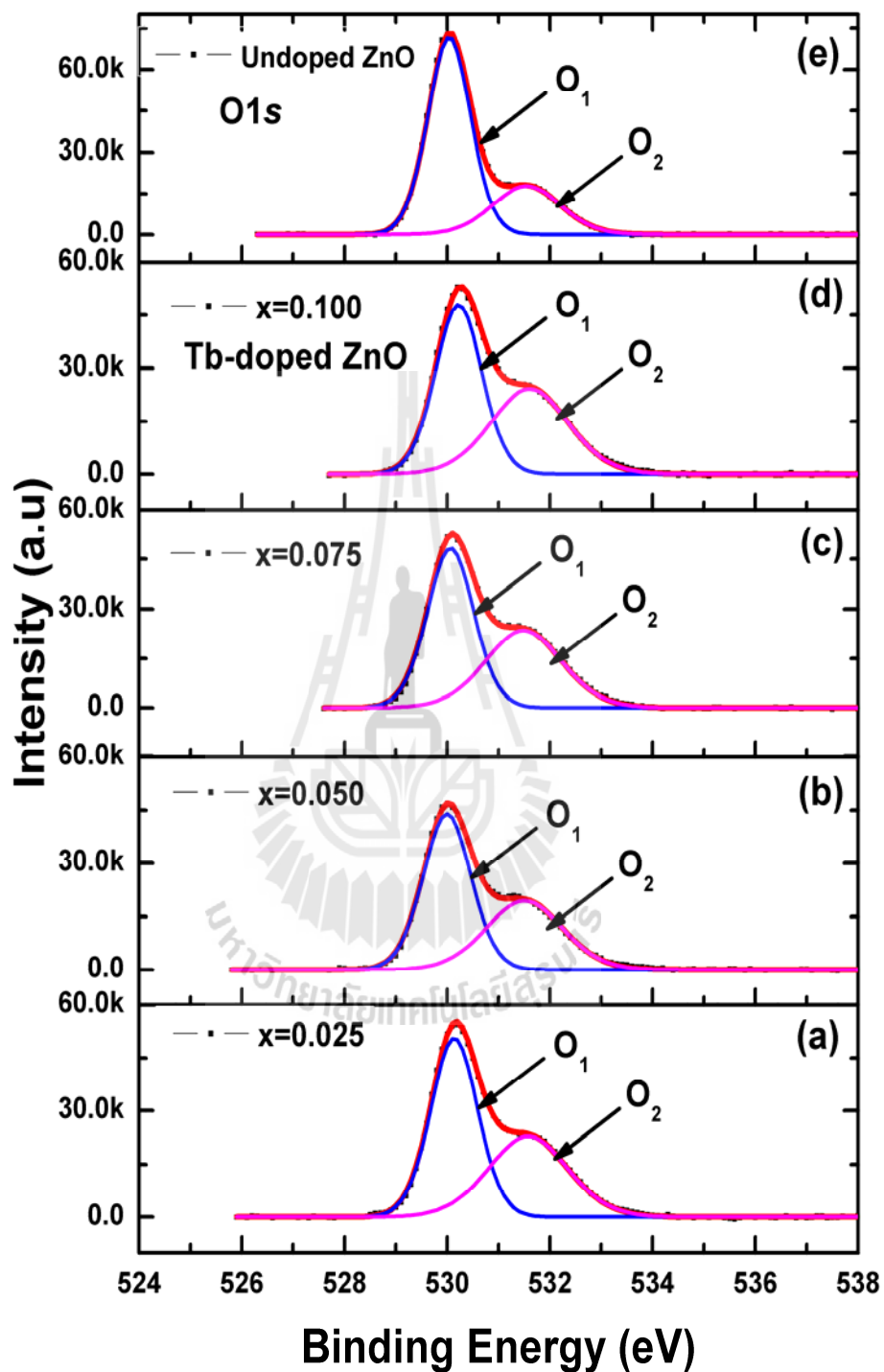


Figure 4.58 High-resolution scan of O1s for Tb-doped ZnO with $x = 0.025$ (a), 0.050 (b), $x = 0.075$ (c) and $x = 0.100$ (d).

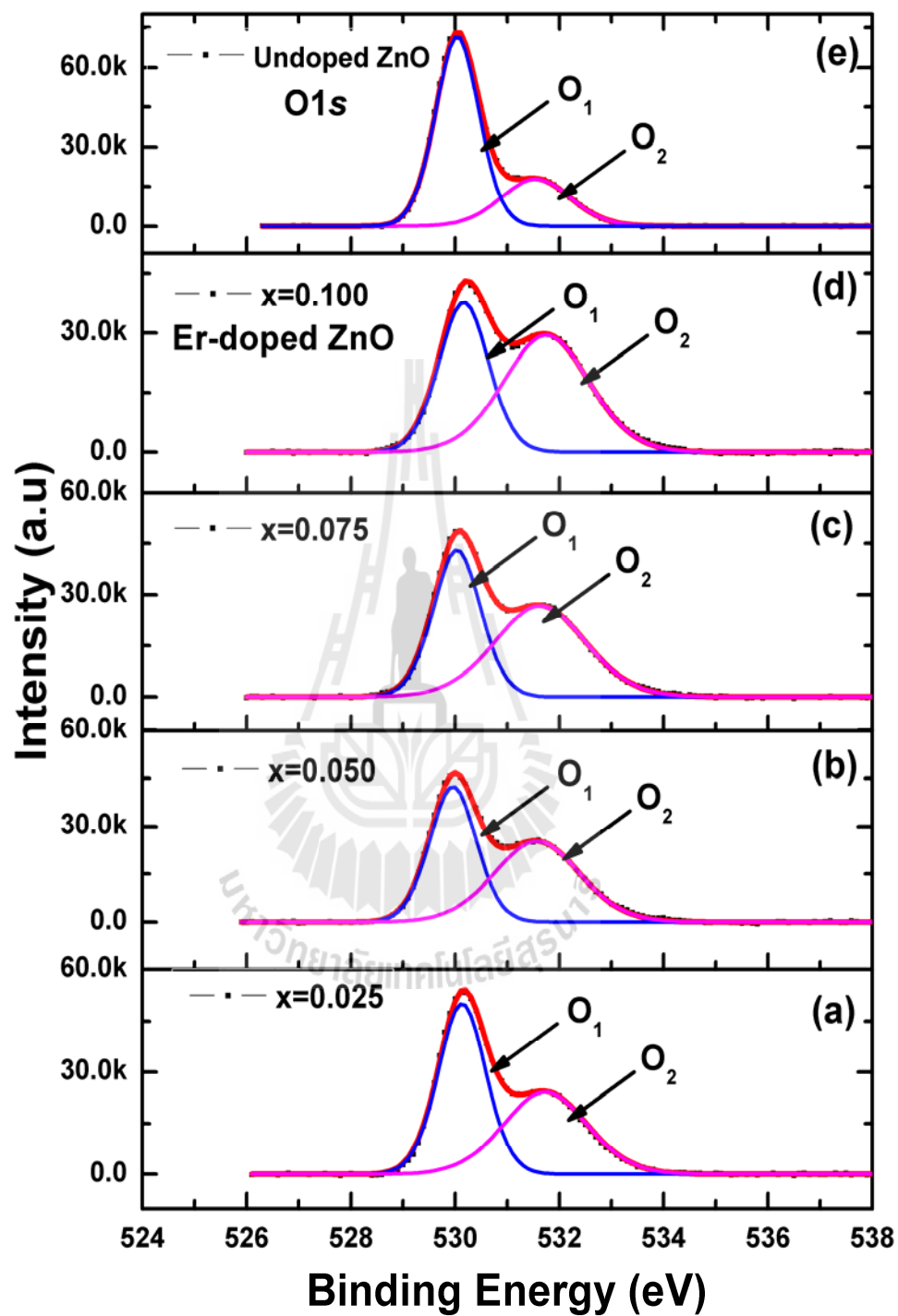


Figure 4.59 High-resolution scan of O1s for Er-doped ZnO with $x = 0.025$ (a), 0.050 (b), $x = 0.075$ (c) and $x = 0.100$ (d).

Table 4.11 The binding energy and atomic percentages of Tb 4*d*, O₁ and O₂ calculated by XPS spectra of undoped ZnO and Tb-doped ZnO nanorods.

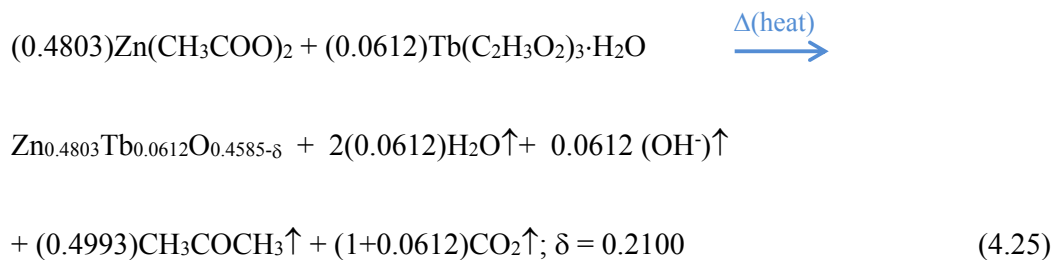
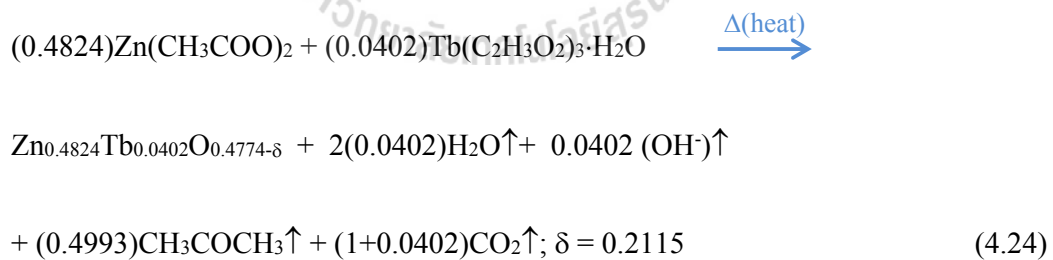
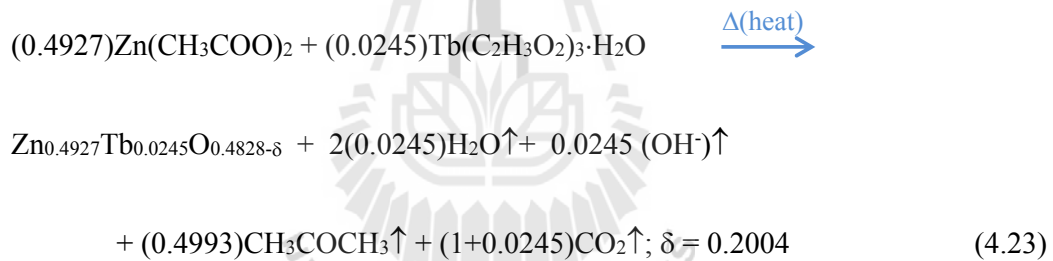
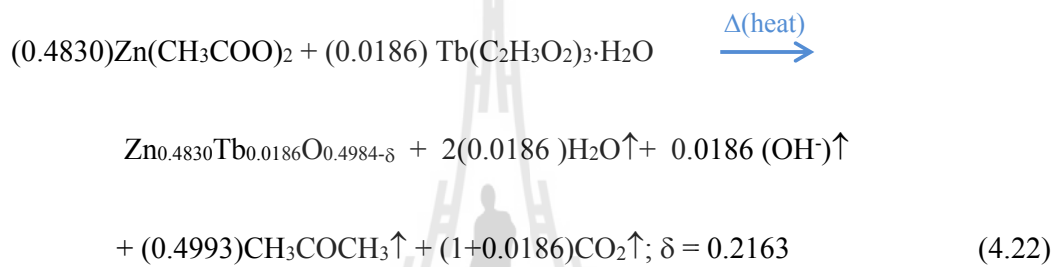
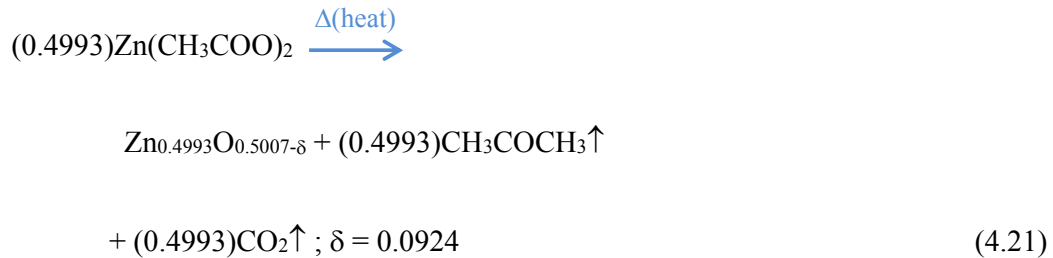
Doping level	BE of Tb ³⁺ (eV)	Atomic percentages (at.%) of Tb ³⁺	BE of O1 <i>s</i>		Atomic percentages (at.%) of O ₁ and O ₂ (eV)	
			O ₁	O ₂	O ₁	O ₂
x = 0	-	-	530.35	531.48	40.83	9.24
x = 0.025	154.97	1.86	530.15	531.52	28.21	21.63
x = 0.050	152.45	2.45	529.97	531.40	28.24	20.04
x = 0.075	153.40	4.02	530.05	531.48	26.59	21.15
x = 0.100	154.84	6.12	530.22	531.58	24.85	21.00

Table 4.12 The binding energy and atomic percentages of Er 4*d*, O₁ and O₂ calculated by XPS spectra of undoped ZnO and Er-doped ZnO nanorods.

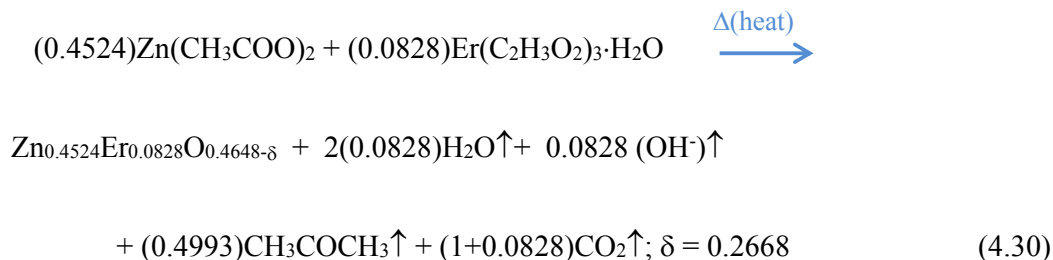
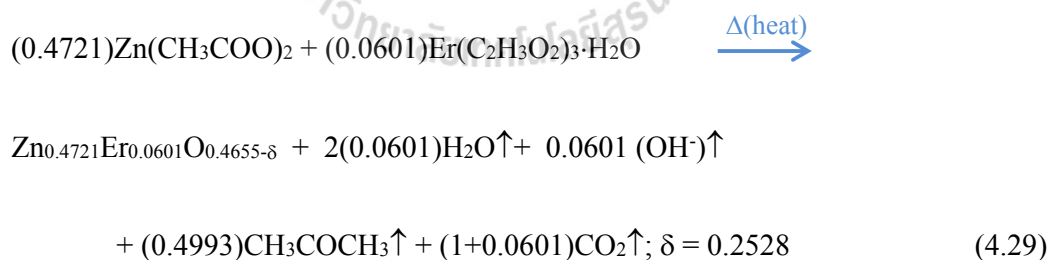
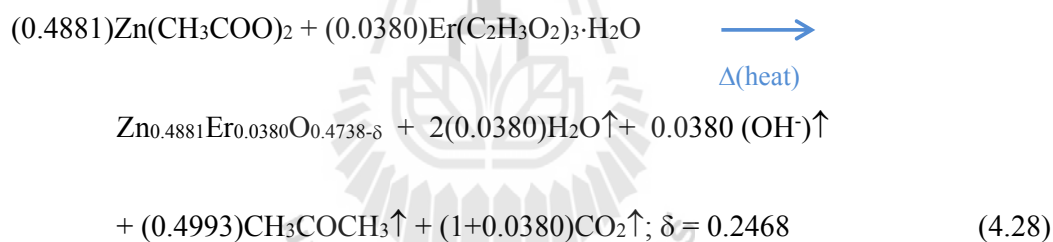
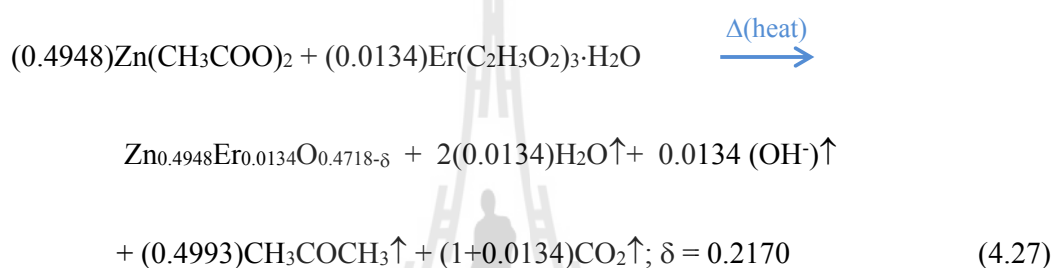
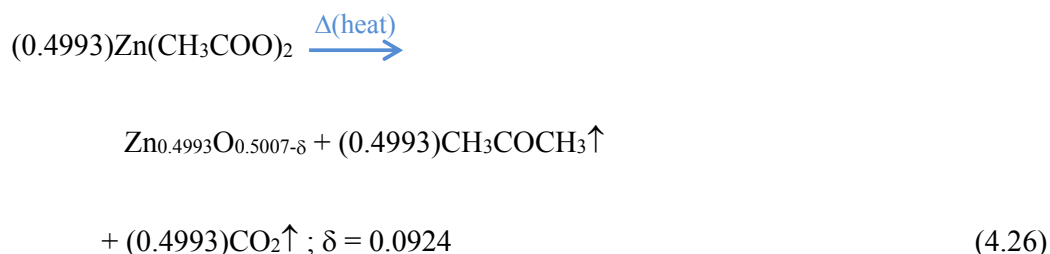
Doping level	BE of Er ³⁺ (eV)	Atomic percentages (at.%) of Er ³⁺	BE of O1 <i>s</i>		Atomic percentages (at.%) of O ₁ and O ₂ (eV)	
			O ₁	O ₂	O ₁	O ₂
x = 0	-	-	530.35	531.48	40.83	9.24
x = 0.025	169.21	1.34	530.12	531.74	25.48	21.70
x = 0.050	169.32	3.80	529.97	531.40	22.70	24.68
x = 0.075	169.62	6.01	530.02	531.63	21.27	25.28
x = 0.100	169.68	8.28	530.16	531.75	19.80	26.68

From the data in Tables 4.10, 4.11 and 4.12, which is calculated by XPS analysis, the formations of RE-doped ZnO nanorods can be explained by the following reactions as given in Equations (4.21) - (4.30), respectively,

For the samples of Tb-doped ZnO with Tb = 0, (x = 0), 0.0186 (x = 0.025), 0.0245 (x = 0.05), 0.0402 (x = 0.075) and 0.0612 (x = 0.100):



For the samples of Er-doped ZnO with Er = 0, (x = 0), 0.0134 (x = 0.025), 0.0380 (x = 0.05), 0.0601 (x = 0.075) and 0.0828 (x = 0.100):



All the process reactions suggest that the thermal events are related to the combustion of acetone (CH_3COCH_3), water (H_2O), Hydroxyl (OH^\cdot), carbon dioxide (CO_2) in the precursors and oxygen vacancy concentration (δ) form on the prepared products.

4.3.2 The absorption and photoluminescence of RE-doped ZnO nanorods (i.e. RE = Tb and Er)

In order to determine the valences of Tb in a direct approach, we performed X-ray absorption near edge spectroscopy (XANES) of Tb L_3 -edge study of our samples. Figure 4.60(a) show XAS curves for Tb-doped ZnO with included reference materials for Tb^{3+} ions, which was $\text{Tb}(\text{C}_2\text{H}_3\text{O}_2)_3 \cdot x\text{H}_2\text{O}$. The position of the color line peak of our sample are close to $\text{Tb}(\text{C}_2\text{H}_3\text{O}_2)_3 \cdot x\text{H}_2\text{O}$ curves, it can be considered that Tb ions in all the ZnO nanorods were incorporated as Tb^{3+} . In addition, XAS were assigned as 8365 eV for the Er L_3 -edge by using the reference $(\text{C}_2\text{H}_3\text{O}_2)_3\text{Er} \cdot x\text{H}_2\text{O}$ powder sample. Figure 4.60(b) shows the XANES at the Er L_3 -edge for the Er-doped ZnO samples and reference $(\text{C}_2\text{H}_3\text{O}_2)_3\text{Er} \cdot x\text{H}_2\text{O}$ powder. In Figure 4.60(b), the principal x-ray absorption peak appearing at the lower energy side of the Er L_3 -edge absorption is assigned as the “white line” with a pronounced peak at the threshold. The position and intensity of the white line is governed by the electron transition from erbium $2p_{2/3}$ to the erbium $4f5d$ final state and is sensitive to the valence state of the absorbing erbium ions as well as their chemical environment (Mao et al., 2008; Wu et al., 2012). These peaks from all of the Er-doped ZnO and reference $(\text{C}_2\text{H}_3\text{O}_2)_3\text{Er} \cdot x\text{H}_2\text{O}$ powder samples have the same shape and position. Therefore, the valence state of Er ions in the doped ZnO nanorods is +3.

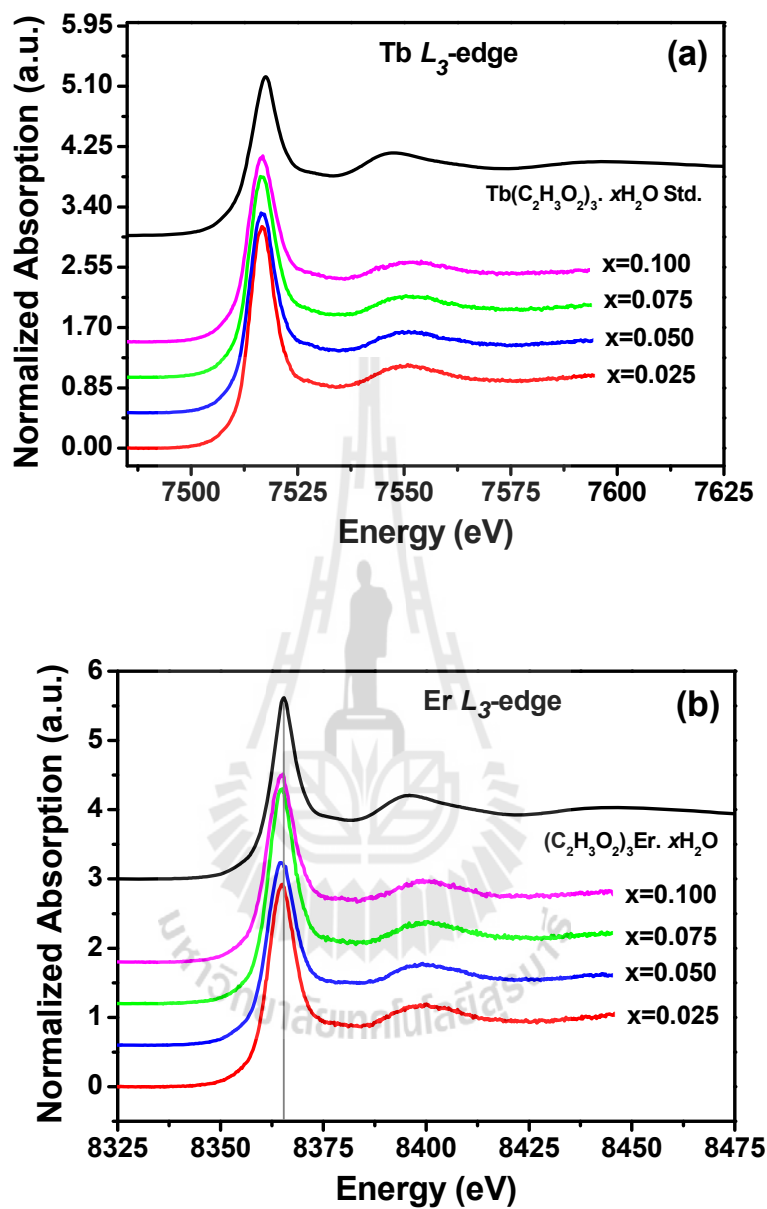


Figure 4.60 (a) Tb L_3 -edge XANES spectra of the Tb-doped ZnO and (b) Er L_3 -edge XANES spectra of Er-doped ZnO as well as of those standard Tb and Er acetates, respectively.

To analyse the optical properties, the UV-visible optical absorption spectrum of the undoped ZnO, Tb- and Er-doped ZnO have been carried out at room temperature using UV- visible spectrometer from 200 nm to 800 nm. The absorption spectra indicate that picture of absorption change and exhibit a continuous blue shift as shown in Figure 4.61, which may be due to the formation of wide band gap by doping. In addition, the optical absorption spectra of the RE-doped ZnO nanorods show just positive trend of the optical band gap for all Tb- and Er-doped ZnO samples except at $x = 0.100$ sample. Moreover, the wide energy band gap was evaluated using the Equation 4.19 (Polat et al., 2011). The direct energy band gap of the Tb- and Er-doped ZnO nanorods can be obtained by plotting $(ah\nu)^2$ versus $h\nu$ and extrapolating the linear portion of the absorption edge to find the intercept with energy axis as shows in Figure 4.62. The energy band gaps of all the Tb- and Er-doped ZnO samples are slightly increases, and then decreases with increasing Tb and Er atom concentrations which are show in Table 4.13 and Figure 4.63. These results are very similar to those of RE-doped nanoparticles reported in literatures (Dai et al., 2013). The variations in energy band gap (E_g) may be described by quantum size effect and electronic structure modifications. Considering the fact that quantum size effect lead to a blue shift of energy band gap, with decreasing particle size down to less than a few nanometers and hence our results are not probable due to this effect, revealing a diameter of ZnO nanostructures are several nanometers. In this case, the energy band gap of all Tb- and Er-doped ZnO samples are found to be higher than the energy band gap (3.180 eV) of undoped ZnO, the most interesting observation here is blue shift of energy band gap of RE-doped ZnO nanorods with increasing the RE atom concentrations. Thus, the noticed slightly blue shift in energy band gap with electronic

structure modifications may be explained by the Burstein–Moss effect. This effect is the phenomenon of which the apparent band gap of a semiconductor is increased as the absorption edge is pushed to higher energies as a result of all states close to the conduction band being populated. This is observed for a degenerate electron distribution and is known as a Burstein–Moss shift (Fang et al., 2005). This effect occurs when the electron carrier concentration exceeds the conduction band edge density of states, which corresponds to degenerate doping in semiconductors. In the doping semiconductors with TM or RE metal ions, the Fermi level lies between the conduction and valence bands. As the doping concentration is increased, electrons populate states within the conduction band which pushes the Fermi level higher in energy and in the case of degenerate level of doping, the Fermi level lies inside the conduction band. In the case of a degenerate semiconductor, an electron from the top of the valence band can only be excited into conduction band above the Fermi level (which now lies in conduction band) since all the states below the Fermi level are occupied states. Pauli's exclusion principle forbids excitation into these occupied states as a result of observation with increasing in the apparent band gap. Apparent band gap = Actual band gap + Moss-Burstein shift (as shown inset of Figure 4.62(a)).

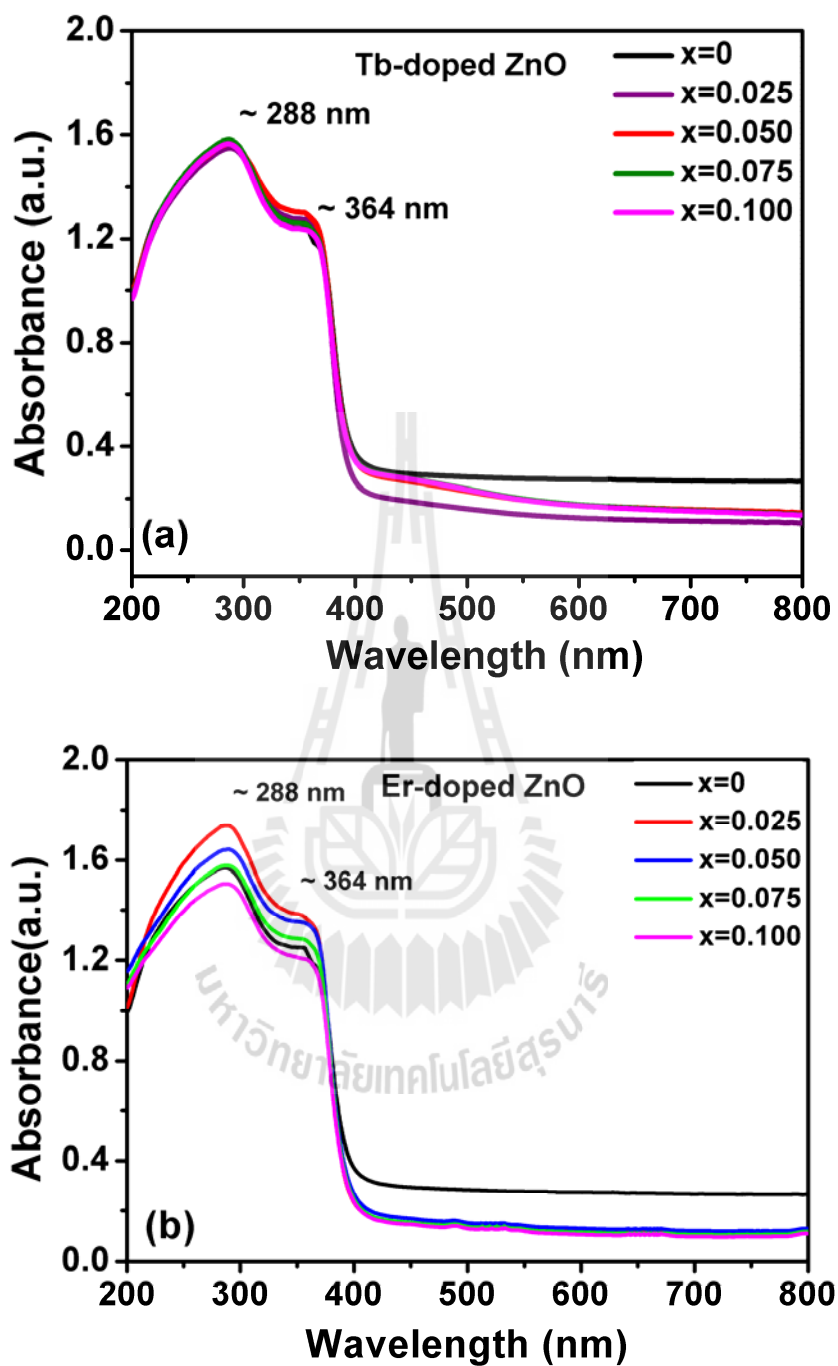


Figure 4.61 Room-temperature optical absorbance spectra of undoped ZnO nanorods calcined at 400 °C for 6 h and RE-doped ZnO nanorods prepared in air at 300 °C for 6 h, (a) Tb-doped ZnO and (b) Er-doped ZnO nanorods, respectively.

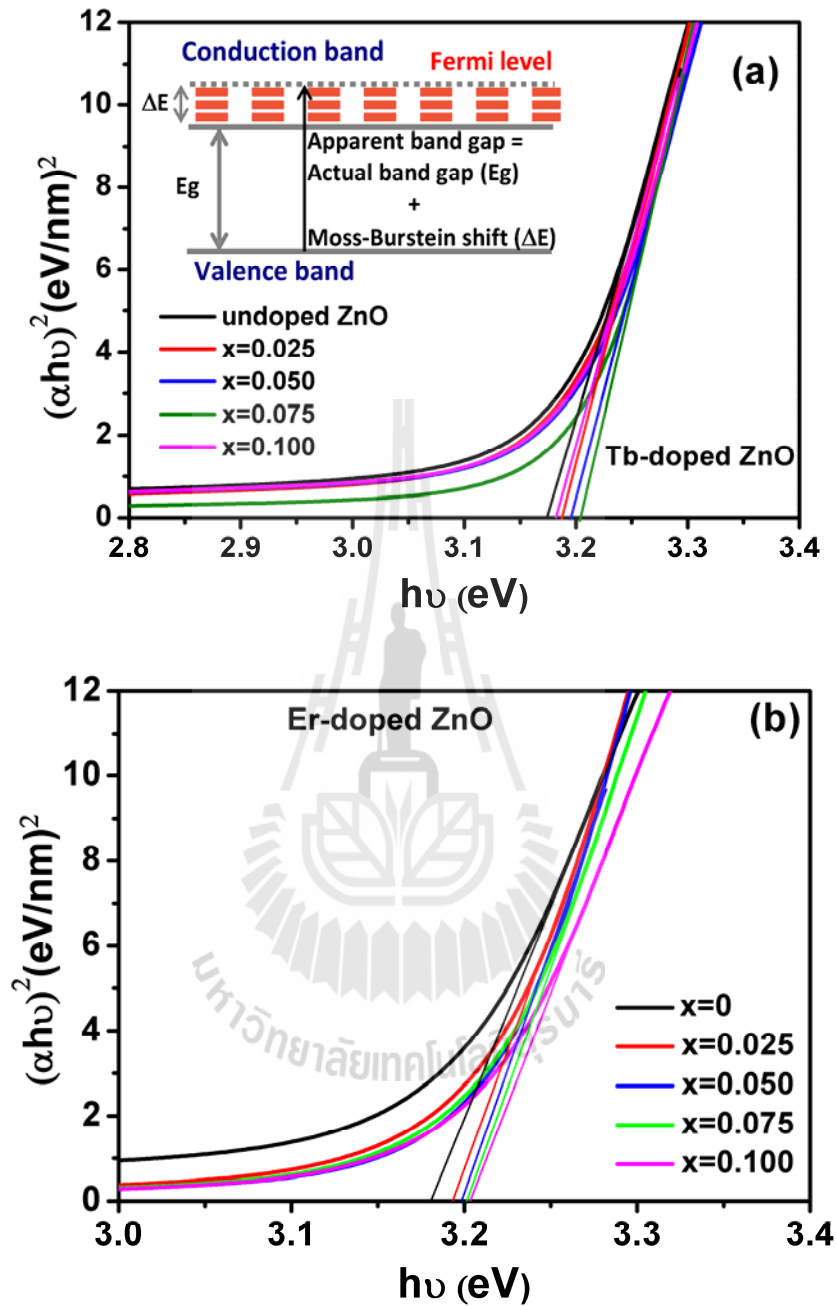


Figure 4.62 Plot of $(\alpha h\nu)^2$ as a function of photon energy ($h\nu$) for undoped ZnO and RE-doped ZnO nanorods, (a) Tb-doped ZnO nanorods and (b) Er-doped ZnO nanorods prepared in air at 300 °C for 6 h, respectively.

Table 4.13 Summary of band gap energy (E_g) of undoped ZnO nanorods and RE-doped ZnO nanorods prepared at 300 °C for 6 h.

Doping Level	E_g (eV) of RE-doped ZnO	
	Tb	Er
x = 0	3.18	3.18
x = 0.025	3.19	3.20
x = 0.050	3.20	3.21
x = 0.075	3.21	3.22
x = 0.100	3.20	3.22

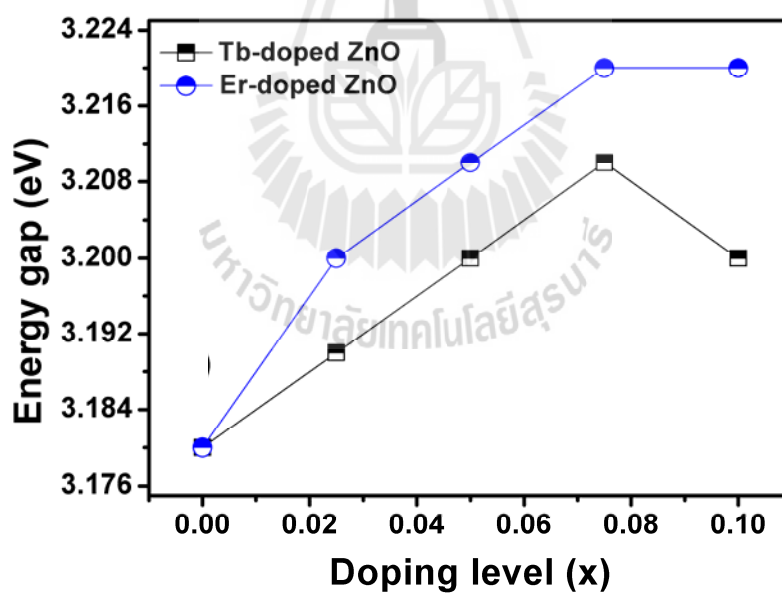
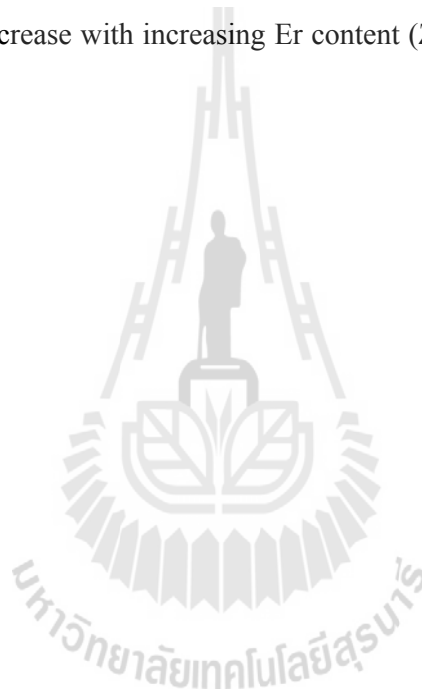


Figure 4.63 Band gap versus doping concentration of undoped ZnO calcined at 400 °C for 6 h of Tb-doped ZnO and Er-doped ZnO nanorods prepared in air at 300 °C for 6 h, respectively.

Generally, the densities of defects and oxygen vacancies affect significantly the optical properties. The room temperature PL results of the undoped ZnO, Tb- and Er-doped ZnO samples are shown in Figure 4.64(a) and Figure 4.64(b) show the PL spectrum of Tb- and Er-doped ZnO with excitation wavelength 328 nm, respectively. It is seen that the band-edge emission spectra of the prepared products sequentially increased with increasing Tb and Er concentrations leveling the band edge intensity depend on the implanted Tb^{3+} and Er^{3+} into Zn site. These results are similar to those of RE-doped ZnO films reported by Masamoto et al. (2011). In addition, the spectra of all the samples mainly consist of four emission bands including a strong UV emission band at ~ 396 nm, corresponding to the near band edge emission, which is attributed to the recombination of free excited ions, a weak blue band at ~ 431 nm are caused by the transition between the vacancy of oxygen and interstitial oxygen. Normally, the additional emission peaks at about 488 nm correspond to transition of Tb^{3+} from 5D_4 to 7F_6 and the weak peak around 544 nm which is associated with the $^5D_4 \rightarrow ^7F_5$ transitions, respectively. The PL part of the diagram ZnO host to rare earth ion energy transfer can be seen inset the Figure 4.64(a). When ZnO was excited, electron jumps from the valence band to the conduction band. Since the 5D_3 and 5D_4 energy level of Tb^{3+} ion are just below the conduction band of ZnO, energy transfer takes place between ZnO and Tb^{3+} , and excitation of ZnO results in the co-luminescence of ZnO and Tb^{3+} (Cetin et al., 2007; Masamoto et al., 2011). In the case of Er-doped ZnO, the PL spectrum exhibits strong near-band-edge emission at 381 nm- 394 nm and also broad emission peak at 381 nm, 394 nm and 478 nm are observed. However, Er-doping are not show peak related to Er emissions on our samples. There is no shifting in the defects related peaks observed in PL spectra and the intensity of the emission

peaks gets quenched with Er-doping, which are consistent with earlier report (Lotey et al., 2013). The mismatch between the ionic radii of Zn and Er results in more number of oxygen vacancy defects in the host ZnO. Depending upon the number of trapped electron, these oxygen vacancy act radiative (*F*-center) which may trap the photo-excited electrons which get strongly localized in oxygen vacancy, thereby decreasing the availability of electrons for recombination with the hole, and consequently the emission intensity decrease with increasing Er content (Zou et al., 2012) as shown in Figure 4.64(b).



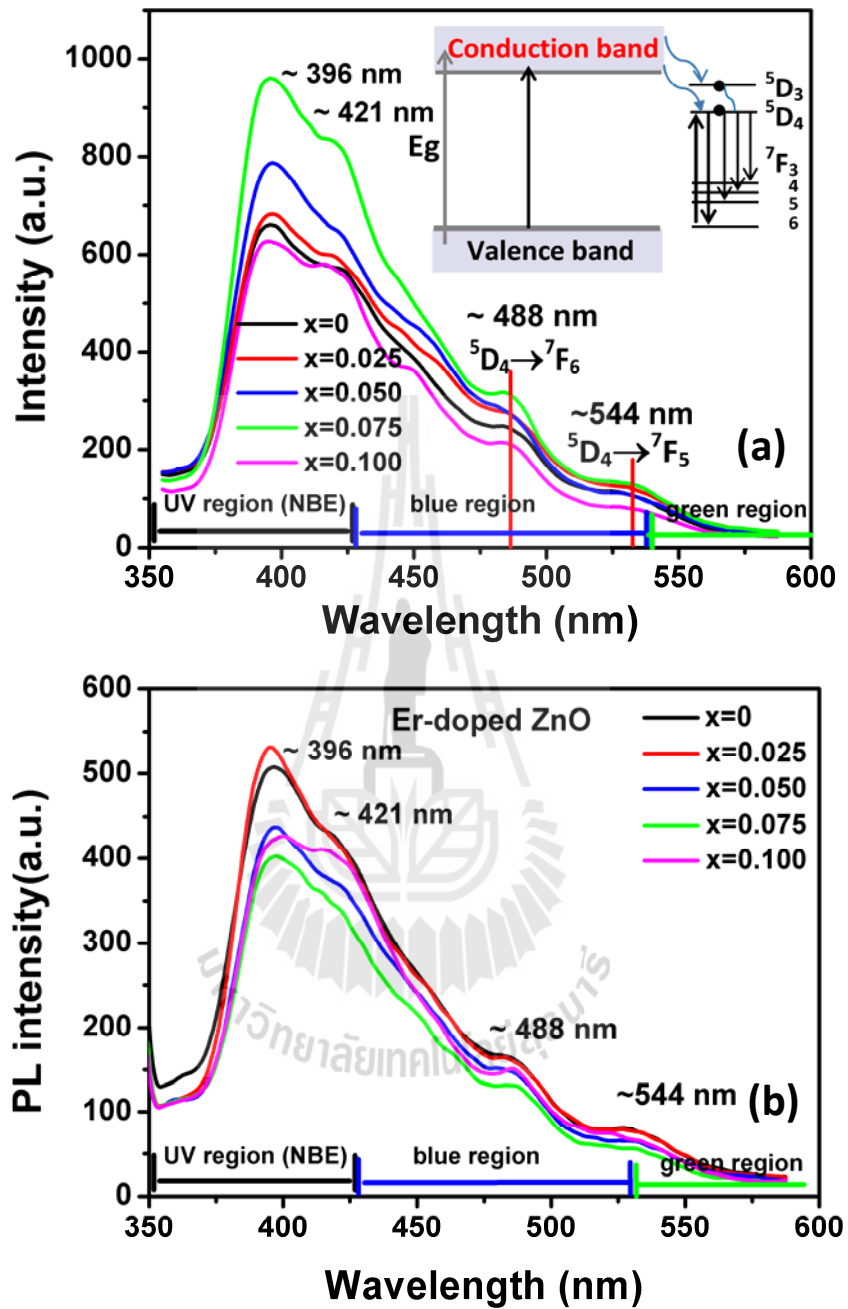


Figure 4.64 Room temperature photoluminescence spectra of undoped ZnO and RE-doped ZnO nanorods, (a) Tb-doped ZnO nanorods (Inset shows schematically emission process) and (b) Er-doped ZnO nanorods under 325 nm light excitation.

4.3.3 The magnetic properties of magnetic ions in Tb- and Er-doped ZnO nanorods.

In this section, the magnetic properties have been interpreted in the ZnO nanorods through Tb- and Er-doping. The magnetization magnetic measurement (M) versus applied magnetic field (H) were performed on undoped ZnO and Tb-doped ZnO nanorods at 293 K, Figure 4.65 shows magnetization versus magnetic field (M - H) curves of thermally decomposed at 400 °C for 6 h for undoped ZnO sample and at 300 °C for 6 h of Er- and Tb-doped ZnO nanorods (i.e. $x = 0.025, 0.050, 0.075$ and 0.100). The specific magnetization curves showed a diamagnetic behavior for undoped ZnO. All samples observed that the increasing of x value enhanced the para/antiferromagnetic contribution, whereas ferromagnetic ordering for Tb-doped ZnO nanorods of $x = 0.025$ was clearly observed at room temperature (as shown in inset of Figure 4.65(a)). These results are in agreement with the previous reports in which they are increased the x values in Eu^{3+} -doped ZnO films and Tb-doped ZnO nanoparticles (Zhong et al., 2007; Bandyopadhyay et al., 2012)

In order to emphasize the magnetic contribution on Tb-doped ZnO nanorods with $x = 0.025$ at 50 K and 293 K, the experimental $M \times H$ curve were performed as shown in Figure 4.66(a). The magnetization slight increase with decreasing temperature revealing Tb-doped ZnO nanorods exhibit RT-FM with a T_c at below room temperature. Calculated values of the coercive field (H_c) and the remanent magnetization (M_r) for Tb-doped ZnO nanorods ($x = 0.025$) at 50 K and 293 K (inset of Figure 4.66(a)) found to be 56.42 (Oe), 0.0036 (emu/g) and 44.68 (Oe), 0.0025 (emu/g) respectively. These results are in agreement with the previous reports in Tb-doped ZnO nanocrystalline films (Bandyopadhyay et al., 2012), whereas Er-doped

ZnO nanorods presented paramagnetism both at 293 K and 50 K for the sample of $x = 0.100$ as shown in Figure 4.66(b).

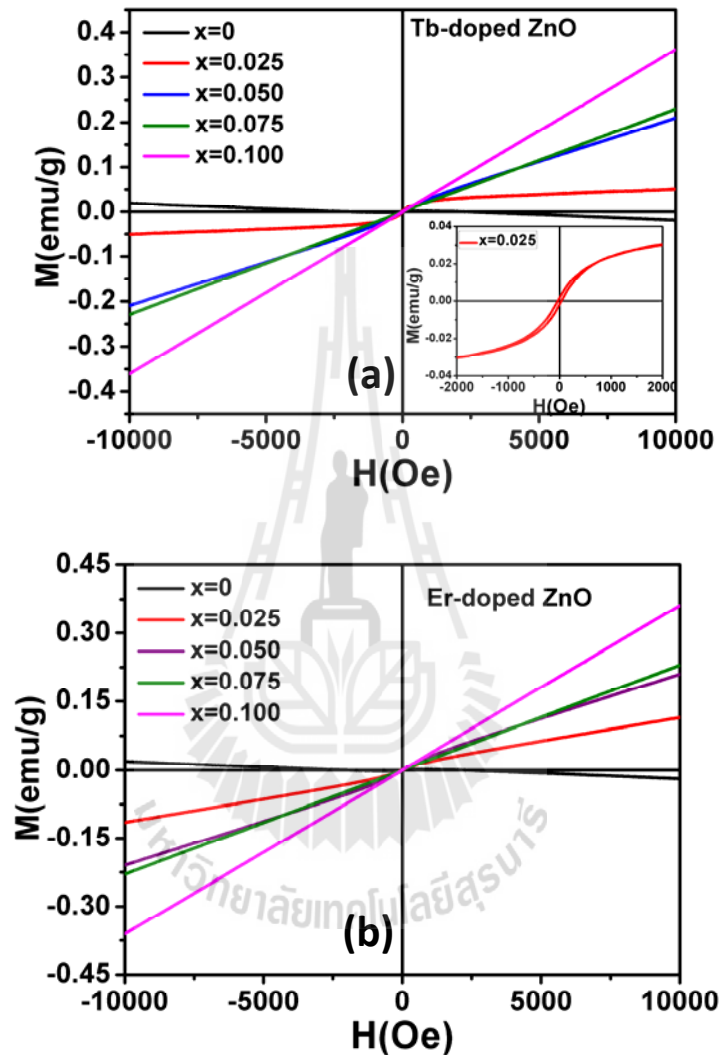


Figure 4.65 The magnetization magnetic measurements (M) versus applied magnetic field (H) were performed on undoped ZnO, (a) Tb-doped and (b) Er-doped ZnO nanorods with different the rare-earth metal content obtained at 293 K from VSM measurement.

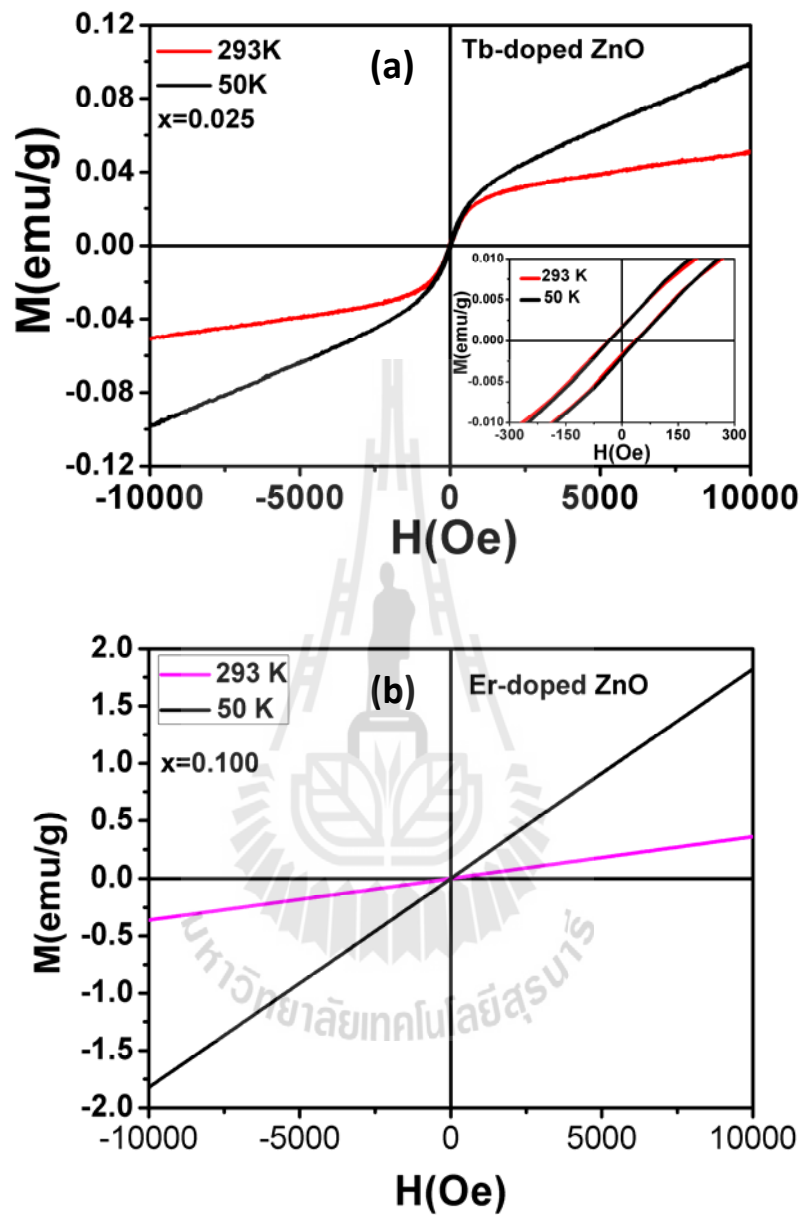


Figure 4.66 $M \times H$ curves for $Zn_{0.975}Tb_{0.025}O$ and $Zn_{0.900}Er_{0.100}O$ samples taken at $T = 50$ K and 293 K, showing the existence of ferromagnetism and paramagnetism respectively.

There are several groups in literature reported that the doping with a few percent of a magnetic $3d$ cation (Co, Mn, etc.), the magnetism appears well below the solubility limit of cations, cannot be understood in terms of the conventional theory of magnetism in insulators; nor can a carrier-mediated ferromagnetic exchange mechanism account for the magnitude of the Curie temperatures, which are well in excess of 400 K (Wu et al., 2013). The phenomenon is observed in thin films and nanocrystals, but not in well-crystallized bulk material. In particular, the calculations of Dietl et al. (2000) showed that Mn-doped ZnO would exhibit ferromagnetism above room temperature (Dietl et al., 2000). Sato et al. (2000) have also investigated ferromagnetism of ZnO-based DMS by *ab initio* electronic structure calculations based on the local spin density approximation and they reported ferromagnetic ordering of $3d$ transition metal ions in ZnO. These theoretical predictions initiated a number of experimental studies of TM-doped ZnO (Sato et al., 2000; Dai et al., 2013). In addition, the discovery of room temperature ferromagnetism in Co-doped anatase TiO₂ has also generated much interest in the Co-doped TiO₂ system as a potential oxide-based DMSs (Matsumoto et al., 2001). However, the origin of ferromagnetism in DMOs systems is not well understood yet. Thus, several models of FM have been proposed for these DMOs, including a new exchange mechanism involving donor electrons in an impurity (Coey et al., 2005), the carrier (electron) mediated exchange mechanism (Ueda et al., 2001), superexchange or double exchange interaction and a defect mediated mechanism like Bound Magnetic Polaron model (BMP) (Coey, 2006). In addition to the magnetic doping effect, oxygen vacancies have been proposed to play an important role in the magnetic origin for DMOs (*F*-center exchange interaction), leading to be the exchange interactions

between localized electron spin moments. Nevertheless, the main unresolved question is whether the observed ferromagnetism originates from uniformly distributed TM ions in the host matrix or whether it is due to the precipitation of secondary phases such as metallic clusters. If a DMS contains TM ions below their equilibrium solubility limit no secondary phases are expected. In this case, since the strength of magnetism is proportional to the number of TM ions substituted on the cation sites in a DMS, the realization of high T_C ferromagnetism is difficult. On the other hand, at higher TM dopant concentrations doped transition metals start to form unwanted metallic clusters. For this reason, to achieve a high T_C ferromagnetism in a single phase DMS, non-equilibrium sample preparation techniques such as low temperature thermal cleaning method for Si molecular beam epitaxy (MBE) and ion implantation are required. Ion implantation is widely used in silicon technology for integrated circuits due to its reliability, precision and reproducibility. It has also proven to be a reliable method for injecting transition metals into a host semiconductor material beyond their solubility limits (Zhou et al., 2008). In the present case, since the XRD studies did not show any evidence for the presence of secondary phases, the origin of ferromagnetism can be intrinsic or because of defects. However, the presence of secondary phases in very small quantities cannot be ruled out if the amount present is less than the detection limit of XRD. In case of R-ion, the $4f$ shell is well protecting by $5d$ and $4s$ shell, whereas the $3d$ electrons are exposed to free neighboring ions in the lattice. Xiyang et al. (2012) report that the moment of the rare earth metals originates from the $4f$ electrons and screened by the outer shell $5s^2p^6d^{10}6s^2$ electrons (for the case of Gd ions). Two neighboring rare earth metals ions are unable to exchange couple directly or interact via superexchange interaction because the space

between two neighboring Gd-ions is too large (up to 3×10^{-10} m). Such a colossal moment may result from a very effective Runderman-Kittel-Yosida (RKKY) exchange interaction. The RKKY couple is an indirect exchange interaction via the *s* conduction electrons, which results in high total magnetic moments per Gd. Since the *4f* electrons in the Gd-ion are completely localized and the *6s* electrons can move feely as conduction electrons. The *f* and *s* electrons can give rise to an exchange couple, which leads to a polarization of the *s* electron. The spin of the polarized *s* electrons can influence the spin direction of the *f* electrons. As a result, the electrons play a role in which the localized *4f* of the neighboring Gd-ions. These differences between *3d* and *4f* electrons may facilitate in the onset of exchange interactions among the electrons in the *3d* ion-doped system compared to that of R^{3+} -doped ZnO. In the case of Tb- and Er-doped ZnO nanorods, it has been shown that both ferromagnetism and para/antiferromagnetism at room temperature can be obtained by slightly modifying the synthesis conditions where ferromagnetism was found to be due to the absence of impurity phases (Duan et al., 2011). It is possible that the observed ferromagnetic and para/antimagnetic behavior are possibly due to the exchange interaction between local spin-polarized electrons (such as the electrons of Tb^{3+} and Er^{3+} ions) and conduction electrons. The conduction electrons are regarded as a media to interact among the Tb^{3+} and Er^{3+} ions. This interaction leads to the spin polarization of conduction electrons. Subsequently, the spin-polarized conduction electrons perform an exchange interaction is short range and oscillating nature based on the concentration of Tb, Er and its nearest neighbor distance. This may be the plausible explanation of the observed para/antiferromagnetic interaction. Similar phenomena have been observed and reported in previous studies for Er and

Tb-doped ZnO nanocrystalline sample (Deka et al., 2007; Yang et al., 2007). However, very few studies on the synthesis and magnetic properties of nanocrystalline Tb- and Er- doped ZnO DMSs have been reported.

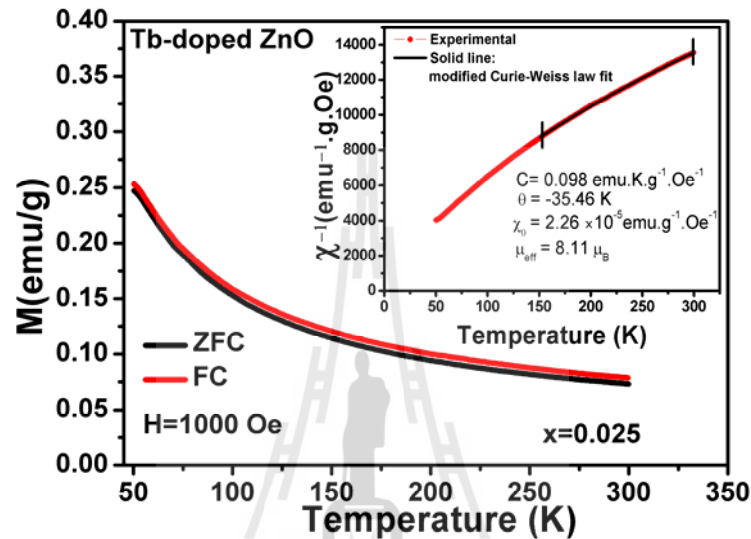
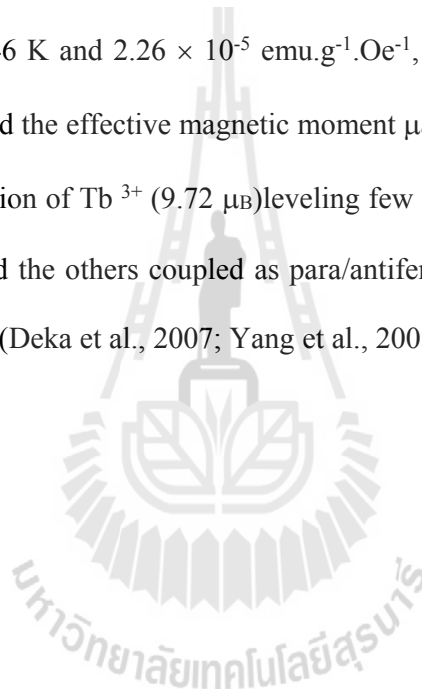


Figure 4.67 display the temperature-dependent magnetization (M - T) curves of Tb-doped ZnO nanorods with $x = 0.025$ was studied in field of 1 kOe. Inset: the modified curie - weiss fitting to the data between 150 K and 293 K under 1 kOe as a function of temperature and fitting result using the modified Curie-weiss law.

Figure 4.67 display the temperature-dependent magnetization (M - T) curves of Tb-doped ZnO nanorods with $x = 0.025$ was studied in field of 1 kOe. The result shows a similar nature in the zero field cooled (ZFC) and field cooled (FC) measurement. The ZFC and FC curves did not show any blocking temperature, which indicates that no bulk ferromagnetism exists in this sample. Moreover, it is no obvious differences in T - M curves between it and also the samples doped with $x = 0.050$,

0.075 and 0.100 consistent with Tb-doped ZnO of $x = 0.025$ sample but are not show here. The effect of antiferromagnetic behavior could be described using the modified Curie-weiss equation (Peleckis, Wang and Duo., 2006) $\chi^{-1} = (C/(T-\theta) + \chi_0)^{-1}$ where C is Curie constant, θ is Curie temperature and χ_0 is the temperature independent part. The linear fits were done in temperature range of 150 – 293 K by solid line as shown in the inset of Figure 4.67. As a result, the value of C , θ and χ_0 are 0.098 emu.K.g⁻¹.Oe⁻¹, -35.46 K and 2.26×10^{-5} emu.g⁻¹.Oe⁻¹, respectively. From the Curie constant we calculated the effective magnetic moment $\mu_{\text{eff}} = 8.11 \mu_B$, These values are smaller than the free ion of Tb³⁺ (9.72 μ_B)leveling few amount of Tb ions coupled as ferromagnetically and the others coupled as para/antiferromagnetically due to RKKY exchange interaction (Deka et al., 2007; Yang et al., 2007).



REFERENCES



REFERENCES

- Anderson, P. W. (1950). Antiferromagnetism: Theory of Superexchange Interaction. **Physical Review**. 79: 350-356.
- Anane, A., Dupas, C., Dang, K. L., Renard, J. P., Veillet, P., Guevara Leon de, A. M., Millot, F., Pinsard, L., and Revcolevschi, A. (1995). Transport properties and magnetic behaviour of $\text{La}_{1-x}\text{Sr}_x\text{MnO}_3$ single crystals. **Journal of Physics: Condensed Matter**. 7(35): 7015.
- Akdogan, N., Nefedov, A., Westphalen, A., Zabel, H., Khaibullin, R. I., and Tagirov, L. R. (2007). Dose dependence of magnetism in Co-doped TiO_2 . **Superlattices and Microstructures**. 41: 132-137.
- Awschalom, D. D., and Flatte, M. E. (2007). Challenges for semiconductor spintronics. **Nature Physics**. 3: 153
- Baibich, M. N., Broto, J. M., Fert, A., Nguyen van, D. F., Petroff, F., Etienne, P., Creuzet, G., Friederich, A., and Chazelas, J. (1988). Giant magneto resistance of (001) Fe/(001) Cr magnetic superlattices. **Physical Review Letters**. 61: 2472.
- Binasch, G., Grünberg, P., Saurenbach, F., and Zinn, W. (1989). Enhanced magneto resistance in layered magnetic structures with antiferromagnetic interlayer exchange. **Physics Review B**. 39: 4828.
- Berciu, M., and Bhatt, R. N. (2001). Effects of disorder on ferromagnetism in diluted magnetic semiconductors. **Physics Review Letters**. 87: 107203.
- Bettina, B., Deanna, M. D., David, M., Jenkins, Anthony, T. I., Starla, D. G., Clifford P. K., and Jeffrey, R. L. (2010). High-spin ground states via electron

- delocalization in mixed-valence imidazolate-bridged divanadium complexes. **Nature Chemistry**. 2(5): 362-368.
- Coey, J. M. D., Douvalis, A. P., Fitzgerald, C. B., and Venkatesan, M. (2004). Ferromagnetism in Fe-doped SnO₂ thin films. **Applied Physics Letters**. 84: 1332-4.
- Coey, J. M. D. (2005). High-temperature ferromagnetism in dilute magnetic oxides. **Journal of Applied Physics**. 97: 10D313.
- Coey, J. M. D., Venkateshan, M., and Fitzgerald, C. B. (2005). Donor impurity band exchange in dilute ferromagnetic oxides. **Nature Materials**. 4: 173-179.
- Coey, J. M. D. (2006). Dilute magnetic oxides. **Current Opinion in Solid State and Materials Science**. 10: 83.
- Cheng, C., Xu, G., Zhang, H., and Luo, Y. (2008). Hydrothermal synthesis Ni-doped ZnO nanorods with room-temperature ferromagnetism. **Materials Letters**. 62: 1617-1620.
- Chen, Y., and Xu, X. L. (2011). Effect of oxygen deficiency on optical band gap shift in Er-doped ZnO thin films, **Physica B**. 40: 63121.
- Dietl, T., Ohno, H., Matsukura, F., Cibert, J., and Ferrand, D. (2000). Zener model description of ferromagnetism in Zinc-Blende magnetic semiconductors. **Science**. 287: 1019-1022.
- Dietl, T., Matsukura, F., and Ohno, H. (2002). Ferromagnetism of magnetic semiconductors: Zhang-Rice limit. **Physical Review B**. 66: 033203(4).
- Daniel A. A. S., and Marcelo A. M. (2012). Study of the magnetic and structural properties of Mn-, Fe-, and Co-doped ZnO powder. **Physica B**. 407: 3229-3232.

- Dai, J., Meng, C., and Li, Q. (2013). First-principles study on the magnetism of Mn and Co codoped ZnO. **Physica B**. 409: 5-9.
- El-Hilo, M., Dakhel, A. A., and Ali-Mohamed, A. Y. (2009). Room temperature ferromagnetism in nanocrystalline Ni-doped ZnO Synthesized by co-precipitation. **Journal of Magnetism and Magnetic Materials**. 321: 2279-2283.
- Fierro, J. L. G. (2006). Metal Oxides: **Chemistry and Applications**. CRC Press. p. 182.
- Genes de, P. G. (1960). Effects of Double Exchange in Magnetic Crystals. **Physical Review**. 118(1): 141.
- Gutowski, J., Presser, N., and Broser, I. (1988). **Acceptor-exciton complexes in ZnO**: A comprehensive analysis of their electronic states by high-resolution magneto-optics and excitation spectroscopy. **Physics Review B**. 38: 9746.
- Han, S. J., Song, J. W., Yang, C. H., Park, S. H., Park, J. H., and Jeong, Y. H. (2002). A key to room-temperature ferromagnetism in Fe-doped ZnO; Cu. **Applied Physics Letters**. 81: 4212-4214.
- Hong, N. H., Sakai, J., Prellier, W., Hassini, A., Ruyter, A., and Gervais, F. (2004). Ferromagnetism in transition-metal-doped TiO₂ thin films. **Physical Review B**. 70: 195204.
- He, J., Xu, S., Yoo, Y., Xue, O., Lee, H. C., and Cheng, S. (2005). Room temperature ferromagnetic n-type semiconductor in (In_{1-x}Fe_x)₂O_{3-δ}. **Applied Physics Letters**. 86: 052503.

- Herranz, G., Ranchal, R., Bibes, M., Jaffre's, H., Jacquet, E., and Maurice, J. L. (2006). Co-doped (La,Sr)TiO_{3-δ}, a high Curie temperature diluted magnetic system with large spin polarization. **Physical Review Letters**. 96: 027207.
- Hilo, M. E., Dakhel, A. A., and Mohamed, A. Y. A. (2009). Room temperature ferromagnetism in nanocrystalline Ni-doped ZnO synthesized by co-precipitation. **Journal of Magnetism and Magnetic Materials**. 321: 2279-2283
- Hao, H., Qin, M., and Li, P. (2012). Structural, optical, and magnetic properties of Co-doped ZnO nanorods fabricated by a facile solution route. **Journal of Alloys and Compounds**. 515: 143-148.
- Jayakumar, O. D., Gopalakrishna, I. K., Sudakar, C., and Kulshreshtha, S. K. (2006). Synthesis of manganese doped ZnO single crystals and their magnetization studies. **Journal of Crystal Growth**. 294: 432-436.
- Kasuya, T. (1970). Mobility of the antiferromagnetic large polaron. **Solid State Communications**. 8: 1635-1638.
- Kale, S. N., Ogale, S. B., Shinde, S. R., Sahasrabuddhe, M., Kulkarni, V. N., and Greene, R. L. (2003). Magnetism in cobalt-doped Cu₂O thin films without and with Al, V, or Zn codopants. **Applied Physics Letters**. 82: 2100-2102.
- Kohan, A. F., Ceder, G., Morgan, D., and de Walle, C. G. V. (2000). First-Principles study of native point defects in ZnO. **Physical Review B**. 61: 15019-15027.
- Lee, H. J., Jeong, S. Y., Cho, C. R., and Park, C. H. (2002). Study of diluted magnetic semiconductor: Co-doped ZnO. **Applied Physics Letters**. 81: 4020-4022.
- Liao, Y.F., Huang, T. W., Lina, M. Z., Yu, K. L., Hsu, H. S., Lee, T. H., Lee, C. H., and Huang, J. C. A. (2007). X-ray study of the structure and magnetic

property of the co-doped ZnO nanoparticles prepared by thermal hydrolysis.

Journal of Magnetism and Magnetic Materials. 310: e818-e820.

Liu, H. L., Yang, J. H., Zhang, Y. J., Wang, Y. X., Wei, M. B., Wang, D. D., Zhao

L. Y., Lang J. H., and Gao, M. (2009). Ferromagnetism in Cu-doped ZnO nanoparticles at room temperature. **Journal of Materials Science : Mater**

Electron. 20: 628-631.

Munekata, H., Ohno, H., von Molnar, S., Segmuller, A., Chang, L. L., and Esaki, L.

(1989). Diluted magnetic III-V semiconductors. **Physical Review Letters**. 63: 1849-1852.

Matsumoto, Y., Murakami, M., Shono, T., Hasegawa, T., Fukumura, T., and

Kawasaki, M. (2001). Room-temperature ferromagnetism in transparent transition metal- doped titanium dioxide. **Science**. 291: 854-856.

Maensiri, S., Wongsaprom, W., Swatsitang, E., and Seraphin, S. (2007). Fe-doped

$\text{La}_{0.5}\text{Sr}_{0.5}\text{TiO}_{3-\delta}$ nanoparticles: A diluted magnetic oxide system. **Journal of Applied Physics**. 102: 076110.

Maensiri, S., Masingboon, C., Laokul, P., and Jareonboon, W. (2007). Egg white

synthesis and photoluminescence of plate like clusters of CeO_2 nanoparticles.

Crystal Growth and Design. 7: 950-955.

Nagai, Y., Kurimoto, T., Nagasaka, K., Nojiri, H., Motokawa, M., and Matsukura, F.

(2001). Spin Polarization Dependent Far Infrared Absorption in $\text{Ga}_{1-x}\text{Mn}_x\text{As}$.

Japanese Journal of Applied Physics. 40: 6231-6234.

Ohno, H. (1998). Making nonmagnetic semiconductors ferromagnetic. **Science**.

281: 951-956.

- Ohno, H. Matsukura, F., and Ohno, Y. (2002). General Report : Semiconductor Spin Electronics. **JSAP International**. 5: 4.
- Ogale, S. B., Choudhary, R. J., Buban, J. P., Lofland, S. E., Shinde, S. R., and Kale, S. N. (2003). High temperature ferromagnetism with a giant magnetic moment in transparent Co-doped SnO_{2-δ}. **Physical Review Letters**. 91: 077205.
- Özgür, Ü., Alivov, Y. I., Lui, C., Teke, A., Reshchikov, M. A., Dogan, A. V., Cho, S. J., and Morkoc, H. (2005). A comprehensive review of ZnO materials and devices. **Journal of Applied Physics**. 98: 041301.
- Philip, J., Theodoropoulou, N., Berera, G., Moodera, J. S., and Satpati, B. (2004). High-temperature ferromagnetism in manganese-doped indium–tin oxide films. **Applied Physics Letters**. 85: 777-779.
- Pearton, S. J., Norton, D. P., Frazier, R., Han, S. Y., Abernathy, C. R., and Zavada, J. M. (2005). Spintronics device concepts. **IEEE Progress-Circuits DevicesSystem**. 152: 312-322.
- Patterson, C. H. (2005). Magnetic defects promote ferromagnetism in Zn_{1-x}Co_xO. **Journal of Physics: Condensed Matter**. 1: 0512101.
- Peng, Y. Z., Liew, T., Song, W. D., An, C. W., Teo, K. L., and Chong, T. C. (2005). Structural and Optical Properties of Co-doped ZnO Thin Films. **Journal of Superconductivity: Incorporating Novel Magnetism**. 18: 1.
- Pivin, J. C., Socol, G., Mihailescu, I., Berthet, P., Singh, F., Patel, M. K., and Vincent, L. (2008). Structure and magnetic properties of ZnO films doped with Co, Ni or Mn synthesized by pulsed laser deposition under low and high oxygen partial pressures. **Thin Solid Films**. 517: 916-922.

- Pal, B., and Giri, P. K. (2010). High temperature ferromagnetism and optical properties of Co doped ZnO nanoparticles. **Journal of Applied Physics**. 108: 084322.
- Partha, P. P., and Manam, J. (2013). Photoluminescence and thermoluminescence studies of Tb³⁺ doped ZnO nanorods, **Materials Science and Engineering B**. 178: 400.
- Qi, J., Yang, Y., Zhang, L., Chi, J., Gao, D., and Xue, D. (2009). Room-temperature ferromagnetism in Er-doped ZnO thin films. **Scripta Materialia**. 60: 289-292.
- Qi, J., Gao, D., Liu, J., Yang, W., Wang, Q., Zhou, J., Yang, Y., and Liu, J. (2010). Magnetic properties of Er-doped ZnO films prepared by reactive magnetron sputtering. **Applied Physics A**. 100: 79-82.
- Roy, M., Mitchell, J. F., Ramirez, A. P., and Schiffer, P. (1998). Doping-induced transition from double exchange to charge order in La_{1-x}Ca_xMnO₃ near x = 0.50. **Physical Review B**. 58(9): 5185.
- Radovanovic, P. V., and Gamelin, D. R. (2003). High temperature ferromagnetism in Ni²⁺- doped ZnO aggregates prepared from colloidal diluted magnetic Semiconductor quantum dots. **Physical Review Letters**. 91: 157202.
- Ran, F. Y., Tanemura, M., Hayashi, Y., and Hihara, T. (2009). Effect of substrate temperature on the room-temperature ferromagnetism of Cu-doped ZnO films. **Journal of Crystal Growth**. 311: 4270-4274.
- Story, T., Galazka, R. R., Frankel, R. B., and Wolff, P. A. (1986). Carrier-concentration induced ferromagnetism in PbSnMnTe. **Physical Review Letters**. 56: 777.

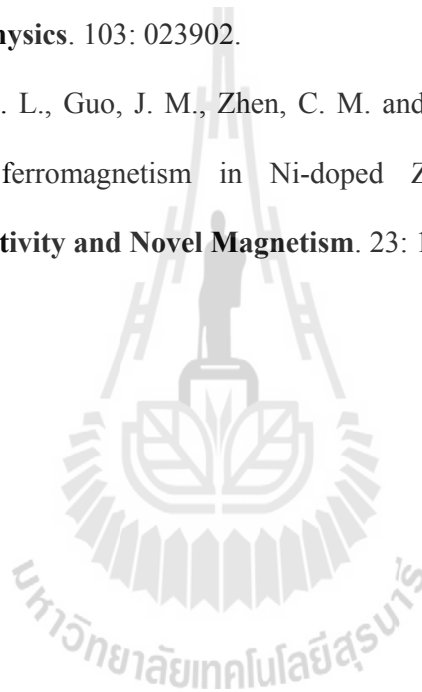
- Sawicki, M., Dietl, T., Kossut, J., Igalson, J., Wojtowicz, T., and Plesiewicz, W. (1986). Influence of s-d Exchange Interaction on Conductivity of $Cd_{1-x}Mn_xSe$: In in the Weakly Localized Regime. **Physics Review Letter**. 56: 508.
- Sun, X. W., and Kwok, H. S. (1999). Optical properties of epitaxially grown zinc oxide films on sapphire by pulsed laser deposition. **Journal of Applied Physics**. 86: 408.
- Sato, K., and Katayama-Yoshida, H. (2000). Material Design for Transparent Ferromagnets with ZnO-Based Magnetic Semiconductors. **Japanese Journal of Applied Physics**. 39: L555-L558.
- Saeki, H., Tabata, H., and Kawai, T. (2001). Magnetic and electric properties of vanadium doped ZnO films. **Solid State Communications**. 120: 439-443
- Schifgaarde van, M., and Mryasov, O. N. (2001). Anomalous exchange interactions in III-V dilute magnetic semiconductors. **Physics review B**. 63: 233205.
- Sharma, S. D., Hwang, E. H., and Kaminski, A. (2003). Temperature-dependent magnetization in diluted magnetic semiconductors. **Physical Review B**. 67: 155-201(16).
- Shinde, S. R., Ogale, S. B., Das, S. S., Simpson, J. R., Drew, H. D., and Lofland, S. E. (2003). Ferromagnetism in laser deposited anatase $Ti_{1-x}Co_xO_{2-\delta}$ films. **Physical Review B**. 67: 115211.
- Shen, L., Wu, R. Q., Pan, H., Peng, G. W., Yang, M., Sha, Z. D., and Feng, Y. P. (2008). Mechanism of ferromagnetism in nitrogen-doped ZnO: First-principle calculations. **Physical Review B**. 78(7): 073306.

- Sharma, A., Dhar, S., Singh, B. P., and Kundu, T. (2011). Influence of Tb incorporation on the structural and the optical properties of ZnO Nanoparticles, **Solid State Communications**. 151: 1885.
- Sharma, V. K., Najim, M., Srivastav, A. K., and Varma, G. D. (2012). Structural and magnetic studies on transition metal (Mn,Co) doped ZnO nanoparticles. **Journal of Magnetism and Magnetic Materials**. 324: 683-689.
- Saravanan, R., Santhi, K., Sivakumar, N., Narayanan, V., and Stephen, A. (2012). Synthesis and characterization of ZnO and Ni doped ZnO nanorods by thermal decomposition method for spintronics application. **Materials Characterization**. 67: 10-16.
- Tiwari, A., Bhosle, V. M., Ramachandran, S., Sudhakar, N., Narayan, J., and Budak, S. (2006). Ferromagnetism in Co doped CeO₂; Observation of a giant magnetic moment with a high Curie temperature. **Applied Physics Letters**. 88: 142511.
- Tan, Y., Fangb, Z., Chen, W., and Hea, P. (2011). Structural, optical and magnetic properties of Eu-doped ZnO films. **Journal of Alloys and Compounds**. 509: 6321.
- Ueda, K., Tabata, H., and Kawai, T. (2001). Magnetic and electric properties of transition metal-doped ZnO films. **Applied Physics Letters**. 79: 988-990.
- Wolf, S. A., Awschalom, D. D., Buhrman, R. A., Daughton, J. M., Molnar vo, S., Roukes, M. L., Chtchelkanov, A. Y., and Treger, D. M. (2001). Spintronics: A Spin-Based Electronics Vision for the Future, **Science**. 294: 1488.

- Wang, Z., Wang, W., Tang, J., Tung, L. D., Spinu, L., and Zhou, W. (2003). Extraordinary Hall effect and ferromagnetism in Fe-doped reduced rutile. **Applied Physics Letters**. 83: 518-520.
- Wongsaprom, W., Swatsitang, E., Srijaranai, S., Maensiri, S., and Seraphin, S. (2007). Room temperature ferromagnetism in Co-doped $\text{La}_{0.5}\text{Sr}_{0.5}\text{TiO}_{3-\delta}$ nanoparticles. **Applied Physics Letters**. 90: 1625061.
- Wang, B., Xia, C., Iqbal, J., Tang, N., Sun, Z., Lv, Y., and Wu, L. (2009). Influences of Co doping on the structural, optical and magnetic properties of ZnO nanorods synthesized by hydrothermal route. **Solid State Sciences**. 11: 1419-1422.
- Wu, Z., Liu, X. C., and Huang, J. C. A. (2012). Room temperature ferromagnetism in Tb- doped ZnO nanocrystalline films. **Journal of Magnetism and Magnetic Materials**. 324: 642.
- Wua, Z., Liu, X. C., and Huang, J. C. A. (2012). Room temperature ferromagnetism in Tb doped ZnOnanocrystalline films. **Journal of Magnetism and Magnetic Materials**. 324: 642-644.
- Xu, X., and Cao, C. (2009). Structure and ferromagnetic properties of Co-doped ZnO powders. **Journal of Magnetism and Magnetic Materials**. 32: 12216.
- Xu, X., and Cao, C. (2010). Hydrothermal synthesis of Co-doped ZnO flakes with room temperature ferromagnetism. **Journal of Alloys and Compounds**. 501: 265-268.
- Xu, L., Shen, K., and Xu, Q. (2011). Room temperature magnetism in Co-doped ZnO nanorods. **Journal of Superconductivity and Novel Magnetism**. 24: 176-177.

- Xu, X., Cao, C., and Chen, Z. (2011). Effects of temperature and atmosphere on the magnetic properties of Co-doped ZnO rods. **Journal of Magnetism and Magnetic Materials**. 323: 1886-1889.
- Yu, Y. L., Harrington, S., Yates, K. A., Mei, M., Blamire, M. G., MacManus-Driscoll, J. L. (2005). Epitaxial ferromagnetic $\text{Cu}_{2-x}\text{Mn}_x$ films on (001) Si by near-room-temperature electrodeposition. **Applied Physics Letters**. 87: 222108.
- Yang, J. C., Na, H. G., Kwak, D. S., and Kim, H. W. (2013). ZnO-cored heteronanowires sheathed with Cu shells: Structural, magnetic, and photoluminescence properties. **Surface and Coatings Technology**. 228: 5374-5378.
- Zener, C. (1951). Interaction Between the d Shells in the Transition Metals. **Physical Review**. 81: 440-444.
- Zener, C. (1951). Interaction between the d -Shells in the Transition Metals II. Calculation of the Weiss Factors in Fe, Co, and Ni. **Physical Review**. 83: 299-301.
- Zutic, I., Fabian, J., and Sarma, D. (2004). Spintronics: Fundamentals and applications. **Review of Modern Physics**. 76: 323.
- Zhou, S., Potzger, K., Cklich, A. M., Eichhorn, F., Helm, M., Skorupa, W., and Fassbender, J. (2008). Structural and magnetic properties of Tb implanted ZnO single crystals. **Nuclear Instruments and Methods in Physics Research B**. 266: 589-593.

- Zhang, Y., Er-Wei, S., and Zhi-Zhan, C. (2008). Synthesis and magnetic properties of Mn-doped ZnO hollow nanospheres. **Journal of Crystal Growth**. 310: 2928-2933.
- Zhou, S., Potzger, K., Talut, G., Reuther, H., Borany von, J., Grötzschel, R., Skorupa, W., Helm, M., Fassbender, J., Volbers, N., Lorenz, M., and Herrmannsdörfer, T. (2008). Fe-implanted ZnO: Magnetic precipitates versus dilution. **Journal of Applied Physics**. 103: 023902.
- Zhao, R. B., Hou, D. L., Guo, J. M., Zhen, C. M. and Tang, G. D. (2010). Room temperature ferromagnetism in Ni-doped ZnO powders. **Journal of Superconductivity and Novel Magnetism**. 23: 1261-1263.





APPENDICES

APPENDIX A

RESULTS AND DISCUSSION ON NiO AND Fe-DOPED NiO SYSTEM

1. Introduction

In recent years, diluted magnetic semiconductors (DMSs) produced by doping a small amount of magnetic impurities in semiconductors have attracted much attention due to their potential application in spintronics^[1-5]. Early and ongoing efforts on diluted magnetic impurity in III-V or II-VI compound were intensively studied even though they show ferromagnetism only at low temperatures^[6, 7]. Recently, transition metal (3d) ion doped oxide semiconductors (O-DMSs) such as ZnO, TiO₂, SnO₂, In₂O₃, and CeO₂ have been investigated extensively^[8-11]. These O-DMSs exhibit ferromagnetism (FM) at room temperature (RT) and even at well above RT. They are also optically transparent enabling them to be promising candidates for magneto-opto-electronic applications. So far, most of the RT O-DMSs reported in literatures have *n*-type DMS and non-cubic crystal structure. It is anticipated that if one can introduce RT ferromagnetism in *p*-type DMS and cubic systems, it will facilitate the integration of spintronic devices with advanced silicon microelectronic devices.

Nickel Oxide (NiO) has a cubic structure with lattice parameter $a = 0.41771$ nm^[12]. It can become a *p*-type semiconductor after introduction of Ni²⁺ vacancies or doping with monovalent cation^[13]. Magnetic properties of bulk NiO reveals

antiferromagnetic behavior ($T_N = 523$ K) [14]. The size to the nanometer scale was affected with magnetic properties of NiO and this has been reported in literatures [15, 16]. Wang et al. [17] first reported the RT-FM observed in Fe-doped NiO nanoparticles of size 30–60 nm synthesized by a chemical coprecipitation method and post-thermal decomposition processing. A maximum magnetization of about 0.575 emu/g has been measured at 10 kOe in $\text{Ni}_{0.98}\text{Fe}_{0.02}\text{O}$. The authors concluded that the observed RT-FM and the large loop shift at low temperature could be associated with ferromagnetic clusters and ferromagnetic/antiferromagnetic coupling due to the composition inhomogeneity. Since then, more studies on Fe-doped NiO system have been reported. Lin et al. [18] reported that Fe-doped NiO nanopowders exhibit RT-FM mainly arising from the double exchange mechanism through the doped Fe ions and free charge carriers. He et al. [19, 20] studied the magnetic properties of Fe-doped NiO synthesized by co-precipitation. The samples exhibited large RT-FM behavior ascribed to a ferromagnetic impurity phase. Simultaneously, an exchange bias and training effect were also observed in all the samples, indicating the possibility of the existence of a strong ferromagnetic/antiferromagnetic exchange coupling in the samples. Recently, Manna et al. [21] reported RT-FM in Fe-doped NiO nanorods synthesized by the hydrothermal method. They found that incorporation of Fe into NiO induces ferromagnetism with high coercivity, and ferromagnetic properties significantly improved with increase of Fe concentration. The authors proposed that the surface spins and shape anisotropy also play important roles in the magnetic properties of Fe-doped NiO nanorods. Most recently, Khemprasit et al. [22] investigated the effect of calcining temperature on structural and magnetic properties of Fe-doped NiO nanoparticles prepared by diol-based sol-gel process. RT-FM for all

calcined samples was observed and the origin of ferromagnetism could be caused by the double exchange interaction between the induced magnetic Fe ions and the defects. When the calcining temperature was increased, the saturation magnetization decreased whereas the coercivity increased, corresponding to the less dense and larger particles. It is seen from the above that synthesis route plays important roles in magnetic properties of Fe-doped NiO system. In addition, most of these synthesis conditions involve a strictly controlled synthesis environment, expensive reagent, and complicated procedures. Therefore, alternative simple and cost-effective routes to synthesize NiO-based magnetic oxides are needed.

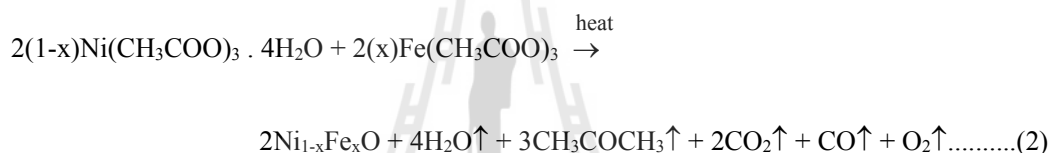
In the present work, we report RT-FM nanocrystalline Fe-doped NiO powders (i.e., $\text{Ni}_{1-x}\text{Fe}_x\text{O}$; $x = 0, 0.005, 0.01, 0.015, 0.02, \text{ and } 0.025$) synthesized by a simple direct thermal decomposition of high purity Ni and Fe acetates in air at $600\text{ }^\circ\text{C}$ for 6 h. This direct thermal decomposition method is fast, simple, and cost-effective for synthesis of nanocrystalline Fe-doped NiO powders. The structure and morphology of synthesized Fe-doped NiO samples were characterized by X-ray diffraction (XRD), energy-dispersive x-ray spectroscopy (EDS), scanning electron microscopy (SEM), and transmission electron microscopy (TEM). The RT magnetic properties of the Fe-doped NiO samples were also investigated, and the origin of ferromagnetism observed in the prepared samples is discussed.

2. Experimental

For the synthesis of Fe-doped NiO nanoparticles, nickel (III) acetate tetrahydrate (99.998% Purity, Aldrich), and iron (III) acetate (99.995% Purity, Aldrich) were mixed using a mortar and pestle until a homogeneous mixture powder was obtained.

For each sample, the mole ratio of Fe:Ni was kept corresponding to the nominal composition of $\text{Ni}_{1-x}\text{Fe}_x\text{O}$ ($x = 0, 0.005, 0.01, 0.015, 0.02, \text{ and } 0.025$). The mixed powder was then placed in an alumina crucible covered by alumina lid before loading it into the oven, and was thermally decomposed in air at $600\text{ }^\circ\text{C}$ for 6 h. The formation of pure NiO and $\text{Ni}_{1-x}\text{Fe}_x\text{O}$ ($x = 0.005, 0.01, 0.015, 0.02, \text{ and } 0.025$) can be explained by the following reactions:

For pure NiO,



All the process reactions suggest that the thermal events are related to the combustion of acetone (CH_3COCH_3), water (H_2O), carbon dioxide (CO_2), carbon monoxide (CO), and oxygen (O_2) in the precursor. A similar process is applied for the preparation of Fe-doped NiO.

The prepared samples were analyzed by means of X-ray diffraction (XRD) using $\text{CuK}\alpha$ radiation with $\lambda = 0.15418\text{ nm}$ (Phillips PW3040, The Netherlands). The particle size and external morphology of the nanocrystalline samples were characterized by SEM attached with EDS (LEO SEM 1450VP, UK) and TEM (JEOL TEM 2010). The magnetic properties were examined at RT (293K) using a vibrating sample magnetometer (Lake Shore VSM 7403, USA).

3. Results and discussion

Fig. 1 shows XRD patterns of all the samples having peaks that correspond to the (111), (200), (220), (311), and (222) planes for a cubic structure of NiO in the standard data^[11]. This indicates that the cubic structure is not affected by Fe substitution. No diffraction peaks of Ni and other impurities such as Fe, Fe₂O₃, Fe₃O₄, and NiFe₃O₄ were observed. The crystallite sizes of all samples were calculated from X-ray line broadening of the reflections of (200) using Scherrer's equation (i.e., $D = K\lambda / (\beta \cos \theta)$), where λ is the wavelength of the X-ray radiation, K is a constant taken as 0.89, θ is the diffraction angle, and β is the full width at half maximum (FWHM)^[23], and were obtained to be 34 nm, 31 nm, 29 nm, 28 nm, 29 nm, and 26 nm for the samples with $x = 0, 0.005, 0.01, 0.015, 0.02, \text{ and } 0.025$, respectively. The crystallite sizes of the samples whose Fe concentration x varies from 0 to 0.025 have a little decrease on increasing the Fe concentration, in agreement with the results reported previously by Wang et al.^[16] These results indicate that the effective Fe ions disturb the NiO crystal structure. The values of lattice parameter a of all the samples calculated from the XRD spectra are close to that reported for NiO ($a = 0.41771$ nm) in the standard data^[11]. The lattice parameters are also summarized in Table 1.

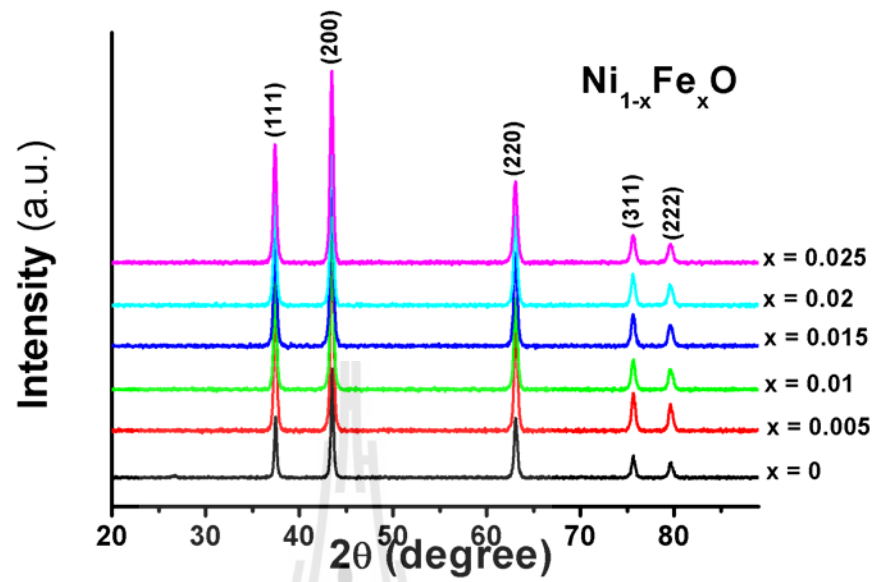


Fig. 1 XRD patterns of nanocrystalline Fe-doped NiO powders thermally decomposed in air at 600°C for 6 h.



Table 1. Average particle sizes from XRD line broadening, cubic lattice parameter a calculated from XRD patterns of nanocrystalline Fe-doped NiO samples thermally decomposed in air at 600 °C for 6h.

samples	Particle size (nm) From XRD	Cubic lattice parameter a (nm)	M_s at 10 kOe (emu/g)	H_c (Oe)
NiO	34.13 ± 0.99	0.4176 ± 0.000196	-	-
Ni _{0.995} Fe _{0.005} O	30.73 ± 1.07	0.4175 ± 0.000132	0.033	155.5
Ni _{0.990} Fe _{0.010} O	28.95 ± 0.21	0.4172 ± 0.000122	0.044	219.9
Ni _{0.985} Fe _{0.015} O	28.17 ± 0.15	0.4174 ± 0.000146	0.074	223.4
Ni _{0.980} Fe _{0.020} O	28.80 ± 1.13	0.4173 ± 0.000123	0.099	357.1
Ni _{0.975} Fe _{0.025} O	26.30 ± 0.42	0.4171 ± 0.000107	0.102	371.2

The morphology of the Fe-doped NiO samples was investigated by SEM. It is clearly seen from the SEM micrographs (Figs. 2(a)-(f)) that the morphology of all the materials are agglomerated particles with sizes of ~50–300 nm. It is known from XRD results that the crystal sizes are 34.13 ± 0.99 nm, 30.73 ± 1.07 nm, 28.95 ± 0.21 nm, 28.17 ± 0.15 nm, 28.80 ± 1.13 nm, and 26.3 ± 0.42 nm for the samples of $x = 0$, 0.005, 0.01, 0.015, 0.02, and 0.025, respectively. These were larger than those obtained from X-ray line broadening due to agglomeration.

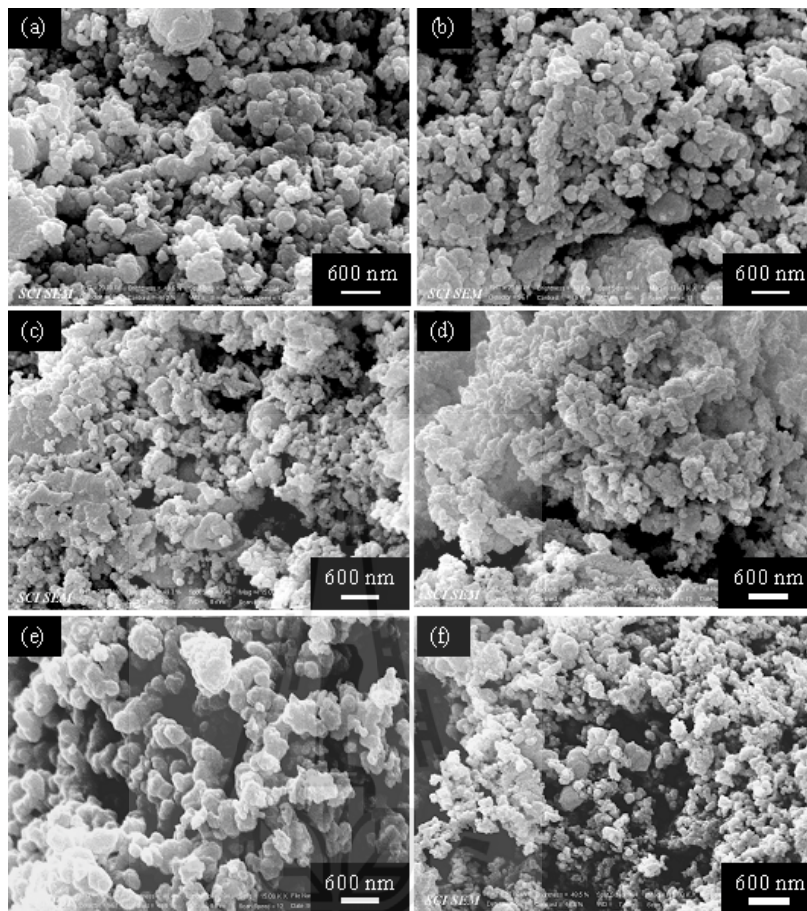


Fig. 2 SEM micrographs of the Fe-doped NiO nanoparticles thermally decomposed in air at 600 °C for 6 h. (a) $x = 0$, (b) $x = 0.005$, (c) $x = 0.01$, (d) $x = 0.015$, (e) $x = 0.02$, and (f) $x = 0.025$

The morphology, structure, and elemental composition of NiO and Ni_{0.98}Fe_{0.02}O samples were further investigated by TEM. TEM bright field images (Figs. 3(a) and 3(b)) show nanoparticles with sizes of ~ 30–50 nm for the NiO and of ~ 20–40 nm for the Ni_{0.98}Fe_{0.02}O. The corresponding selected-area electron diffraction (SAED) patterns (inset in Fig. 3) of both samples show spotty ring patterns of cubic structure without any contribution from Fe, Fe₂O₃, and Fe₃O₄ phases, which is in agreement

with the XRD results. Fig. 3(c) shows the elemental composition of $\text{Ni}_{0.98}\text{Fe}_{0.02}\text{O}$ samples revealed by EDS. We observed peaks of Ni and O without Fe. The Au came from gold contamination. Our results indicate that either Fe does not form metallic or stoichiometric compound of secondary phases or the concentration is below the detection limit. It may also be suggested that Fe ions were substituted into Ni in Fe-doped NiO structure. Therefore, the ferromagnetism of our nanocrystalline Fe-doped NiO powders should not come from secondary phases of Fe.

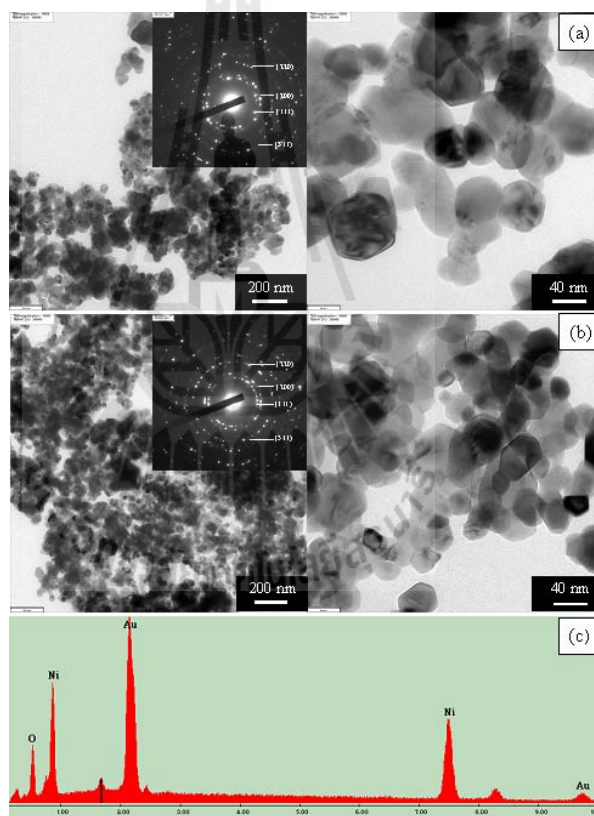


Fig. 3 (a) and (b) are TEM bright field images with corresponding selected-area electron diffraction (SAED) patterns (insets) of NiO and $\text{Ni}_{0.98}\text{Fe}_{0.02}\text{O}$ samples thermally decomposed in air at 600 °C for 6 h, respectively. (c) EDS spectrum of $\text{Ni}_{0.98}\text{Fe}_{0.02}\text{O}$ sample thermally decomposed in air at 600 °C for 6 h.

Fig. 4 shows the field dependence of specific magnetization (M - H curve) of the NiO and Fe-doped NiO samples obtained from RT VSM measurement. The undoped NiO sample exhibits antiferromagnetic behavior, whereas all samples with nominal Fe concentration exhibit ferromagnetic behavior. Hysteresis loops can be observed at 300 K showing obvious ferromagnetic characteristics. The saturation magnetization increased from ~ 0.033 emu/g to 0.102 emu/g at 10 kOe by increasing the Fe-doped concentration. These values are lower than those of previous reports on Fe-doped NiO system^[17, 18, 21]. From Fig. 4, the coercive force (H_c) was obtained to be 155.5 Oe, 219.9 Oe, 223.4 Oe, 357.1 Oe, and 371.2 Oe for the samples of $x = 0, 0.005, 0.01, 0.015, 0.02, \text{ and } 0.025$, respectively. These values are lower than ~ 614 Oe for $\text{Ni}_{0.098}\text{Fe}_{0.02}\text{O}$ nanorods reported by Manna et al^[21]. The lower H_c in our case is possibly due to their lower crystal sizes that can be explained on the basis of domain structure, critical diameter, and the anisotropy of the crystal^[24].

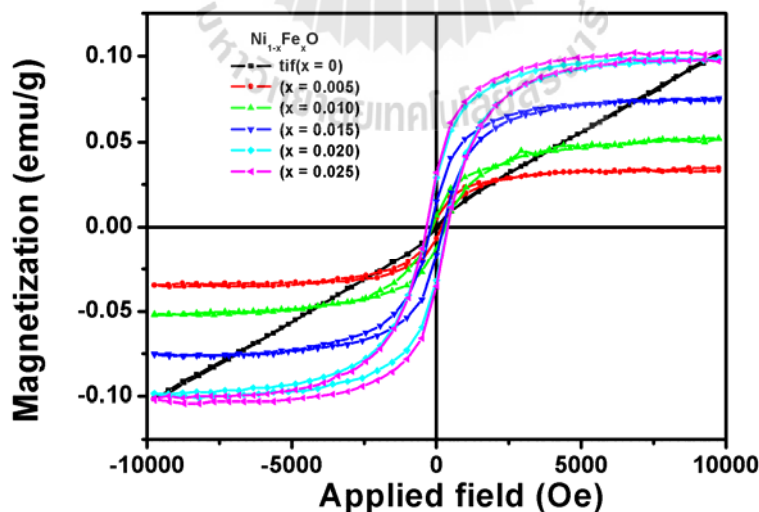
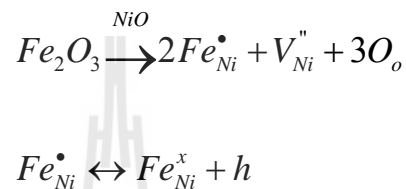


Fig. 4 Magnetization of nanocrystalline Fe-doped NiO samples as a function of field measured at RT.

From our results, we exclude Fe segregation as the origin of the ferromagnetism in our Fe-doped NiO samples, and thus, their ferromagnetisms are intrinsic. In case of the undoped NiO sample, its antiferromagnetic behavior below Neel temperature (573 K) can be understood through the ordinary two sublattice model, while as doped by magnetic Fe ions, some defects could be introduced into NiO as follows [17]:



This would interrupt the magnetic order in NiO grains and cause relatively weak coupling between the sublattices giving rise to ferromagnetism by double exchange through the introduced magnetic Fe ions and free charge carriers [25]. Therefore, the increase of Fe-doped concentration enhances the double exchange interaction in Fe-doped NiO samples, which leads to higher magnetic moment, as previously reported by Manna et al [21]. However, further work is needed to achieve a thorough understanding, and this will be of great interest to researchers in the field of diluted magnetic oxides.

4. Conclusions

In summary, nanocrystalline Fe-doped NiO powders with ~26–34 nm in size were successfully synthesized by a simple direct thermal decomposition method, and their structures, morphology, and magnetic properties were investigated. XRD and SAED analyses of the samples showed that they are single phase without the presence of any

Fe-related impurity phases such as Fe, Fe₂O₃, Fe₃O₄, or NiFe₃O₄. The NiO sample exhibits antiferromagnetic behavior, whereas all the Fe-doped samples are ferromagnetic at RT. The saturation magnetization increased from ~0.033 emu/g to 0.102 emu/g at 10 kOe by increasing the Fe-doped concentration. The increase of Fe-doped concentration enhances the double exchange interaction in Fe-doped NiO samples, which leads to higher magnetic moment. This work demonstrates that a simple method can be used to incorporate Fe into NiO for making diluted magnetic oxides, which may potentially be useful for many nanotechnology applications.

Acknowledgments

The authors would like to thank the Department of Chemistry for providing VSM facilities, the Department of Physics, Ubon Ratchathani University, for providing XRD facilities, and The National Metal and Materials Technology Center (MTEC) for providing TEM facilities. This work was supported by Suranaree University of Technology (SUT) and by the Office of the Higher Education Commission under NRU project of Thailand.

References

1. H. Ohno, *Science* **281**, 951 (1998)
2. G.A. Prinz, *Science* **282**, 1660 (1998)
3. S. A. Wolf, D. D. Awschalom, R. A. Buhrman, J. M. Daughton, S. V. Molnár, M. L. Roukes, A. Y. Chtchelkanova, and D. M. Treger, *Science* **294**, 1488 (2001)
4. S. J. Pearton, C. R. Abernathy, D. P. Norton, A. F. Hebard, Y. D. Park, L. A. Boatner, and J. D. Budai, *Mater. Sci. Eng. R* **40**, 137 (2003)
5. S. D. Sarma, *Am. Sci.* **89**, 516 (2001)
6. H. Ohno, A. Shen, F. Matsukura, A. Oiwa, A. Endo, S. Katsumoto, and Y. Iye, *Appl. Phys. Lett.* **69**, 363 (1996)
7. J. K. Furdyna and J. Kossut, *DMSs Semiconductor and Semimetals*. Vol. **25**, Academic Press, New York (1998)
8. W. Prellier, A. Fouchet, and B. Mercey, *J. Phys. Condens. Matter.* **15**, R1583 (2003)
9. S. J. Pearton, W. H. Heo, M. Ivill, D. P. Norton, and T. Steiner, *Semicond. Sci. Technol.* **19**, R59 (2004)
10. J. M. D. Coey, *Curr. Opin. Solid State Mater. Sci.* **10**, 83 (2006)
11. S. Maensiri, S. Phokha, P. Laokul, and S. Seraphin, *J. Nanosci. Nanotech.* **9**, 6415 (2009).
12. JCPDS Card No. 78-0429, International Centre for Diffraction Data
13. A. J. Bosman and C. Crevecoeur, *Phys. Rev.* **144**, 763 (1966)

14. L. C. Bartel and B. Morosin, *Phys. Rev. B*, **3**, 1039 (1971)
15. R. H. Kodama, S. A. Makhlof, and A. E. Berkowitz, *Phys. Rev. Lett.* **79**, 1393 (1997)
16. L. Li, L. Chen, R. Qihe, and G. Li, *Appl. Phys. Lett.* **89**, 134102 (2006)
17. J. F. Wang, J. N. Cai, Y. H. Lin, and C. W. Nan, *Appl. Phys. Lett.* **87**, 202501 (2005)
18. Y. H. Lin, J. Wang, J. Cai, M. Ying, R. Zhao, M. Li, and C. W. Nan, *Phys. Rev. B*, **73**, 193308 (2006)
19. J. H. He, S. L. Yuan, Z. M. Tian, Y. S. Yin, P. Li, Y. Q. Wang, K. L. Liu, S. J. Yuan, X. L. Wang, and L. Liu, *J. Magn. Magn. Mater.* **320**, 3293 (2008)
20. J. H. He, S. L. Yuan, Y. S. Yin, Z. M. Tian, P. Li, Y. Q. Wang, K. L. Liu, and C. H. Wang, *J. Appl. Phys.* **103**, 023906 (2008)
21. S. Manna, A. K. Deb, J. Jagannath, and S. K. De, *J. Phys. Chem.* **112**, 10659 (2008)
22. J. Khemprasit, S. Kaen-ngam, B. Khumpaitool, and P. Kamkhon, *J. Magn. Magn. Mater.* **320**, 2408 (2011)
23. B. D. Cullity and S. R. Stock, *Elements of X-ray Diffraction*, 3rd ed., Prentice Hall, New York (2001)
24. M. George, A. Mary John, S. S. Naira, P. A. Joy, and M. R. Anantharaman, *J. Magn. Magn. Mater.* **302**, 190 (2006)
25. K. Sato and H. Katayama-Yoshida, *J. Japan, Appl. Phys.* **39**, L555 (2000)

APPENDIX B

PUBLICATION AND PRESENTATION

B. 1 List of publications

Noipa, K., Labuayai, S., Swatsitang, E., and Maensiri, S. (2014). Room-temperature ferromagnetism in nanocrystalline Fe-doped NiO powders synthesized by a simple direct thermal decomposition method. **Electronic Materials Letters**. 10(1). 147-152.

Noipa, K., Rujirawat, S., Yimnirun, R., Promarak, V., Maensiri, S. (2014). Synthesis, structural, optical and magnetic properties of Cu-doped ZnO nanorods prepared by a simple direct thermal decomposition route. **Applied Physics A**. 117. 927-935.

B. 2 List of oral presentations

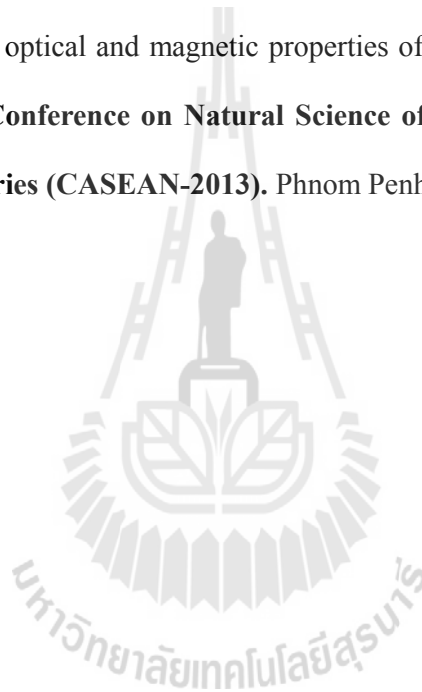
Noipa, K., Rujirawat, S., Yimnirun, R., Promarak, V., Maensiri, S. (2014). Synthesis, structural, optical and magnetic properties of Tb-doped ZnO nanorods prepared by a simple direct thermal decomposition route. In **The 12th International Nanotech Symposium & Nano-Convergence Expo**. Coex, Seoul, Korea.

Noipa, K., Rujirawat, S., Yimnirun, R., Pinitsoontorn, S., Maensiri, S. (2014). Structural and magnetic properties of thermally decomposed ZnO-based nanorods. In **The 4th Thailand International Nanotechnology Conference 2014**. Convention Center, Thailand Science Park, Pathumthani, Thailand.

B. 3 List of poster presentations

Noipa, K., Rujirawat, S., Yimmirun, R., Promarak, V., Maensiri, S. (2014). Structure, optical and Magnetic Properties of Thermally Decomposed Ni-doped ZnO Nanorods. **The 27th International Microprocessor and Nanotechnology Conference (MNC)**. In Hilton Fukuoka Sea Hawk, Fukuoka, Japan.

Noipa, K., Rujirawat, S., Yimmirun, R., Promarak, V., Maensiri, S. (2013). Synthesis, structural, optical and magnetic properties of RE-doped ZnO nanorods. In **The 3rd Academic Conference on Natural Science of Master and Ph.D. Student from ASEAN countries (CASEAN-2013)**. Phnom Penh Cambodia.



CURRICULUM VITAE

Name Mr. Kiattisak Noipa

Date of Birth November 25, 1976

Place of Birth 215 Moo 2 Tambol Chaiso, Chumphae Didtrict, Khon Kaen Province, 40130, Thailand.

Education

1995 - 1999 Mahasarakham University, Mahasarakham, Thailand.
B. Ed. Science-Physics.

2008- 2010 Ubon Ratchathani University, Thailand.
M. Sc. Physics.

2010-2015 Suranaree University of Technology, Nakhon Ratchasima, Thailand, Ph.D. Physics.

Position and Place of Work Samyangwittayayon school, Khon Kaen, Thailand.

